Micro- and macro-rheological studies of the structure and association dynamics of biopolymer gels

by

Caroline Elizabeth Wagner

B.Eng., McGill University (2013)
S.M., Massachusetts Institute of Technology (2015)

Submitted to the Department of Mechanical Engineering
in partial fulfillment of the requirements for the degree of

Doctor of Philosophy in Mechanical Engineering

at the

MASSACHUSETTS INSTITUTE OF TECHNOLOGY

June 2018

Author ..... Signature redacted
Department of Mechanical Engineering
May 4, 2018

Certified by ..... Signature redacted
Gareth H. McKinley
Professor, Mechanical Engineering
Thesis Supervisor

Certified by ..... Signature redacted
Katharina Ribbeck
Professor, Biological Engineering
Thesis Supervisor

Accepted by ..... Signature redacted
Rohan Abeyaratne
Chairman, Committee on Graduate Students

Micro- and macro-rheological studies of the structure and association dynamics of biopolymer gels

by
Caroline Elizabeth Wagner

Submitted to the Department of Mechanical Engineering
on May 4, 2018, in partial fulfillment of the
requirements for the degree of
Doctor of Philosophy in Mechanical Engineering

Abstract

The cross-linked polymeric microstructures of biological hydrogels (or biogels) give rise to their mechanical properties, which in turn contribute to their proper biological function. For example, cartilage is stiff, elastic, and capable of withstanding substantial compressive forces in the knee, while saliva is thin, highly lubricious, and crucial for the maintenance of oral health. Quantification and modeling of the mechanical properties of these materials can provide insight into their microstructures, which is particularly important when structural changes are associated with impaired biological function.

In this thesis, we use a combination of rheological testing and constitutive modeling to study this relationship between microstructure and mechanical properties in three biologically-relevant complex fluid systems. First, we explore the network structure and association dynamics of reconstituted mucin gels using micro- and macrorheology in order to gain insight into how environmental factors, including pathogens and therapeutic agents, alter the mechanical properties of fully-constituted mucus. We find that analyses of thermal fluctuations on the length scale of micron-sized particles are not predictive of the linear viscoelastic response of mucin gels. However, when taken together, the results from both techniques help to provide complementary insight into the structure of the network. For instance, we show that macroscopic stiffening of mucin gels can be brought about in different ways by targeting specific associations within the network using environmental triggers such as modifications to the pH, surfactant, and salt concentration. Additionally, by varying the size of the microrheological probe particles, we show that the disagreement between the rheological techniques on both length scales can be largely attributed to microphase separation and the presence of localized gel regions of varying stiffness. This finding is further supported through imaging techniques and direct visualization of the mucin network.

As a second system, we study the temporal stability of saliva and its sensitivity to degradation in order to highlight the importance of considering sample age and enzymatic degradation when reporting extensional rheological measurements of saliva. Measurements show that the shear rheology of salivary mucin solutions (as measured by steady shear viscosity and small amplitude oscillatory shear (SAOS)) is quite insensitive to sample age over a 24 hour period following sample collection. By contrast, the filament thinning dynamics vary dramatically, with the characteristic relaxation time of the saliva and the breakup time of a fluid thread decreasing significantly with sample age. We interpret our results within the framework of a Sticky Finitely Extensible Network (SFEN) model which respects the known physical dimensions and properties of the mucin molecules in saliva, and models them as a network of physically associating and finitely extensible polymer chains. We show that the

model can accurately capture the changes observed in the filament thinning dynamics with sample age by incorporating a steady decrease in the molecular weight of the supramolecular aggregates of mucin.

As a third and final system, we develop a fractional calculus-based framework for improving the quantification of the mechanical properties of polysaccharide-based food solutions in order to facilitate the development of specific textures for liquid food consumption and for the design of dysphagia products. We demonstrate that fractional rheological models, including the fractional Maxwell model (FMM) and the fractional Jeffreys model (FJM), are able to succinctly and accurately predict the linear and nonlinear viscoelastic response of these food solutions and outperform conventional multi-mode Maxwell models with up to 50 physical elements in terms of the goodness of fit to experimental data. By accurately capturing the shear viscosity of the various liquid food solutions at a shear rate widely deemed relevant for oral evaluation of liquid texture, we show that two of the constitutive parameters of the fractional Maxwell model can be used to construct a state diagram that succinctly characterizes both the viscous and elastic properties of the different fluids.

The experimental and theoretical tools employed to interpret the underlying microstructures of the biological fluids considered in these three studies are diverse, ranging from microrheological measurements to the adaptation and development of appropriate nonlinear polymeric constitutive models. As a result, the findings of this thesis should provide a starting point for interpreting the mechanical properties of a variety of complex fluids in a broad range of contexts. In particular, one application for which these techniques have already shown promise is in the emerging use of the material properties of physiological fluids as biomedical diagnostics. By continuing to develop analytical methods for improving the understanding of the relationship between rheology and biological structure, it is expected that these methods will be beneficial in studying the etiology and pathological basis for a number of medical conditions such as preterm birth and cystic fibrosis.

Thesis Supervisor: Gareth H. McKinley
Title: Professor, Mechanical Engineering

Thesis Supervisor: Katharina Ribbeck
Title: Professor, Biological Engineering

Acknowledgments

This work would not have been possible without the support and encouragement of my two advisors, Gareth and Katharina.

I joined Gareth's lab soon after arriving at MIT, and I could not have ended up with a better mentor and scientist. It goes without saying that Gareth is a giant in his field and I have learned an incredible amount from him, but beyond his wealth of knowledge he has a truly unique way of bringing out the best in his students, and helping them gain the confidence over time to explore things independently. It took me a while to figure out my career path (I am still not sure that I have it figured out), but every time I came up with a new idea Gareth threw his support behind me enthusiastically. This PhD journey has been immensely challenging for me both intellectually as well as psychologically and emotionally, and I have benefited so much from Gareth's presence and support in every possible way.

I joined Katharina's lab during the third year of my PhD, and I am so grateful that she took on a mechanical engineering student who knew little to nothing about biological engineering at the time. Thanks to her guidance, support, and confidence in me (generally exceeding that which I had in myself), I like to think that I now know a little bit. Katharina inspires in all of her students the notion that if you believe that a story is worth telling, it can be told, and I feel very lucky that I got to be part of her scientific vision.

I would also like to thank my third committee member Al Grodzinsky, who I had the privilege of TA-ing for during my third year. Al is one of the kindest and brightest people at MIT, and someone I truly look up to as a role model of an excellent teacher and mentor. Additionally, although he was not officially my committee member, I would like to thank Michael Rubinstein from whom I learned an incredible amount during our time working together. Michael's immense knowledge and attention to detail helped to elevate our work to levels that simply would not have been possible without him.

I had the privilege of working with an awesome team of students in both the NNF and Biogel groups over the years. Early on I benefited so much from the presence of Adi and Alex in the NNF, who were excellent mentors, teachers, and friends. I am also very grateful to Justin, Sid, Bavand, Michela, Divya, Thibaut, Safa, Ahmed, Anoop, Jianyi, Crystal, Jake, Dayong, Jai, Shabnam, Miguel, Michelle, Philippe, Yonatan, and Amir for their friendship and help along the way, and to Setareh for helping me keep things in perspective always and for being a great desk-mate. We are fortunate in the NNF to work in a communal space known as the HML, which allowed for even more friendship, learning, and lunchtime picnics, so a special thank you also to Sean, Alice, Thanasi, and José. I am also indebted to everyone in the Biogel group for putting up with my endless questions and teaching me to do things like pipette as a third year graduate student. Kate, Erica, Wes, Emi, Gerardo, Ben, Kelsey, Caro, Chloe, Julie, Jacob, and Miri, you are all amazing friends and coworkers, thank you for making every day so much fun. I do have to single two people out though. Brad, you are an incredible scientist and I have learned so much from you. Tahoura, thank you for being such a great friend and a constant source of support and knowledge.

To my parents: thank you so much for always being there for me, and for all of your love. My Dad encouraged his two little girls to study science, and got two scientists out of

it. I am so proud to have him as my father, and hope that all dads will teach their little girls that they can do anything just like he taught us. I also gained two parents-in-law in the last few months, and Sally and Michael I am so grateful for your love and support as well.

To my siblings Yuli and Dave: I love you both more than I could ever say. It's been very special to go through graduate school all together (with little Dave joining the ranks this past year and getting Bella and Casey as new siblings too). Sharing an experience this challenging has made me feel closer to you than ever before, and even though we're all in different parts of the world, I feel your love and support always.

Finally, to my Sam and Bertie, our little family is truly my greatest pride and joy. I would not have made it through this journey without you, and I can't wait to spend the rest of our lives taking more journeys together.

Contents

1 Introduction **31**

2 Rheology and the characterization of complex fluids **35**

2.1 What is a complex fluid? 35

2.2 Macrorheology: characterization of the bulk mechanical properties of a material 36

2.2.1 Experimental techniques 37

2.2.2 Theory 48

2.3 Microrheology: characterizing local material properties 54

2.3.1 Single particle tracking: Experimental details 54

2.3.2 Single particle tracking: Theory and analysis 58

3 Physicochemical properties of native mucus and mucin gels **67**

3.1 Biological function and structure of mucus 67

3.2 Mucin gels as a model system for native mucus 70

3.2.1 Mucin purification method 71

3.2.2 Effect of non-mucin components on gel properties 72

3.2.3 Effect of batch preparation on mucin gel rheology 74

3.2.4 Comparison of the rheological properties of native mucus and reconstituted mucin gels 75

3.2.5 Section summary 82

4 Studying the network structure and association dynamics of reconstituted mucin gels using micro- and macrorheology **85**

4.1 Introduction 85
4.2 Effect of environmental perturbations on the micro- and macrorheology of MUC5AC gels 86
4.2.1 Materials and methods 86
4.2.2 Effect of pH and salt concentration on rheology of MUC5AC gels . 87
4.2.3 Effect of surfactant on rheology of MUC5AC gels 99
4.2.4 Section summary 102
4.3 Exploration of the mechanisms leading to the breakdown of the GSER in mucin gels 103
4.3.1 Materials and methods 103
4.3.2 Effect of polymer concentration on the rheology of MUC5AC and CMC solutions 106
4.3.3 Effect of particle size on the microrheology of CMC and MUC5AC solutions 109
4.3.4 Effect of particle surface chemistry on the microrheology of MUC5AC solutions 119
4.3.5 Effect of sample age on the microrheology of MUC5AC solutions . 121
4.3.6 Visualization of the mucin network 122
4.3.7 Section summary 124

5 Development of a constitutive model for assessing the temporal stability of saliva **127**

5.1 Introduction 127
5.2 The Salivary Network 128
5.3 Model Description 130
5.3.1 Response of the SFEN model under simple elongational flow conditions 134
5.3.2 Response of the SFEN model during Capillary Breakup Extensional Rheometry (CaBER) 135
5.4 Results and Discussion 141

5.5 Summary 146

6 Characterization and quantification of food solution texture using fractional models 149

6.1 Introduction 149

6.2 Background 152

6.2.1 Experimental details 152

6.2.2 Theoretical and modeling details 152

6.3 Fractional rheological modeling of aqueous solutions of Resource ® Thicken Up Clear 156

6.3.1 Linear rheology of TUC 156

6.3.2 Non-linear rheology of TUC 159

6.4 Rheology of food biopolymer solutions and saliva 161

6.4.1 Linear rheology of food biopolymer solutions and saliva 162

6.4.2 Non-linear rheology of food biopolymer solutions and saliva 164

6.5 Rheological interpretation of food consistency and texture using fractional models 165

6.5.1 The Nutting Square 165

6.5.2 Development of a material parameter space for quantifying food texture 167

6.6 Summary 171

7 Conclusions and future directions 173

A Supplementary information to Chapter 4 177

A.1 Matlab code for calculation of the MSD with non-constant camera frame rate 177

B Supplementary information to Chapter 5 179

B.1 Determination of the microstructural deformation at the transition point between regimes I and II 179

B.2 Filament thinning rate in the limit of large sticky effects 182

B.3 Comparison of experimental data and SFEN model predictions for shear rheological experiments 183
B.4 Effect of varying the SFEN model parameters on the predicted filament thinning dynamics 186

List of Figures

1.0.1 (a) Schematic depiction of a biogel. The network of polymers is swollen in water and maintained by a variety of interactions which may include topological entanglements (shown as sites of overlapping chains), covalent bonds (black circles) and physical bonds (yellow diamonds). (b) The primary matrix-forming component of a biofilm is extracellular polymeric substance (EPS); a predominantly polysaccharide-based bacterial secretion [1]. Left: macroscopic view of a biofilm coating the hull of a ship (image credit MIT Woods Hole Oceanographic Institution). Right: scanning electron micrograph of a biofilm taken from the inner surface of a medical device [1]. (c) The extracellular matrix of articular cartilage consists primarily of collagen and the proteoglycan aggrecan. Left: cartilage on a normal human femoral condyle (courtesy of Alan J. Grodzinsky). Right: tapping mode AFM height images of newborn human aggrecan monomers [5], adapted with permission from Elsevier. 32

1.0.2 Road map depicting three possible paths for navigating this thesis based on interest of the reader. 34

2.1.1 Examples of everyday complex fluids. (a) Milk is an emulsion of fat globules in milk serum (image credit BBC Good Food). (b) The 'head' of a glass of well-poured beer is a foam (image credit American Homebrewer's Association). (c) The slimy secretion contained within okra pods is a polysaccharide-based polymer solution (image credit MIT Non-Newtonian Fluids group). 35

2.2.1 Experimental setups for the shear rheological data presented in this thesis, and a sketch of a representative experimental response for typical polymer solutions for small amplitude oscillatory shear (SAOS) experiments. (a) 8 mm parallel plate set up on the ARESG2 rheometer, in which the bottom plate is rotated and the geometric fixture remains stationary. A thin coating of mineral oil is used to minimize sample evaporation. (b) Cone-and-plate set up on the AR-G2 rheometer, in which the geometric fixture is rotated and the bottom plate remains stationary. Sufficiently large fixtures feature a groove in which the volatile solvent of the sample can be added to minimize evaporation, and the fixture and sample are sealed off by a containment device known as a solvent trap. (c) Typical response of the storage modulus G' during a strain sweep experiment, where the frequency ω is held constant and the largest value of the strain $\gamma_{0,c}$ for which the material responds linearly is determined. (d) Typical frequency sweep experimental output at a strain amplitude value $\gamma_0 \leq \gamma_{0,c}$, with the crossover frequency ω_c indicated. 39

2.2.2 Effect of geometry size on the linear viscoelastic measurements of 1 wt % CMC solutions at pH2. The red triangles correspond to the average of three different measurements performed using an 8 mm parallel plate setup on an ARESG2 rheometer with a mineral oil coating around the sample to prevent evaporation. The blue circles correspond to one measurement performed using a 40 mm 2° cone-and-plate setup on an AR-G2 rheometer with the solvent trap to prevent evaporation. Filled symbols correspond to the storage modulus G', and unfilled symbols correspond to the loss modulus G''. (a) Amplitude sweep at $\omega = 10\,\mathrm{rad\,s^{-1}}$. The dashed lines indicate the minimum measurable moduli G_{min} for a given strain (Equation (2.5)) using the nominal values for the minimum torque T_{min} in oscillation as provided by the manufacturer (blue dashed line: $T_{\mathrm{min}} = 0.05\,\mu\mathrm{N\,m}$, ARESG2 , red dashed line: $T_{\mathrm{min}} = 0.003\,\mu\mathrm{N\,m}$, AR-G2). For the ARESG2 rheometer, the nominal low torque limit in oscillation appears to be an overestimate, and a value of $T_{\mathrm{min}} = 0.01\,\mu\mathrm{N\,m}$ appears to be more consistent with the experimental data, as shown by the red dotted line defined by Equation (2.5) using this apparent value for T_{min}. (b) Frequency sweep, with the low torque limits defined by Equation (2.5) at the appropriate strain values indicated, using $T_{\mathrm{min}} = 0.003\,\mu\mathrm{N\,m}$ for the AR-G2 and $T_{\mathrm{min}} = 0.01\,\mu\mathrm{N\,m}$ for the ARESG2. For the measurements performed on the AR-G2 rheometer, data points with raw phase angles $\geq 175°$ are plotted in darker blue. 41

2.2.3 Effect of a mineral oil coating and sample evaporation on the linear viscoelastic response of 1 wt % CMC solutions at pH2. Measurements were performed using an 8 mm parallel plate setup on an ARESG2 rheometer. The red squares correspond to a rim of 'heavy' mineral oil (density $\rho = 0.862\,\mathrm{g\,ml^{-1}}$ at 25 °C, Catalog No 330760, Sigma Aldrich, St Louis, MO), the blue circles correspond to a rim of 'light' mineral oil (density $\rho = 0.838\,\mathrm{g\,ml^{-1}}$ at 25 °C, Catalog No 330779, Sigma Aldrich, St Louis, MO), and the green diamonds correspond to an experiment where no mineral oil was used, and hence no measures were taken to minimize sample evaporation. Filled symbols denote the storage modulus G', and unfilled symbols denote the loss modulus G''. 42

2.2.4 Low viscosity, small sample volume effects highlighted for 0.05 wt % MUC5B solutions at pH7. Frequency sweep at $\gamma_0 = 700\,\%$ performed using an 8 mm parallel plate setup on an ARESG2 rheometer with a coating of mineral oil to prevent evaporation. Filled symbols denote the storage modulus G', and unfilled symbols denote the loss modulus G''. The low torque limit calculated using $T_{\mathrm{min}} = 0.01\,\mu\mathrm{N\,m}$ is indicated by the dashed grey line, and the thin black dashed line corresponds to the high frequency wave propagation limit of Equation (2.9). 43

2.2.5 Low viscosity, small sample volume effects highlighted for 0.05 wt % MUC5B solutions at pH7. Steady state shear flow data performed using an 8 mm parallel plate setup on an ARESG2 rheometer with a coating of mineral oil to prevent evaporation. Orange square symbols denote data points that did not equilibrate within the allotted 300 s window, while red circles denote those that did. The low torque limit in steady state shear flow (Equation (2.10)) evaluated using $T_{\mathrm{min}} = 0.1\,\mu\mathrm{N\,m}$ (as provided by the manufacturer) is shown as the dashed grey line. The predicted value of the viscosity from Figure 2.2.4 is shown as the red dotted line. . . . 45

2.2.6 Effect of sample equilibration on shear rheological measurements. Measurements were performed using a 40 mm 2° cone-and-plate fixture on an AR-G2 rheometer with the 'nectar' preparation (1.2 wt %) of Resource ® Thicken Up Clear. Data is shown for both an 'up' ramp (increasing $\dot{\gamma}$, filled circles) and a 'down' ramp (decreasing $\dot{\gamma}$, unfilled circles). The low torque limit in shear evaluated using $T_{\mathrm{min}} = 0.01\,\mu\mathrm{N\,m}$ (Equation (2.5)) is shown by the dashed grey line. (a) 2 minute continuous ramp data for the apparent shear viscosity $\eta(\dot{\gamma})$. A local maximum in $\eta(\dot{\gamma})$ is observed during the up ramp only. (b) Steady state flow experimental data. Allowing the solution to equilibrate at low shear rates eliminates the previously observed local maximum regardless of ramp trajectory. 46

2.2.7 Series of pictures capturing a Capillary Breakup Extensional Rheology (CaBER) experiment performed on human whole saliva. The sample is placed between two 6 mm plates initially separated by a gap of 2 mm, and the plates are rapidly separated during a strike time of approximately 50 ms to a final separation distance of approximately 10 mm. Images are shown from this earliest time corresponding to the moment the plates reached their final separated positions until filament 'breakup', or in this case the formation of a stable 'beads-on-a-string' structure that is a signature of viscoelastic polymer solutions in extension. The radius of the filament is recorded throughout the thinning process using a laser micrometer, and from the temporal evolution of this quantity, a relaxation time for the material can be extracted. 48

2.2.8 The response of a viscoelastic material interpolates between that of a viscous liquid (left, represented mechanically as a dashpot) and a purely elastic solid (right, represented mechanically as a spring). The Maxwell model for linear viscoelasticity (center) models the response of complex fluids as that of a spring and a dashpot in series. 49

2.2.9 Definition of a spring-pot of fractional derivative order α and quasiproperty $\mathbb{V}$ as a mechanical element that interpolates between a spring ($\alpha \to 0$, $\mathbb{V} \to G$) and a dashpot ($\alpha \to 1$, $\mathbb{V} \to \eta$). 52

2.2.10 Overview of the process developed in kinetic theory for deriving the rheological response of a polymer solution from the molecular structure and properties of the polymer itself. In general, the polymer is first coarse-grained to a simpler mechanical structure such as an elastic dumbbell (Panel 2), and the stress tensor and configurational distribution function of the dumbbells are established (Panel 3). From these results, a constitutive equation can be developed (Panel 4), which when combined with the actual kinetics of the problem in question permit the prediction of a rheological response (Panel 5). For an in-depth treatment of kinetic theory, the reader is referred to [36]. 53

2.3.1 Overview of the method of single particle tracking (SPT). (a) Schematic of a borosilicate square capillary containing a particle-laden sample, and sealed on either end with Valap. Inset: (Top) For uniformly homogeneous samples such as water, the particle size is significantly larger than any length scales associated with heterogeneity within the sample. (Bottom) In a heterogeneous sample, the particles may probe a local microenvironment only. (b) Sample trajectory for a 1 µm particle in water. The initial particle position is normalized to $\{x = 0\,\mu\text{m}, y = 0\,\mu\text{m}\}$ at time $t = 0\,\text{s}$ (large green circles), and subsequent particle positions at all later times (small black circles) are given in reference to this initial location. The final particle position recorded is shown as the red circle. (c) Schematic of particle position data obtained following image analysis and tracking. (d) Various analytical parameters can then be acquired with this information. 55

2.3.2 Estimation of the static error $2\epsilon^2$ (Equation (2.22)) for the experimental set up used in this thesis. The MSD of 1 µm particles embedded in 3 wt % agarose gels imaged at a magnification of 20x and a camera frame rate of $\approx$ 30 fps for two different exposure times: $\sigma_t = 10$ ms (black circles) and $\sigma_t = 33$ ms (grey diamonds) is shown. The dashed lines denote the estimates for $2\epsilon^2$ obtained from the average MSD for $\sigma_t = 10$ ms (black dashed line), and the average MSD of just the early lag time plateau ($\Delta\tau \lesssim 0.33$ ms) for $\sigma_t = 33$ ms (grey dashed line). 57

2.3.3 Example of the 'back-and-forth' motion associated with incorrect particle localization, frequently due to the presence of an optical halo. In this case the particle is 1 µm in size, and the sample is human cervical mucus. . 58

2.3.4 Analysis of the GSER for particles of different sizes in water. Imaging was performed at $\approx$ 30 fps with an exposure time of 10 ms and for a total duration of 10 s. (a) By scaling the particle MSDs by their radii, collapse onto a single master curve is achieved with the exception of the 200 nm particles which appear to be diffusing more slowly than would be predicted. Further, the collapsed result is in good agreement with that obtained from Equation (2.42) using a viscosity of $\eta = 0.89$ mPa s (solid black line). (b) MSD of 200 nm particles in glycerol (Catalog No G5516, Sigma-Alrich, St-Louis, MO). The solid black line is a fit of Equation (2.28) to the experimental data points at lag times $\Delta\tau > 1$ s. The shaded grey region corresponds to MSD values lying below the value of $2\epsilon^2$ calculated for an exposure time of 10 ms, but we note that this is simply an approximation for the true static error, particularly since imaging for these small particles was performed at a magnification of 40x (see Equation (2.22)). (c) The estimated medium viscosity of $\eta = 0.70$ Pa s (solid black line) obtained from Equation (2.43) using the fitted value for the diffusivity D_α from (b) and assuming a linear response (i.e. $\alpha = 1$) is in good agreement with macroscopic steady state shear flow data for a 60 : 1 glycerol : water mixture (filled black circles). 62

3.1.1 Epithelial surfaces of the body coated by mucus. Figure adapted from [61] with characteristic pH levels shown. 68

3.1.2 Schematics of the general structure of secreted (a) and tethered (b) mucin molecules adapted from [66, 74, 75] with permission from Elsevier and Springer Nature. (c) An illustration of the network established by the gel-forming, secreted mucins (adapted from [7]). Individual mucin subunits associate via end-to-end disulfide bonds to form even larger macromonomer chains. The network is formed from reversible associations including hydrophobic interactions between the non-glycosylated, cysteine-rich regions of the molecules, and is stabilized by electrostatic repulsion between the charged sugar side chains. 69

3.2.1 Scanning electron microscopy (SEM) courtesy of Dr. Nicole Kavanaugh reveals structural changes to mucins associated with different purification processes. (a) MUC5AC mucin purified from pig gastric mucus by the Ribbeck lab. (b) Industrially purified PGM supplied by Sigma-Aldrich. 71

3.2.2 Rheological response of 1 wt % MUC5AC gels purified with (CsCl, circles) and without (N-CsCl, diamonds) CsCl gradient centrifugation at pH2 (red symbols) and pH7 (blue symbols). In (a) the linear viscoelastic response measured macroscopically (symbols) using an 20 mm 4° cone-and-plate fixture are presented. The filled symbols denote the storage modulus G' and the unfilled symbols denote the loss modulus G''. In (b) the MSD as a function of the lag time is shown for both mucin preparation conditions at pH2 and pH7. In (c) the van Hove distributions for the same conditions as in (b) are shown, with their corresponding non-Gaussian parameters κ tabulated in (d). The error bars in (b) and the standard deviations reported in (d) reflect the multiple repeats performed for the N-CsCl conditions. The N-CsCl data is the same as that presented in Chapter 4. Note that the standard deviations reported in (d) are the same as those published in [7] for consistency, but were mistakenly calculated assuming an entire population and consequently underestimate the true standard deviation by a factor of $\sqrt{\frac{N}{N-1}}$, where $N = 2$ or $N = 3$ depending on the number of experimental replicates. 73

3.2.3 SAOS measurements of mucin gels at pH2 (red symbols) and pH7 (blue symbols) from different purification batches. The distinction of batches is arbitrary for each pH; however for the label 'Batch 2', the mucins used for both the pH2 and pH7 gels were obtained during the same purification. The filled symbols denote the storage modulus G', and the unfilled symbols denote the loss modulus G''. 75

3.2.4 Domain structures of major gel-forming mucins expressed in salivary, cervical, gastric, and intestinal mucus reveal distinct structural differences. Note that MUC5AC and MUC2 are obtained from porcine and not human sources, but from the analogous tissues to those indicated. All three gel-forming mucins contain Von Willibrand Factor (VWF), cysteine-rich, C-terminal cysteine knot, and heavily O-glycosylated PTS domains that are common to all gel-forming mucins in the MUC family. Domain locations and total protein lengths are approximated from Dekker et al. [66]. The micro- and macro-rheological properties of gels reconstituted from the appropriate mucin to the physiological concentration and pH levels of the source tissue are compared with those of the native mucus itself. For the cervical niche, MUC5B from salivary secretions is utilized for the reconstituted mucin gel as a result of the difficulty of obtaining sufficient quantities of cervical mucus in order to purify MUC5B from this source. 77

3.2.5 Comparison of the micro-and macro-rheological response of native mucus and reconstituted mucin gels for four physiological niches. For the macrorheological data, filled symbols denote the storage modulus G' and unfilled symbols denote the loss modulus G''. For the microrheological data, dashed lines denote the ensemble average MSD of an individual experiment, and filled symbols denote the average over all experiments. For clarity on these logarithmic plots, error bars are only shown extending above the data points. Values of the non-Gaussian parameter κ measured at a delay time of $\Delta\tau = 0.1\,\mathrm{s}$ are provided, along with the anomalous diffusion exponent α obtained by fitting Equation (2.28) to the MSD for lag times in the range $0.03\,\mathrm{s} \leq \Delta\tau \leq 5\,\mathrm{s}$. (a) In the gastric niche, porcine gastric mucus (black circles) is compared with 5 wt % MUC5AC gels at pH2 (red diamonds) and 5 wt % Sigma-Aldrich PGM gels at pH2 (blue triangles). (b) In the intestinal niche, porcine intestinal mucus (black circles) is compared with 2.5 wt % MUC2 gels at pH4 (red diamonds). (c) In the oral niche, human whole saliva (black circles) is compared with 0.05 wt % MUC5B solutions at pH7 (red diamonds) and 0.05 wt % CMC solutions at pH7 (blue triangles) (d) In the cervical niche, human cervical mucus (black circles) is compared with 1.5 wt % MUC5B gels at pH4 (red diamonds) and 1.5 wt % MUC5B gels at pH7 (blue triangles). 80

4.2.1 Effect of pH and salt on the rheology of $10\,\mathrm{mg\,ml^{-1}}$ MUC5AC gels. The linear viscoelastic response measured macroscopically (symbols) as well as the predicted moduli from the MSD data (lines) are presented. Filled symbols and solid lines represent the elastic property $G'(\omega)$, while the hollow symbols and dashed lines represent the viscous property $G''(\omega)$. The aggregate MSD of all particle trajectories was used to calculate the viscoelastic moduli for all gels except the pH2 sample, for which only the MSD of a specific subset of 'exponential' particles (see text for details) was used. In (a) the pH is varied with no added salt, and data is presented at pH2, pH4, and pH7. In (b), the pH is maintained at pH7 and data is presented for salt concentrations of 0 mM, 50 mM, 200 mM and 400 mM. 88

4.2.2 Schematic illustration of the proposed effects of the various environmental modifications on the supramolecular structure of the mucin network. The mesoscopic porous structure of the mucin gels is represented by the gray regions and the diffusing probe particles are shown by large green circles. At neutral pH (a), the mucin molecules possess a net negative charge and are semi-flexible. Under acidic conditions (b), the protonated mucin molecules possess a nearly neutral net charge, and stiffen via breaking of salt bridges, exposing additional moieties including hydrophobic domains which associate to form additional cross-links (shown by yellow triangles). Collectively, this induces local mesoscopic phase separation into mucin-rich and mucin-poor regions. When salt is added at neutral pH (c), the screening of electrostatic interactions reduces the degree of repulsion between the sugar side chains which permits stronger and longer-lived associations between mucin molecules (indicated schematically by the increased size of the yellow triangles). Finally, when surfactant is added under acidic conditions (d), the hydrophobic domains are out-competed by the small surfactant molecules, which loosens and disrupts the aggregates in the mucin-rich regions prompting the return towards a single phase. 89

4.2.3 Microrheological response of $10\,\mathrm{mg\,ml^{-1}}$ MUC5AC gels to pH variations at zero salt concentration (a,c,e) and salt addition at neutral pH (b,d,f). The MSD as a function of the lag time is shown at different pH levels in (a) and for different salt concentrations at neutral pH in (b). The MSD is that of the aggregate particle populations for all gels. In addition, the individual MSDs corresponding to just the Gaussian and just the exponential particle populations are shown for the pH2 gel, with the error bars omitted for clarity. The van Hove correlations for the aggregate particle populations are shown at different pH levels in (c) and at different salt concentrations in (d). Summary tables of the non-Gaussian parameters κ and the anomalous diffusion exponents α are presented for the different pH levels and salt concentrations in (e) and (f), respectively. Note that the standard deviations reported in (e) and (f) are the same as those published in [7] for consistency, but were mistakenly calculated assuming an entire population and consequently underestimate the true standard deviation by a factor of $\sqrt{\frac{N}{N-1}}$, where $N = 2$ or $N = 3$ depending on the number of experimental replicates for a given sample. 91

4.2.4 In (a), the van Hove distribution for all particles is shown by the diamond symbols, and the thick solid line indicates the composite Gaussian and exponential fit defined in Equation (4.2). The hollow triangles and inverted triangles denote the van Hove distributions of the Gaussian and exponential particles, respectively, and their respective Gaussian (dashed) and exponential (dotted) fits are also shown. In (b), the individual particle MSDs sorted into Gaussian (gray) and exponential (black) trajectories are shown, as well as their ensemble averages (filled symbols of the same color) and that of the aggregate population (solid pink diamonds). In (c), the fraction of Gaussian particles $A(\Delta\tau)$ is shown as a function of the lag time $\Delta\tau$. In (d), the characteristic Gaussian and exponential length scales $\sqrt{\sigma^2(\Delta\tau)}$ and $\sqrt{2\lambda^2(\Delta\tau)}$, respectively, are plotted as a function of the lag time, and the slope of the resulting power law fit is indicated. In (e), the experimental (symbols) and theoretical (lines) values of the non-Gaussian parameters κ (Equation (2.46)) for the exponential (dotted lines and hollow inverted triangles), Gaussian (dashed lines and hollow triangles), and aggregate (solid lines and solid diamonds) populations are shown as a function of lag time $\Delta\tau$. 94

4.2.5 Distributions of the variances σ_i^2 of the individual particle trajectories are presented for the Gaussian (hollow triangles and a dashed line), exponential (hollow inverted triangles and a dotted line) and aggregate (filled diamonds and a solid line) populations, along with the predicted distribution $P_e(\sigma_i^2)$ (Equation (4.7) and the thick dotted line) and a thick dashed line indicating the fitted value σ^2. 96

4.2.6 The effect of added surfactant on the rheology of $10\,\mathrm{mg\,ml^{-1}}$ MUC5AC gels at pH2. In (a), the SAOS results for the pH2 gels with 0 wt %, 5 wt %, 10 wt %, and 20 wt % hexanediol are shown for the macrorheological measurements (symbols) and the SPT predictions (lines) based on the MSDs of the exponential particle populations. In (b), the heterogeneity ratio $\mathrm{HR}(\Delta\tau)$ (black diamonds and solid lines) and fraction of Gaussian particles $A(\Delta\tau)$ (red circles and dashed lines) at a lag time of $\Delta\tau = 0.1\,\mathrm{s}$ are shown as a function of hexanediol concentration, and in (c), the van Hove distributions and associated non-Gaussian parameters κ are presented for all surfactant concentrations. In (d), the MSDs evaluated from SPT for the exponential (hollow inverted triangles and dashed error bars), and Gaussian (filled triangles and solid error bars) populations, as sorted at a lag time of $\Delta\tau = 0.1\,\mathrm{s}$, are plotted as a function of lag time for the same gels. Note that the standard deviations reported in (b) and (c) are the same as those published in [7] for consistency, but were mistakenly calculated assuming an entire population and consequently underestimate the true standard deviation by a factor of $\sqrt{\frac{N}{N-1}}$, where $N = 2$ or $N = 3$ depending on the number of experimental replicates for a given sample. 100

4.3.1 Analytical consequences of a non-constant camera frame rate for SPT analysis. (a) Description of the approximate sequence of frame rates used to obtain the 590 frames over a time period of $\approx 5\,\text{min}$. SPT data corresponding to the motion $1\,\mu\text{m}$ carboxylated particles in 1 wt % CMC solutions at pH2 is shown in (b)-(d). (b) The number of recorded displacements N_{steps} with intervals of duration $\Delta\tau$ that were available for calculation of the MSD are shown as the solid black line as a function of $\Delta\tau$. The retained lag times corresponding to peaks in N_{steps} at least $1/10^{\text{th}}$ of the magnitude of the largest value of N_{steps} are shown as the filled red symbols. (c) MSD calculated using all possible lag times (dotted red line) and using the retained values from (b) only (solid red circles). (d) Predicted viscoelastic moduli from the same two MSD data sets as in (c). 105

4.3.2 SAOS data at polymer concentrations of 0.5 wt %, 1 wt %, 2 wt %, and 3 wt % for MUC5AC solutions at pH2 (a) and pH7 (b), as well as CMC solutions at pH2 (c) and pH7 (d). The filled symbols denote the storage modulus G', while the unfilled symbols denote the loss modulus G''. For the softest samples when a significant number of the data points lie near or below the low torque limit of the rheometer (calculated from Equation (2.5) using $T_{\text{min}} = 0.01\,\mu\text{N m}$ and the appropriate sample strain, see Section 2.2.1) this limiting value is also indicated. In (a) and (b), the shaded grey regions correspond to $\omega \geq 20\,\text{rad s}^{-1}$ where significant experimental noise is visible, presumably due to fluid inertia (see the discussions in Section 2.2.1). 107

4.3.3 Storage (filled symbols and solid lines) and loss (unfilled symbols and dashed lines) moduli at a frequency of $\omega = 1\,\text{rad s}^{-1}$ as a function of polymer concentration at pH2 (red circles) and pH7 (blue squares) for MUC5AC (a) and CMC (b). 108

4.3.4 Effect of the minimum trajectory length requirement on the microrheology of CMC solutions at 1 wt % and pH2 using 200 nm particles. (a) MSD as a function of $\Delta\tau$ for different values of the minimum trajectory length. (b) Number of particles retained and (c) non-Gaussian parameter $\kappa(\Delta\tau = 0.1\text{s})$ as a function of the minimum frame length requirement. 110

4.3.5 MSD as a function of the lag time $\Delta\tau$ for 200 nm, 500 nm, $1\,\mu\text{m}$, $2\,\mu\text{m}$, and $5\,\mu\text{m}$ particles in 1 wt % CMC solutions at pH2 (a) and pH7 (b). The insets of both figures present the collapsed version of this data in which the MSD is scaled by the particle radius. In (c), the apparent viscosity η_{app} at a lag time of $\Delta\tau = 1\,\text{s}$ (see Equation (4.11)) is shown as a function of the particle radius a at pH2 (red circles) and pH7 (blue squares). The lines denote the complex viscosity $|\eta^*(\omega)|$ at a frequency of $\omega = 1\,\text{rad s}^{-1}$ obtained from separate SAOS experiments (pH2: dashed red lines, pH7: dotted blue lines). The shaded regions (pH2: red, pH7: blue) are guides for the eye that capture the particle size-dependent spread in the apparent microrheological viscosity. 111

4.3.6 (a) Comparison of the viscoelastic moduli of 1 wt % CMC gels at pH2 measured in SAOS (symbols; G': filled, G'': unfilled) and the predictions from the microrheological response of 1 µm particles (lines; G': solid, G'': dashed). Data obtained using an 8 mm parallel plate setup on an ARESG2 is shown as triangular symbols, while data obtained using a 40 mm 2° cone-and-plate setup on an AR-G2 is shown as circular symbols. (b) Fit of the linear viscoelastic Maxwell model (lines; G': solid, G'': dashed) to the SAOS data obtained with the 40 mm 2° cone-and-plate setup. The values of the fitted parameters are indicated. 112

4.3.7 Effect of the minimum trajectory length requirement on the MSD of 200 nm particles in 1 wt % MUC5AC solutions at pH2 (a) and pH7 (b). In (c) and (d), the number of particles retained and the non-Gaussian parameter $\kappa(\Delta\tau = 0.1\,\mathrm{s})$, respectively, are plotted as a function of the frame requirement at pH2 (red circles and dashed lines) and pH7 (blue squares and dotted lines). In (e), the van Hove distributions at a lag time of $\Delta\tau = 0.1\,\mathrm{s}$ at pH2 are shown for trajectory length requirements of 50 and 300 frames. The distribution corresponding to trajectory lengths of 50 frames is also fit with a mixed probability distribution function constructed as the weighted sum of a Gaussian and an exponential distribution, as described in [7], and the fitting parameters used are indicated. 114

4.3.8 MSD as a function of lag time $\Delta\tau$ for 200 nm, 500 nm, 1 µm, 2 µm, and 5 µm particles in 1 wt % MUC5AC solutions at pH2 (a) and pH7 (b). The insets of both figures present the collapsed version of this data in which the MSD is scaled by the particle radius. The lines denote the complex viscosity $|\eta^*(\omega)|$ at a frequency of $\omega = 1\,\mathrm{rad\,s^{-1}}$ obtained from separate SAOS experiments (pH2: dashed red lines, pH7: dotted blue lines). In (c), the apparent viscosity η_{app} at a lag time of $\Delta\tau = 1\,\mathrm{s}$ (see Equation (4.11)) is shown as a function of the particle radius a at pH2 (red circles) and pH7 (blue squares). The shaded regions (pH2: red, pH7: blue) are guides for the eye that capture the particle size-dependent spread in the apparent microrheological viscosity. In (e) and (f), the non-Gaussian parameter $\kappa(\Delta\tau = 0.1\,\mathrm{s})$ and the anomalous diffusion exponent α are plotted as a function of the particle radius a at pH2 (red circles and dashed lines) and pH7 (blue squares and dashed lines). 116

4.3.9 (a) Storage modulus G' predicted from microrheology at a frequency of $\omega = 1\,\mathrm{rad\,s^{-1}}$ as a function of the particle radius a (black filled circles). The dashed black line indicates the value of G'_{SAOS} measured using SAOS at the same frequency. These data are fit to an exponential distribution of the form $G' = G'_{\infty} + (G'_{\mathrm{SAOS}} - G'_{\infty}) \exp\left(-\frac{a}{l}\right)$, resulting in an exponential length scale of $l = 78.3\,\mathrm{nm}$. This fit is shown as the dotted red line. In the inset, the microrheological measurements of $\tan\delta(\omega = 1\,\mathrm{rad\,s^{-1}}) = \frac{G''(\omega=1\,\mathrm{rad\,s^{-1}})}{G'(\omega=1\,\mathrm{rad\,s^{-1}})}$ are shown as a function of the particle radius a (solid black circles), and the dashed black line once again denotes the value of this parameter measured using SAOS. (b) Comparison of the macrorheological response of 1 wt % MUC5AC gels at pH2 (black circles; G': filled, G'': unfilled) and the predicted viscoelastic moduli from SPT for minimum trajectory length requirements of 450 frames using 200 nm (G': solid lines and filled squares, G'': dashed lines and unfilled squares) and 1 µm (G': solid lines and filled upright triangles, G'': dashed lines and unfilled upright triangles) particles. 118

4.3.10 MSD as a function of the lag time $\Delta\tau$ for a minimum trajectory length of 450 frames for 500 nm (circles) and 1 µm (triangles) PEG-ylated (yellow symbols) and carboxylated particles at pH2 ((a), pink symbols for carboxylated particles) and pH7 ((b), blue symbols for carboxylated particles). The values of the non-Gaussian parameter κ measured at a lag time of $\Delta\tau = 0.1\,\mathrm{s}$ and the anomalous diffusion exponent α are also indicated. 120

4.3.11 MSD as a function of the lag time $\Delta\tau$ for a minimum trajectory length of 450 frames for 1 µm carboxylated particles imaged after approximately 1 h as well as after a delay of several hours in 1 wt % MUC5AC gels at pH2 (a) and pH7 (b). In (a), the pink triangles correspond to a sample age of $\approx 1\,\mathrm{h}$, and the purple circles correspond to a sample age of approximately 7 h, while in (b) the blue triangles correspond to a sample age of $\approx 1\,\mathrm{h}$, and the purple circles correspond to a sample age of approximately 8.5 h. The values of the non-Gaussian parameter κ measured at a lag time of $\Delta\tau = 0.1\,\mathrm{s}$ and the anomalous diffusion exponent α are also indicated. 122

4.3.12 Images of the 1 wt % MUC5AC gels at pH2 (left) and pH7 (right) with a 300 µM solution of the positively charged, fluorescent reporting peptide $(AK)_{10}$-NH_2 added at a volume ratio of 1 : 20 peptide solution: MUC5AC gel. 123

4.3.13 Control images of the pH2 (left) and pH7 (right) 10 mM phosphate and sodium citrate buffers only with a 300 µM solution of the positively charged, fluorescent reporting peptide $(AK)_{10}$-NH_2 added at a volume ratio of 1 : 20 peptide solution: buffer. 124

4.3.14 Schematic of the 1 wt % MUC5AC gel network at pH2 inspired by the image in [19], in turn adapted from [121]. The gel is microphase separated into regions of varying apparent viscosity η_{app}, which are either soft enough to be accessible to all particles (i.e. $\xi \gtrsim 5\,\mu m$), the smallest particles (i.e. $\xi \lesssim 500\,nm$), or stiff enough to be accessible to no particles at all. Importantly, however, these stiffest regions still provide an important contribution to the macrorheological response of the gel. 126

5.2.1 Schematic description of the MUC5B mucin network parameters used in this chapter. (a) Coarse-graining of an individual MUC5B molecule to a bead-spring chain. The schematic representations of the MUC5B mucmer and macromonomer are reproduced from [4] with permission from Elsevier. (b) Organization of the MUC5B supramolecular network with both dangling and bridged sticky segments, as well as a schematic representation of the SFEN parameters relevant for considerations of network formation and inter-chain associations. 129

5.3.1 (a) SFEN model predictions for the normalized extensional viscosity $\eta_e^+/\eta_{e,0}$ under simple, homogeneous, elongational flow conditions at constant strain-rate $\dot{\epsilon} = \dot{\epsilon}_0$ as a function of the total accumulated strain $\epsilon = \dot{\epsilon}_0 t$ for $Wi = \dot{\epsilon}_0 \lambda_{exit} = 0.01, 0.5, 10$, and 100. (b) Surface plot of the SFEN model predictions for the normalized extensional viscosity $\eta_e^+/\eta_{e,0}$ as a function of both Wi and the non-dimensionalized time $\tau = t/\lambda_{exit}$ under simple, homogeneous elongational flow conditions (coloured surface) as well as the trajectory followed during a filament thinning (CaBER) experiment for which $\dot{\epsilon} = -(2/R)\,dR/dt$ (solid black line). The regions indicated with roman numerals in the CaBER trajectory correspond to viscocapillary thinning (I), elastocapillary thinning (II), and the terminal thinning regime (III) [146]. In both (a) and (b), the chosen parameters correspond to those determined for saliva at $t_{age} = 0\,h$ in Section 5.4: $b = 8000$, $X = 0.02$, $\Delta G = 6k_BT$, $\lambda_{exit} = 0.26\,s$, $\eta_s/\eta_0 = 0.003$, and $E_c = \nu k_B T/(\sigma/R_0) = 0.02$. 134

5.3.2 Filament thinning dynamics of the SFEN model, with $\Delta G = 6k_BT$, $E_c = 0.1$, and $\dot{\epsilon}^{(II)} = 3.8\,s^{-1}$. In (a), the effect of the stickiness number Sk on the evolution of the filament radius is shown for a value of the finite extensibility parameter comparable to those estimated for the mucin macromonomers ($b = 5000$). The exponential elastocapillary (II) and terminal (III) thinning regimes described in Equations (5.29) and (5.39) for the case of vanishing stickiness effects $Sk \to 0$ are shown as the dotted and dashed lines, respectively. In (b), the asymptotic decay to breakup of the SFEN model during filament thinning experiments is shown as a function of time from the singularity ($\tau_{crit} - \tau$) for four values of the finite extensibility parameter b with the energy well width to the equilibrium macromonomer size ratio fixed at $X = 10^{-3}$. The b-dependent decay during regime III (Equation (5.41)) is shown as the dotted line. The final late-time linear decay of the filament radius as a result of the residual solvent contribution at very small length scales is made apparent by the indication of the region with slope 1. 140

5.4.1 (a) Comparison of the SFEN model predictions with CaBER data for saliva at various sample ages. In (b) and (c), the fitted values for the weight averaged macromonomer molecular weight $\overline{M_W}$ and the reaction probability p, respectively, are shown as filled circles, and the theoretical predictions for the same parameters obtained using a randomly initiated depolymerization model are shown as the solid lines. 142

5.4.2 The shear rheology of whole saliva as measured by (a) small amplitude oscillatory shear (SAOS) and (b) steady simple shear flow. In Appendix B.3 we show that in the shear-thinning regime, the SFEN model predictions are only weakly dependent on the sample age (set using the appropriate parameters from Table 5.2), in agreement with our experimental observations. 143

6.2.1 Schematic representation of the fractional Maxwell model (FMM) as two 'spring-pots' in series and the definition of a spring-pot as a mechanical element that interpolates between a spring ($\alpha = 0$) and a dashpot ($\alpha = 1$). (b) Fractional Jeffreys model (FJM) with two spring-pots in series arranged in parallel with a purely viscous (dashpot) element to account for solvent viscosity. 153

6.2.2 Comparison of the goodness of fit for M-mode Maxwell models against the FMM, as fitted to experimental SAOS data for $c = 1.2\,\mathrm{wt}\,\%$ TUC. In (a), the error (penalty function) is plotted as a function of the number of model parameters N (parsimony) for both models. In (b) and (c), the predictions of the 4 parameter FMM (red lines) and the experimental data (circles) are plotted, along with the model predictions for an M = 2 mode (N = 4 parameter) Maxwell model (b) and an M = 25 mode (N = 50 parameter) Maxwell model (c) (blue lines). 155

6.3.1 (a) Storage modulus $G'(\omega)$ and (b) loss modulus $G''(\omega)$ for the TUC solutions. The symbols denote the experimentally obtained data and the solid and dashed lines denote the model fits, with individual parameter values specified for each concentration in Table 6.1. The data from Figures (a) and (b) are shifted to form a master curve using the $c = 1.2\,\mathrm{wt}\,\%$ preparation of TUC as a reference. The frequency is reduced using a shift factor a_c and the moduli $G'(\omega)$ and $G''(\omega)$ are reduced using a common shift factor b_c. The master curves are shown in (c), and the shift factors are plotted as a function of TUC concentration in (d). 157

6.3.2 Steady state flow data for the TUC solutions. The filled symbols denote the data obtained experimentally during a steady state flow experiment, the unfilled symbols denote the calculated Cox-Merz result using the SAOS data presented in Figure 6.3.1, while the lines denote the fractional model predictions, specified for each concentration in Table 6.1. 159

6.3.3 Master curve for steady state flow data of TUC solutions. Only alternate concentrations are shown for clarity. The shift factors a_c and b_c are those determined previously for the G', G'' master curve. The filled symbols denote the data obtained experimentally during a steady state flow experiment, the unfilled symbols denote the calculated Cox-Merz result using the linear viscoelastic data presented in Figure 6.3.1, and the lines denote the fractional model predictions using Equation (6.13) and the model parameters specified for each concentration in Table 6.1. 161

6.4.1 (a) Storage modulus $G'(\omega)$ and (b) loss modulus $G''(\omega)$ for the food biopolymer solutions and saliva. The symbols denote the experimentally obtained data, while the lines denote the model fits, specified for each sample in Table 6.2. As for the TUC solutions, all SAOS measurements were performed at a strain amplitude within the linear viscoelastic regime of each biopolymer solution as determined by separate strain sweep experiments (results not shown). 163

6.4.2 Steady state flow data for the food biopolymer solutions and saliva, divided into two separate plots (a) and (b) for clarity. The filled symbols denote experimental data obtained from steady state flow, and the hollow symbols denote the calculated values using the SAOS data from Figure 6.4.1 in conjunction with the Cox-Merz rule. The lines denote the model fits evaluated using Equations (6.10) and (6.11), specified for each concentration in Table 6.2. 164

6.5.1 'Nutting Square' proposed by Scott Blair and Caffyn [13] for representing the properties of complex materials. Reproduced with permission from IOP Publishing. 166

6.5.2 Fractional parameter phase space for food consistency. The markers correspond to the values of the quasiproperty $\mathbb{K}$ and fractional exponent n best describing the shear-thinning in the steady shear viscosity of the TUC solutions, food extracts, and whole saliva at $\dot{\gamma} = 50\,\mathrm{s}^{-1}$. The dashed diagonal lines bordering the shaded regions denote iso-viscosity curves at $\dot{\gamma} = 50\,\mathrm{s}^{-1}$ corresponding to the 'nectar', 'honey', and 'pudding' preparations of starch solutions by the NDDTF. The line connecting the TUC solution markers is a guide for the eye. 170

B.1.1 (a) Evolution of the axial microstructural deformation A_{zz} (solid black curve) near the transition time t^* between regimes I and II. The curve corresponding to the analytic expression for A_{zz} during the viscocapillary regime (Equation (B.3)) is shown as the dashed blue line, and the approximate value of A^*_{zz} calculated using the method outlined in Wagner et al. [150] is shown as the black dashed-dotted line. (b) Full temporal evolution of A_{zz} (solid black line) and the network junction destruction rate M (dotted red line) for the model parameters in Table 5.2 corresponding to $t_{age} = 0\,\mathrm{h}$ ($b = 8000$, $\lambda^{-1}_{exit} = 3.8\,\mathrm{s}^{-1}$). The value of the finite extensibility $b = 8000$ is shown as the black dashed line, and the approximate values of $A^{(\mathrm{II})}_{zz}$ and $M^{(\mathrm{II})}$ at the crossover from regime I to regime II are shown as the dashed-dotted black and red lines, respectively. 180

B.3.1 The numerical predictions of the SFEN model under steady simple shearing flow conditions for the parameter sets in Table 5.2 corresponding to all five sample ages at which CaBER experiments were performed (dashed lines). In addition, the the semi-analytic SFEN result for $t_{age} = 0\,\mathrm{h}$ is shown as filled red diamonds. 184

B.4.1 Effect of varying the finite extensibility b (a), the energy well depth ΔG (b), the energy well width r_c (c), and the initial filament radius R_0 (d) on the temporal evolution of the non-dimensional filament radius ξ predicted by the SFEN model. The solid black curves in each model correspond to the original set of parameters defined in Tables 5.1 and 5.2 for the sample at $t_{age} = 0\,\mathrm{h}$. The dashed blue and dotted red lines correspond to the predictions of the SFEN model with a single parameter changed compared to this original set, with the new value indicated in the figure. In (a), the stickiness parameters associated with each curve are $Sk = 6.3 \times 10^{-4}$ for $b = 10^3$, $Sk = 2.2 \times 10^{-4}$ for $b = 8 \times 10^3$, and $Sk = 6.3 \times 10^{-5}$ for $b = 10^5$, while in (b) $Sk = 2.7 \times 10^{-4}$ for $r_c = 10\,\mathrm{nm}$, $Sk = 2.2 \times 10^{-4}$ for $r_c = 8.35\,\mathrm{nm}$, and $Sk = 1.6 \times 10^{-4}$ for $r_c = 6\,\mathrm{nm}$. 188

List of Tables

5.1 List of SFEN model parameters, along with their definitions and numerical values. The effect of varying a subset of these parameters on the filament thinning dynamics is considered in Appendix B.4. 144

5.2 Age-dependent SFEN model parameters for saliva. For stickiness numbers $Sk \gtrsim 5.0\times10^{-4}$, the higher order approximation relating the network junction exit rate (λ_{exit}^{-1}) to the rate of filament decay in regime II ($\dot{\epsilon}^{(\mathrm{II})}$) presented in Appendix B.2 was used. These values are indicated by an asterisk. 145

6.1 FMM and FJM model parameters for the TUC solutions of various concentration. For each solution, the best fitting model (FMM or FJM) is indicated, along with the quasiproperties $\mathbb{V}$ and $\mathbb{G}$, fractional exponents α and β, and solvent viscosity η_s (when appropriate) obtained from the model fits to the experimental data (Equations (6.1) and (6.6)). In addition, the characteristic relaxation times τ_c (Equation (6.4)) and fitting errors (ϵ_N) for the selected models are shown. Finally, the difference between the Cox-Merz prediction and the measured shear viscosity at $\dot{\gamma} = 50\,\mathrm{s}^{-1}$ is denoted by the parameter f_{50} (see [17] and Section 6.3.2). 158

6.2 FMM and FJM model parameters for the food solutions and saliva. The material parameters are defined in Equations (6.2), (6.3), and (6.6). . . . 163

Remember your humanity, and forget the rest.
-The Russell-Einstein Manifesto

1 | Introduction

Soft, squishy materials known as hydrogels are ubiquitous in the biological world. Structurally, as shown in Figure 1.0.1a, these biological hydrogels (or biogels) consist of a network of polymers swollen in water and held together by a variety of physicochemical interactions known generically as cross-links. The mechanical properties of biogels are sensitive to both the identity of the solid, polymer component as well as the types of cross-linking interactions maintaining the network, which can include topological polymer entanglements as well as strong covalent and weak physical bonds. Natural tuning of the type of both of these structural features has resulted in biogels with a wide range of physicochemical properties capable of serving high specialized biological functions. For example, biofilms (Figure 1.0.1b) are microbial communities that reside within a hydrogel whose primarily solid component is extracellular polymeric substance (EPS), a predominantly polysaccharide-based bacterial secretion [1]. Their rapid and wide-spread growth on nearly all non-shedding, non-sterile aqueous surfaces as well as their resistance to antimicrobial agents present substantial challenges for the proper functioning of engineering systems across a range of industries, including implantable medical devices [2]. Further, the swelling induced by the heavily glycosylated, negatively charged proteoglycan aggrecan in articular cartilage is largely responsible for its impressive ability to resist sizable compressive forces (Figure 1.0.1c), while the integrity and elasticity of this tissue is generally attributed to the presence of the structural protein collagen [3]. Finally, the glycoprotein mucin is the primary structural component of mucus, a slimy secretion that coats every non-keratinized, wet epithelial surface of the body and provides protection against mechanical and microbial assault [4].

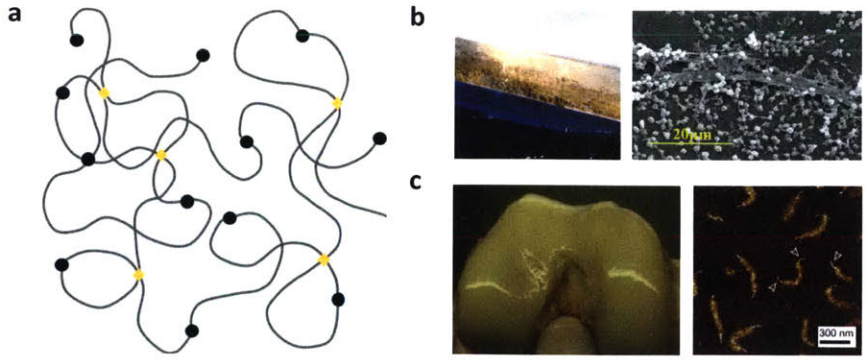

Figure 1.0.1: (a) Schematic depiction of a biogel. The network of polymers is swollen in water and maintained by a variety of interactions which may include topological entanglements (shown as sites of overlapping chains), covalent bonds (black circles) and physical bonds (yellow diamonds). (b) The primary matrix-forming component of a biofilm is extracellular polymeric substance (EPS); a predominantly polysaccharide-based bacterial secretion [1]. Left: macroscopic view of a biofilm coating the hull of a ship (image credit MIT Woods Hole Oceanographic Institution). Right: scanning electron micrograph of a biofilm taken from the inner surface of a medical device [1]. (c) The extracellular matrix of articular cartilage consists primarily of collagen and the proteoglycan aggrecan. Left: cartilage on a normal human femoral condyle (courtesy of Alan J. Grodzinsky). Right: tapping mode AFM height images of newborn human aggrecan monomers [5], adapted with permission from Elsevier.

For a given biogel, changes to the structure of its polymeric component or to the strength and density of its cross-links can result in substantial changes to its mechanical properties. For instance, while most elastic materials dilate when exposed to a shearing deformation, biopolymer gels exhibit the curious opposite phenomenon of of contracting, which manifests as the measurement of negative normal stress differences under shear [6]. Using aqueous gels of the blood clotting protein fibrin as a model system, de Cagny et al. [6] have demonstrated that this normal stress response is driven by the porosity of the gel. Specifically, the frequently large pore sizes (i.e. in the micrometer range) of biogels permit the expulsion of interstitial fluid during shearing, allowing for the relaxation of pressure gradients and a contraction of the network [6]. Further, the time scales associated with this relaxation process increase as the pore size decreases and viscous coupling effects between the solvent and the network become stronger [6].

This adaptability of the mechanical properties of biogels to the structure of the polymer network is regularly taken advantage of during normal physiological function. For instance, the wide range of pH levels spanned by the different organ systems of the body gives rise to mucus of varying stiffness, ranging from a thin, watery, lubricating layer on the pH-neutral ocular surface to a thick, adherent gel that shields the stomach lining from the acidic gastric juices [7]. Mechanistically, variation in the local pH level modulates the overall charge and conformation of the mucin molecules, which regulates the strength and number of electrostatic and hydrophobic interactions in the network [4, 7]. However, these changes may also come about pathologically in cases of disease. For example, in cystic fibrosis (CF), abnormal CFTR and sodium channel activity [8, 9] as well as mucin overproduction [9] are among the

causes of 'sticky' mucus which is less readily cleared by the cilia and hence more susceptible to biofilm formation. Irrespective of the cause of such changes, these observations suggest that careful measurements of the mechanical properties of biogels can serve as sensitive indicators of their underlying microstructures and functional viability. Indeed, precisely for this reason, there is significant interest in utilizing the mechanical properties of physiological biogels such as mucus as biomarkers for disease, as well as in developing theoretical tools for interpreting these measured properties within the framework of structural changes that may be part of the disease etiology [10, 11, 12].

Therefore, the goal of this thesis is to build on and develop experimental and theoretical tools for relating the mechanical properties of biogels to their microstructure and biological function. We begin in Chapter 2 by providing theoretical background on the characterization of complex fluids, as well as in-depth discussions of the experimental systems used in this work. Because of its relevance for the majority of the work presented in this thesis, in Chapter 3 we provide review the structure and properties of mucus and its primary solid component, the glycoprotein mucin. In this chapter, we also discuss the mucin purification method used in this work, and provide a comparison of the physicochemical properties of native mucus and reconstituted mucin gels. We then apply these theoretical and experimental concepts to the study of three biologically relevant complex fluid systems: in Chapter 4 we study the association dynamics and network structure of reconstituted mucin gels using micro- and macrorheology in order to gain insight into the structure of native mucus. Next, in Chapter 5 we study the temporal stability of saliva and its sensitivity to degradation using extensional rheology and a Sticky Finitely Extensible Network (SFEN) model, which respects the known physical dimensions and properties of mucins and models them as a network of physically associating and finitely extensible polymer chains. As a last system, in Chapter 6 we develop a fractional calculus-based framework for improving the quantification of the mechanical properties of polysaccharide-based food solutions in order to facilitate the development of specific textures for general consumption and for the design of dysphagia products. In effect, we propose a revised two-dimensional 'Nutting Square' [13] defined by the parameters of the fractional constitutive models, in which food textural terms appear to be better described by more complex loci than the straight lines associated with constant shear viscosities. Finally, in Chapter 7 we provide concluding remarks and future directions for the work presented in this thesis.

Because of the diversity of the subject matter covered, ranging from experimental details for performing rheological measurements to biochemical aspects of mucin molecules, in Figure 1.0.2 we provide a road map of three possible paths for navigating this thesis based on the interest of the reader.

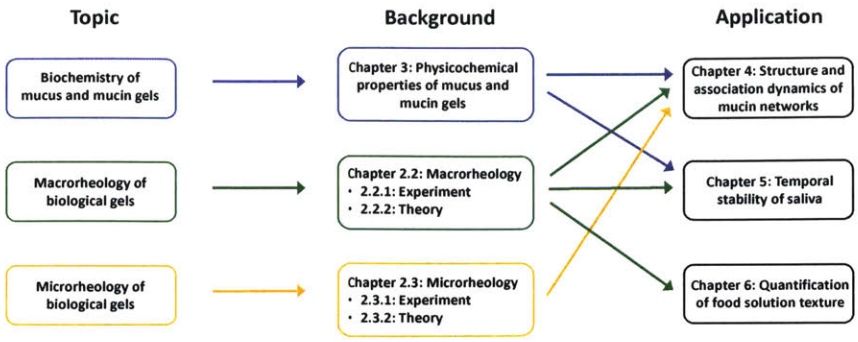

Figure 1.0.2: Road map depicting three possible paths for navigating this thesis based on interest of the reader.

For readers interested in the biochemistry of mucus and mucin gels, the background information provided in Chapter 3 on this subject may be of interest, as well as the applications of these concepts to the study of the structure and association dynamics of mucin networks (Chapter 4) and the temporal stability of saliva (Chapter 5). Readers interested in studying the macrorheology of soft biological gels may be interested in the discussions of the relevant experimental and theoretical details on this topic provided in Section 2.2, as well as the two applications previously listed and the quantification of food solution texture using fractional constitutive models (Chapter 6). Finally, readers interested in the microrheology of biological gels may be interested in the experimental and theoretical treatment of this subject in Section 2.3, as well as the experiments and analysis pertaining to mucin gels presented in Chapter 4.

2 | Rheology and the characterization of complex fluids

2.1 What is a complex fluid?

Complex fluids possess mesoscopic length scales due to the presence of several constituent elements [14]. For instance, emulsions, or dispersions of one liquid within another immiscible one, are one class of complex fluids, with milk (composed of lipid globules dispersed within a milk serum [15], Figure 2.1.1a) being a common example. Foams, such as the head of a well-poured beer (Figure 2.1.1b), are dispersions of gas bubbles in liquids [16] and make up another class [17]. Finally, liquid-solid mixtures such as polymer solutions, including the slimy, polysaccharide-based substance contained within okra pods (Figure 2.1.1c) and the biological gels introduced in Chapter 3, are a third category of complex fluids upon which the remainder of this thesis will focus.

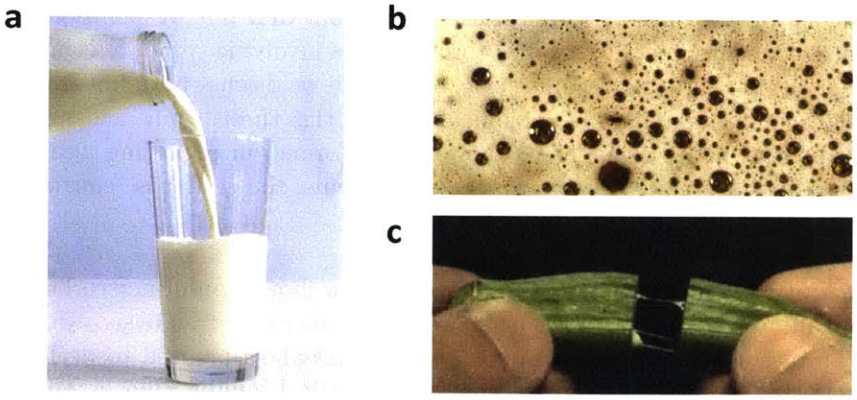

Figure 2.1.1: Examples of everyday complex fluids. (a) Milk is an emulsion of fat globules in milk serum (image credit BBC Good Food). (b) The 'head' of a glass of well-poured beer is a foam (image credit American Homebrewer's Association). (c) The slimy secretion contained within okra pods is a polysaccharide-based polymer solution (image credit MIT Non-Newtonian Fluids group).

As a result of the coexistence of both dissolved solids and a liquid within polymer solutions and biological gels, their mechanical response to an imposed deformation lies somewhere between that of a pure solid (typically modeled using Hookes Law of elasticity) and

that of a pure liquid (generally taken to obey Newton's law of viscosity). Hence, these materials are frequently described as being *viscoelastic*, and in order to model biological phenomena involving them, it is necessary to develop more sophisticated models in order to capture and understand their response to various types of deformations. We note here as a point of nomenclature that the study of the flow of matter is the subject of the field of *rheology*, and hence use this term in reference to the study of the mechanical response of biological gels for the remainder of this thesis.

Interestingly, however, because of the structural complexity of these materials at the microscopic scale, the response of biological gels to one type of deformation is frequently not predictive of their response to another. For instance, in order to understand why CF patients must rely so strongly on coughing for mucociliary clearance (MCC) while regular ciliary clearance is sufficient for healthy patients, it may be of interest to model the bulk response of both CF and healthy mucus to a strong shearing flow designed to mimic a real coughing event. As the relevant length scale for such an experiment is comparable to the size of the large airways where such a coughing event would occur, the bulk or macroscopic properties of the various types of mucus would be relevant for this measurement. On the other hand, in order to study drug delivery through CF mucus, microscopic measurements of the environment faced by the nanoscale or microscale drug delivery vehicles would be required, as heterogeneity and hierarchical structures within the mucus gel result in a very different mechanical environment at this length scale compared to those predicted by bulk measurements.

Even within the general categories of macroscopic of microscopic mechanical properties, however, a single measurement technique may be insufficient to fully characterize the material response. In particular, the non-linearity of the deformation profiles of biological elements such as proteins and polysaccharides implies that they may respond quite differently to small, linear measurements compared to large ones involving rapid deformation rates at both the macroscopic and microscopic scale. Although we discuss both linear and nonlinear macrorheological measurements of biological gels in this thesis, only linear microrheological measurements will be considered. For more information regarding active techniques for performing nonlinear microrheological measurements, the reader is referred to excellent discussions in [18, 19].

The remainder of this chapter then is devoted to a discussion of macrorheological (Section 2.2) and microrheological (Section 2.3) measurements and analysis. In each section, we provide an overview of the experimental techniques and tips used to perform the measurements reported in this thesis as well as the theoretical building blocks relied on for the development of the various models and analysis presented in Chapters 4-6.

2.2 Macrorheology: characterization of the bulk mechanical properties of a material

Macrorheological measurements characterize the bulk mechanical response of a material to an imposed deformation. Broadly speaking, the deformations of interest may be divided into two categories: shearing flows, such as those experienced by the mucus layer lining the trachea during a coughing event due to the high speed flow of air, or extensional flows, such

as those relevant for modeling the stretching and atomization of saliva droplets during a sneezing event [20]. We begin this section by providing an overview of the experimental techniques used in the work presented in this thesis for both shear and extensional rheology, and then outline some fundamental theoretical concepts for macrorheological modeling that will be applied in Chapters 4-6.

2.2.1 Experimental techniques

Shearing flows

Shearing flows are frequently established using a rheometer and a parallel plate or cone-and-plate set up, in which the sample of interest is placed between a (generally) stationary bottom plate and a moveable top plate or shallow-angled cone as depicted in Figures 2.2.1a and 2.2.1b. Other set ups such as Couette cells which feature two rotating concentric cylinders are also used to perform shear rheology, but their large volume requirements generally make them prohibitive for studying sample-limited biological fluids.

Two of the most commonly used experiments for probing the shear rheological response of biological fluids are small amplitude oscillatory shearing (SAOS) flow in order to determine the linear viscoelastic moduli of the sample, and steady state shearing flow in order to determine the steady state viscosity of the material as a function of the shear rate. The remainder of this subsection is devoted to descriptions of these experiments, with a particular emphasis on experimental particularities that frequently arise when measuring soft, sample-limited materials. Many of the concepts in this section are drawn from the excellent book chapter in [21], and for further details on this subject the reader is directed there.

Small amplitude oscillatory shear (SAOS) flows Small amplitude oscillatory shear (SAOS) flows are used to study the linear viscoelastic response of a material by decomposing the material stress in response to an imposed sinusoidal deformation into frequency-dependent components corresponding to solid-like (elastic) and liquid-like (viscous) contributions to the overall material behaviour. In the context of biological hydrogels, these measurements are particularly useful for determining whether gelation has occurred, which may be important in the design self-assembling peptides [22] or other complex materials.

To perform these experiments, either the bottom plate (Figure 2.2.1a) or the top geometric fixture (Figure 2.2.1b) is oscillated with a time-varying strain described by

$$\gamma(t) = \gamma_0 \sin(\omega t), \tag{2.1}$$

where γ_0 is the strain amplitude and ω is the oscillation frequency. In general, as will be explained in detail in Section 2.2.2, the stress response of a viscoelastic material will be out of phase with the imposed strain deformation by a phase angle of δ, and can be expressed as [23]

$$\tau(t) = A(\omega)\gamma_0 \sin(\omega t + \delta). \tag{2.2}$$

This expression can subsequently be decomposed into two components: one that is in phase with the strain deformation, and one that is in phase with the *rate* of strain

$\dot{\gamma}(t) = \gamma_0 \omega \cos(\omega t)$ (or $\frac{\pi}{2}$rad *out of phase* with $\gamma(t)$), i.e.

$$\tau(t) = A(\omega)\gamma_0 \left[\cos(\delta)\sin(\omega t) + \sin(\delta)\cos(\omega t)\right]. \tag{2.3}$$

Using the definitions $A(\omega) = \sqrt{G'(\omega)^2 + G''(\omega)^2} = |G^*(\omega)|$ and $\tan\delta = G''/G'$, Equation (2.3) can be rewritten as [23]

$$\tau(t) = \gamma_0 \left[G'(\omega)\sin(\omega t) + G''(\omega)\cos(\omega t)\right]. \tag{2.4}$$

$G'(\omega)$, the component in phase with the strain response, is known as the storage or elastic modulus, and $G''(\omega)$, the component in phase with the rate of strain response, is known as the viscous or loss modulus. The term $G^*(\omega) = G'(\omega) + iG''(\omega)$ is known as the complex modulus [23], with its magnitude denoted by $|G^*(\omega)|$.

Since these experiments probe the linear viscoelastic regime of the sample, the first step in performing them is to determine the range of values for γ_0 within which the material responds linearly. This is done by selecting a constant value of ω, and oscillating the plate at increasing values of γ_0, as depicted in Figure 2.2.1c. Up to a critical value of the strain $\gamma_{0,c}$, the storage modulus is independent of γ_0; this is the linear regime. Beyond this point, the viscoelastic moduli are strain amplitude dependent, and other oscillatory analysis such as large amplitude oscillatory shear (LAOS) must be performed [24, 25].

Following the determination of $\gamma_{0,c}$, any value of the strain amplitude $\gamma_0 <= \gamma_{0,c}$ may be selected while the frequency is varied. As we will see shortly, however, larger strain amplitudes correspond to larger instrument torques, and so for soft materials it is suggested to select as large a value of γ_0 as possible that still ensures a linear response. A typical response for a polymer solution is depicted in Figure 2.2.1d. For sufficiently slow deformations, or oscillation frequencies smaller than ω_c (known as the crossover frequency), the response of the solution is predominantly liquid-like, with $G'' > G'$. Beyond this limit, for fast deformations, the material responds in a predominantly solid-like way, and $G' > G''$.

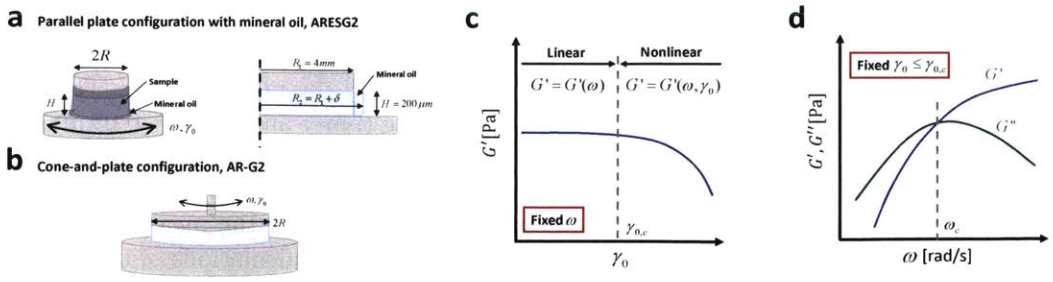

Figure 2.2.1: Experimental setups for the shear rheological data presented in this thesis, and a sketch of a representative experimental response for typical polymer solutions for small amplitude oscillatory shear (SAOS) experiments. (a) 8 mm parallel plate set up on the ARESG2 rheometer, in which the bottom plate is rotated and the geometric fixture remains stationary. A thin coating of mineral oil is used to minimize sample evaporation. (b) Cone-and-plate set up on the AR-G2 rheometer, in which the geometric fixture is rotated and the bottom plate remains stationary. Sufficiently large fixtures feature a groove in which the volatile solvent of the sample can be added to minimize evaporation, and the fixture and sample are sealed off by a containment device known as a solvent trap. (c) Typical response of the storage modulus G' during a strain sweep experiment, where the frequency ω is held constant and the largest value of the strain $\gamma_{0,c}$ for which the material responds linearly is determined. (d) Typical frequency sweep experimental output at a strain amplitude value $\gamma_0 \leq \gamma_{0,c}$, with the crossover frequency ω_c indicated.

For soft and sample-limited materials such as mucus and mucin gels, the selection of the appropriate strain amplitude γ_0 for SAOS measurements frequently results in a compromise between being sufficiently large for the resulting torque T to exceed the noise floor of the rheometer T_{min}, but sufficiently small to still be within the material's linear range. Indeed, for the softest materials and the smallest geometries, it is possible that the linear window of the sample is missed entirely by the time γ_0 is sufficiently large such that $T > T_{\text{min}}$.

The minimum measurable viscoelastic modulus G_{min} (which can be taken to be either G' or G'') is related to the minimum torque limit through the relationship [21]

$$G_{\text{min}} = \frac{FT_{\text{min}}}{\gamma_0}, \tag{2.5}$$

where F is a geometric factor given by $F = \frac{3}{2\pi R^3}$ for a cone-and-plate setup and $F = \frac{2}{\pi R^3}$ for a parallel plate setup [26], and R is the geometry radius. Consequently, G_{min} is highly sensitive to the radius of the geometry, and the minimum measurable modulus can be significantly decreased by increasing the size of the cone or plate, which is of particular importance for soft biological materials. From Equation (2.5), we see that G_{min} can also be reduced by increasing the strain amplitude γ_0, as previously mentioned.

In Figure 2.2.2, these concepts are demonstrated for a 1 wt % pH2 solution of carboxymethyl cellulose (CMC), a frequently used synthetic polymer analog for mucins. In Figure 2.2.2a, strain sweep experiments at $\omega = 10\,\text{rad}\,\text{s}^{-1}$ are shown, with red triangles corresponding to measurements taken with an 8 mm plate on an ARESG2 rheometer (TA Instruments), and the blue circles corresponding to measurements taken with a 40 mm 2°

cone-and-plate fixture on an AR-G2 rheometer (TA Instruments). The filled symbols correspond to the storage modulus G' and the hollow symbols denote the loss modulus G''. The dashed lines are obtained from Equation (2.5) using the nominal values of the low torque limit in oscillation for the various rheometers as provided by the manufacturer. These correspond to $T_{\text{min}} = 0.003\,\mu\text{N}\,\text{m}$ for the AR-G2 rheometer (blue) and $T_{\text{min}} = 0.05\,\mu\text{N}\,\text{m}$ for the ARESG2 rheometer (red). This nominal value appears to be in good agreement with the experimental noise for the AR-G2, but a value of $T_{\text{min}} = 0.01\,\mu\text{N}\,\text{m}$ (red dotted line) appears to be in better agreement with the experimental data for the measurements performed with the ARESG2, and thus we use this value in future calculations of torque limits for this rheometer in this thesis. Consistent with Equation (2.5), the effect of increasing the geometry size is to shift these limits on G_{min} down and to the left, increasing the range of modulus values that can be measured at a given strain amplitude γ_0. In Figure 2.2.2b, the corresponding frequency sweep experiments are shown. For the 8 mm plate, a value of $\gamma_0 = 100\,\%$ was selected, as this value appears to still be within the linear range of the material, and measurements for smaller γ_0 lie below the torque limit. Using a 40 mm 2° cone, we are better able to resolve the linear viscoelastic window for the sample in question, and can perform the SAOS measurements at at a strain amplitude of $\gamma_0 = 12\,\%$ which, by visual inspection, appears to lie more comfortably within the material's linear range. The frequency sweep measurements performed using both geometries are in good agreement, and the low torque limits calculated from Equation (2.5) using the previously described appropriate values of T_{min} are indicated. Clearly then, there are advantages to using larger geometries to measure soft materials. However, the trade off is the amount of sample that is required. With a 200 µm gap, the 8 mm parallel plate setup requires approximately 15 µl of sample, while the 40 mm 2° cone-and-plate requires closer to 0.5 ml; approximately 30 times the volume.

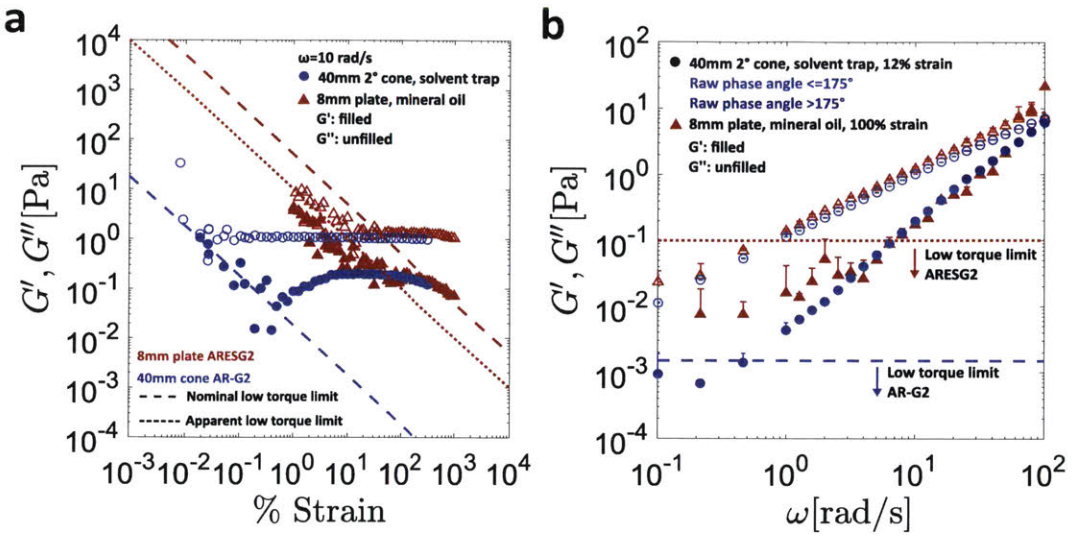

Figure 2.2.2: Effect of geometry size on the linear viscoelastic measurements of 1 wt % CMC solutions at pH2. The red triangles correspond to the average of three different measurements performed using an 8 mm parallel plate setup on an ARESG2 rheometer with a mineral oil coating around the sample to prevent evaporation. The blue circles correspond to one measurement performed using a 40 mm 2° cone-and-plate setup on an AR-G2 rheometer with the solvent trap to prevent evaporation. Filled symbols correspond to the storage modulus G', and unfilled symbols correspond to the loss modulus G''. (a) Amplitude sweep at $\omega = 10\,\mathrm{rad\,s^{-1}}$. The dashed lines indicate the minimum measurable moduli G_{min} for a given strain (Equation (2.5)) using the nominal values for the minimum torque T_{min} in oscillation as provided by the manufacturer (blue dashed line: $T_{\mathrm{min}} = 0.05\,\mu\mathrm{N\,m}$, ARESG2 , red dashed line: $T_{\mathrm{min}} = 0.003\,\mu\mathrm{N\,m}$, AR-G2). For the ARESG2 rheometer, the nominal low torque limit in oscillation appears to be an overestimate, and a value of $T_{\mathrm{min}} = 0.01\,\mu\mathrm{N\,m}$ appears to be more consistent with the experimental data, as shown by the red dotted line defined by Equation (2.5) using this apparent value for T_{min}. (b) Frequency sweep, with the low torque limits defined by Equation (2.5) at the appropriate strain values indicated, using $T_{\mathrm{min}} = 0.003\,\mu\mathrm{N\,m}$ for the AR-G2 and $T_{\mathrm{min}} = 0.01\,\mu\mathrm{N\,m}$ for the ARESG2. For the measurements performed on the AR-G2 rheometer, data points with raw phase angles $\geq 175°$ are plotted in darker blue.

Another complication of working with such small sample volumes is the pronounced effect that sample evaporation can have. One solution to mitigate this, particularly for small geometries that are not large enough to feature solvent traps, is to place a thin coating of mineral oil around the edge of the sample, as shown in Figure 2.2.1a. In Figure 2.2.3, frequency sweep data is shown for 1 wt % CMC solutions at pH2 using an 8 mm parallel plate setup with an ARESG2 rheometer. The green diamonds correspond to an experiment where no mineral oil was used on the geometry rim (and hence no measures were taken to minimize sample evaporation), the red squares correspond to the use of 'heavy' mineral oil (density $\rho = 0.862\,\mathrm{g\,ml^{-1}}$ at 25 °C, Catalog No 330760, Sigma Aldrich, St Louis, MO), and the blue circles correspond to the use of 'light' mineral oil (density $\rho = 0.838\,\mathrm{g\,ml^{-1}}$ at 25 °C, Catalog No 330779, Sigma Aldrich, St Louis, MO). As before, the filled symbols denote G'

and the unfilled symbols denote G''.

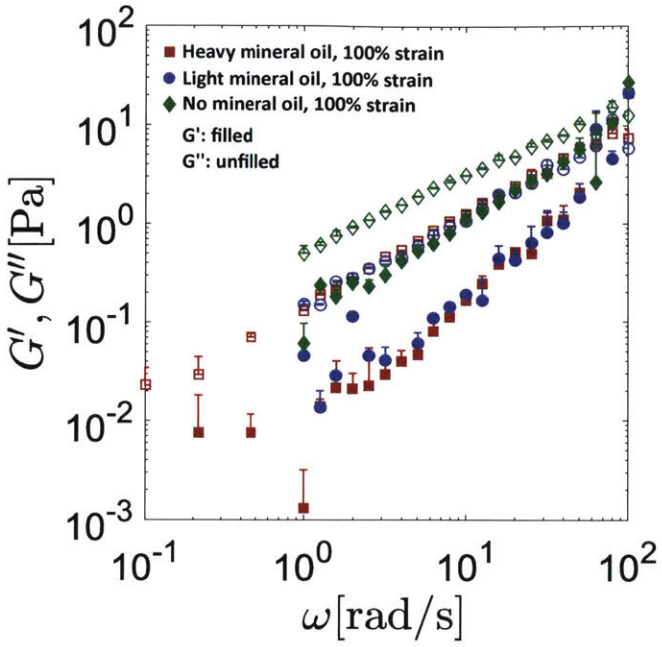

Figure 2.2.3: Effect of a mineral oil coating and sample evaporation on the linear viscoelastic response of 1 wt % CMC solutions at pH2. Measurements were performed using an 8 mm parallel plate setup on an ARESG2 rheometer. The red squares correspond to a rim of 'heavy' mineral oil (density $\rho = 0.862\,\mathrm{g\,ml^{-1}}$ at 25 °C, Catalog No 330760, Sigma Aldrich, St Louis, MO), the blue circles correspond to a rim of 'light' mineral oil (density $\rho = 0.838\,\mathrm{g\,ml^{-1}}$ at 25 °C, Catalog No 330779, Sigma Aldrich, St Louis, MO), and the green diamonds correspond to an experiment where no mineral oil was used, and hence no measures were taken to minimize sample evaporation. Filled symbols denote the storage modulus G', and unfilled symbols denote the loss modulus G''.

Despite reducing the range of frequencies for which the sample with no oil was measured in order to eliminate the long data acquisition times associated with low frequencies, these data exhibit higher viscoelastic moduli than the samples that were coated with mineral oil, and the sample had visibly evaporated over the course of the experiment. The effect of this evaporation is to make the sample appear more concentrated than its original preparation conditions. On the other hand, the viscoelastic moduli are virtually identical regardless of the type of mineral oil used. Indeed, this result is expected based on a quick estimate of the magnitude of the additional torque arising from the mineral oil rim compared to the torque arising from the sample itself. Let us approximate the mineral oil rim as hollow cylinder of height H corresponding to the truncation gap and thickness δ, where the inner radius of the annulus is given by R, the geometry radius, and the outer radius is then $R + \delta$ (see Figure 2.2.1a). The torque associated with this oil cylinder is by definition [21]

$$T_{\mathrm{oil}} = I\theta_0\omega^2, \tag{2.6}$$

where $\theta_0 = \gamma_0 \frac{H}{R}$ is the plate angular displacement and $I = \frac{1}{2}\rho H\pi((R+\delta)^4 - R^4)$ is the moment of inertia of the oil cylinder. Given $\gamma_0 = 1$, $H = 200\,\mu\mathrm{m}$, $R = 4\,\mathrm{mm}$,

$\rho = 862\,\mathrm{kg\,m^{-3}}$ for the heavy mineral oil, and assuming $\delta = 100\,\mu\mathrm{m}$, then in the range of $0.1\,\mathrm{rad\,s^{-1}} \leq \omega \leq 100\,\mathrm{rad\,s^{-1}}$, we obtain that $3.6 \times 10^{-12}\,\mu\mathrm{N\,m} \leq T_{\mathrm{oil}} \leq 0.0036\,\mu\mathrm{N\,m}$. Hence even at the highest frequency probed, the torque contribution from the oil rim is still significantly smaller than the oscillatory torque limit of the ARESG2 rheometer. As a result, the use of heavy and light mineral oil is indistinguishable, and good agreement between the measurements performed with the smaller geometry using mineral oil and those performed with the larger geometry using the solvent trap is observed (Figure 2.2.2).

As a final note for SAOS measurements, we consider the effect of fluid inertia on SAOS measurements at high frequencies. To do so, in Figure 2.2.4 we consider frequency sweep data obtained using an 8 mm parallel plate set up on an ARESG2 rheometer for a 0.05 wt % MUC5B solution at pH7. Despite this very low biopolymer concentration, an elastic modulus G' is apparently measured at all frequencies, and in fact at the highest frequencies the response of the material appears to be predominantly solid-like.

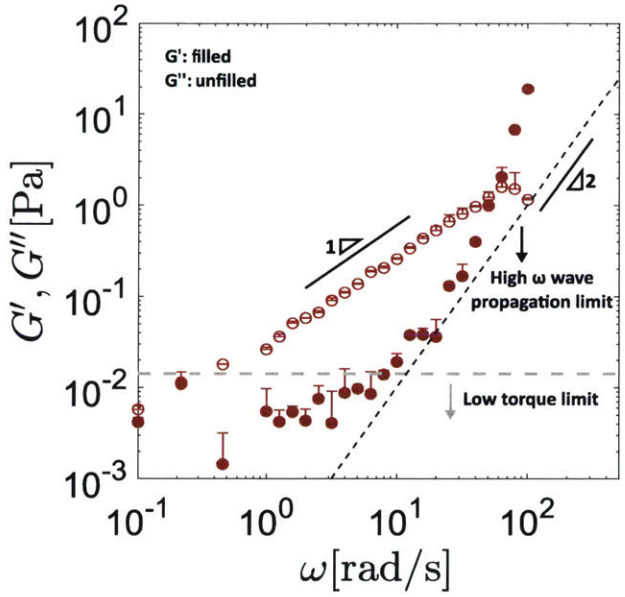

Figure 2.2.4: Low viscosity, small sample volume effects highlighted for 0.05 wt % MUC5B solutions at pH7. Frequency sweep at $\gamma_0 = 700\,\%$ performed using an 8 mm parallel plate setup on an ARESG2 rheometer with a coating of mineral oil to prevent evaporation. Filled symbols denote the storage modulus G', and unfilled symbols denote the loss modulus G''. The low torque limit calculated using $T_{\mathrm{min}} = 0.01\,\mu\mathrm{N\,m}$ is indicated by the dashed grey line, and the thin black dashed line corresponds to the high frequency wave propagation limit of Equation (2.9).

In a first instance, by plotting the low torque limit defined by Equation (2.5) for this system using $\gamma = 700\,\%$ and taking $T_{\mathrm{min}} = 0.01\,\mu\mathrm{N\,m}$ (thick grey dashed line), we see that effectively all of the data points for G' at frequencies less than $\omega \approx 10\,\mathrm{rad\,s^{-1}}$ lie below the low torque limit. Furthermore, at high frequencies, particularly as a result of the low viscosity of this material, the possibility of secondary flow effects arising from fluid inertia should be considered. In general, we can estimate a Reynolds number for the material in

oscillatory shear as [21]

$$Re \sim \frac{\rho \gamma_0 \omega H^2}{\eta_0}, \tag{2.7}$$

where η_0 is the zero shear viscosity. Given $\gamma_0 = 7$, assuming $\rho = 1000\,\mathrm{kg\,m^{-3}}$, and estimating $\eta_0 \approx 0.07\,\mathrm{Pa\,s}$ from the complex viscosity at $\omega = 0.1\,\mathrm{rad\,s^{-1}}$, we obtain that at $\omega = 100\,\mathrm{rad\,s^{-1}}$, $Re \approx 0.4$. For Newtonian fluids in a parallel plate set up, the ratio of the measured torque T (including contributions from secondary flows) to the torque associated with shear flow alone T_0 depends on the Reynolds number as [21]

$$\frac{T}{T_0} = 1 + \frac{3}{4,900} Re^2, \tag{2.8}$$

allowing for the definition of a critical Reynolds number $Re_{\mathrm{crit}} \approx 4$ at which the measured torque T deviates by more than 1 % from T_0 [21]. Although the estimated Reynolds number in our system does approach this value at the highest frequencies, it is still sufficiently small for it to appear that high velocity secondary flows are not dominating the material response. Another effect particular to high frequencies, however, is the change in strain field associated with wave propagation in the material [21]. By requiring that the wavelength l of any propagating wave in the system be at least 10 times as large as the geometry gap H, a lower bound on the magnitude of the complex modulus $G^*(\omega)$ can be defined as [21]

$$|G^*(\omega)| > \left(\frac{10}{2\pi}\right)^2 \rho \omega^2 H^2, \tag{2.9}$$

which is shown as the thin dashed line in Figure 2.2.4. Although the data points for $G''(\omega)$ lie comfortably above this limit, those of the storage modulus $G'(\omega)$ are right at the boundary, suggesting that fluid inertia effects, and wave propagation in particular, may be dominating the material response. In fact, the linear dependence of the loss modulus $G''(\omega)$ on the frequency ω is suggestive of the response of a Newtonian fluid, and for this class of materials the slope of $G''(\omega)$ is, in fact, the viscosity of the fluid [27]. In the next section, we will apply this analysis to the examination of steady state shear flow data for the same material.

Steady state shear flow In a steady state shear flow experiment, the geometric fixture (or bottom plate) is rotated at a constant shear rate $\dot{\gamma}$, and a steady state value for the material viscosity $\eta(\dot{\gamma})$ is extracted. By varying $\dot{\gamma}$, a flow curve for η across a range of shear rates can be determined. For Newtonian fluids, the viscosity is independent of the shear rate. On the other hand, when polymer solutions are subjected to shearing flows, the ability of the constituent chains to flow-align, disentangle, and unravel in the flow direction often leads to the phenomenon of *shear thinning*, in which the viscosity of the solution is observed to decrease with increasing applied rate of shear due to the increasing flow alignment of the chains [23, 28]. In a smaller number of cases, the opposite effect of *shear thickening* is observed, characterized by an increase in the viscosity of the solution with applied rate of shear over a specific range [23]. The mechanisms behind these behaviours depend on the chemistry of the dissolved macromolecules. By way of one specific example, Jaishankar, et al. observed shear thickening in their study of solutions of Mamaku gum, a polysaccharide extracted from the black fern tree in New Zealand [29]. In this system, shear thickening occurred as a result of the exposure of additional hydrophobic binding sites along the backbone

of the chains as they unraveled and extended during shearing, resulting in the formation of physical cross-links and an effective increase in the hydrodynamic size of the polymer chains [29].

For biopolymer solutions, experimental subtleties can arise during steady state flow experiments, as was observed for SAOS measurements. In order to examine some of these effects, we consider two sets of experimental data in Figures 2.2.5 and 2.2.6 below.

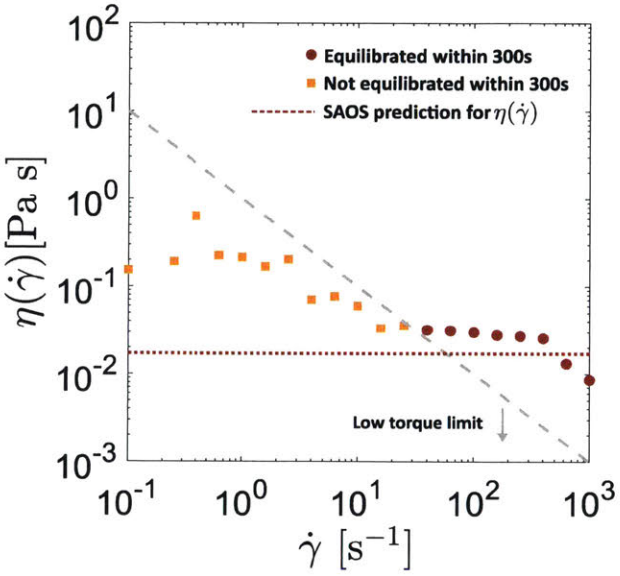

Figure 2.2.5: Low viscosity, small sample volume effects highlighted for 0.05 wt % MUC5B solutions at pH7. Steady state shear flow data performed using an 8 mm parallel plate setup on an ARESG2 rheometer with a coating of mineral oil to prevent evaporation. Orange square symbols denote data points that did not equilibrate within the allotted 300 s window, while red circles denote those that did. The low torque limit in steady state shear flow (Equation (2.10)) evaluated using $T_{\text{min}} = 0.1\,\mu\text{N m}$ (as provided by the manufacturer) is shown as the dashed grey line. The predicted value of the viscosity from Figure 2.2.4 is shown as the red dotted line.

In Figure 2.2.5, steady state flow data for a 0.05 wt % MUC5B solution at pH7 is shown, acquired using an 8 mm parallel plate setup on an ARESG2 rheometer. At first glance, the material appears to shear thin, before reaching an approximate Newtonian plateau prior to another period of shear thinning at high shear rates. Similarly to how the minimum modulus limit was obtained, the low torque limit for the shear viscosity is given by [21]

$$\eta_{\text{min}} = \frac{FT_{\text{min}}}{\dot{\gamma}}, \tag{2.10}$$

where once again $F = \frac{2}{\pi R^3}$ for a parallel plate, and in steady state shear flow the torque limit for the ARESG2 rheometer as provided by the manufacturer is $T_{\text{min}} = 0.1\,\mu\text{N m}$. In Figure 2.2.5, this limit is indicated as the dashed grey line, making apparent that the entire set of data corresponding to the low shear rate region of shear thinning lies below the noise

floor. As a second independent consideration, the data points plotted in orange squares correspond to those which did not equilibrate to a steady state value within the allotted acquisition time of 300 s for each measurement, while those that did are shown as red symbols. The fact that the transition between these equilibrated and non-equlibrated points is coincident with the low torque limit is also suggestive that the orange square data points may not be truly representative of the material properties. In fact, if a Newtonian response is assumed and the viscosity measured as the slope of $G''(\omega)$ from Figure 2.2.4 is plotted (red dotted line), reasonable agreement with the plateau shear viscosity values is obtained. At high shear rates, the origin of the onset of a second shear thinning regime is not entirely obvious, as secondary flows generally manifest as apparent shear *thickening* and not thinning [21], but it may be related to the displacement of of the mineral oil (and possibly the sample itself) that was observed at these high rotational speeds.

As a final consideration, in Figure 2.2.6 we consider the shear response of a commercially available food thickening agent for the treatment of dysphagia which is composed primarily of Xanthan gum, Resource ® Thicken Up Clear, at its 'nectar' preparation of 1.2 wt %. Measurements were made with a 40 mm 2° cone-and-plate setup on an AR-G2 rheometer.The rheology of this particular material will be discussed in further detail in Chapter 6.

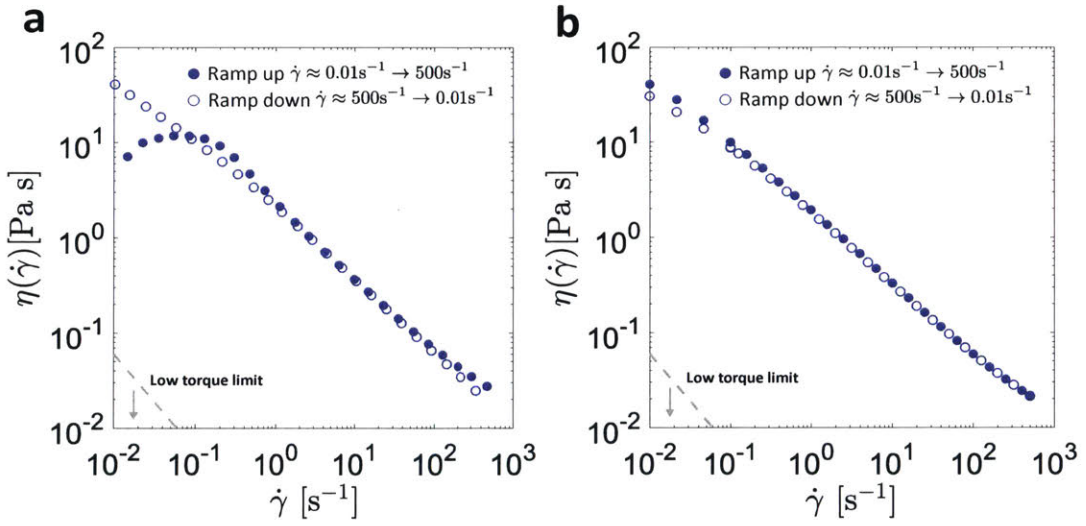

Figure 2.2.6: Effect of sample equilibration on shear rheological measurements. Measurements were performed using a 40 mm 2° cone-and-plate fixture on an AR-G2 rheometer with the 'nectar' preparation (1.2 wt %) of Resource ® Thicken Up Clear. Data is shown for both an 'up' ramp (increasing $\dot{\gamma}$, filled circles) and a 'down' ramp (decreasing $\dot{\gamma}$, unfilled circles). The low torque limit in shear evaluated using $T_{\min} = 0.01\,\mu\text{N m}$ (Equation (2.5)) is shown by the dashed grey line. (a) 2 minute continuous ramp data for the apparent shear viscosity $\eta(\dot{\gamma})$. A local maximum in $\eta(\dot{\gamma})$ is observed during the up ramp only. (b) Steady state flow experimental data. Allowing the solution to equilibrate at low shear rates eliminates the previously observed local maximum regardless of ramp trajectory.

In Figure 2.2.6a, the results of 2 minute continuous ramp experiments in the 'up' (increasing shear rate, filled circles) and 'down' (decreasing shear rate, hollow circles) directions

for $0.01\text{s}^{-1} \leq \dot{\gamma} \leq 500\text{s}^{-1}$ at 5 points per decade are shown. In these experiments, the measurement time for each data point is simply the quotient of the total ramp time and the number of data points —there is no verification of equilibration by the software before continuation to the next shear rate of interest. The 'up' data suggests that the viscosity passes through a local maximum at $\dot{\gamma} \approx 0.1\text{s}^{-1}$ prior to the onset of strong shear thinning at all higher rates. In this case, the non-monotonic flow behaviour observed is clearly not related to low torque effects, as all data points lie well above the instrument limit shown as the dashed grey line, determined from Equation (2.10) using $T_{\text{min}} = 0.01\,\mu\text{N m}$ as provided by the manufacturer for steady state flow.

Instead, in this instance, the apparent shear thickening is an artifact of non-equilibration of the sample during the allotted acquisition time. In order to ensure equilibration for reliable measurements of the steady shear viscosity in the range of $\dot{\gamma} \leq 0.1\text{s}^{-1}$, the steady state flow equilibration settings on the AR-G2 rheometer were modified such that the maximum allotted measurement time per point allowed a total strain of $\gamma \geq 5$ to accumulate in the system given the imposed shear rate $\dot{\gamma}$. The results of steady state shear flow measurements performed using these criteria are shown in Figure 2.2.6b. As can be seen, by allowing the fluid to come to equilibrium at each point within this low shear rate range, no shear thickening is observed. Thus, although shear thickening is a genuine feature of some biopolymer solutions, the appearance of a local maximum in the shear viscosity η at very low rates of shear ($\dot{\gamma} \lesssim 0.1\text{s}^{-1}$) may often be an artifact attributable to non-equilibration of the sample. Specifically, if the allotted time for the measurement of the transient response during steady state flow (which is related to rearrangements of the fluid on the microstructural scale) is insufficient, the viscosity will generally be under-predicted at the shear rate in question. In order to mitigate these effects, we propose two possible modifications to the default settings of the rheometer when testing biopolymer solutions with complex microstructures. A first option is to allow for the data acquisition time at each point to be sufficiently large such that a strain of at least $\gamma = 5$ is acquired by the sample. Secondly, more stringent software convergence criteria can be specified in order to prevent the misinterpretation of slowly varying transient stress response signals as steady state measurements. In particular, for the Thicken Up Clear system and other food biopolymer solutions such as flax seed extract, we have found that specifying in the software 10 consecutive readings within a tolerance of 1% resulted in sample equilibration.

Extensional flows

In addition to establishing specific mechanical properties under shear, the unique microstructure of biopolymer solutions also provides them with an extensional character. For mucus, for example, these extensional rheological properties are essential for proper function during physiological processes such as mucociliary clearance [30], bolus formation [31], and swallowing [31]. Experimentally, extensional flows are commonly established by stretching a sample between two vertically aligned plates. Depending on the experimental set up, the final height at breakup of the stretched sample may be measured (i.e. using tools such as the Filament Stretching Rheometer (FiSER) developed by the Cambridge Polymer Group [32] or the Filancemeter developed by Zahm et al. [33]), or the radius of the thinning filament may be monitored in order to extract a relaxation time associated with the material (i.e. using a Capillary Breakup Extensional Rheometer (CaBER) developed by the Cambridge Polymer Group [34]). This latter technique will be used extensively in Chapter 5, and is

depicted through still pictures in Figure 2.2.7, where the test fluid is human whole saliva. Briefly, following a period of rapid plate separation, a cylindrical filament established. As a result of capillary pressure, this filament thins over time, and its radius is monitored using a laser micrometer until breakup occurs. In the final panel of Figure 2.2.7, a phenomenon known as 'beads on a string', a signature of polymer solutions arising from extensional thickening of these materials due to the ability of the stretched polymers to sustain additional stresses [35], is observed.

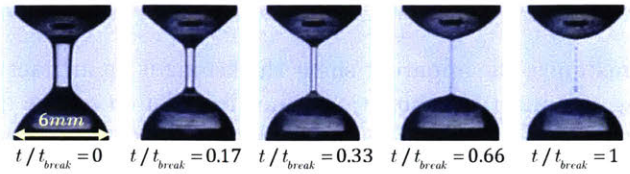

Figure 2.2.7: Series of pictures capturing a Capillary Breakup Extensional Rheology (CaBER) experiment performed on human whole saliva. The sample is placed between two 6 mm plates initially separated by a gap of 2 mm, and the plates are rapidly separated during a strike time of approximately 50 ms to a final separation distance of approximately 10 mm. Images are shown from this earliest time corresponding to the moment the plates reached their final separated positions until filament 'breakup', or in this case the formation of a stable 'beads-on-a-string' structure that is a signature of viscoelastic polymer solutions in extension. The radius of the filament is recorded throughout the thinning process using a laser micrometer, and from the temporal evolution of this quantity, a relaxation time for the material can be extracted.

2.2.2 Theory

In Section 2.2.1, we have presented a variety of experimental techniques for measuring the macroscopic mechanical properties of complex fluids in response to several deformations of interest. Now, in order to be able to interpret and understand these findings, we set out to develop predictive models for the fluid behaviour that can be compared with experimental measurements. The general process for doing so involves first solving the conservation equations for mass and momentum in combination with what is known as a *constitutive equation*, a fluid-specific relationship that relates the fluid stresses to the kinematics of the problem, in order to obtain the velocity fields within the fluid in question [23]. While the process of solving these equations is in and of itself an interesting one, we focus here on the theory and background relevant to the selection or development of an appropriate constitutive equation for a given complex fluid. In this section, we first introduce several classical constitutive equations, beginning with the Maxwell model for linear viscoelasticity, and discuss how this simple model can be extended and modified to capture the response of more complex fluids. Note that the interested reader is referred Chapters 4-6 in [23], the source from which much of the content in this section is based, for excellent detailed discussions on these subjects. Next, we introduce fractional constitutive equations, which have been found to be particularly useful for describing the rheological response of biological fluids with numerous length- and time-scales. Finally, we introduce the concept of kinetic theory and polymer models as another approach for deriving constitutive equations for complex fluids more directly. Once

again, the reader is referred to [36] for detailed information on this subject.

Classical constitutive equations

For purely viscous liquids or elastic solids, simple, well-established constitutive equations relating the material stresses to the imposed deformation exist. The former category obey Newton's law of viscosity (and are hence known as Newtonian fluids), with the material shear stress τ_d given by

$$\tau_d(t) = \eta \frac{d\gamma(t)}{dt}, \tag{2.11}$$

where $\frac{d\gamma}{dt} = \dot{\gamma}$ is the shear rate and η is the viscosity. Mechanical analogs for Newtonian fluids are dashpots, as shown in the left panel of Figure 2.2.8. At the other extreme, for infinitesimal displacement gradients, the shear stress in an elastic solid τ_s obeys Hooke's law and is given by

$$\tau_s(t) = G\gamma(t_0, t), \tag{2.12}$$

where G is the elastic modulus and $\gamma(t_0, t)$ is the strain. Unlike for a liquid, the strain in a solid at time t must be specified in reference to the isotropic stress state at time t_0, since a solid 'remembers' its initial deformation state, whereas a Newtonian fluid has no memory at all. Further, the requirements of infinitesimal displacement gradients for the application of Hooke's law enforce that it is only applicable for *linear* deformations. Mechanically, an elastic solid is represented by a spring, as shown in the right panel of Figure 2.2.8.

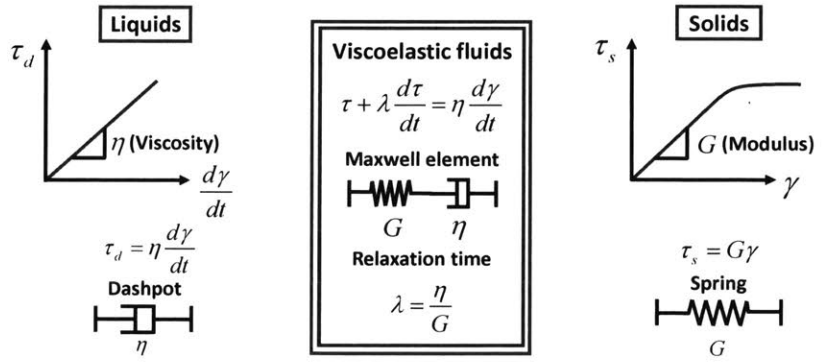

Figure 2.2.8: The response of a viscoelastic material interpolates between that of a viscous liquid (left, represented mechanically as a dashpot) and a purely elastic solid (right, represented mechanically as a spring). The Maxwell model for linear viscoelasticity (center) models the response of complex fluids as that of a spring and a dashpot in series.

It seems natural then that a simple approach for modeling the linear viscoelastic response of a complex fluid might be to consider the response of both a spring and a dashpot in series. Indeed this is precisely the Maxwell model, and a mechanical representation is depicted in the center panel of Figure 2.2.8. Since the spring and dashpot of the Maxwell element are

arranged in series, then the total strain is cumulative $\gamma = \gamma_d + \gamma_s$, while the stress must be constant across all elements such that $\tau = \tau_s = \tau_d$. Using Equations (2.11) and (2.12), it is straightforward to show that the stress response predicted by the Maxwell model is given by

$$\tau = \eta \frac{d\gamma}{dt} - \frac{\eta}{G}\frac{d\tau}{dt}. \tag{2.13}$$

The ratio $\frac{\eta}{G} = \lambda$ has units of time, and is known as the relaxation time of the material. Generally speaking, if the imposed deformation is faster than this time scale, the material does not have time to relax and hence responds as a solid. For deformations characterized by timescales slower than λ, the material does have time to relax, and hence it responds as a fluid. A pure solid then with perfect memory of its past has $\lambda \to \infty$, while a Newtonian fluid, which does not remember its deformation history, has $\lambda \to 0$; i.e. any time scale of deformation applied to a Newtonian fluid is sufficiently long for it to have 'relaxed' completely or forgotten its prior deformation history.

Although the Maxwell model is very useful for providing intuition regarding the behaviour of polymer solutions in response to different flow conditions, its restriction to linear deformations limits its broad applicability for modeling complex fluids. In order to develop nonlinear constitutive equations, the more familiar time derivatives of Equations (2.11) and (2.13) must be replaced with *convected derivatives*, which hold independent of any superposed rigid body rotations [23]. Specifically, the rate-of-strain tensor and its time derivatives $\frac{\partial \gamma^n}{\partial t}$ must be replaced with the tensors $\gamma_{(n)}$, $n = 1, 2, 3...$, defined as

$$\gamma_{(1)} \equiv \dot{\gamma} \tag{2.14}$$

and subsequently recursively as

$$\gamma_{(n+1)} = \frac{D}{Dt}\gamma_{(n)} - \left[(\nabla \mathbf{v})^T \cdot \gamma_{(n)} + \gamma_{(n)} \cdot (\nabla \mathbf{v})\right], \tag{2.15}$$

where $\nabla \mathbf{v}$ is the velocity gradient tensor and $\frac{D}{Dt}$ is the material derivative defined as

$$\frac{D}{Dt} = \frac{\partial}{\partial t} + (\mathbf{v} \cdot \nabla). \tag{2.16}$$

Similarly, time derivatives of the stress tensor must be replaced with convected derivatives, i.e.

$$\frac{\partial \tau}{\partial t} \to \tau_{(1)},$$

and the strain tensor must be replaced with the relative finite strain tensor. With these changes, examination of Equation (2.13) reveals that the convected Maxwell equation is given by

$$\tau + \lambda \tau_{(1)} = -\eta \gamma_{(1)}. \tag{2.17}$$

The simplicity of this constitutive equation has resulted in its application to a wide variety of flow problems, but also limits its ability to capture complex viscoelastic flow phenomena. One approach for increasing the complexity of constitutive equations has been to express them as polynomials of the rate-of-strain tensors $\gamma_{(n)}$, an approach known as the retarded motion expansion. In a similar way, the complexity of the model can also be

increased by including terms that involve products of the stress and rate-of-strain tensors. The inclusion of these terms results in a noted increase in the complexity and number of terms of the governing equations, but may also permit the prediction of more complex nonlinear rheological phenomena.

Fractional constitutive equations

Biological polymers such as polysaccharides and proteins frequently possess a polydisperse distribution of chain lengths and a variety of binding/cross-linking and/or macromolecular association mechanisms, which when swollen in water produce a gel network with a seemingly continuous distribution of chain lengths between associative junctions. These features contrast with the classical Green–Tobolsky [37] network model in which a single relaxation mode corresponding to an active elastic segment of a given length (represented mechanically by a spring and dashpot in series) describes the linear viscoelastic response of the physical network. A large ensemble of these Maxwell modes in parallel is required to approximate the experimental response of multi-scale materials like biopolymers, which has been argued by some, including Tschoegl, to lead to a 'loss of physicality' [38]. To this end, fractional rheological models, originally pioneered by Nutting and Scott Blair [39, 40, 41], have proven to be a concise and elegant framework for predicting the response of complex fluids using a small number of parameters. The introduction of what Scott Blair called *quasiproperties* [39], i.e. material parameters that interpolate between a viscosity and an elastic modulus, as well as the incorporation of fractional time derivatives of the imposed strain and resulting stress, offers a compact alternative to fitting a spectrum of material constants to the numerous length and time scales typically found in many complex fluids [17].

As outlined in Section 2.2.2, one approach for developing classical constitutive equations involves devising various arrangements of springs and dashpots as conceptual models for the linear response of viscoelastic materials. Analogously, the simplest fractional constitutive model considers the response of a *spring-pot*, a mechanical element that interpolates between a spring and a dashpot, to an imposed deformation, as depicted in Figure 2.2.9. Just as the stress in a spring τ_s is proportional to the strain γ itself (Equation (2.12)), or in other words the 0^{th} derivative of the strain, and the stress in a dashpot τ_d is proportional to the first derivative of the strain $d\gamma/dt$ (Equation (2.11)), the stress in a spring-pot τ_{sp} is proportional to the α^{th} derivative of the strain, i.e.

$$\tau_{\text{sp}} = \mathbb{V}\frac{d^{\alpha}\gamma}{dt^{\alpha}}, \tag{2.18}$$

where the fractional derivative order α satisfies $0 \leq \alpha \leq 1$. Although the mathematical steps leading to this relationship lie outside of the scope of this thesis, the reader is referred to excellent papers by [42, 17, 27] for additional details. The parameter $\mathbb{V}$ with units of Pa s^{α} is known a *quasiproperty*, and although its physical meaning is perhaps initially less straightforward to grasp as compared to an elastic modulus or a viscosity, its magnitude can nevertheless be taken as an indicator of the 'stiffness' of the complex fluid in question and the scale of the stress expected in a system once a characteristic timescale or deformation rate is specified.

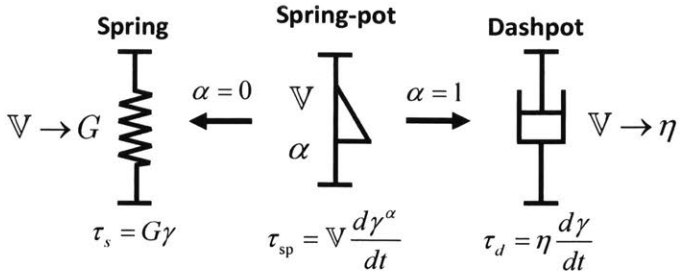

Figure 2.2.9: Definition of a spring-pot of fractional derivative order α and quasiproperty $\mathbb{V}$ as a mechanical element that interpolates between a spring ($\alpha \to 0$, $\mathbb{V} \to G$) and a dashpot ($\alpha \to 1$, $\mathbb{V} \to \eta$).

Analogously to the procedure outlined in Section 2.2.2, by imposing different deformations for the strain $\gamma(t)$, the linear viscoelastic material functions for the spring-pot can be obtained. For instance, the complex shear modulus $G^*(\omega)$ can be found by taking the Fourier transform of Equation (2.18), which is admissible due to the linearity of the integral in the definition of the fractional derivative [27]. From the definition of the Fourier transform of a fractional derivative [27]

$$\mathscr{F}\left[\frac{d^\alpha f(t)}{dt^\alpha};\omega\right] = (i\omega)^\alpha \tilde{f}(\omega) \tag{2.19}$$

and the relationship $G^*(\omega) = \tilde{\tau}(\omega)/\tilde{\gamma}(\omega)$ [27], it is straightforward to show that $G^*_{sp}(\omega) = \mathbb{V}(i\omega)^\alpha$, which upon taking the real and imaginary parts using of Euler's identity reveals that

$$G'_{sp}(\omega) = \mathbb{V}\omega^\alpha \cos(\pi\alpha/2) \tag{2.20}$$

and

$$G''_{sp}(\omega) = \mathbb{V}\omega^\alpha \sin(\pi\alpha/2). \tag{2.21}$$

It is instructive to verify the predictions of this model in the limit of a pure solid ($\alpha = 0$) and a pure liquid ($\alpha = 1$). In the case of the former, Equations (2.20) and (2.21) reduce to $G'_{sp}(\omega) = \mathbb{V} = G$ and $G''_{sp}(\omega) = 0$, respectively, while when $\alpha = 1$ the same limits are $G'_{sp}(\omega) = 0$ and $G''_{sp}(\omega) = \mathbb{V}\omega = \eta\omega$, which are indeed the expected results [27].

Using a similar approach involving Laplace transformations, other linear viscoelastic parameters such as the relaxation modulus and creep compliance can also be derived [27].

Kinetic theory and polymer models

So far in this section, we have discussed one approach for developing constitutive equations that involves drawing on the known mechanical response of solids and liquids in order to describe the behaviour of viscoelastic fluids. Another approach, known broadly as kinetic theory, considers the statistical likelihood of certain distributions of the macromolecules over

all of their possible configurations, in combination with mechanical models for the polymers themselves, in order to obtain information regarding the rheological properties of the material [36]. Therefore, in this section we provide a brief introduction to some of the concepts of kinetic theory that will be developed in Chapter 5. The interested reader is directed to Chapters 11-13 of [36] for in-depth considerations of this topic.

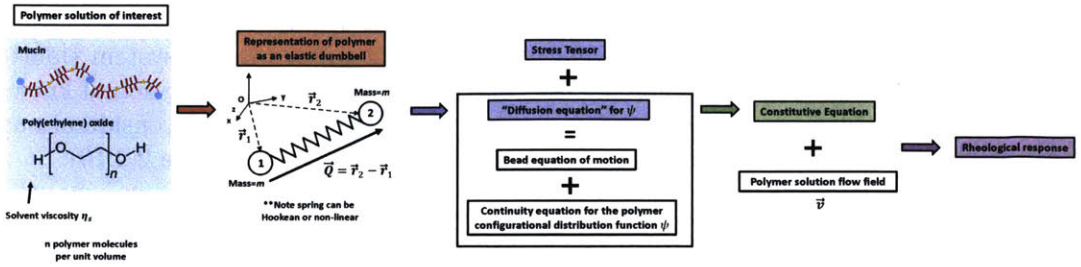

Figure 2.2.10: Overview of the process developed in kinetic theory for deriving the rheological response of a polymer solution from the molecular structure and properties of the polymer itself. In general, the polymer is first coarse-grained to a simpler mechanical structure such as an elastic dumbbell (Panel 2), and the stress tensor and configurational distribution function of the dumbbells are established (Panel 3). From these results, a constitutive equation can be developed (Panel 4), which when combined with the actual kinetics of the problem in question permit the prediction of a rheological response (Panel 5). For an in-depth treatment of kinetic theory, the reader is referred to [36].

In general, the structure of polymer molecules (and biopolymers in particular) is highly complex, and as a result it is usually impossible to account for their every degree of freedom and chemical feature in a mechanical model. Instead, the usual approach is to *coarse-grain* the intricate native structure of the molecule to a mechanically simple one whose degree of deformation and orientation can be more readily modeled. One of the simplest coarse-grained structures which has been extensively employed in the development of constitutive equations is known as the elastic dumbbell. Using this approach, the macromolecules are modeled as two beads of mass m connected by a massless, non-bendable spring [36], as shown in the second panel of Figure 2.2.10. In the simplest case, the spring is Hookean, meaning that the force incurred is linearly proportional to the spring deformation, and infinitely extensible [36]. More realistically for physical systems, a finite limit to the degree of extension of the spring can be imposed, which results in a divergence of the force as the spring is stretched to its full length, and hence the spring is said to be *non-linear*. This is the approach that will be used in Chapter 5 in the development of the SFEN model for mucin solutions. More complex models for the coarse grained polymer structure have also been studied extensively, such as the bead-rod-chain and bead-spring-chain models, with the famous Rouse and Zimm results arising from the latter when hydrodynamics are disregarded or included, respectively [36].

Once the mechanical model for the macromolecule is selected, the configurational distribution function ψ, which characterizes the deformation and orientation of the population of dumbbells, as well as the stress tensor, which accounts for the mechanisms of force trans-

mission in the system [36], must be established. For non-equilibrium processes, the former generally takes the form of a second order partial differential 'diffusion equation' for ψ, derived from a force balance or equation of motion on the beads of the dumbbell as well as a continuity equation for the dumbbells. The stress tensor can be derived through considerations of intramolecular and external forces on the system, as well as bead motion which can contribute to accumulated stresses as a result of momentum transport. This is summarized in the third panel of Figure 2.2.10.

From the stress tensor and the configurational distribution function, a constitutive equation can be obtained, which relates the velocity field to the stresses in the system (fourth panel of Figure 2.2.10). Finally, combining the constitutive equation with the actual known flow field of the problem in question as well as any other relevant kinematic considerations, the rheological response of the material can be modeled (fifth panel of Figure 2.2.10).

2.3 Microrheology: characterizing local material properties

Microrheological techniques involve measuring the mechanical response of materials using embedded colloidal probes which can either be driven actively, for instance through the use of optical or magnetic tweezers, or passively by thermal fluctuations of the material [18]. In addition to the highly sensitive measures of spatial heterogeneity and gelation kinetics that these techniques can provide [43], the very limited sample volume (e.g. microliters) that they require [18, 19] makes them particularly attractive for characterizing sample-limited materials such as mucus.

In this section, we begin by briefly reviewing some of the experimental details associated with the passive microrheological method of single particle tracking (SPT) which was used to obtain the microrheological data presented in Chapters 3 and 4. For additional details on this subject, the reader is referred to [19]. As first shown by Mason and Weitz [44], the mean squared displacement (MSD) of passive colloidal beads can be directly related to the linear viscoelasticity of the samples that they are embedded in through the Generalized Stokes Einstein Relationship (GSER) provided that certain assumptions, including that the embedded probes be significantly larger than the characteristic length scale of heterogeneity within the gels and that they do not interact with the gel components, are met [18]. Therefore, we next review this derivation, and discuss the applicability of the GSER to complex biological fluids such as mucus and mucin gels. Finally, we provide a preliminary discussion of some additional analytical tools for interpreting SPT data, with further details on this subject provided in Chapter 4.

2.3.1 Single particle tracking: Experimental details

In single particle tracking (SPT), the spatial location of colloidal particles embedded into the sample of interest is recorded over time at set intervals, as illustrated in Figure 2.3.1.

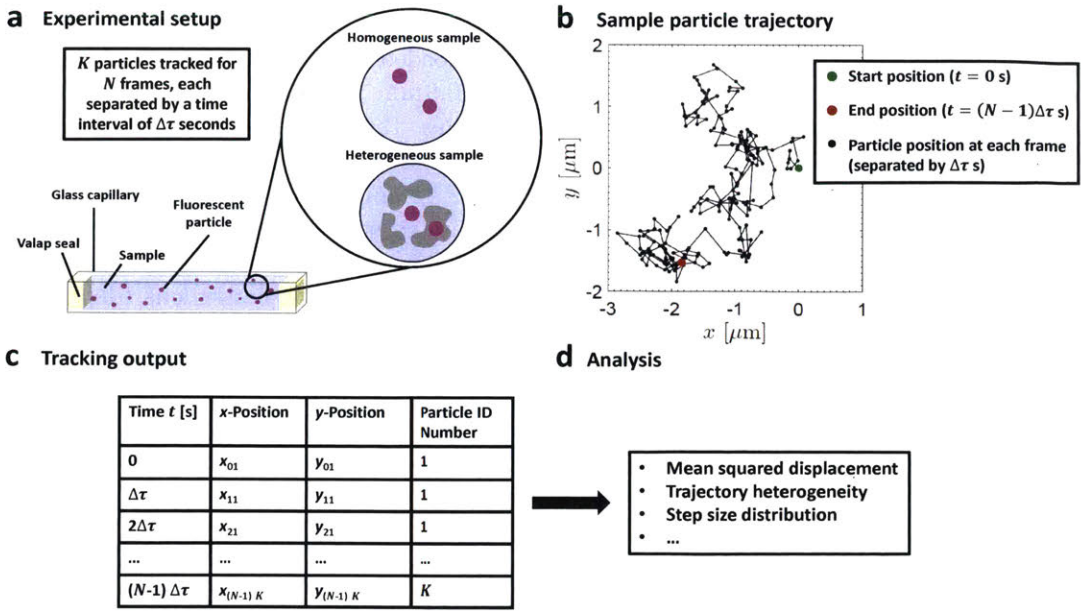

Figure 2.3.1: Overview of the method of single particle tracking (SPT). (a) Schematic of a borosilicate square capillary containing a particle-laden sample, and sealed on either end with Valap. Inset: (Top) For uniformly homogeneous samples such as water, the particle size is significantly larger than any length scales associated with heterogeneity within the sample. (Bottom) In a heterogeneous sample, the particles may probe a local microenvironment only. (b) Sample trajectory for a 1 μm particle in water. The initial particle position is normalized to $\{x = 0\,\mu\text{m}, y = 0\,\mu\text{m}\}$ at time $t = 0\,\text{s}$ (large green circles), and subsequent particle positions at all later times (small black circles) are given in reference to this initial location. The final particle position recorded is shown as the red circle. (c) Schematic of particle position data obtained following image analysis and tracking. (d) Various analytical parameters can then be acquired with this information.

For the experiments performed in this thesis, previously diluted solutions of colloidal particles in miliQ water were combined with the sample of interest at a ratio of 60 : 1 sample : particle solution. Samples were subsequently mixed well through a combination of vortexing and/or pipette mixing in order to ensure adequate particle dispersion.

For highly viscoelastic samples such as native mucus, there is a tradeoff between mixing sufficiently well to obtain adequate particle dispersion, but gently enough so as to not introduce air bubbles into the system. Indeed, air bubbles are problematic during imaging as a result of their ability to expand, contract, and wander by buoyancy [19], which frequently manifests as a bulk 'expansive' or 'contractile' motion within the field of view which, unlike a uniform drift, cannot be easily removed during image processing and analysis. If introduced by vortexing, air bubbles could often be eliminated by gentle and brief centrifugation of the sample/particle mixture prior to loading into the capillaries. However, for highly viscoelastic samples, residual air bubbles frequently remained within the sample even after this step. In this case, care was taken to perform imaging sufficiently far away from the air bubbles in order to not capture bulk motion associated with their presence in the videos. When this

was not achieved and the 'expansive' motion was observed, the video was discarded.

The resulting particle-laden samples were then loaded using a positive displacement pipette into borosilicate square capillaries 0.9 mm × 0.9 mm × ≈ 20 mm in dimension (Vitrocom 8290). We note that for low viscosity samples, the use of such a pipette is not necessary as the sample will be readily drawn into the channel through capillary action. The capillaries were sealed on either end using a 1 : 1 : 1 mixture of Vaseline, lanolin, and paraffin (Valap) to prevent evaporation, and then mounted onto microscope slides for imaging. Imaging was performed with an Axio Observer D.1 inverted microscope using either a Zeiss LD Plan-Neofluar 40x/0.4, 20x/0.4, or 10x/0.4 Corr Ph2 objective lens (depending on the particle size being imaged) and a Hamamatsu Flash 4.0 C11440-22CU camera. The camera frame rate and the length of the recorded videos varied depending on the experiment in question, and consequently these parameters are specified at appropriate locations throughout the thesis. The number of particles imaged for a given sample varied between approximately 100 and 300, which corresponded to between 3 and 12 videos depending on the particle size, density, and quality of dispersion within the sample. Care was taken to perform imaging sufficiently far from the Valap edges as well as from the capillary walls in order to minimize hydrodynamic effects [19]. However, for highly viscoelastic samples, the difficulty of achieving an even particle dispersion often limited the number of planes of particles that were visible, and in these cases videos were simply taken wherever particles were present.

As explained by Furst and Squires, achieving high quality particle tracking data requires the optimization of many factors amongst which are the system magnification, the brightness of the particles, and the noise of the camera and electronics systems [19]. Two important factors that may introduce error into the tracking output are the static and dynamic errors associated with video microscopy [19]. The former arises due to the finite resolution of the detectors used and the inaccuracy associated with locating a particle within a specific spatial resolution denoted by ϵ [19]. This sets the minimum MSD that can be resolved, and consequently provides an upper bound on the modulus of the sample that can be measured [19].

One important parameter that affects the static error is the exposure time σ_t of the camera. By increasing the exposure time, the signal to noise ratio and consequently the contrast of the image is improved, which reduces the static error [19]. In principle, the static error for a given set up can be estimated by performing imaging with the particles 'immobilized' in a very stiff gel [19]. In order to demonstrate this, in Figure 2.3.2, we plot the MSD of 1 µm particles in 3 wt % agarose (Catalog No CA3510-6, Denville Scientific, Holliston, MA) gels measured at a magnification of 20x and a camera frame rate of ≈ 30 fps, using exposure times of $\sigma_t = 10$ ms (black circles) and $\sigma_t = 33$ ms (grey diamonds; implemented by linking the exposure time to the frame rate of the camera).

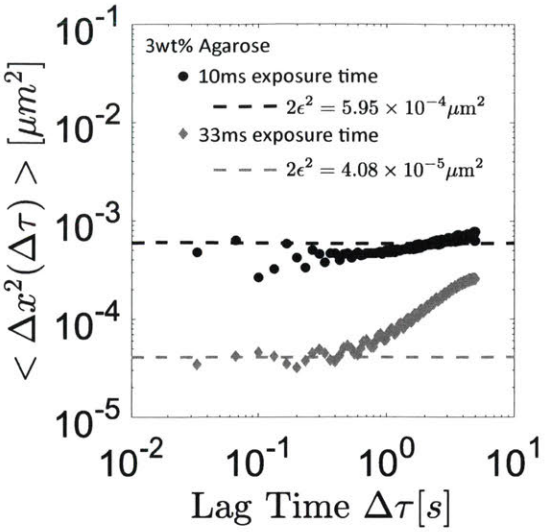

Figure 2.3.2: Estimation of the static error $2\epsilon^2$ (Equation (2.22)) for the experimental set up used in this thesis. The MSD of 1 µm particles embedded in 3 wt % agarose gels imaged at a magnification of 20x and a camera frame rate of $\approx$ 30 fps for two different exposure times: σ_t = 10 ms (black circles) and σ_t = 33 ms (grey diamonds) is shown. The dashed lines denote the estimates for $2\epsilon^2$ obtained from the average MSD for σ_t = 10 ms (black dashed line), and the average MSD of just the early lag time plateau ($\Delta\tau \lesssim 0.33$ ms) for σ_t = 33 ms (grey dashed line).

As can be seen, with the longer exposure time the minimum resolvable MSD is reduced by nearly an order of magnitude, indicating an improved static error. In order to quantify this, the MSD in a Newtonian fluid can be expressed as the sum of a Brownian contribution ($2D\Delta\tau$) and another arising from static error ($2\epsilon^2$) [19], i.e.

$$\langle \Delta x^2(\Delta\tau) \rangle = 2D\Delta\tau + 2\epsilon^2. \tag{2.22}$$

In Figure 2.3.2, we determine the value of $2\epsilon^2$ as the average MSD for the case of the σ_t = 10 ms exposure time (dashed black line), and as the average MSD in the early lag time plateau ($\Delta\tau \lesssim 0.33$ ms) for the σ_t = 33 ms exposure time (dashed grey line). However, it is important to note that Equation (2.22) omits contributions from *dynamic error*. Since the particle location recorded at a given time point is actually an average of its positions throughout the exposure time [19], increasing the exposure time of the camera also increases the dynamic error associated with determining the exact location of the particle. Equation (2.22) can then be more accurately rewritten to account for dynamic error as

$$\langle \Delta x^2(\Delta\tau) \rangle = 2D\Delta(\tau - \sigma_t) + 2\epsilon^2. \tag{2.23}$$

Therefore, the selection of an optimal exposure time is a tradeoff between maximizing the minimum resolvable particle displacement (i.e. reducing the static error), and minimizing the dynamic error, and as such the chosen value will likely need to be tailored to the experiment in question.

Finally, we note that the static error is sample dependent [19], and also likely depends

on the optical magnification used. Consequently, it is advised that estimates such as the ones in Figure 2.3.2 be used with caution [19], and in this thesis they are interpreted as an approximation to the minimum resolvable MSD of the SPT setup rather than a hard limit. Additional discussions on static and dynamic error can be found in [45].

2.3.2 Single particle tracking: Theory and analysis

In general, the images recorded during SPT undergo a degree of preprocessing that removes low and high frequency noise as they are saved by the imaging software [19]. Subsequently, for each recorded image, particles were identified using publicly available Matlab (Natick, MA) code which identifies candidate features using high intensity matches and filters them using criteria such as maximum feature eccentricity and radius of gyration [46, 47]. The x and y positions of every validated particle in each frame were recorded using the same publicly available Matlab code as the center of mass of the localized image intensity. In some cases, particularly for viscoelastic samples, unphysical particle trajectories, such as that shown in Figure 2.3.3 of a 1 µm particle in human cervical mucus, were observed.

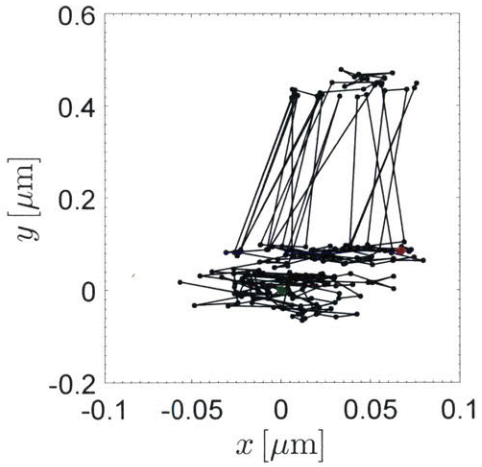

Figure 2.3.3: Example of the 'back-and-forth' motion associated with incorrect particle localization, frequently due to the presence of an optical halo. In this case the particle is 1 µm in size, and the sample is human cervical mucus.

By inspection of the corresponding videos, it appears that this 'back-and-forth' motion is due to the incorrect localization of the particle resulting from the presence of an optical halo associated with either the particle itself or another one slightly out of plane. Although such events were rare, this type of recorded motion manifested itself as a very large value of the MSD for the particle in question at very early lag times due to the erroneous 'jumps' between successive frames. Since ensemble averages of the MSD over all particles are taken (as will be explained in Section 2.3.2) and the 'true' values of this displacement were often orders of magnitude smaller, such large MSD values at early times, even for just one or two particles, could significantly alter the overall MSD recorded. Consequently, the tracks of all particles were visually scanned, and if motion such as that corresponding in Figure 2.3.3 was observed, the particle was discarded.

Following verification for erroneous trajectories, a drift correction code from the same publicly available source [46], which subtracts the center of mass motion of all of the particles in a given frame from each individual trajectory, was applied to all SPT data.

Determination of the mean squared displacement (MSD)

From the drift-corrected data corresponding to the particle positions during individual trajectories, as depicted in Figure 2.3.1c, the time-averaged MSD (in one dimension) of the k^{th} particle for a movie N images in length is given by [48, 49]

$$\overline{\Delta x_k^2(\Delta\tau)} = \frac{1}{N - \Delta\tau/\Delta t} \sum_{i=1}^{N-\Delta\tau/\Delta t} [x(i\Delta t + \Delta\tau) - x(i\Delta t)]^2, \tag{2.24}$$

where Δt is the time between successive frames and $\Delta\tau$ is the lag time. The ensemble averaged MSD over all K particles is then [49]

$$\langle \Delta x^2(\Delta\tau) \rangle = \frac{1}{K} \sum_{k=1}^{K} \overline{\Delta x_k^2(\Delta\tau)}. \tag{2.25}$$

For normal diffusive motion such as that occurring in a homogeneous Newtonian medium with no fluid memory and with which the microspheres do not interact, the MSD is expected to scale linearly with lag time, and in one dimension the explicit form of this scaling is [49]

$$\langle \Delta x^2(\Delta\tau) \rangle = 2D\Delta\tau, \tag{2.26}$$

where D is the translational diffusion coefficient of the microsphere in the medium. In higher dimensions, Equation (2.26) is generally expressed as

$$\langle \Delta r^2(\Delta\tau) \rangle = 2dD\Delta\tau, \tag{2.27}$$

where d is the system dimension. This normal diffusion in Equations (2.26) and (2.27) is known as Brownian motion, and when this scaling does not hold, the diffusion is termed *anomalous* or *non-Brownian* [49], and the mean squared displacement is generally expressed as an arbitrary, monotonically increasing function of the lag time, often assigned a power law form as

$$\langle \Delta x^2(\Delta\tau) \rangle = 2D_\alpha \Delta\tau^\alpha, \tag{2.28}$$

where D_α is a generalized diffusion coefficient [50]. When $\alpha < 1$, the motion of the particle is *subdiffusive*, and when $\alpha > 1$, the motion is *superdiffusive* [49].

The Generalized Stokes Einstein Relation (GSER)

The Generalized Stokes Einstein Relation (GSER) is the defining equation for SPT that relates the thermal motion of the probe particles, or their observable displacement, to the rheological response of the material they are embedded in [19]. A brief derivation of this result derived from [18, 19] will be given below, but for a more in-depth treatment the reader

is referred to those original sources.

The equation of motion of a tracer particle of mass m in a viscoelastic medium is given by the Generalized-Langevin equation

$$m\dot{\boldsymbol{V}}(t) = \boldsymbol{f}_R - \int_{-\infty}^{t} \zeta(t-t')\boldsymbol{V}(t')dt', \tag{2.29}$$

where $\boldsymbol{V}(t)$ is the instantaneous velocity of the particle, $\zeta(t)$ is the microscopic probe resistance, and $\boldsymbol{f}_R$ is a random, fluctuating Brownian force that arises from thermal motion of the surrounding molecules. Taking the Laplace transform of Equation (2.29) we obtain

$$\hat{V}(s) = \frac{mV(0) + \hat{f}_R(s)}{ms + \hat{\zeta}(s)}, \tag{2.30}$$

where s is the Laplace variable and the circumflex accent denotes the Laplace transform of a function. Multiplying Equation (2.31) by the initial velocity $V(0)$ and taking en ensemble average, we arrive at

$$\langle \hat{V}(s)V(0)\rangle = \frac{m\langle V(0)V(0)\rangle + \langle \hat{f}_R(s)V(0)\rangle}{ms + \hat{\zeta}(s)}. \tag{2.31}$$

The expression on the left had side of Equation (2.31) can be expressed in terms of the particle displacement through the identity [19]

$$\langle \hat{V}(s)V(0)\rangle = \frac{1}{2}s^2\langle \Delta\hat{r}^2(s)\rangle. \tag{2.32}$$

Further, the first term on the numerator of Equation (2.31) is twice the initial kinetic energy of the particles, and for an N dimensional system in thermal equilibrium with its surroundings the equipartition theorem states that

$$\frac{1}{2}m\langle V(0)V(0)\rangle = \frac{1}{2}Nk_BT, \tag{2.33}$$

where k_B is the Boltzmann constant and T is the temperature. Additionally, since the random Brownian force $\hat{f}_R(s)$ is uncorrelated with the particle velocity, the second term in the numerator of Equation (2.31) vanishes, and we make the assumption that the measurement frequencies are sufficiently low such that $s \ll m/\hat{\zeta}(s)$. Therefore, using Equations (2.32) and (2.33) as well as these additional assumptions, Equation (2.31) simplifies to

$$\hat{\zeta}(s) = \frac{2Nk_BT}{s^2\langle \Delta\hat{r}^2(s)\rangle}. \tag{2.34}$$

For a Newtonian fluid, the resistance of a spherical probe of radius a is related to the viscosity η of the medium through the Stokes relation $\zeta = 6\pi a\eta$. The Correspondence Principle demonstrates that an identical solution exists in the frequency domain for a spherical probe moving quasi-steadily through an incompressible viscoelastic medium, i.e. $\tilde{\zeta}(\omega) = 6\pi a\eta^*(\omega)$, where $\tilde{\zeta}(\omega)$ is the Fourier transform of the probe resistance and $\eta^*(\omega)$ is the complex viscosity. By analytic continuation, this implies that

$$\hat{\zeta}(s) = 6\pi a\hat{\eta}(s). \tag{2.35}$$

Substituting Equation (2.35) into Equation (2.34), we obtain

$$\hat{\eta}(s) = \frac{Nk_BT}{3\pi as^2 \langle \Delta \hat{r}^2(s) \rangle}, \tag{2.36}$$

or its analog in frequency space

$$\eta^*(\omega) = \frac{Nk_BT}{3\pi a(i\omega)^2 \langle \Delta \tilde{\boldsymbol{r}}^2(\omega) \rangle}, \tag{2.37}$$

both of which (Equations (2.36) and (2.37)) are known as the Generalized Stokes Einstein Relation (GSER).

The complex viscosity $\eta^*(\omega)$ is related to the complex modulus $G^*(\omega)$ through the expression

$$G^*(\omega) = i\omega\eta^*(\omega), \tag{2.38}$$

and consequently we see that the GSER provides a direct relationship between $G^*(\omega)$ and the MSD in frequency space $\langle \Delta \tilde{\boldsymbol{r}}^2(\omega) \rangle$, namely

$$G^*(\omega) = \frac{Nk_BT}{3\pi ai\omega \langle \Delta \tilde{\boldsymbol{r}}^2(\omega) \rangle}. \tag{2.39}$$

Because a transformed function appears on the denominator of Equation (2.39), it is not possible to invert it directly back to real-time space for a given $G^*(\omega)$. Instead, since the MSD is in the time domain, SPT data must first be converted to frequency space in order to obtain $G^*(\omega)$. While this is a wide-spread approach, it is important to note that the limited time-range over which MSD data is available may result in the introduction of numerical artifacts during this conversion.

Another approach is to think of the MSD as the strain ($\langle \Delta \boldsymbol{r}^2(t) \rangle / a^2$) accumulated by the material due to the average thermal stress (k_BT/a^3) imposed on the probe particle arising from the random Brownian forces [19]. In this sense, the MSD is related to the creep compliance $\tilde{J}(\omega) = \frac{1}{i\omega G^*(\omega)}$ through

$$\tilde{J}(\omega) = \frac{3\pi a \langle \Delta \tilde{\boldsymbol{r}}^2(\omega) \rangle}{Nk_BT}, \tag{2.40}$$

which can be inverted directly to yield

$$\tilde{J}(t) = \left[\frac{3\pi a}{Nk_BT} \right] \langle \Delta \boldsymbol{r}^2(t) \rangle . \tag{2.41}$$

In order to demonstrate the applicability of the GSER in an incompressible, Newtonian fluid, in Figure 2.3.4a we plot the MSD of fluorescent carboxylated polystyrene latex particles (Magsphere Inc, Pasadena, CA) of different sizes ranging from 200 nm to 5 µm. Since they will be used in Chapter 4, we also plot these results for 500 nm and 1 µm particles whose surface chemistry has been modified through the addition of a polyethylene glycol (PEG) corona (obtained courtesy of the Hanes research group at John Hopkins University). Imaging was performed at $\approx$ 30 fps with an exposure time of 10 ms and for a total duration of 10 s. We note that in practice the particle sizes exhibit a certain degree of polydispersity. For particles obtained from Magsphere Inc, the actual average value of the particle radii for a

given batch is indicated on the container, and may vary by up to $\approx 10\,\%$ from the nominal value of the purchased product. For the work in this thesis, we assume that the particles are sized according to their nominal values, as the error associated with polydispersity and batch-to-batch variation is generally small enough to not contribute significantly to the microrheological predictions.

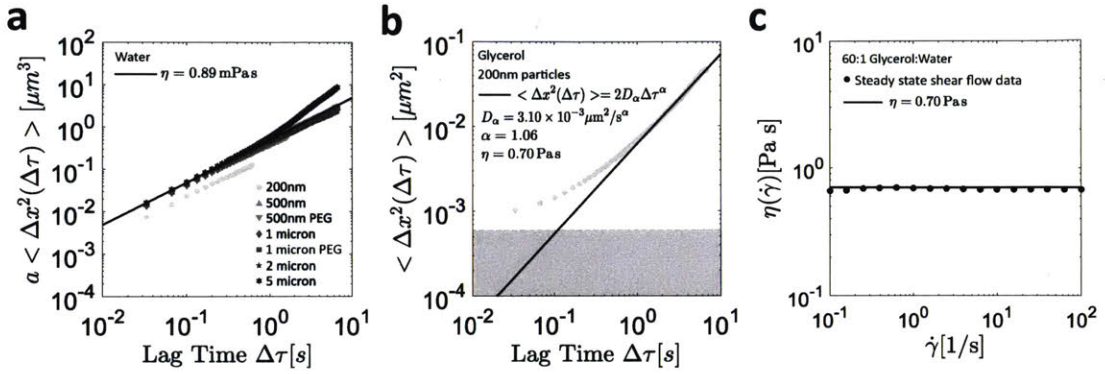

Figure 2.3.4: Analysis of the GSER for particles of different sizes in water. Imaging was performed at ≈ 30 fps with an exposure time of 10 ms and for a total duration of 10 s. (a) By scaling the particle MSDs by their radii, collapse onto a single master curve is achieved with the exception of the 200 nm particles which appear to be diffusing more slowly than would be predicted. Further, the collapsed result is in good agreement with that obtained from Equation (2.42) using a viscosity of $\eta = 0.89$ mPa s (solid black line). (b) MSD of 200 nm particles in glycerol (Catalog No G5516, Sigma-Alrich, St-Louis, MO). The solid black line is a fit of Equation (2.28) to the experimental data points at lag times $\Delta\tau > 1$ s. The shaded grey region corresponds to MSD values lying below the value of $2\epsilon^2$ calculated for an exposure time of 10 ms, but we note that this is simply an approximation for the true static error, particularly since imaging for these small particles was performed at a magnification of 40x (see Equation (2.22)). (c) The estimated medium viscosity of $\eta = 0.70$ Pa s (solid black line) obtained from Equation (2.43) using the fitted value for the diffusivity D_α from (b) and assuming a linear response (i.e. $\alpha = 1$) is in good agreement with macroscopic steady state shear flow data for a 60 : 1 glycerol : water mixture (filled black circles).

Taking the inverse transform of Equation (2.36) in one dimension for a Newtonian fluid of constant probe resistance $\tilde{\zeta}(s) = \zeta_0 = 6\pi a\eta$, we obtain that

$$\langle \Delta x^2(t) \rangle = \frac{2k_B T}{6\pi a\eta} t. \tag{2.42}$$

Comparing this result withe Equation (2.26) yields the well known Stokes-Einstein formula for particle diffusivity

$$D = \frac{k_B T}{6\pi a\eta}. \tag{2.43}$$

Further, analysis of Equation (2.42) implies that by scaling the MSDs of particles of various sizes by their respective radii, i.e. by plotting $a\,\langle \Delta x^2(t) \rangle$, the MSDs should collapse onto a single curve. Indeed, despite the appearance of some residual drift in the MSD of the largest particles (5 µm), this is what is observed in Figure 2.3.4a, with the exception of

the 200 nm particles which appear to be diffusing more slowly than would be expected. The black curve in Figure 2.3.4a is calculated from Equations (2.26) and (2.43) using a value of $\eta = 0.89\,\text{mPa}\,\text{s}$ corresponding to a room temperature of approximately 25 °C.

One important thing to note is the reduced lag time for which the MSD of the 200 nm probes is plotted in Figure 2.3.4a. This is because in such a low viscosity medium, the duration for which these small and highly mobile probes remained in the imaging plane and could consequently be tracked was extremely short. Specifically, in order to track a reasonable number of particles, it was necessary to require that a given particle only be present 20 images, which corresponds to a total imaging time of 0.67 s. Since information between all steps separated by a given lag time is used to calculate the time averaged MSD (Equation (2.24)), this short in-frame duration implies that the MSD calculation is made with a greatly reduced quantity of position information compared to that done for larger ($2a \geq 1\,\mu\text{m}$) particles, for which a 200 frame (or 6.7 s) cutoff was used. We note that for the 500 nm particles a minimum requirement of 50 frames (or 1.67 s) was used in order to retain a reasonable number of particles, but this appears to have been sufficient to obtain statistically robust results.

Therefore, in Figure 2.3.4b, we repeat the experiment with the 200 nm probes, but this time track them in glycerol (Catalog No G5516, Sigma-Alrich, St-Louis, MO); a Newtonian medium with a significantly higher viscosity. Correspondingly, the reduced mobility of the probes allowed for a reasonable number of them to be tracked for the entire 200 frame (or 6.7 s) duration. Interestingly, despite this being a Newtonian medium, the MSD appears to approach a constant plateau value at the earliest lag times. This has been observed before in high viscosity Newtonian solutions, and is attributed to static error as the MSD approaches the value of $2\epsilon^2$ [19], which corresponds to the upper surface of the shaded grey region in Figure 2.3.4b obtained from Figure 2.3.2 for the 10 ms exposure time. We note, however, that this upper surface is simply an approximation for the true static error, particularly since imaging for these small particles was performed at a magnification of 40x (see Equation (2.22)).

Nevertheless, by fitting Equation (2.28) to the MSD for lag times $\tau \geq 1\,\text{s}$ in Figure 2.3.4b, we obtain that $\alpha = 1.06$ and $D_\alpha = 3.10 \times 10^{-3}\,\mu\text{m}^2 s^{-\alpha}$, confirming that regular diffusion is recovered at longer delay times. This fit is shown as the solid black line in Figure 2.3.4b. Finally, from Equation (2.43) (which assumes $\alpha = 1$) and using $D = D_\alpha$, an estimate for the viscosity of the medium is found to be $\eta = 0.70\,\text{Pa}\,\text{s}$. This result is shown as the solid black line in Figure 2.3.4c, and excellent agreement with macroscopic steady state shear flow measurements of a 60 : 1 glycerol : water mixture is observed.

The results shown in this section are not surprising; the GSER should hold in simple Newtonian liquids such as water and glycerol, and the measured microrheological properties should be probe-size independent. We will see in Chapter 4, however, that for complex biological fluids such as mucin gels, this is frequently not the case. In particular, while the GSER is a powerful tool for relating microrheological measurements to macroscopic viscoelastic properties, it requires that several assumptions hold in order for it to be valid. Of particular importance for the work presented in this thesis, the Stokes component (Equation (2.35)) can break down owing to non-continuum effects such as probe-size dependencies and material heterogeneity, as well in the face of particle-medium interactions [18]. The end result of the presence of such effects and the breakdown of Equation (2.35) is a disagree-

ment between macroscopic measurements of the viscoelastic moduli and the predictions of Equation (2.39). Nevertheless, as we will see in Chapter 4, even when this occurs, the information provided by microrheology is still highly valuable and can be used in complement to that obtained macroscopically, as SPT allows for the interrogation of length-scales and dynamics generally inaccessible to macrorheology. In fact, we devote the final part of this section to reviewing some theoretical concepts that will be of use for studying probe motion in heterogeneous, complex fluids which frequently deviates from the normal Brownian motion observed in Newtonian liquids.

Heterogeneity and the van Hove distribution

Anomalous diffusive motion is encountered in a wide range of fields [51], from particle diffusion in biological gels [52] to transport in semi-conductors [53]. The underlying mechanisms leading to these deviations from normal Brownian motion are system-specific, but generally arise in conjunction with anomalies in one or both of the following: (i) the distribution of waiting times between steps and (ii) the distribution $P(\Delta x, \Delta\tau)$ of step sizes Δx at a given lag time $\Delta\tau$ (known as the van Hove distribution function) [50, 54]. Anomalies in both distributions have been observed in a number of experimental systems including the diffusion of probe particles in F-actin gels [55] and the motion of potassium channels in cell plasma membranes [56] for the former case (i), and the diffusion of colloidal beads on lipid tubes [57] as well as particle dynamics in random-energy landscape [58] for the latter case (ii). For the work presented in this thesis, we focus our attention on van Hove distributions as a tool with which to study subdiffusion. In particular, the one-dimensional step size distribution for a random walk at a given lag time $\Delta\tau$ is a Gaussian distribution about a displacement $\Delta x = 0$ [50]

$$P(\Delta x, \Delta\tau) = \frac{1}{\sqrt{4\pi D\Delta\tau}} \exp\left(-\frac{\Delta x^2}{4D\Delta\tau}\right), \tag{2.44}$$

where, as before, D is the diffusion coefficient of the walker in the medium.

For a Gaussian distribution, the kurtosis (or ratio of the 4^{th} moment to the 2^{nd} moment of the distribution) is calculated to be

$$\beta = \frac{\langle \Delta x^4 \rangle}{\langle \Delta x^2 \rangle^2} = 3, \tag{2.45}$$

and hence following Evers et al. [58], we can define a suitable non-Gaussian parameter κ as

$$\kappa = \frac{\langle \Delta x^4 \rangle}{3\langle \Delta x^2 \rangle^2} - 1. \tag{2.46}$$

For a normal Brownian motion, we expect $|\kappa| \ll 1$. Deviations from this expression are frequently attributed to heterogeneity of the surrounding medium [58], and have been observed using SPT in several systems including Laponite clay dispersions [59] and colloidal gels [60].

In Chapters 3 and 4, we utilize and build on the analytical methods outlined in this section for interpreting the motion of tracer particles in mucus and mucin gels in order

to infer information about the microstructure and association dynamics of the biopolymer networks of these materials.

3 | Physicochemical properties of native mucus and mucin gels

Because of their importance for the majority of the work in this thesis, we devote this chapter to a discussion of the physicochemical features of mucus and gels derived from the primary solid component of mucus, mucin. We begin by discussing the biological structure and function of mucus. Next, we explore the use of mucin gels as a model system for mucus from a rheological perspective. In order to do so, we first provide details of the mucin purification methods used in this thesis, including discussions regarding the effect of non-mucin proteins as well as batch variation on the rheology of mucin gels. Then, we conclude this chapter with a systematic comparison of the rheological properties of native mucus and mucin gels reconstituted to physiological conditions, in order to highlight both the usefulness and subtleties of this frequently used model system.

3.1 Biological function and structure of mucus

Mucus is a biological hydrogel that coats every wet epithelial surface of the body including the eyes, lungs, stomach, and female genital tract, as depicted in Figure 3.1.1 adapted from [61]. It serves as a lubricant to protect the underlying epithelia against shear-induced damage arising from mechanical forces associated with processes such as digestion and blinking [62, 63, 64], and also acts as a selective physicochemical barrier by excluding foreign or harmful molecules while permitting the passage of desirable agents such as nutrients [4, 65].

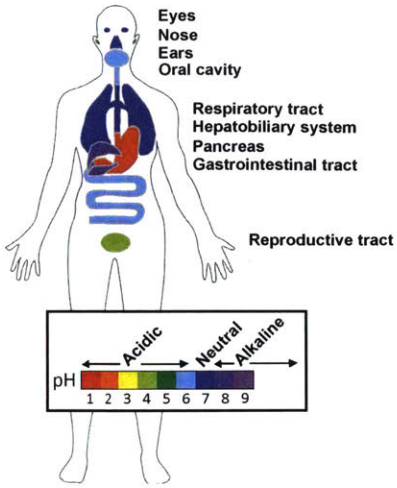

Figure 3.1.1: Epithelial surfaces of the body coated by mucus. Figure adapted from [61] with characteristic pH levels shown.

The primary structural component of mucus is the glycoprotein mucin (Figure 3.1.2), and to date twenty-one mucin-type glycoproteins, which collectively belong to the MUC gene family, have been identified in the human body and are recognized by the HUGO gene nomenclature committee (http://www.genenames.org). The protein backbone of the mucin molecule is composed of a variable number of tandem repeats (VNTR) rich in proline, threonine and/or serine (PTS domains), as well as cysteine-rich regions at the amino and carboxy terminals and sometimes interspersed between the PTS domains [4, 66]. These PTS domains are characterized by dense O-linked glycosylation and structurally resemble bottle brushes, with moderately branched oligosaccharide chains arranged radially from the protein core [4]. Indeed, this glycosylation is so extensive that approximately 80 % of the mass of these high molecular weight molecules is derived from carbohydrates, with the protein backbone making up the remaining 20 % [4]. Within the mucin family, two important subgroups are frequently distinguished: secreted mucins and tethered, cell surfaced associated mucins. Within the secreted mucins, there exist five oligomeric, gel-forming mucins (MUC2, MUC5AC, MUC5B, MUC6, and MUC19) [67], as well as two non-polymeric glycoproteins (MUC7 and MUC8) [67]). The gel-forming mucins (Figure 3.1.2a) reside entirely outside of the epithelial cell layer [68], and the individual mucin subunits polymerize via end-to-end disulphide bonds to form even larger macromonomer chains which are generally believed to be arranged in a linear fashion [69, 70], although some studies have suggested the possibility of branched, trimer structures for specific mucins [71, 72, 73]. In contrast, the eleven tethered mucins (MUC1, MUC3A, MUC3B, MUC4, MUC12, MUC13, MUC15, MUC16, MUC17, MUC20, MUC21) have short cytoplasmic domains that reside inside of the cell, as well as extensive extracellular domains [68] (Figure 3.1.2b). The three remaining mucins are oviductal glycoprotein 1 (OVGP1, previously known as MUC9), endomucin (EMCN, also known as MUC14), and MUC22. Collectively, mucins are generated in and secreted from specialized cells in the surface epithelium known as goblet cells as well as submucosal glands known as mucous cells [67, 68]. Excellent detailed reviews on the structure of both types of

mucins can be found in prior literature [67, 68].

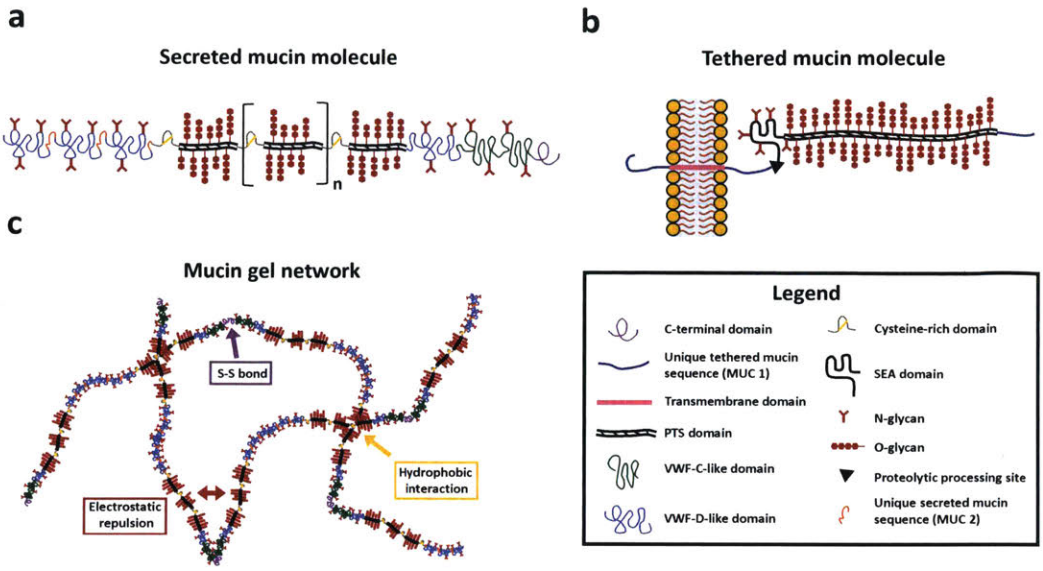

Figure 3.1.2: Schematics of the general structure of secreted (a) and tethered (b) mucin molecules adapted from [66, 74, 75] with permission from Elsevier and Springer Nature. (c) An illustration of the network established by the gel-forming, secreted mucins (adapted from [7]). Individual mucin subunits associate via end-to-end disulfide bonds to form even larger macromonomer chains. The network is formed from reversible associations including hydrophobic interactions between the non-glycosylated, cysteine-rich regions of the molecules, and is stabilized by electrostatic repulsion between the charged sugar side chains.

As depicted in Figure 3.1.2c, in aqueous solution, the high molecular weight mucin molecules form a network mediated by a complex series of reversible physical bonds including hydrophobic interactions and chain entanglements, and stabilized by electrostatic repulsion between the negatively charged polysaccharide side chains [76]. The configuration of the mucin molecules as well as the strength of the network interactions are sensitive to the variations in pH as well as concentration of ions and small molecules across the organ systems of the body (see Figure 3.1.1) [7]. Consequently, different mucus layers possess vastly different mechanical and biochemical properties depending on their location and intended physiological function. For instance, the tear film on the ocular surface responsible for hydration and lubrication [64] is a thin and watery mucin solution, intestinal mucus is somewhat more solid-like and serves as an ecological niche for the gut microbiome, and the relatively stationary mucus layer lining the stomach is an even stiffer mucin gel that serves as a buffer to protect the epithelial lining against the harshly acidic gastric juices (pH$\approx 1-2$) contained within this organ [77]. Altered mechanical and biochemical properties can also indicate disease or pathological manipulation, such as the increased bacterial load and thick or 'sticky' mucus commonly associated with cystic fibrosis (CF) [78].

3.2 Mucin gels as a model system for native mucus

Native mucus is composed primarily of water ($\approx 95\,\%$), and in addition to mucins also contains lipids, salts, and proteins involved in defense such as immunoglobulins [4]. Despite the presence of so many other molecules, the mechanical properties of mucus are primarily owed to the presence of mucins [4]. Consequently, gels reconstituted from purified mucin molecules are a frequently-used experimental system for studying the physicochemical properties of mucus [52, 77, 79]. Reconstituted mucin gels generally exhibit less heterogeneity between samples due to the elimination of other mucus components, and, in contrast to native mucus, can also be prepared to specified conditions. However, whether or not the mechanical properties of reconstituted mucin gels are truly representative of those of native mucus requires further analysis. For instance, Sellers et al. [62] found that gels of purified gastric, colonic, and duodenal mucin reconstituted to physiological concentrations had the same form of mechanical spectra as their corresponding native mucus secretion. Meldrum et al. [80] have recently shown that the macrorheological properties native porcine intestinal mucus are very similar to those of concentrated gels reconstituted from MUC2 isolated under non-denaturing (ND-mucin) conditions, but not to gels reconstituted from extensively purified MUC2 isolated using the chaotropic agent guanidinium chloride (GdmCl) referred to as GH-mucin. These authors found that gels reconstituted from ND-mucin, which contained associated non-mucin proteins, were strongly influenced by the addition of both calcium (which resulted in a more elastic network) and the calcium-chelating agent EDTA (which resulted in a reduction or loss in gel viscoelasticity), while gels reconstituted from GH-mucin were largely unaffected by the addition of both agents [80]. In a similar vein, Raynal et al. [81] found that the diffusion of microspheres and mucin components in saliva was significantly different from that in gels reconstituted from MUC5B purified with 6M GdmCl, and in a later publication these same authors concluded that unlike native mucins, GdmCl purified MUC5B mucins were unable to bind calcium [82]. Furthermore, gels reconstituted from Sigma Aldrich purified porcine gastric mucin (Sigma PGM), which undergo a certain degree of proteolytic digestion during their harsh commercial purification process and consequently do not exhibit pH-responsiveness [4, 74], have been shown to not be accurate models for porcine intestinal mucus based on the diffusion of drug molecules [83] and 200 nm polystyrene particles with different surface chemistries [84]. Indeed, significant structural differences are apparent in the SEM images of Figure 3.2.1 depicting native mucin purified by the Ribbeck lab (Figure 3.2.1a) as well as Sigma-Aldrich PGM (Figure 3.2.1b). Finally, the properties of native mucus are also sensitive to enzymatic degradation [12] and mechanical manipulation such as freeze-thaw cycles [10], demonstrating the importance of storage and handling procedures for faithful characterization of these materials as well.

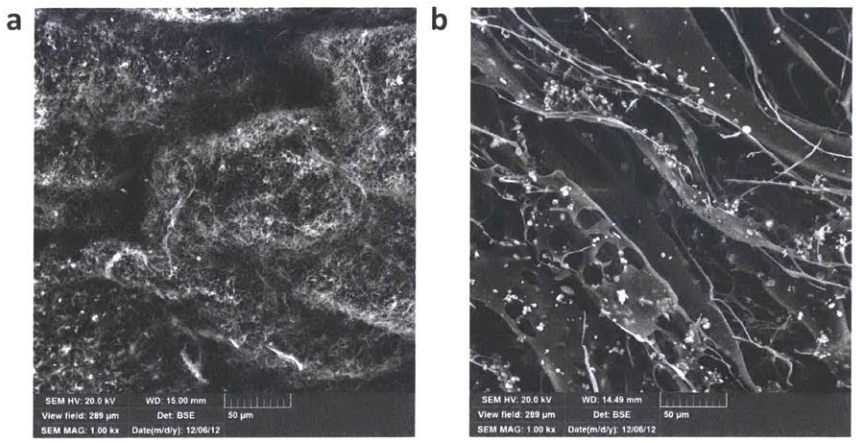

Figure 3.2.1: Scanning electron microscopy (SEM) courtesy of Dr. Nicole Kavanaugh reveals structural changes to mucins associated with different purification processes. (a) MUC5AC mucin purified from pig gastric mucus by the Ribbeck lab. (b) Industrially purified PGM supplied by Sigma-Aldrich.

Therefore, as a result of the frequent use of mucin gels as a model system for native mucus, we devote the remainder of this chapter to a comparison of the rheological properties of both materials. First, however, we provide a detailed discussion of the purified methods used in this work, as well as subtleties of the purification process such as the presence of non-mucin proteins and batch-to-batch variation.

3.2.1 Mucin purification method

Porcine-derived mucins used in the work presented in this thesis were purified from fresh pig stomach scrapings (MUC5AC) or fresh pig intestinal scrapings (MUC2). Full details of this method can be found in [85, 86]. Briefly, the isolated mucus layer was solubilized in sodium chloride buffer containing protease inhibitors and sodium azide to prevent mucin degradation and bacterial proliferation, respectively [86]. Following centrifugation to remove insoluble components, the mucins were isolated using gel filtration chromatography on a Sepharose column (CL2B), and then concentrated and lyophilized [86].

Human-derived MUC5B mucin was purified from submandibular gland secretions following the methods described in Frenkel and Ribbeck [87]. Briefly, unstimulated human submandibular saliva was collected on ice using a custom vacuum pump set up. Cotton swabs were used to absorb the donor's parotid gland secretions. Immediately after collection, the saliva was diluted in a sodium chloride buffer containing sodium azide, and additional antibacterial agents and protease inhibitors were added. Salivary mucins were then solubilized overnight with gentle stirring at 4 °C. Following centrifugation to remove cellular debris, the mucins were isolated using gel filtration chromatography on a Sepharose column (CL2B), and then concentrated and lyophilized for storage at −80 °C.

3.2.2 Effect of non-mucin components on gel properties

To assess the potential impact of the presence of non-mucin proteins on the properties of the mucin gels used in this thesis, we compared the results of both micro- and macrorheological measurements of 1 wt % MUC5AC gels at pH2 and pH7 using MUC5AC prepared as described above as well as with an additional cesium chloride (CsCl) gradient centrifugation step, as described by Smith and Lamont [85]. The results of these experiments are shown in Figure 3.2.2. For convenience in this discussion, we refer to mucins that have been prepared using CsCl gradient centrifugation as CsCl-MUC5AC, and those that have not as N-CsCl-MUC5AC.

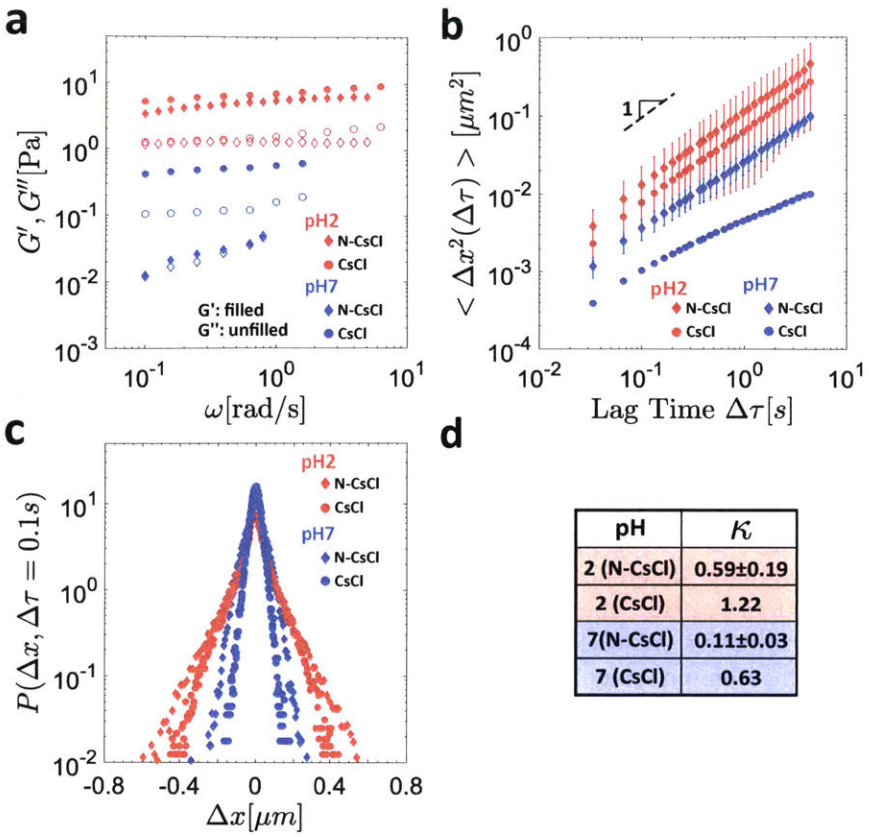

pH	κ
2 (N-CsCl)	0.59±0.19
2 (CsCl)	1.22
7(N-CsCl)	0.11±0.03
7 (CsCl)	0.63

Figure 3.2.2: Rheological response of 1 wt % MUC5AC gels purified with (CsCl, circles) and without (N-CsCl, diamonds) CsCl gradient centrifugation at pH2 (red symbols) and pH7 (blue symbols). In (a) the linear viscoelastic response measured macroscopically (symbols) using an 20 mm 4° cone-and-plate fixture are presented. The filled symbols denote the storage modulus G' and the unfilled symbols denote the loss modulus G''. In (b) the MSD as a function of the lag time is shown for both mucin preparation conditions at pH2 and pH7. In (c) the van Hove distributions for the same conditions as in (b) are shown, with their corresponding non-Gaussian parameters κ tabulated in (d). The error bars in (b) and the standard deviations reported in (d) reflect the multiple repeats performed for the N-CsCl conditions. The N-CsCl data is the same as that presented in Chapter 4. Note that the standard deviations reported in (d) are the same as those published in [7] for consistency, but were mistakenly calculated assuming an entire population and consequently underestimate the true standard deviation by a factor of $\sqrt{\frac{N}{N-1}}$, where $N = 2$ or $N = 3$ depending on the number of experimental replicates.

Macroscopically, as with the N-CsCl-MUC5AC, the CsCl-MUC5AC gels are substantially stiffer at pH2 than at pH7, as seen in Figure 3.2.2a. However, the CsCl-MUC5AC gels are stiffer at *both* pHs compared to equivalent preparations of N-CsCl-MUC5AC. In particular, at pH7 G' and G'' of the N-CsCl-MUC5AC gels are very similar, which is suggestive of sticky Rouse relaxation of an unentangled reversible gel [88], while the CsCl-MUC5AC gels exhibit significantly more elastic, solid-like behaviour ($G' > G''$) under identical preparation

conditions. The MSD of the same carboxylated, 1 μm particles used in the main text is larger at pH2 than at pH7 in the CsCl-MUC5AC gels as seen in Figure 3.2.2b, as is the case for the N-CsCl-MUC5AC gels. In Figure 3.2.2c, the van Hove distributions for all four preparation conditions at a lag time of $\Delta\tau = 0.1\,\mathrm{s}$ are shown. Interestingly, the associated value of κ is higher at pH7 for the CsCl-MUC5AC gels than for the same preparation of N-CsCl-MUC5AC gels; in fact, the step size distribution for CsCl-MUC5AC at pH7 in Figure 3.2.2c is closer to an exponential than a Gaussian. The non-Gaussian parameters κ for all four conditions are summarized in Figure 3.2.2d.

The increased stiffness of the CsCl mucin gels is consistent with CsCl-MUC5AC containing a higher percentage of the large, gel-forming MUC5AC mucins for an equivalent dry weight of purified mucin than N-CsCl-MUC5AC as a result of the removal of non-mucin proteins in this additional purification step. Further, we suspect that CsCl gradient centrifugation results in a mild denaturation of the MUC5AC mucins [89], and that in particular it may cause a partial unfolding of the hydrophobic domains of the molecules which are otherwise concealed at pH7. Under acidic conditions (pH2), these domains are believed to already be unfolded on the mucin molecules (a crucial step in the gelation process), and hence this may explain why greater differences between the CsCl-MUC5AC and N-CsCl-MUC5AC gels are seen at pH7 than at pH2. The higher degree of heterogeneity within the CsCl-MUC5AC gels at pH7 is also consistent with this idea of denaturation. Specifically, partial unfolding of the hydrophobic domains may promote a certain degree of mesoscopic phase separation, which would result in a higher degree of heterogeneity at pH7 than expected based on the response of the N-CsCl-MUC5AC gels at neutral pH. These concepts are discussed in detail in Chapter 4.

To summarize then, CsCl gradient centrifugation is suspected to influence the purified mucin product in two ways: i) it increases the relative quantity of MUC5AC by removing non-mucin proteins, and ii) it may cause a mild denaturing of the MUC5AC by partially unfolding the globular hydrophobic domains. This results in both qualitative and quantitative differences in the microrheological and macrorheological measurements, and these differences are more pronounced at pH7. In particular, at neutral pH the CsCl-MUC5AC gels are more heterogeneous and are predominantly solid-like on the macroscopic scale over the entire frequency range probed, whereas the N-CsCl-MUC5AC solutions are homogeneous and exhibit sticky Rouse-like dynamics [88]. In order to assess the methods of network formation in MUC5AC gels for as close to the native state of the mucin molecules as possible, we choose to use N-CsCl mucins for the remainder of the work in this thesis. Therefore, as a result of the omission of the additional CsCl gradient centrifugation step, it is possible that non-mucin proteins contribute to the rheological response of the gels. However, the lion's share of this rheological response is almost certainly still owed to the presence of the large mucin molecules [4].

3.2.3 Effect of batch preparation on mucin gel rheology

Because the mucins are derived from native tissues, normal biological variations in mucin content and structure, both between donors and within a single donor, inevitably affect the final purified product. Therefore, as a final consideration of mucin purification-related effects, we briefly bring attention to the role of batch variation in mucin gel rheology.

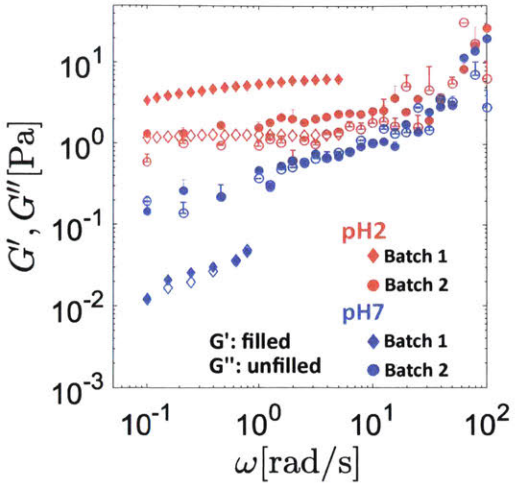

Figure 3.2.3: SAOS measurements of mucin gels at pH2 (red symbols) and pH7 (blue symbols) from different purification batches. The distinction of batches is arbitrary for each pH; however for the label 'Batch 2', the mucins used for both the pH2 and pH7 gels were obtained during the same purification. The filled symbols denote the storage modulus G', and the unfilled symbols denote the loss modulus G''.

In Figure 3.2.3, SAOS frequency sweep data is shown at pH2 (red symbols) and pH7 (blue symbols) for mucin gels prepared using mucin from different purification batches. The distinction of batches is arbitrary for each pH; however for the label 'Batch 2', the mucins used for both the pH2 and pH7 gels were obtained during the same purification. As can be seen, there is a fair amount of quantitative variation between measurements performed with different mucins. However, what remains consistent is the pH-responsiveness of these materials, and the large increase in the viscoelastic moduli at pH2 compared to at neutral pH conditions. Therefore, it is generally suggested that *qualitative* trends of the experimental data presented in this thesis for mucin gels or native mucus samples be taken as stronger indicators of the underlying physicochemical properties of this material than the absolute numerical quantities.

3.2.4 Comparison of the rheological properties of native mucus and reconstituted mucin gels

With the above considerations regarding mucin purification, purity, and batch effects in mind, we conclude this chapter with one-to-one comparisons of the degree to which reconstituted mucin gels are capable of reproducing the rheological properties of native mucus. In order to do so, we compare the response of native mucus and mucin gels reconstituted to physiological pH levels and mucin concentrations from four niches of the body: the gastric, intestinal, oral, and cervical niches. Because of the inevitable biological variation between native mucus samples, we base our preparations of the mucin gels on typical literature values of the pH level and mucin concentration for the type of mucus in question as opposed to attempting to measure these quantities directly from the native sample.

Specifically, in the gastric niche we compare porcine gastric mucus with MUC5AC gels reconstituted to 5 wt % (based off of the value listed in [90]) and at pH2, a typically cited value for the pH of the gastric lumen [79]. In order to assess the importance of the purification method and biochemical structure of the mucins, we also compare these results with Sigma PGM gels reconstituted to the same preparation conditions as the MUC5AC gel. In the intestinal niche, we compare porcine intestinal mucus with MUC2 gels reconstituted to 2.5 wt % (determined as the average of the values cited for porcine small and large intestinal mucus in [90]). Although the pH in human intestines has been reported to range from slightly acidic to alkaline ($\text{pH} \approx 6.4 - 7.5$) [91], we performed our experiments at pH4 due to the large pH range encountered physiologically during digestion between the stomach and the large intestine. In the oral niche, we compare human whole saliva with MUC5B solutions at 0.05 wt % (determined as an approximately average value of that presented in [81] (0.02 wt %) and our own unpublished enzyme-linked immunosorbent assay (ELISA) measurements) and at pH7 (the published pH range for saliva is $6.2 \leq \text{pH} \leq 7.4$ [76]). We also compare human whole saliva with solutions of CMC, a common synthetic substitute for saliva, reconstituted to the same preparation conditions as the MUC5B gel. Finally, although our purified MUC5B is not sourced from it, in the cervical niche we compare the response of human cervical mucus with MUC5B gels at 1.5 wt % based on the value reported in [92] at both pH4 and pH7. These two pH values were selected due to the variation in the pH of cervical mucus from slightly alkaline ($\text{pH} \approx 8.6$ [93]) to $\text{pH} \approx 4$ upon entering the vagina and being acidified by lactic acid-secreting lactobacilli [94].

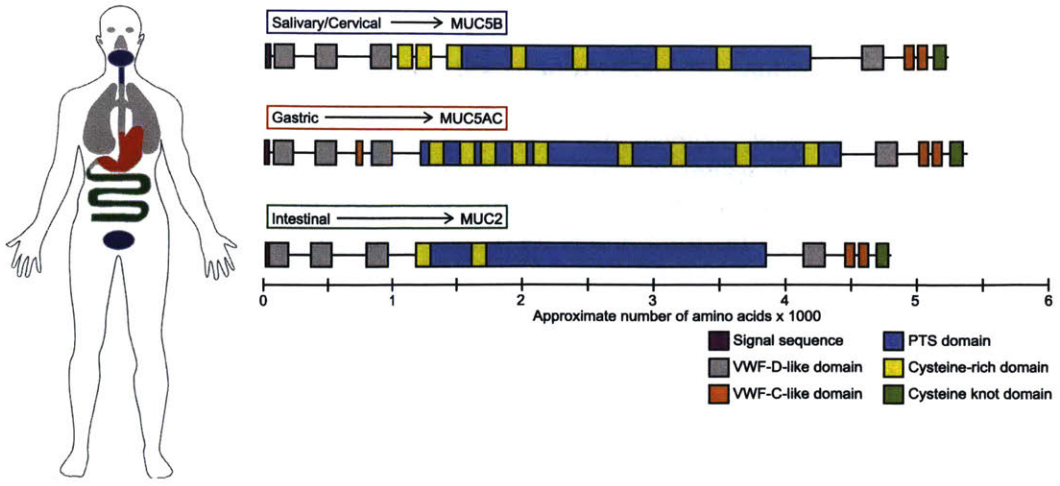

Figure 3.2.4: Domain structures of major gel-forming mucins expressed in salivary, cervical, gastric, and intestinal mucus reveal distinct structural differences. Note that MUC5AC and MUC2 are obtained from porcine and not human sources, but from the analogous tissues to those indicated. All three gel-forming mucins contain Von Willibrand Factor (VWF), cysteine-rich, C-terminal cysteine knot, and heavily O-glycosylated PTS domains that are common to all gel-forming mucins in the MUC family. Domain locations and total protein lengths are approximated from Dekker et al. [66]. The micro- and macro-rheological properties of gels reconstituted from the appropriate mucin to the physiological concentration and pH levels of the source tissue are compared with those of the native mucus itself. For the cervical niche, MUC5B from salivary secretions is utilized for the reconstituted mucin gel as a result of the difficulty of obtaining sufficient quantities of cervical mucus in order to purify MUC5B from this source.

Materials and methods

Preparation of CMC and Sigma PGM Industrially-purified mucin from porcine stomach, type III (M1778-100G) was purchased from Sigma-Aldrich (St Louis, MO). Dry mucin powder was dissolved in distilled water to a concentration of approximately $10\,\mathrm{mg\,ml^{-1}}$. The solution was dialyzed using 20 kDa molecular weight cutoff dialysis tubing against four exchanges of distilled water (at 4 °C) to remove salt and low-molecular weight impurities. Undissolved solids were extracted by centrifugation at $10,000 \times g$ for 10 min at room temperature. The supernatant was frozen in liquid nitrogen and lyophilized. Lyophilized aliquots were stored at −80 °C until use.

Carboxymethyl cellulose sodium salt (CMC) (CAS: 9004-32-4; average molecular weight = 250 kDa) was purchased from Acros Organics (Thermo Fisher Scientific, Waltham, MA). A solution of CMC in distilled water at $10\,\mathrm{mg\,ml^{-1}}$ was dialyzed against distilled water with an Amicon stirred cell (Amicon) equipped with a 100 kDa molecular weight cutoff membrane. Dialysis was performed with four exchanges of water and the resulting solution was concentrated before lyophylization. Dried CMC was stored at −80 °C until use.

Preparation of purified mucin MUC2, MUC5AC, and MUC5B mucin were purified following the method outlined in Section 3.2.1.

Preparation and storage of native mucus samples

Human sublingual gland expressions
Saliva was collected from volunteers after obtaining written informed consent. Salivary secretions were gently suctioned from underneath the tongue into a collection vial on ice. Volunteers had not eaten or drank fluids for 1 hour prior to saliva collection. The fresh saliva was flash cooled in liquid nitrogen and stored at −80 °C. Saliva samples from 4-6 volunteers were thawed on ice and homogenized by shaking at 4 °C for 30 min. The homogenized saliva was centrifuged at $10,000 \times g$ for 5 min. The supernatant was concentrated 5-50 fold with a centrifugal filter (EMD Millipore UFC500324 and UFC900324 Amicon Ultra Centrifugal Filters, 3 kDa Ultracel, 0.5 ml and 15 ml). Both the whole and concentrated saliva were divided into small aliquots to prevent repeated freeze-thaw cycles, flash cooled in liquid nitrogen, and stored at −80 °C until use. Prior to use, samples were thawed at 4 °C.

Porcine gastric mucus
Previously frozen porcine stomachs were thawed on ice after being delivered frozen from a local slaughterhouse. Stomach contents were emptied and a spatula was used to scrape samples of mucus from the interior epithelium. Stomachs containing blood were discarded and no mucus was collected. After collection, all samples were stored on ice until being flash frozen in liquid nitrogen and stored at −80 °C until use. Prior to use, samples were thawed at 4 °C.

Porcine intestinal mucus
Porcine small intestines were transported on ice from a local slaughterhouse. Intestines were sectioned and loosely-adhered mucus was squeezed into a collection vial. Adhered mucus was also collected by cutting each section length-wise and gently scraping with a spatula. After collection, all samples were stored on ice until being flash frozen in liquid nitrogen and stored at −80 °C until use. Prior to use, samples were thawed at 4 °C.

Human cervical mucus
Cervical mucus from non-pregnant, ovulating women was collected at the Women and Infants Hospital of Rhode Island. Inclusion/exclusion criteria for patients enrolled can be found in the methods section of [10] (WIHRI Approval: WIH 15-0073; MIT Approval: 1501006840R001). A cervical mucus sample was collected from one ovulating non-pregnant individual, with no restrictions based on race, ethnicity, or spoken language. The exclusion criteria were recent sexually transmitted infection, intercourse within 24 h of collection, abnormal PAP smear within the last 6 months, or cervical surgery within the last 6 months. Patients with polycystic ovarian syndrome were excluded from the current study. Patients receiving treatment for infertility were excluded. Patients receiving treatment for infertility were excluded.

Ovulation was detected via self-administration of a urine luteinizing hormone test kit (recommended kit: Clear Blue Easy, SPD Swiss Precision Diagnostics GmbH, Switzerland) prior to a procedure (i.e., intrauterine insemination). The number of days of the menstrual

cycles did not define 'ovulation': the window of 'ovulation' for collecting ovulatory mucus was defined as 36 h from a positive ovulation result. After informed consent was obtained from 20 patients, specimens were collected during a sterile speculum exam with a 1 ml insulin syringe immediately before any other procedure. Specimens were gathered directly from the external cervical os after clearing the area of vaginal discharge. Vaginal discharge, if present, was removed by wiping with a large-tip swab (Scopette). Cervical mucus was not removed by this process because cervical mucus is adherent to the cervical canal. Mucus was immediately snap-frozen in liquid nitrogen and stored at $-80\,^{\circ}$C. Prior to use, samples were thawed at $4\,^{\circ}$C.

Preparation of the reconstituted gels Mucin, Sigma PGM, or CMC was solubilized for up to two nights with gentle shaking at $4\,^{\circ}$C in deionized (milli-Q) water. Gels were prepared the same day as the experiments were performed by diluting the solubilized materials with milli-Q water and adjusting the pH through the addition of a phosphate and sodium citrate buffer to a final concentration of 10mM.

Experimental details for macrorheology SAOS tests were performed using an ARESG2 rheometer with an 8 mm parallel plate fixture at a gap of 200 μm. All experiments were performed on a Peltier plate at a constant temperature $T = 25\,^{\circ}$C. SAOS measurements were performed at a strain amplitude within the linear viscoelastic regime of each sample as determined from separate strain sweep experiments. For all experiments, a thin coating of mineral oil was placed around the edge of the sample in order to prevent evaporation (see Section 2.2.1). Data points for the mucin, Sigma PGM, and CMC gels denote the average of 'up' and 'down' frequency sweeps for a single sample, with the standard deviation between these measurements shown. For clarity on these logarithmic plots, error bars are only shown extending above the data points. For the native mucus, data points denote the average and standard deviation of 1 to 2 different tissue samples, including averaging over 'up' and 'down' ramps.

Experimental details for microrheology SPT experiments were performed largely as detailed in Section 2.3.1. 1 μm fluorescent, negatively charged (carboxylated) microspheres (Magsphere Inc, Pasadena, CA, USA) previously diluted at a ratio of 1 : 200 by volume in milli-Q water were combined at a ratio of 60 : 1 (sample : bead solution) with the sample of interest, resulting in an overall dilution ratio of 1 : 12,000 for the microspheres. Negatively charged particles were selected as a result of previous findings of increased charge-mediated diffusion impairment for positively charged (amine functionalized) particles as compared to negatively charged (carboxylated) ones in mucus and mucin gels [48, 84, 95]. Imaging was performed at a magnification of 20x with a camera frame rate of ≈ 30 fps and with an exposure time of $\sigma_t = 10$ ms. 300 frames were recorded, corresponding to a total imaging time of ≈ 10 s. For the mucin, Sigma PGM, and CMC gels, three experimental replicates were performed for each condition; i.e. sufficient sample was prepared in order to perform particle tracking in three separate particle-laden capillaries. For native mucus, the number of different specimens measured varied between 1 and 3 depending on sample availability, and the number of experiments performed consequently varied between 3 and 6.

Results and Discussion

In Figure 3.2.5, we present the macrorheological (SAOS) and microrheological (SPT) response of the mucus and mucin gels previously described for each physiological niche considered, along with the corresponding value of the non-Gaussian parameter κ at a lag time of $\Delta\tau = 0.1\,\mathrm{s}$ and the slope of the MSD α fit between lag times of $0.03\,\mathrm{s} \leq \Delta\tau \leq 5\,\mathrm{s}$.

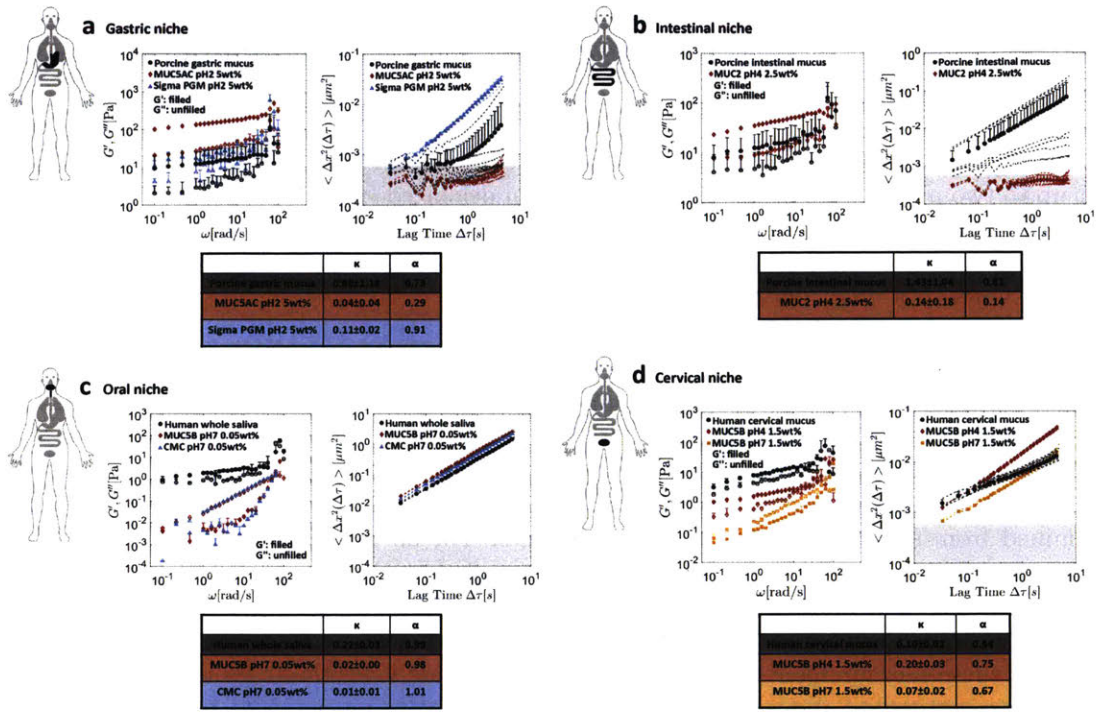

Figure 3.2.5: Comparison of the micro-and macro-rheological response of native mucus and reconstituted mucin gels for four physiological niches. For the macrorheological data, filled symbols denote the storage modulus G' and unfilled symbols denote the loss modulus G''. For the microrheological data, dashed lines denote the ensemble average MSD of an individual experiment, and filled symbols denote the average over all experiments. For clarity on these logarithmic plots, error bars are only shown extending above the data points. Values of the non-Gaussian parameter κ measured at a delay time of $\Delta\tau = 0.1\,\mathrm{s}$ are provided, along with the anomalous diffusion exponent α obtained by fitting Equation (2.28) to the MSD for lag times in the range $0.03\,\mathrm{s} \leq \Delta\tau \leq 5\,\mathrm{s}$. (a) In the gastric niche, porcine gastric mucus (black circles) is compared with 5 wt % MUC5AC gels at pH2 (red diamonds) and 5 wt % Sigma-Aldrich PGM gels at pH2 (blue triangles). (b) In the intestinal niche, porcine intestinal mucus (black circles) is compared with 2.5 wt % MUC2 gels at pH4 (red diamonds). (c) In the oral niche, human whole saliva (black circles) is compared with 0.05 wt % MUC5B solutions at pH7 (red diamonds) and 0.05 wt % CMC solutions at pH7 (blue triangles) (d) In the cervical niche, human cervical mucus (black circles) is compared with 1.5 wt % MUC5B gels at pH4 (red diamonds) and 1.5 wt % MUC5B gels at pH7 (blue triangles).

In the gastric niche (Figure 3.2.5a), the reconstituted MUC5AC gels are stiffer macro-

scopically than the porcine gastric mucus, yet the response of both materials is predominantly solid-like ($G' > G''$), with both moduli exhibiting weak power law dependencies on the oscillation frequency ω; a characteristic of cross-linked gels with multiple length and time scales [17]. As can be seen from the dashed lines denoting the ensemble average MSD of the individual experiments, the SPT results for these two samples are also similar, with the exception of one experimental replicate in the porcine gastric mucus for which unusually large particle displacement was observed. This large variation between native mucus samples is reflected in the significantly higher value of κ (and its standard deviation) for porcine gastric mucus ($\kappa = 0.86 \pm 1.18$) compared to the MUC5AC gel ($\kappa = 0.04 \pm 0.04$). It is important to note here that SPT measurements for both samples lie within the limit of the measured static error (see Section 2.3.1) and hence it is not advised that these measurements be interpreted quantitatively. Macroscopically, the stiffness of the Sigma PGM gel is nearly an order of magnitude lower than that of the MUC5AC gel, but also exhibits power law dependencies of its moduli on ω. Microscopically, as with the MUC5AC gel, the particle trajectories in the Sigma PGM gel are also quite homogeneous ($\kappa = 0.11 \pm 0.02$). However, unlike in both the MUC5AC gel and the porcine gastric mucus, the particle motion in the Sigma PGM gel is only weakly subdiffusive ($\alpha = 0.91$), which is suggestive of an altogether different microstructure compared to the other two samples.

In the intestinal niche (Figure 3.2.5b), similarly to porcine gastric mucus, substantial variation in the micro- and macrorheology of porcine intestinal mucus is once again observed between samples. However, macroscopically both the MUC2 gel and the native sample exhibit similar weak power law dependencies of G' and G'' on ω, and are also predominantly solid-like ($G' > G''$). Microscopically, the MUC2 gel once again exhibits fairly homogeneous particle trajectories ($\kappa = 0.14 \pm 0.18$) and strongly subdiffusive motion $\alpha = 0.14$, although as with the MUC5AC gel care should be taken in interpreting these results quantitatively due to their lying below the estimated static error of the experimental setup. The microrheology of the native specimens varies significantly between samples ($\kappa = 1.43 \pm 1.04$), although several of them also exhibit strongly subdiffusive particle motion.

In the oral niche (Figure 3.2.5c), the macroscopic rheological responses of the MUC5B and CMC solutions are both qualitatively and quantitatively different from that of human whole saliva. In particular, saliva displays the characteristic trends observed in other native mucus samples of weak power law dependencies of the moduli on ω and $G' > G''$, while both the MUC5B and CMC solutions respond essentially as liquids, with a linear dependence of $G''(\omega)$ observed for all frequencies. Further, the elastic moduli of the CMC and MUC5B solutions lie within the low-torque limit of the instrument at low-frequencies and exhibit quadratic dependencies on ω at high frequencies; a signature of fluid inertial effects [21] (see Section 2.2.1). This suggests that unlike in other native mucus samples, the very low salivary MUC5B concentration of approximately 0.05 wt % cannot fully account for the weak-gel rheological response of saliva, and that other components such as non-mucin proteins and salivary micelles [76] play an important role. Microscopically, diffusive particle motion ($\alpha \approx 1$) is observed for all three materials along with homogeneous particle motion, with the human whole saliva sample exhibiting the largest degree of heterogeneity ($\kappa = 0.22 \pm 0.03$).

Finally, in the cervical niche, similar weak power law responses are observed in the moduli of cervical mucus as well as the MUC5B gels, although the reconstituted gels are

softer than the native sample at both pH levels. The pH-sensitivity of the purified mucin gels is keenly demonstrated in this niche by the predominantly liquid-like response of the gel at pH7 ($G' < G''$) and solid-like response at pH4 ($G' > G''$). The biochemical reasons behind this pH dependence will be studied in detail for MUC5AC, which is a genetic relative of MUC5B showing significant homology in its non-glycosylated domains [66], in Chapter 4. Microscopically, all three samples exhibit fairly homogeneous particle trajectories (with $\kappa = 0.20 \pm 0.03$ largest for the native mucus sample), as well as subdiffusive MSD scalings to various degrees ($\alpha = 0.44$ for cervical mucus, $\alpha = 0.75$ for MUC5B at pH4, and $\alpha = 0.67$ for MUC5B at pH7). Interestingly, the particles are less mobile in the MUC5B gels at pH7 than at pH4, despite these neutral samples appearing to be softer macrorheologically.

3.2.5 Section summary

In summary, the non-negligible variation between native mucus samples and also between purified mucins can complicate drawing quantitative conclusions regarding the rheological response of mucus and mucin gels. Furthermore, the use of literature values for the pH levels and mucin concentrations of the reconstituted mucin gels considered in this study also excludes the possibility of quantitatively comparing the response of these materials with native mucus. However, for porcine gastric and intestinal mucus and their mucin gel analogs, as well as human cervical mucus and MUC5B at 1.5 wt % and pH4, the macrorheological response of both the native samples and the reconstituted gels share many qualitative similarities. In particular, the predominantly solid-like ($G' > G''$) responses and weak power law dependencies of the moduli on the oscillation frequency are characteristic of cross-linked gels with numerous length and time scales [17], which does suggest that mucin molecules, with their complex biochemical structure and numerous interaction moieties, are primarily responsible for the network structure of these native samples. Interestingly, the macrorheological response of MUC5B solutions at 0.05 wt % and pH7 is qualitatively and quantitatively different from saliva; the former responds essentially as a liquid, while saliva exhibits a weak-gel response. This suggests an important role for non-mucin solid components in the creation of the salivary network. Overall, the microrheological response of the native mucus samples and reconstituted mucin gels across all four niches examined also exhibited similarities, with subdiffusive motion observed in all materials except for saliva. However, one major difference was the high degree of heterogeneity measured between native mucus samples, particularly for porcine intestinal and porcine gastric mucus.

Finally, at 0.05 wt % and pH7, the rheological responses of both CMC and MUC5B solutions were so solvent-dominated that it is difficult to compare them (Figure 3.2.5c). We do note, however, that at higher concentrations of up to 3 %, CMC exhibits liquid-like behaviour across a wide range of frequencies, while mucin gels exhibit the characteristic weak power law response seen throughout the niches of Figure 3.2.5 (see Figure 4.3.2). At 5 wt % and pH2, Sigma PGM gels were approximately an order of magnitude softer than MUC5AC gels prepared to the same conditions (Figure 3.2.5b), but did exhibit a predominantly solid-like, weak power law response across the range of frequencies investigated. Microscopically, however, particle trajectories in the Sigma PGM gels were only weakly subdiffusive ($\alpha = 0.91$), while particles in the MUC5AC gels were effectively immobilized, with their MSD lying within the static error of the experimental setup and an apparent measured subdiffusive exponent of $\alpha = 0.29$. Additionally, unlike purified mucins, the rheology of both CMC (see Figure 4.3.2) and Sigma PGM [74] are not pH-responsive, which demonstrates the critical

roles that the biochemical structure and interaction moieties of intact mucin molecules play in making mucus such a versatile and adaptable biological hydrogel.

4 | Studying the network structure and association dynamics of reconstituted mucin gels using micro- and macrorheology

4.1 Introduction

The rich variety of interaction moieties on mucin molecules (see Figure 3.1.2) makes mucus an impressively adaptable biological fluid, existing in different forms and serving different purposes across all (non-keratinized) wet epithelial surfaces of the body [4]. Indeed, mucus gels formed from a specific secretory mucin, MUC5AC, provide a particularly good example of this adaptability [66]. On the ocular surface of the eye, a thin, watery form of these gels known as the tear film is responsible for hydration and lubrication [96]. In the pH-neutral environment of the lungs and respiratory tract, a MUC5AC (and MUC5B) based mucus bilayer serves as a barrier against bacteria and environmental particulate matter [97]. The bottom layer, known as the perciliary fluid, has been modeled as a polymer brush [97] and permits continuous clearance by the periodic beating action of cilia that line these surfaces, while the superficial mucus gel layer is designed for pathogen containment and transport [97, 98]. As a final example, the relatively stationary mucus layer lining the stomach is a much stiffer MUC5AC-based gel that serves as a buffer to protect the epithelial lining against the harshly acidic gastric juices (pH $\approx 1-2$) contained within this organ [77]. Inevitably, however, the same structural adaptability that makes mucus so multifunctional also exposes it to pathological manipulation. For example, in cystic fibrosis (CF), abnormal CFTR and sodium channel activity [8, 9] as well as mucin overproduction [9] are among the causes of 'sticky' mucus which is less readily cleared by the cilia and hence more susceptible to biofilm formation.

Despite it being well-established that the local milieu plays a major role in determining the viscoelastic properties of mucus, the mechanisms by which this occur remain unclear [74]. To this end, rheological measurements can be used to obtain quantitative information about both bulk gel properties and their underlying microstructural details. Further, by performing these experiments under a variety of environmental conditions which favour specific classes of interactions, a more holistic picture of how mucin networks change under variations in physiological conditions can be gleaned from the corresponding rheological data. Therefore, we begin this chapter in Section 4.2, by using a combination of macroscopic (SAOS) and microscopic (SPT) rheological studies to investigate the effect of a series

of perturbations, including modifications of the pH, surfactant, and salt concentration, on the structure and mechanical response of purified MUC5AC gels. We demonstrate that the results from SPT, including the degree of trajectory heterogeneity and the statistical distribution of step sizes, can provide independent and complementary information about the gel microstructure to that obtained from bulk rheological measurements, which is pertinent even when the results from these two techniques are not in quantitative agreement.

We next seek to improve our understanding of the mechanisms leading to the substantial disagreement between the micro- and macrorheological response of MUC5AC gels. Our first approach to doing so in Section 4.3 is through additional rheological studies. First, we explore the effect of mucin concentration on the macrorheology of the gels, and compare these results at both pH levels with those measured in solutions of carboxymethyl cellulose (CMC), a charged, synthetic polymer frequently used as a mucin substitute. Next, we explore three plausible reasons for the breakdown of the GSER in mucin gels that could lead to the disagreement between the rheological measurements on both length scales [18]: non-continuum effects related to material heterogeneity, interactions between the particles and mucin molecules, and aging of the mucin gels. To study non-continuum effects, we maintain the mucin concentration fixed at 1 wt % and vary the size of the carboxylated probe particles from 200 nm to 5 μm at both pH levels, and compare the results with those measured in CMC solutions. To investigate possible particle-mucin interactions, we vary the surface chemistry of the probes by using PEG-ylated particles with near-neutral zeta potentials which have been previously determined to be non-adherent to bovine submaxillary mucins. Finally, to investigate the effect of sample aging, we repeat the experiments after a prolonged delay of several hours and compare the microrheological response at both time points.

In addition to rheological methods, we also discuss the development of imaging techniques to visualize the mucin network at pH2 and pH7 in Section 4.3.6. In order to do so, we introduce fluorescently labeled, positively charged peptide probes into the mucin gels. These probes have previously been shown to exhibit attractive electrostatic interactions with negatively charged mucins at neutral pH [99], and consequently their spatial distribution should be representative of the organization of the mucin network.

Finally, combining the results from all of these approaches, we conclude this chapter in Section 4.3.7 with an updated view of the structure of mucin gels under acidic pH conditions.

4.2 Effect of environmental perturbations on the micro- and macrorheology of MUC5AC gels

4.2.1 Materials and methods

Mucin gel preparation

MUC5AC was solubilized overnight in deionized (milli-Q) water, and gels were prepared the same day as the experiments were performed by combining the solubilized mucins with the appropriate buffers (and surfactant or salt solutions when appropriate). The pH of the gels was modulated through the addition of a phosphate and sodium citrate buffer to a final concentration of 10 mM. The salt concentration was modified through the addition of NaCl dissolved in deionized water, while the surfactant used was 1, 2-hexanediol (Sigma-Aldrich,

St. Louis, MO). This particular surfactant was chosen as a result of previous studies that have shown that a similar compound, the mild detergent trans-cyclohexane-1,2-diol, can reversibly interfere with hydrophobic interactions in the nuclear pore complexes (NPCs) of eukaryotic cells [100]. Gels were vortex mixed to ensure adequate mixing following addition of all components, and kept on ice until experimental use. All gels in this section contain $10\,\mathrm{mg\,ml^{-1}}$ or 1 wt % of purified MUC5AC.

Macrorheology

All shear rheology tests were performed using a stress controlled AR-G2 (TA Instruments, New Castle, DE, USA) or a DHR-3 rheometer (TA Instruments, New Castle, DE, USA) with a 20 mm, 4° cone-and-plate fixture. All experiments were performed on a Peltier plate at a constant temperature T = 25 °C. SAOS measurements were performed at a strain amplitude within the linear viscoelastic regime ($\gamma_0 \leq 10\,\%$) of each mucin gel as determined from separate strain sweep experiments.

Microrheology

Imaging was performed at 30.3 fps per second for 10 s at room temperature with an Axio Observer D.1 inverted microscope using a Zeiss LD Plan-Neofluar 20x/0.4 Corr Ph2 objective lens and a Hamamatsu Flash 4.0 C11440-22CU camera. An average of 160 particles were imaged for each sample from an average of ten movies recorded at different spatial locations within the glass capillaries. Additional details are provided in Section 2.3.1.

4.2.2 Effect of pH and salt concentration on rheology of MUC5AC gels

Decreasing the pH and increasing the salt concentration at neutral pH increase MUC5AC gel macroscopic viscoelastic moduli

The macroscopic linear viscoelastic response for $10\,\mathrm{mg\,ml^{-1}}$ MUC5AC gels at pH2, pH4 and pH7 is shown in Figure 4.2.1a, and for pH7 gels with salt concentrations of 0 mM, 50 mM, 200 mM (near-physiologic condition[101]) and 400 mM in Figure 4.2.1b.

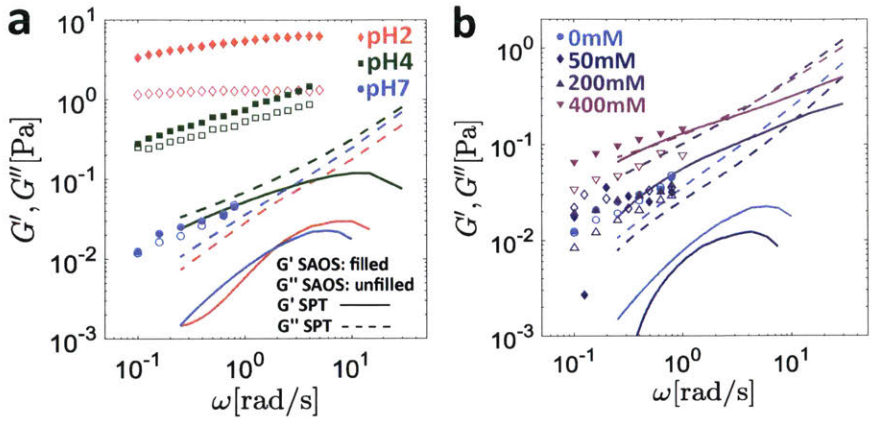

Figure 4.2.1: Effect of pH and salt on the rheology of 10 mg ml^{-1} MUC5AC gels. The linear viscoelastic response measured macroscopically (symbols) as well as the predicted moduli from the MSD data (lines) are presented. Filled symbols and solid lines represent the elastic property $G'(\omega)$, while the hollow symbols and dashed lines represent the viscous property $G''(\omega)$. The aggregate MSD of all particle trajectories was used to calculate the viscoelastic moduli for all gels except the pH2 sample, for which only the MSD of a specific subset of 'exponential' particles (see text for details) was used. In (a) the pH is varied with no added salt, and data is presented at pH2, pH4, and pH7. In (b), the pH is maintained at pH7 and data is presented for salt concentrations of 0 mM, 50 mM, 200 mM and 400 mM.

Consistent with previous findings [77], as seen in Figure 4.2.1a, both the storage (G') and loss (G'') moduli measured rheometrically increase uniformly as the pH is decreased. In particular, at pH7 the close agreement between G' and G'' resembles sticky Rouse relaxation of an unentangled reversible gel [88]. As the pH is decreased, the response of the MUC5AC gels becomes increasingly solid-like as seen by the relative increase of the storage modulus compared to the loss modulus, which is suggestive of additional cross-links with longer lifetimes under acidic conditions. Although the data in Figure 4.2.1b is somewhat noisier (due to the low torque values exerted by these very soft gels) we observe an increase in both the storage and loss moduli of the MUC5AC gels as the salt concentration is increased to 400 mM.

From a biochemical perspective, at pH7 the carboxylate side groups of the amino acid backbone are largely deprotonated, and correspondingly the mucin chains possess a net negative charge. Under these conditions, the conformation of the mucin molecules is random coil-like, as estimated by Cao et al. [102] by fitting a theoretical formulation for the friction coefficient of a worm-like chain [103] to dynamic light scattering data. Further, the polyampholytic mucin molecules are stabilized by electrostatic interactions known as salt bridges between oppositely charged residues on the globular, non-glycosylated portions of the polymer backbone [4, 104]. These salt bridges maintain the flexible hydrophobic regions of the mucin chains (indicated schematically as gray and yellow loops between the red bottle-brush like segments of the polymer in Figure 3.1.2a) in folded conformations, thus sequestering them to the interior of the molecules [4]. Upon lowering the pH of the system to pH2, the carboxylate groups of the negatively charged amino acid residues (such as aspartic and glutamic acid) become protonated, resulting in destruction of the salt bridges and a subsequent unfolding of the mucin chains [4].This unfolding is thought to expose additional moieties including hydrophobic sites within each mucin chain that were previ-

ously hidden [4], permitting phase separation of these near neutrally charged molecules into mucin-rich domains maintained by hydrophobic interactions and diminished electrostatic repulsion [105]. A schematic depicting this transition for the case of mucin gels in response to an acidic pH environment is depicted in Figures 4.2.2a and 4.2.2b, with the location of the additional interaction sites indicated by yellow triangles.

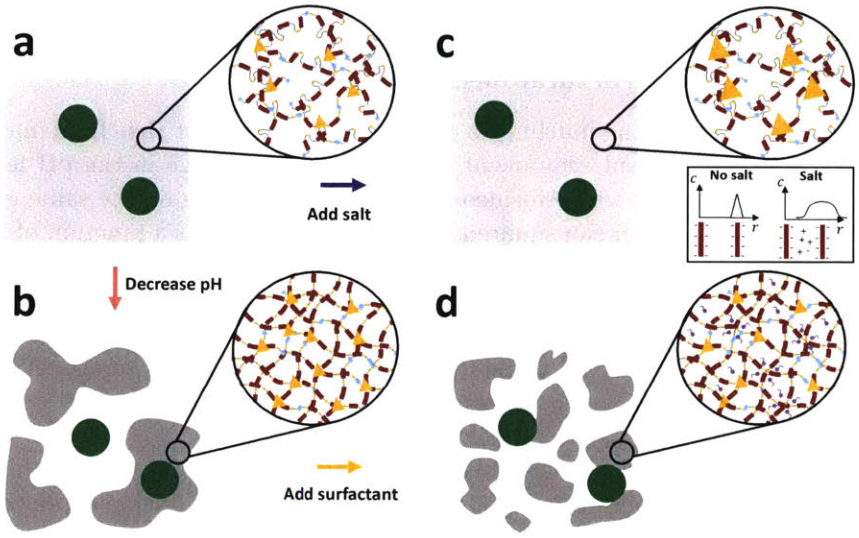

Figure 4.2.2: Schematic illustration of the proposed effects of the various environmental modifications on the supramolecular structure of the mucin network. The mesoscopic porous structure of the mucin gels is represented by the gray regions and the diffusing probe particles are shown by large green circles. At neutral pH (a), the mucin molecules possess a net negative charge and are semi-flexible. Under acidic conditions (b), the protonated mucin molecules possess a nearly neutral net charge, and stiffen via breaking of salt bridges, exposing additional moieties including hydrophobic domains which associate to form additional cross-links (shown by yellow triangles). Collectively, this induces local mesoscopic phase separation into mucin-rich and mucin-poor regions. When salt is added at neutral pH (c), the screening of electrostatic interactions reduces the degree of repulsion between the sugar side chains which permits stronger and longer-lived associations between mucin molecules (indicated schematically by the increased size of the yellow triangles). Finally, when surfactant is added under acidic conditions (d), the hydrophobic domains are out-competed by the small surfactant molecules, which loosens and disrupts the aggregates in the mucin-rich regions prompting the return towards a single phase.

The net negative charge of the mucin molecules at pH7 suggests that under neutral pH conditions, increasing the ionic strength through the addition of NaCl (which screens electrostatic interactions between the mucin chains by lowering the Debye length [101]) should be an effective means with which to modify the viscoelastic network. For polyampholytic molecules such as mucin, the addition of salt can either increase or decrease the viscosity or viscoelastic moduli of the gel depending on the environmental pH and corresponding charge-state of the molecule [106, 107]. In general, however, the screening of electrostatic interactions at the intra-molecular level should result in a decrease in the persistence length of the mucin chains and hence a reduction in their bending rigidity. At the inter-molecular

level, the presence of salt decreases the strength of repulsive forces between the negatively charged sugar side chains, which allows for stronger and potentially longer lived associative interactions between mucin molecucles. These structural changes are depicted schematically in Figures 4.2.2a and 4.2.2c by the increased size of the yellow triangles which symbolically represent the reversible interactions.

Modulation of pH and salt concentration alters MUC5AC gel viscoelasticity through different microstructural mechanisms

The biochemical changes to the mucin gels described above suggest that fundamentally different structural rearrangement may occur in response to a change in the pH level or salt concentration. To verify this, we performed single particle tracking on the same gels, and in Figures 4.2.3a and 4.2.3b the mean squared displacement (MSD) as a function of lag time is presented for the various pH levels and salt concentrations, respectively. Although in general the functional form of the MSD varies with lag time, the approximately power law nature of our experimental data allowed a single characteristic anomalous diffusion exponent α and generalized diffusion coefficient D_α to be defined by fitting Eq.(2.28) to the MSD data for lag times $0.1 \leq \Delta\tau \leq 2\,\mathrm{s}$.

As seen in Figure 4.2.3a, when the pH is initially lowered from pH7 to pH4, the motion of the particles becomes increasingly confined, with the anomalous diffusion exponent decreasing from $\alpha = 0.85 \pm 0.17$ at pH7 to $\alpha = 0.61 \pm 0.08$ at pH4. As the pH is further decreased to pH2, however, the anomalous diffusion exponent appears to *increase* to $\alpha = 0.92 \pm 0.49$. At neutral pH, the particle mobility initially increases slightly at 50 mM NaCl as seen in Figure 4.2.3b, but the overall effect of salt addition is to decrease the anomalous diffusion exponent nearly monotonically from $\alpha = 0.85 \pm 0.17$ at 0 mM NaCl, to $\alpha = 0.86 \pm 0.27$ at 50 mM NaCl, $\alpha = 0.70 \pm 0.05$ at 200 mM NaCl, and $\alpha = 0.51 \pm 0.18$ at 400 mM NaCl.

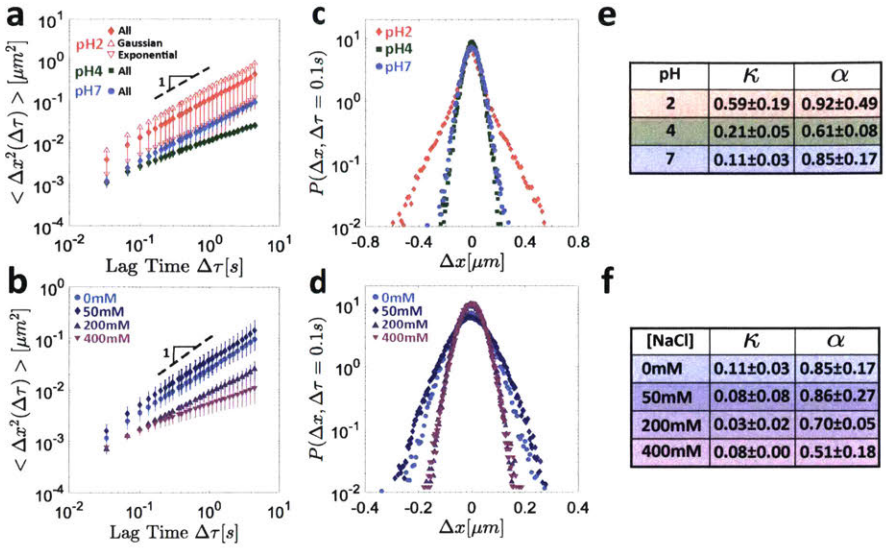

pH	κ	α
2	0.59±0.19	0.92±0.49
4	0.21±0.05	0.61±0.08
7	0.11±0.03	0.85±0.17

[NaCl]	κ	α
0mM	0.11±0.03	0.85±0.17
50mM	0.08±0.08	0.86±0.27
200mM	0.03±0.02	0.70±0.05
400mM	0.08±0.00	0.51±0.18

Figure 4.2.3: Microrheological response of $10\,\mathrm{mg\,ml^{-1}}$ MUC5AC gels to pH variations at zero salt concentration (a,c,e) and salt addition at neutral pH (b,d,f). The MSD as a function of the lag time is shown at different pH levels in (a) and for different salt concentrations at neutral pH in (b). The MSD is that of the aggregate particle populations for all gels. In addition, the individual MSDs corresponding to just the Gaussian and just the exponential particle populations are shown for the pH2 gel, with the error bars omitted for clarity. The van Hove correlations for the aggregate particle populations are shown at different pH levels in (c) and at different salt concentrations in (d). Summary tables of the non-Gaussian parameters κ and the anomalous diffusion exponents α are presented for the different pH levels and salt concentrations in (e) and (f), respectively. Note that the standard deviations reported in (e) and (f) are the same as those published in [7] for consistency, but were mistakenly calculated assuming an entire population and consequently underestimate the true standard deviation by a factor of $\sqrt{\frac{N}{N-1}}$, where $N = 2$ or $N = 3$ depending on the number of experimental replicates for a given sample.

The trend of decreasing particle mobility with increasing salt concentration is consistent with the observation of increasing MUC5AC gel viscoelastic moduli (Figure 4.2.1b). The apparent contradiction between the macroscopic determination of greatest mucin gel stiffness at pH2 and the microscopic observation of largest particle mobility under the same conditions can be partially resolved by considering the individual, time averaged MSD results for each particle (Eq.(2.24)) as opposed to their ensemble average (Eq.(2.25)). Rich et al. [59] define the lag-time dependent spatial heterogeneity of a medium (HR) as the quotient of the variance and squared average of the MSDs of all of the individual particle trajectories, i.e.

$$\mathrm{HR}(\Delta\tau) = \frac{\mathrm{var}\left(\overline{\Delta x_k^2(\Delta\tau)}\right)}{\langle \Delta x^2(\Delta\tau)\rangle^2}. \tag{4.1}$$

At a characteristic lag time of $\Delta\tau = 0.1$s, the HR for water is HR $= 0.03$, while the corresponding values for the MUC5AC gels are HR $= 0.07 \pm 0.02$ at pH7, HR $= 0.22 \pm 0.02$ at pH4, and HR $= 0.64 \pm 0.21$ at pH2. At neutral pH, the heterogeneity ratio at all salt concentrations is low, with HR $\lesssim 0.1$ for each gel. These results are consistent with the

proposed physical mechanism of a local phase separation into mucin-rich and mucin-poor domains (Figures 4.2.2a and 4.2.2b) under acidic conditions, which would result in the observation of a heterogeneous population of slow, trapped particles and freely-diffusing fast particles. In contrast, a single particle population would be expected based on the proposed uniform biochemical response to salt (Figures 4.2.2a and 4.2.2c) in which a single gel phase is preserved. The degree of heterogeneity is also reflected in the corresponding van Hove distributions for the MUC5AC gels as seen in Figures 4.2.3c and 4.2.3d for the pH and salt conditions, respectively. It is clear in Figure 4.2.3c that the shape of the distribution at pH2 deviates significantly from the expected parabolic profile (on a semi-log plot) for a Gaussian distribution (e.g. at pH7), with the probability of large steps significantly greater than would be predicted for normally distributed step sizes. This deviation is also reflected in the value of the non-Gaussian parameter κ which increases from $\kappa = 0.11 \pm 0.03$ at pH7 to $\kappa = 0.21 \pm 0.05$ at pH4 and $\kappa = 0.59 \pm 0.19$ at pH2. In contrast, as seen in Figure 4.2.3d, the step size distributions in response to increased salt concentration remain Gaussian, with $\kappa \lesssim 0.11 \pm 0.03$ for all of the gels. The values of κ and α for the various gels are summarized in tabular form in Figures 4.2.3e and 4.2.3f for the different values of pH and salt concentrations, respectively.

We note that in addition to affecting the charge and conformation of the mucin chains, the environmental pH and salt concentration also influence the surface charge of the carboxylated probe particles [108, 109]. At pH2, protonation of the carboxylate groups on the surfaces of the beads increases their zeta potential [109], rendering them less negatively charged. Further, as the concentration of salt increases, the width of the electrical double layer decreases, permitting attractive van der Waals interactions over shorter and shorter distances [108]. The effect of this screening on the zeta potential ζ of the beads is unclear however. By comparing atomic force microscopy (AFM) curves with theoretical predictions of Derjaguin-Landau-Verwey-Overbeek (DLVO) theory, Assemi et al. [108] measured an increase in the zeta potential of 1 µm carboxylate modified polystyrene (PS) latex beads as the concentration of NaCl was increased. Conversely, Barany et al. [109] reported a decrease in ζ of 1.43 µm carboxylated PS beads at constant pH as the concentration of KCl was increased. Nevertheless, at particle length scales $\geq$ 500 nm, the effect of surface functionalization such as PEG-ylation to reduce particle-mucus interactions has been shown to be minimal [95, 110], and steric interactions between the mucin network and the beads principally determine the particle trajectories. As such, it is our expectation that the variations in probe particle diffusion that we observe under different environmental conditions are dominated by the mechanical properties of the environment that the particles experience, and that interactions with the mucin chains play only a minimal role. This will be further confirmed by the experimental results in Section 4.3.4.

Definition of Gaussian and exponential particle populations for heterogeneous MUC5AC gels at pH2

High levels of heterogeneity have been observed in mucin gels under strongly acidic conditions [74], which suggests that an ensemble average is not a suitable choice to faithfully characterize the displacement of all of the individual particles at pH2. In their studies of particle tracking in porcine respiratory mucus, Murgia et al. [111] noted that analysis of the individual time-averaged MSDs allowed for the specification of two distinct particle populations: 'immobile particles' (defined by these authors as those with MSD slope $\alpha < 0.5$)

which are trapped within the mucus, and 'diffusive particles' ($\alpha > 0.5$) which are not trapped and consequently diffuse much more quickly. Similar observations have been reported in a number of other systems, including colloidal gels [60] and aqueous Laponite dispersions [59] near the sol-gel transition, but the sorting approach for the individual particles has generally been study-specific.

We begin by following the method of Gao and Kilfoil [60] and fit a mixed probability distribution function to the van Hove distribution of all of the particles in a given experimental replicate at an early lag time of $\Delta\tau = 0.1\,\mathrm{s}$ (see Figure 5a of the main text). However, unlike Gao and Kilfoil [60] who consider combinations of Gaussian distributions, we define the mixed probability distribution function for the mucin gel system as the weighted sum of a Gaussian distribution and an exponential distribution, i.e.

$$P_{\mathrm{fit}}(\Delta x, \Delta\tau) = \frac{A(\Delta\tau)}{\sqrt{2\pi\sigma^2}} \exp\left(-\frac{\Delta x^2}{2\sigma^2}\right) + \frac{(1 - A(\Delta\tau))}{2\lambda} \exp\left(-\frac{|\Delta x|}{\lambda}\right). \tag{4.2}$$

The lag time dependent weights $0 \leq A(\Delta\tau) \leq 1$ and $(1 - A(\Delta\tau))$ signify the fraction of steps distributed normally and exponentially, respectively, and sum to unity for a normalized probability distribution. This fit is shown as the thick solid line in Figure 4.2.4a, while the van Hove distribution itself is denoted by the pink diamond symbols.

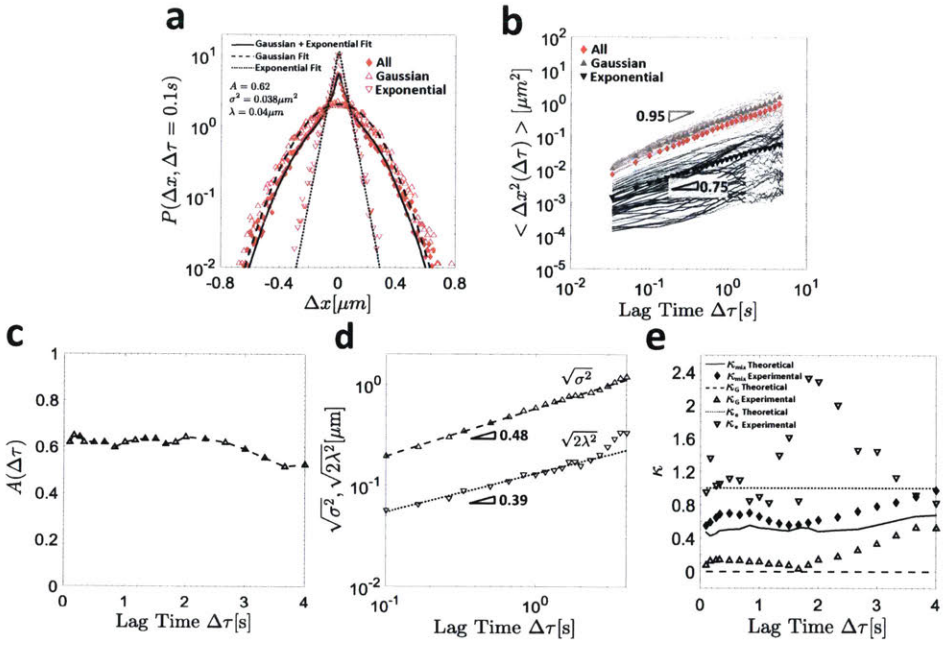

Figure 4.2.4: In (a), the van Hove distribution for all particles is shown by the diamond symbols, and the thick solid line indicates the composite Gaussian and exponential fit defined in Equation (4.2). The hollow triangles and inverted triangles denote the van Hove distributions of the Gaussian and exponential particles, respectively, and their respective Gaussian (dashed) and exponential (dotted) fits are also shown. In (b), the individual particle MSDs sorted into Gaussian (gray) and exponential (black) trajectories are shown, as well as their ensemble averages (filled symbols of the same color) and that of the aggregate population (solid pink diamonds). In (c), the fraction of Gaussian particles $A(\Delta\tau)$ is shown as a function of the lag time $\Delta\tau$. In (d), the characteristic Gaussian and exponential length scales $\sqrt{\sigma^2(\Delta\tau)}$ and $\sqrt{2\lambda^2(\Delta\tau)}$, respectively, are plotted as a function of the lag time, and the slope of the resulting power law fit is indicated. In (e), the experimental (symbols) and theoretical (lines) values of the non-Gaussian parameters κ (Equation (2.46)) for the exponential (dotted lines and hollow inverted triangles), Gaussian (dashed lines and hollow triangles), and aggregate (solid lines and solid diamonds) populations are shown as a function of lag time $\Delta\tau$.

In agreement with the previous observation of Valentine et al. [112], we find that the van Hove plot of each *individual* particle can be approximated as a normal Gaussian distribution even though the composite van Hove distribution accounting for the step sizes of *all* particles is clearly not Gaussian (Figure 4.2.4a). Thus, we next fit Gaussian distributions of the form

$$P_{\text{fit},i}(\Delta x, \Delta\tau) = \frac{1}{\sqrt{2\pi\sigma_i^2}} \exp\left(-\frac{\Delta x^2}{2\sigma_i^2}\right) \tag{4.3}$$

to the step size distribution of each individual particle, obtaining an associated variance σ_i^2 for every fitted trajectory. Note that as a result of the substantially smaller number of steps taken by an individual particle as compared to the total number of steps taken by the entire particle population, we include steps in both the x- and y-direction here in order

to improve the statistics of the step size distribution associated with each individual particle.

In order to recover the overall probability distribution function P_{fit} defined in Equation (4.2), the distributions of these individual variances σ_i^2 must satisfy

$$\int_0^\infty P_G(\sigma_i^2) P_{\text{fit},i} d\sigma_i^2 = \frac{A(\Delta\tau)}{\sqrt{2\pi\sigma^2}} \exp\left(-\frac{\Delta x^2}{2\sigma^2}\right) \tag{4.4}$$

and

$$\int_0^\infty P_e(\sigma_i^2) P_{\text{fit},i} d\sigma_i^2 = \frac{(1 - A(\Delta\tau))}{2\lambda} \exp\left(-\frac{|\Delta x|}{\lambda}\right), \tag{4.5}$$

where $P_G(\sigma_i^2)$ and $P_e(\sigma_i^2)$ are the distributions of the variances of the particles in the Gaussian and exponential subgroups, respectively, at each lag time $\Delta\tau$.

It is straightforward to show that Equation (4.4) is satisfied for

$$P_G(\sigma_i^2) = A(\Delta\tau)\delta(\sigma_i^2 - \sigma^2), \tag{4.6}$$

where δ is the Dirac delta function. For the exponential population, Chechkin et al. [113] have recently shown that when combined with a Gaussian, an exponential distribution of generalized diffusion coefficients $D_{\alpha,i}$ of the individual particle trajectories (or similarly an exponential distribution of their variances σ_i^2) results in the exponential distribution of step sizes defined in Equation (4.5). Consequently, we take $P_e(\sigma_i^2)$ to be

$$P_e(\sigma_i^2) = \frac{(1 - A(\Delta\tau))}{2\lambda^2} \exp\left(-\frac{\sigma_i^2}{2\lambda^2}\right). \tag{4.7}$$

To sort the K particles into the two subgroups, we select the $(1 - A) \times (K)$ particles whose variances σ_i^2 are best described by the distribution function in Equation (4.7) as the exponential ones, and the remainder are taken to comprise the Gaussian population. In the case where a single particle population is observed after fitting the mixed distribution in Equation (4.2) to the van Hove plot (i.e. $A = 0$ or $A = 1$), the trajectories of all particles for that experimental replicate are used in the calculation of the exponential or Gaussian statistics, respectively, as well as the aggregate population statistics for that gel condition.

The distributions of the variances for both of these populations as well as the aggregate one are shown in Figure 4.2.5, along with the unweighted predicted exponential distribution $P_e(\sigma_i^2)$ of the exponential group and the expected variance σ^2 of the Gaussian population. It is clear for this latter group that experimental noise results in a broader distribution for σ_i^2 than the predicted Dirac delta function ($P_G(\sigma_i^2)$ in Equation (4.6)), although its peak is still closely approximated by σ^2.

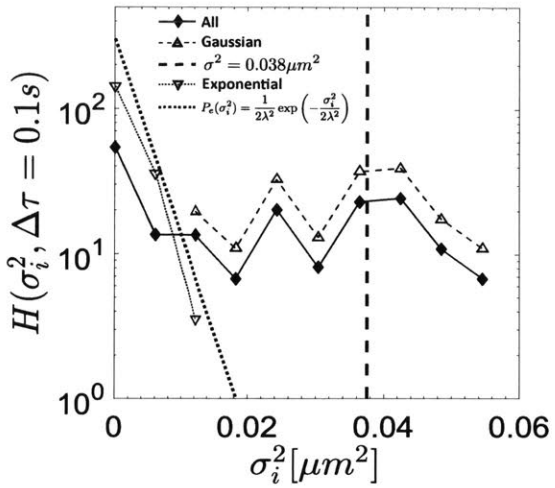

Figure 4.2.5: Distributions of the variances σ_i^2 of the individual particle trajectories are presented for the Gaussian (hollow triangles and a dashed line), exponential (hollow inverted triangles and a dotted line) and aggregate (filled diamonds and a solid line) populations, along with the predicted distribution $P_e(\sigma_i^2)$ (Equation (4.7) and the thick dotted line) and a thick dashed line indicating the fitted value σ^2.

In Figure 4.2.4b, the time averaged MSDs (given by Equation (2.24)) for each individual particle are shown by thin solid lines, with particles classified as Gaussian and exponential shown in gray and black respectively. Using this approach, it is clear that the ensemble average MSDs for these subpopulations (gray triangles and inverted black triangles, respectively) are far more representative of their individual constituents than the aggregate ensemble average (solid pink diamonds). Further, the average motion of the particles in these two subgroups is indeed quite distinct, with the exponential population undergoing subdiffusive motion characterized by $\alpha = 0.75$, and the Gaussian population appearing to diffuse nearly normally with exponent $\alpha = 0.95$ characterizing their ensemble average MSD. Indeed, these data for the Gaussian particles are quite comparable to our control results for the same size carboxylated particles diffusing in water ($\alpha_{water} = 0.95$ and $D_{\text{water}} = 0.41$). We note that although the van Hove distribution is in general a function of the lag time, the fraction of Gaussian particles in this system remains nearly invariant up to lag times of $\Delta\tau_{\max} = 4\,\text{s}$, as seen in Figure 4.2.4c. This justifies our choice of performing this sorting at an early lag time $\Delta\tau = 0.1\,\text{s}$ which maximizes statistical power for the individual particle trajectories (since each trajectory contains a significantly reduced number of steps compared to the combined trajectories of the aggregate population of particles). Further, the time-independence of the fraction of Gaussian particles also implies that within our limited experimental time window ($\Delta\tau \lesssim 4\,\text{s}$), particles essentially remain exponential or Gaussian throughout the entire experiment.

To demonstrate the consequences of this statistical sorting of individual trajectories, in Figure 4.2.3a we have also shown the mean ensemble average MSDs across all experimental replicates for the Gaussian (hollow triangles) and exponential (hollow inverted triangles) particle populations as a function of lag time for the MUC5AC gels at pH2. Although the standard deviation is large between replicates in these heterogeneous gels, the MSD across all experimental replicates is again quite distinct between these two populations, with the

Gaussian particles diffusing nearly normally with $\alpha = 0.95 \pm 0.48$, and the exponential particles undergoing subdiffusive motion characterized by $\alpha = 0.78 \pm 0.35$.

In addition to these differences in the ensemble average MSDs of the Gaussian and exponential particle populations, their van Hove distributions are also fundamentally distinct. In Figure 4.2.4a, these distributions are presented for the Gaussian (hollow triangles) and exponential (inverted hollow triangles) populations at a lag time of $\Delta\tau = 0.1\,\mathrm{s}$. The step sizes of the Gaussian particles are normally distributed with $\kappa = 0.07$, and this distribution is well fit by the unweighted Gaussian portion of the mixed probability distribution in Equation (4.2) shown as the dashed line in Figure 4.2.4a. Further, in Figure 4.2.4d, the characteristic Gaussian length scale $\sqrt{\sigma^2}$ is plotted as a function of the lag time. The nearly square root dependence of this quantity on $\Delta\tau$ ($\sqrt{\sigma^2} \sim \Delta\tau^{0.48}$) is in good agreement with the near linear dependence of the MSD on $\Delta\tau$ previously reported for the Gaussian population (Figure 4.2.4b), and thus both metrics confirm that this population of particles is undergoing nearly regular, diffusive Brownian motion for all lag times considered.

In contrast, the step sizes of the exponential particles follow an exponential distribution with $\kappa = 0.95$, as confirmed by the goodness of fit with the dotted line indicating the unweighted exponential portion of the distribution in Equation (4.2). Further, the exponential length scale $\sqrt{2\lambda^2(\Delta\tau)}$ exhibits a power law dependence on the lag time characterized by $\sqrt{2\lambda^2} \sim \Delta\tau^{0.39}$, as seen in Figure 4.2.4d. The origin of this scaling can easily be understood by considering the second moment of an exponential distribution of step sizes, i.e.

$$\langle \Delta x^2 \rangle_{\mathrm{exp}} = \int_{-\infty}^{+\infty} \frac{\Delta x^2}{2\lambda(\Delta\tau)} \exp\left(-\frac{|\Delta x|}{\lambda(\Delta\tau)}\right) d\Delta x = 2\lambda^2(\Delta\tau). \tag{4.8}$$

Hence, equating this result to the assumed power law form for the MSD in Equation (2.28), we obtain the result $2\lambda^2(\Delta\tau) \sim \Delta\tau^{\alpha}$, which is in excellent agreement with our experimental values of $\alpha = 0.75$ and $\sqrt{2\lambda^2} \sim \Delta\tau^{0.39}$. This analytical result is also consistent with the recent experimental findings of Wang et al. [57] who studied the diffusion of colloidal beads along linear phospholipid bilayer tubes as well as through entangled F-actin networks. In both systems, these authors reported a square root dependence of the exponential length scale on the lag time, i.e. $\sqrt{\lambda^2} \sim \Delta\tau^{1/2}$, as well as Brownian experimental MSDs ($\alpha = 1$). Taken together then, the results from the present study as well as those from Wang et al. [57] suggest that the scaling $\sqrt{\lambda^2(\Delta\tau)} \sim \Delta\tau^{\alpha/2}$ may be even more general than the previously reported square root dependence [57], as it can also be extended to anomalous diffusive motion ($\alpha \neq 1$).

Using the definition of the non-Gaussian parameter presented in Equation (2.46), the theoretical value for exponentially distributed step sizes is $\kappa_e = 1$, where the 4^{th} moment is obtained by replacing Δx^2 in the integral of Equation (4.8) with Δx^4. In addition, a theoretical prediction for the non-Gaussian parameter corresponding to the mixed distribution presented in Equation (4.2) can also be obtained in a similar fashion, resulting in the expression

$$\kappa_{\mathrm{mix}} = \frac{A + 8(1-A)(\lambda/\sigma)^4}{(A + 2(1-A)(\lambda/\sigma)^2)^2} - 1. \tag{4.9}$$

In Figure 4.2.4e, the theoretical (lines) and experimental (symbols) values of κ for the

Gaussian population (with theoretical value $\kappa_G = 0$, dashed lines and hollow triangles) and exponential population (with theoretical value $\kappa_e = 1$, dotted lines and inverted hollow triangles) are presented as a function of the lag time. In addition, κ for the aggregate population (solid lines and diamonds) is shown, with κ_{mix} from Equation (4.9) calculated using the fitted values of A, σ^2, and λ from Equation (4.2) at each lag time $\Delta\tau$. The theoretical predictions and experimental values and are found to be in good agreement. Further, as with the fraction of Gaussian particles (shown in Figure 4.2.4c), these quantities are found to be nearly invariant with lag time, although the fluctuations increase in magnitude at larger values of $\Delta\tau$ where there are fewer total steps over which to calculate these statistical measures.

Comparison of mechanical response predicted by thermal fluctuations and macrorheology

As a final consideration for this section, we note that in their studies of F-actin gels, Wong et al. [55] have observed a similar distinction between diffusive and confined particles, and have shown that bulk linear viscoelastic data can be recovered from the study of thermal fluctuations using the well-known result

$$G(s) = \frac{dk_BT}{3\pi as\left\langle \Delta x^2(s)\right\rangle} \tag{4.10}$$

from Mason and Weitz [44] when only the confined or 'slow' particles are considered. In Equation (4.10), s is the Laplace variable, $G(s)$ is the Laplace transform of the relaxation modulus, $\langle \Delta x^2(s)\rangle$ is the Laplace transform of the MSD, d is the dimensionality of the MSD data, a is the particle radius, k_B is Boltzmann's constant, and T is the absolute temperature. Consequently, in Figure 4.2.1a, we also plot the storage (solid line) and loss (dashed line) moduli predicted from Equation (4.10) for just the exponential particles at pH2, as well as the same results from the aggregate populations for pH4 and pH7. However, consistent with the findings in Bansil et al. [74], even with this separation into Gaussian and exponential populations, there is a significant discrepancy between the macroscopic and microscopic linear viscoelasticity, and this difference increases in magnitude as the pH is lowered. This mismatch suggests that the exponential population of particles do not sample the entire range of microenvironments in the gel, and/or that the mucin molecules and probe particles interact in additional ways that are not considered in the theoretical framework used to derive Equation (4.10) [44]. One possible explanation may be that the viscoelastic moduli measured macroscopically are dominated by the mechanical properties of the stiffest portions of the mucin-dense phase. At the microscopic scale, it is possible that the tracer particles are unable to penetrate these stiffest regions, and as such the exponential particles only probe the softer portions of the heterogeneous mucin-dense phase, while the Gaussian particles diffuse quite freely in the mucin-poor parts of the gel.

The limited electrostatic interaction expected between the negatively charged tracer particles and the negatively charged, flexible mucins at pH7 as well as the presence of a single gel phase suggest that improved agreement between the microscopic and macroscopic rheology should be observed upon salt addition. Indeed, as seen in Figure 4.2.1b, although the SPT prediction underestimates the macroscopic viscoelastic moduli at the two lowest salt concentrations, reasonably good agreement between the two methods is recovered for the 200 mM and 400 mM gels. The disagreement observed at the two lowest salt concentrations

suggests that a certain degree of heterogeneity may still be present at pH7. However, the low value of the heterogeneity ratio for all salt concentrations (HR $\lesssim 0.1$) suggests that at neutral pH, the mucin gel does not appear to be heterogeneous to the particles: any stiff mucin-rich regions that may influence the macroscopic rheology are highly localized and impenetrable to the micron sized probes. At large salt concentrations, the near complete screening of intermolecular interactions may eliminate these microscopic heterogeneities, resulting in the observed agreement between the macroscopic and microscopic rheological measurements. Altogether then, these results are suggestive of increasingly viscoelastic yet homogeneous gels at neutral pH as salt is added. This is verified by the measured increase in the macrosopic viscoelastic moduli of the gels as well as the decreasingly Brownian (or increasingly subdiffusive) motion of the tracer particles, while homogeneity is inferred from the Gaussian step size distributions of these particles at all salt concentrations investigated.

4.2.3 Effect of surfactant on rheology of MUC5AC gels

Ribbeck and Gorlich have shown that the mild detergent trans-cyclohexane-1,2-diol can be used to interfere with hydrophobic interactions in the nuclear pore complexes (NPCs) of eukaryotic cells, reversibly eliminating their selectivity towards specific classes of molecules [100]. Motivated by this, we hypothesized that adding a similar non-ionic surfactant molecule also composed of an ethylene glycol polar group and an apolar butylene moiety [100], 1,2-hexanediol, to the MUC5AC gels at low pH would have the effect of disrupting the hydrophobic cross-links and decreasing the viscoelastic moduli of the gels through a third and distinct structural rearrangement mechanism. This experiment was carried out under acidic conditions as a result of the increased number of hydrophobic interaction sites that have been measured using fluorescent probes by Cao et al. in MUC5AC gels at pH2 compared to pH7 [102], consistent with the biochemical pictures presented in Figures 4.2.2a and 4.2.2b.

In Figure 4.2.6a, the macroscopic SAOS results for surfactant addition to $10\,\mathrm{mg\,ml^{-1}}$ MUC5AC gels at pH2 are reported, and a monotonic decrease in the storage and loss moduli above a critical concentration of $c^* \approx 10\,\mathrm{wt\,\%}$ is observed. At the microscopic level, a first effect of surfactant addition is to decrease the heterogeneity of the particle trajectories (as captured by the value of the heterogeneity ratio at $\Delta\tau = 0.1\,\mathrm{s}$ reported in Figure 4.2.6b) from a value of HR $= 0.64 \pm 0.21$ at $0\,\mathrm{wt\,\%}$ of added surfactant to HR $= 0.60 \pm 0.49$ at $5\,\mathrm{wt\,\%}$, HR $= 0.36 \pm 0.10$ at $10\,\mathrm{wt\,\%}$, and HR $= 0.10 \pm 0.07$ at $20\,\mathrm{wt\,\%}$ hexanediol. This trend is also reflected in the shapes of the step size distributions (presented in Figure 4.2.6c) and the associated non-Gaussian parameters, which decrease close to monotonically from $\kappa = 0.59 \pm 0.19$ for no added surfactant to a near Gaussian value of $\kappa = 0.11 \pm 0.09$ at $20\,\mathrm{wt\,\%}$ hexanediol.

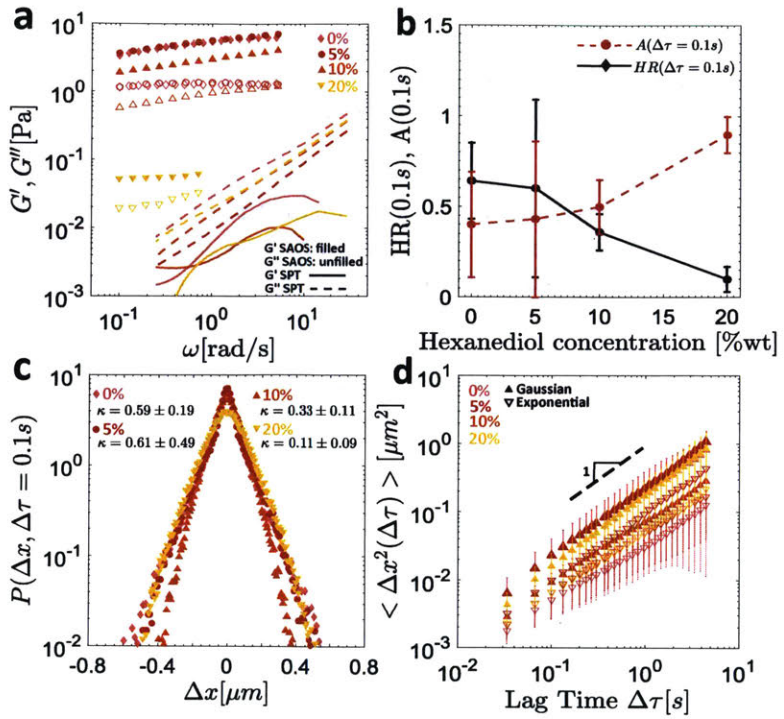

Figure 4.2.6: The effect of added surfactant on the rheology of 10 mg ml^{-1} MUC5AC gels at pH2. In (a), the SAOS results for the pH2 gels with 0 wt %, 5 wt %, 10 wt %, and 20 wt % hexanediol are shown for the macrorheological measurements (symbols) and the SPT predictions (lines) based on the MSDs of the exponential particle populations. In (b), the heterogeneity ratio HR($\Delta\tau$) (black diamonds and solid lines) and fraction of Gaussian particles $A(\Delta\tau)$ (red circles and dashed lines) at a lag time of $\Delta\tau = 0.1$ s are shown as a function of hexanediol concentration, and in (c), the van Hove distributions and associated non-Gaussian parameters κ are presented for all surfactant concentrations. In (d), the MSDs evaluated from SPT for the exponential (hollow inverted triangles and dashed error bars), and Gaussian (filled triangles and solid error bars) populations, as sorted at a lag time of $\Delta\tau = 0.1$ s, are plotted as a function of lag time for the same gels. Note that the standard deviations reported in (b) and (c) are the same as those published in [7] for consistency, but were mistakenly calculated assuming an entire population and consequently underestimate the true standard deviation by a factor of $\sqrt{\frac{N}{N-1}}$, where $N = 2$ or $N = 3$ depending on the number of experimental replicates for a given sample.

Further, by applying the sorting algorithm outlined in Section 4.2.2 at the characteristic early lag time of $\Delta\tau = 0.1$ s, the trajectory statistics and MSDs can once again be analyzed using two distinct subgroups consisting of Gaussian and exponential particles. With the exception of the 10 wt % hexanediol gel, the anomalous diffusion exponents α associated with the Gaussian populations remain approximately constant at the Brownian exponent $\alpha = 1$. Further, as seen in Figure 4.2.6b, the fraction of Gaussian particles $A(\Delta\tau = 0.1\,\text{s})$ increases nearly uniformly as a function of surfactant concentration, from $A = 0.40 \pm 0.29$ with no added surfactant to $A = 0.90 \pm 0.10$ at 20 wt % hexanediol. It is clear then that at this highest surfactant concentration, a nearly single or aggregate population undergoing normal Brownian motion is regained, as evidenced from the values of A, κ, and α. We

note that it is more difficult to discern a clear trend in the values of α associated with the exponential populations, which vary from $\alpha = 0.78 \pm 0.35$ at 0 wt % of added surfactant to $\alpha = 1.00 \pm 0.49$ at 5 wt %, $\alpha = 0.86 \pm 0.22$ at 10 wt %, and $\alpha = 0.91$ at 20 wt % hexanediol. However, the generally subdiffusive motion implied by these results is consistent with the biochemical picture for this subpopulation of less mobile particles confined to the mucin-rich phases of the gel.

Piculell et al.[114] have reviewed existing experimental data on the effect of surfactant addition to solutions of polymers containing hydrophobic groups, and have found that above a threshold surfactant concentration, the viscosity of the solution generally decreases with added surfactant. For certain polymer/surfactant combinations, this threshold concentration curiously corresponds to the critical micelle concentration (CMC) of the surfactant in the polymer-free solution, while in other cases, in particular for charged systems, this decrease in viscosity occurs at a lower surfactant concentration known as the critical aggregation concentration (CAC) [114]. The mechanism behind this observed decrease in viscosity has been attributed to associations between surfactant complexes and the polymer molecules, which crowd out the hydrophobic sites within the network and disrupt the cross-links that previously held it together [114]. This phenomenon has also been observed and clearly illustrated in schematic form by Kjniksen et al. in their studies of chitosan [115].

The expected effect of disrupting the hydrophobic interactions between individual mucin molecules using surfactant molecules at concentrations greater than the CAC is to loosen the mucin-rich phase of the gel, eventually returning it to a single phase. Macroscopically, as seen in our rheological data in Figure 4.2.6a, this manifests as a monotonic decrease in the elastic modulus of the gel for surfactant concentrations above the CAC of 1, 2-hexanediol and MUC5AC. Although quantitative measures of the CAC are often difficult to obtain as a result of the uncertainty associated with the structure of the surfactant/polymer complexes that form in solution, it is generally smaller than the CMC of the surfactant in polymer-free solution [114], which has been measured by Hajji et al. to be CMC= 8.9 wt % for 1, 2-hexanediol [116]. Additionally, this physical picture of gradually loosening mucin-rich domains and elimination of the largest pores created by the pH-induced mesoscopic phase separation as the surfactant molecules crowd out the hydrophobic sites (Figure 4.2.2d) is also consistent with our observations at the microscopic level. As surfactant is added, the heterogeneity ratio is observed to decrease as the hydrophobic cross-links maintaining the mucin dense regions are disrupted, until a single population ($A = 0.9 \pm 0.1$) undergoing nearly Brownian motion, as confirmed by the slope of the MSD ($\alpha = 1.04 \pm 0.37$) as well as the value of the non-Gaussian parameter ($\kappa = 0.11 \pm 0.09$), is observed at 20 wt % hexanediol. Despite this apparent return to homogeneity on the microscopic level as the concentration of surfactant is increased, the viscoelastic moduli predicted from thermal fluctuations of the exponential particles still disagree with those measured macroscopically for all hexanediol concentrations as seen in Figure 4.2.6a. This suggests that our explanation proposed previously of the tracer particles being unable to penetrate the densest local mucin regions which dominate the macrorheology may still be in effect despite the progressive elimination of hydrophobic cross-links upon surfactant addition.

4.2.4 Section summary

In summary, in this section we have analyzed the effect of pH, added salt, and surfactant on the macroscopic and microscopic rheological response of $10\,\mathrm{mg\,ml^{-1}}$ MUC5AC gels in order to gain additional insight into the structure and associative dynamics of mucin gels. The values of the viscoelastic moduli we measure macroscopically using cone-and-plate rheometry are largest at pH2, and the greatest degree of heterogeneity within the trajectories of the tracer particles is also observed at this pH, as measured by both the heterogeneity ratio (HR) and the non-Gaussian parameter (κ). Through the introduction of a novel sorting method, we have shown that, on average, the Gaussian particles diffuse nearly normally, but with a diffusion coefficient approximately 4 times smaller than that in water. By contrast, the exponential step size distribution of the trapped anomalously diffusing particles, with distribution width increasing as a power law of the lag time ($\sqrt{\lambda^2(\Delta\tau)} \sim \Delta\tau^{\alpha/2}$), is suggestive of interactions between the particles and the mucin molecules and/or geometric confinement.

Our combined observations on both length scales are suggestive of mesoscopic phase separation, which may simultaneously increase the overall elastic modulus of the gel as well as the heterogeneity of the measured MSDs of the embedded tracer particles through the creation of mucin-rich regions as well as mucin-poor ones through which some particles can easily diffuse. From a biophysical perspective, these findings are consistent with previous work which has shown that under acidic conditions, additional hydrophobic interaction sites are exposed on mucin chains as salt bridges are destroyed, which creates additional interaction points within the network that can promote and maintain the coexistence of two phases within the mucin gel [4, 102, 105]. This hypothesis is further supported by the rheological changes that are induced by the addition of hexanediol. On the macroscopic level, the addition of surfactant had the effect of softening the mucin gels for surfactant concentrations greater than the CAC, while microscopically this resulted in a systematic decrease in the measured heterogeneity of individual tracer particle trajectories. Both findings are consistent with the excess of small surfactant molecules out-competing and disrupting the hydrophobic interactions responsible for maintaining the mucin-rich regions, thus gradually loosening the network in these domains and shrinking the mucin-poor regions.

Finally on the macroscopic scale, the addition of salt to the pH-neutral MUC5AC gels had the effect of increasing the viscoelastic moduli as was also observed by decreasing the pH. Mechanistically, however, this stiffening was shown to arise from a fundamentally different structural mechanism. On the microscopic scale, increasing the salt concentration had the effect of decreasing the anomalous diffusion exponent α while maintaining homogeneous particle trajectories and Gaussian step size distributions. These observations are consistent with the presence of stronger, longer lived interactions between mucin molecules due to reduced electrostatic repulsion between the sugar side chains in the presence of salt, as well as a homogeneous gel structure with a characteristic mesh size significantly smaller than the one-micron diameter probe particles.

Importantly, although analysis of microscopic thermal fluctuations in mucin gels using the standard analysis developed for homogeneous complex fluids [44] was shown to not be predictive of their macroscopic linear viscoelastic response (particularly for the mucin gels prepared under acidic conditions), the analysis we have outlined clearly demonstrates that the combination of microscopic and macroscopic rheological measurements provides comple-

mentary information that aids in explaining the complex viscoelastic response observed in these physiologically-important hydrogels.

4.3 Exploration of the mechanisms leading to the breakdown of the GSER in mucin gels

In the previous section, we demonstrated that micro- and macrorheological measurements in mucin gels provide complementary information into the structure of the mucin network despite disagreeing both qualitatively and quantitatively. We now seek to improve our understanding of the mechanisms leading to this disagreement. We begin by exploring the effect of mucin concentration on the macrorheology of the gels, and compare these results at both pH levels with those measured in solutions of CMC in order to study gelation in different polymeric systems. Next, we study three possible reasons for the breakdown of the GSER in mucin gels. First, we investigate non-continuum effects in the mucin gels by varying the size of the probe particles, and also compare these results with those measured in solutions of CMC. Next, we investigate possible particle-mucin interactions by repeating our experiments in mucin gels at both pH levels with PEG-ylated, non-mucoadherent particles with near-neutral zeta potentials. As a third mechanism, we investigate the possibility of sample aging by comparing the microrheological responses at time points separated by several hours. Finally, we discuss the development of imaging techniques to visualize the mucin network at pH2 and pH7 through the use of fluorescently labeled, positively charged peptide probes.

4.3.1 Materials and methods

Mucin gel preparation

MUC5AC and CMC were solubilized for up to two nights with gentle shaking at 4 °C in deionized (milli-Q) water, and gels were prepared the same day as the experiments were performed by combining the solubilized mucins with the appropriate phosphate and sodium citrate pH buffers to a final concentration of 10 mM. Gels were vortex mixed to ensure adequate mixing following addition of all components, and kept on ice until experimental use. Experiments were performed within approximately 2 h of the gel being prepared unless otherwise indicated.

Macrorheology

Shear rheology tests were performed an ARESG2 (TA Instruments, New Castle, DE, USA) rheometer with an 8 mm parallel plate fixture with a 200 µm gap. All experiments were performed on a Peltier plate at a constant temperature T = 25 °C. SAOS measurements were performed at a strain amplitude within the linear viscoelastic regime of each mucin gel as determined from separate strain sweep experiments. Data points denote the average of 'up' and 'down' frequency sweeps for a single sample, with the standard deviation between these measurements shown. The one exception was the 1 wt % CMC solution at pH2 for which three samples were measured using macrorheology, with 'up' and 'down' frequency sweeps performed for each sample. For clarity on these logarithmic plots, error bars are only

shown extending above the data points.

Microrheology

Imaging was performed at room temperature with an Axio Observer D.1 inverted microscope using either a Zeiss LD Plan-Neofluar 40x/0.4, 20x/0.4, or 10x/0.4 Corr Ph2 objective lens (depending on the particle size being imaged) and a Hamamatsu Flash 4.0 C11440-22CU camera set to an exposure time of $\sigma_t = 10\,\text{ms}$. The number of particles imaged for a given sample varied between approximately 100 and 300, which corresponded to between 3 and 8 videos depending on the particle size, density, and quality of dispersion within the sample. Imaging was performed on a single sample at each condition.

Fluorescent carboxylated polystyrene latex particles were obtained from Magsphere Inc (Pasadena, CA, USA). PEG-ylated particles were obtained courtesy of the Hanes laboratory at Johns Hopkins University. The zeta potential of these particles was found to be $8.01 \pm 0.74\,\text{mV}$ at pH2 and $-9.24 \pm 0.30\,\text{mV}$ at pH7 for the 500 nm particles, and $7.37 \pm 0.64\,\text{mV}$ at pH2 and $-8.06 \pm 0.41\,\text{mV}$ at pH7 for the 1 µm particles using a Zetasizer Nano ZS90 (Malvern Instruments, Malvern, UK). The PEG-ylated particles had also previously been determined to be non-adherent to bovine submaxillary mucins using a mucin adsorption assay. Although diluted particle solutions were added at a volume ratio of 1 : 60 (particle solution : sample) in all cases, the initial dilutions of the particles varied depending on the particle size. Specifically, 200 nm carboxylated particles were initially diluted at a ratio of 1 : 1000 by volume in milli-Q water, 500 nm carboxylated particles at a ratio of 1 : 200, 500 nm PEG-ylated particles at a ratio of 1 : 200, 1 µm carboxylated particles at a ratio of 1 : 200, 1 µm PEG-ylated particles at a ratio of 1 : 100, 2 µm carboxylated particles at a ratio of 1 : 50, and 5 µm carboxylated particles at a ratio of 1 : 50. Additional details are provided in Section 2.3.1.

In order to increase the range of lag times over which the MSD data was available, images were recorded for $\approx 5\,\text{min}$ (or $\approx 300\,\text{s}$). Because of memory limitations of the electronic devices, it was difficult to image at the previous rate of $\approx 30\,\text{fps}$ for the entire $\approx 5\,\text{min}$ duration. However, because the minimum lag time is set by the inverse of the camera frame rate, it was also not desired to decrease this parameter significantly, as particle displacement information at early lag times would be lost. Therefore, imaging was performed at a 'logarithmically' decreasing rate, as shown in Figure 4.3.1a. Specifically, imaging was performed at $\approx 30\,\text{fps}$ for the first $\approx 1\,\text{s}$ (i.e. ≈ 30 frames), and then the frame rate was lowered to $\approx 10\,\text{fps}$ for the next 9 s (i.e. ≈ 90 frames), and then further lowered to $\approx 3\,\text{fps}$ for the next 90 s (i.e. ≈ 270 frames), and lowered a final time to $\approx 1\,\text{fps}$ for the remaining 200 s (i.e. ≈ 200 frames), resulting in 590 frames in total.

The use of a non-constant frame rate poses several analytical challenges. Firstly, the calculation of the MSD becomes more nuanced, as a given lag time can be composed of several different combinations of time steps of different durations. In order to perform these calculations, a modified version of the publicly available Matlab code 'Kehl.m' (https://www.mathworks.com/matlabcentral/fileexchange/41858-kehl-a-fast-no-loop-method-to-compute-msd), reproduced for convenience in Appendix A.1, was used. This approach allows for a fast, no-loop calculation of the MSD based on all possible step combinations,

and in the limit of a constant frame rate reduces to Equation (2.24). From this code, step sizes at various lag times $\Delta\tau$ were also straightforward to calculate in order to determine the corresponding van Hove distributions and non-Gaussian parameters κ.

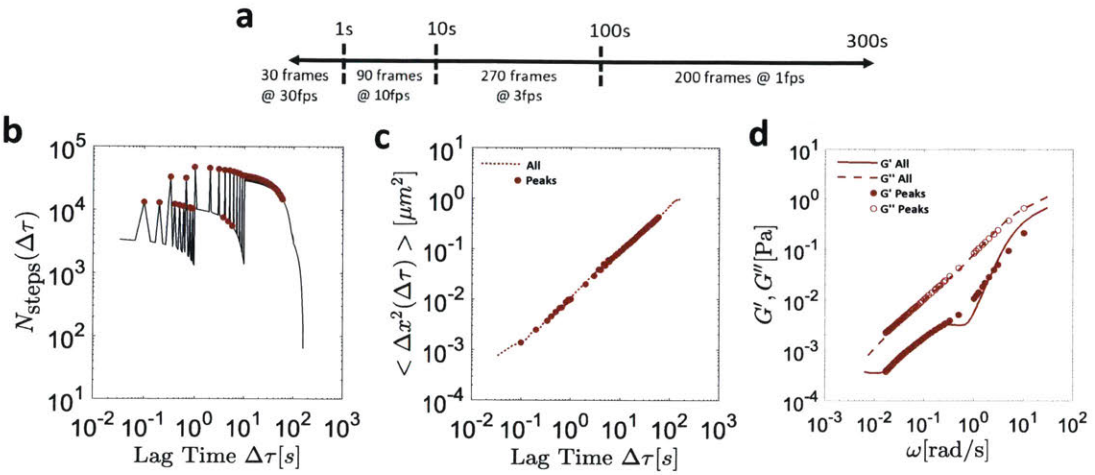

Figure 4.3.1: Analytical consequences of a non-constant camera frame rate for SPT analysis. (a) Description of the approximate sequence of frame rates used to obtain the 590 frames over a time period of $\approx$ 5 min. SPT data corresponding to the motion 1 µm carboxylated particles in 1 wt % CMC solutions at pH2 is shown in (b)-(d). (b) The number of recorded displacements N_{steps} with intervals of duration $\Delta\tau$ that were available for calculation of the MSD are shown as the solid black line as a function of $\Delta\tau$. The retained lag times corresponding to peaks in N_{steps} at least $1/10^{\text{th}}$ of the magnitude of the largest value of N_{steps} are shown as the filled red symbols. (c) MSD calculated using all possible lag times (dotted red line) and using the retained values from (b) only (solid red circles). (d) Predicted viscoelastic moduli from the same two MSD data sets as in (c).

From Equation (2.24), it is straightforward to see that the number of steps used to calculate the MSD decreases from $N-1$ at the earliest lag time $\Delta\tau$, where N is the total number of frames recorded, to 1 at the latest lag time for which information is available, $(N-1)\Delta\tau$. Consequently, it is well established that at later lag times approaching $(N-1)\Delta\tau$, the calculated MSD becomes increasingly noisy due to the reduced number of data points available for statistical averaging. When a non-constant frame rate is used, this same trend with increasing $\Delta\tau$ is not observed. Indeed, one important consequence of using a non-constant frame rate is that the number of lag times at which the MSD can be calculated increases substantially, yet the quantity of step size information available to perform this calculation varies significantly for different values of $\Delta\tau$. In order to visualize this, in Figure 4.3.1b the solid black line denotes the number of particle displacements of a duration $\Delta\tau$, which we denote by $N_{\text{steps}}(\Delta\tau)$, that are available and used to calculate the MSD as a function of $\Delta\tau$ for 1 µm beads in a 1 wt % solution of CMC at pH2. As can be seen, certain values of $\Delta\tau$ carry much more information if they can be composed of larger numbers of combinations of time intervals between images.

The result of this variation in statistical information is noise in the MSD (dotted red line of Figure 4.3.1c), which becomes even more pronounced when this result is converted

to frequency space in order to determine the viscoelastic moduli (solid (G') and dashed (G'') lines of Figure 4.3.1d). In order to mitigate this, we retain only the values of $\Delta\tau$ that correspond to peaks in Figure 4.3.1b, and further enforce that peaks should be no smaller than $1/10^{\text{th}}$ of the magnitude of the largest value of $N_{\text{steps}}(\Delta\tau)$. The values of $\Delta\tau$ corresponding to these criteria are shown as filled red circles in Figure 4.3.1b, and the corresponding MSD values at these lag times only are plotted as the filled red circles in Figure 4.3.1c. Using these values for the MSD only, we obtain a more reliable prediction of the viscoelastic moduli, shown as the filled (G') and hollow (G'') red circles in Figure 4.3.1d. Consequently, for the remainder of this chapter, this approach of retaining only values of $\Delta\tau$ corresponding to peaks in particle displacement information is used.

4.3.2 Effect of polymer concentration on the rheology of MUC5AC and CMC solutions

We begin by exploring the effect of concentration on the macrorheological response of the CMC and MUC5AC solutions at both pH2 and pH7. The results of these measurements are shown in Figure 4.3.2 at concentrations of 0.5 wt %, 1 wt %, 2 wt %, and 3 wt %.

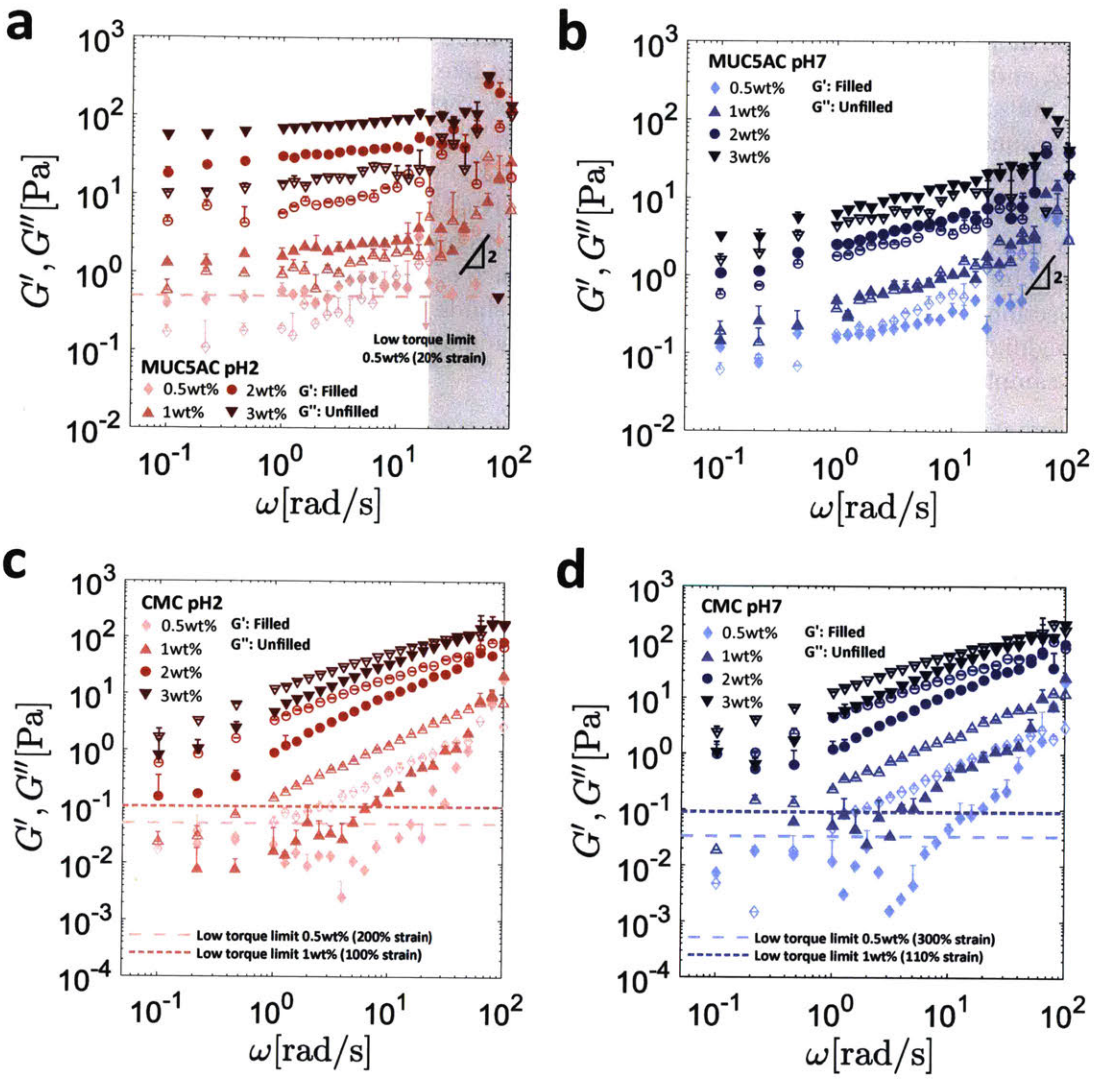

Figure 4.3.2: SAOS data at polymer concentrations of 0.5 wt %, 1 wt %, 2 wt %, and 3 wt % for MUC5AC solutions at pH2 (a) and pH7 (b), as well as CMC solutions at pH2 (c) and pH7 (d). The filled symbols denote the storage modulus G', while the unfilled symbols denote the loss modulus G''. For the softest samples when a significant number of the data points lie near or below the low torque limit of the rheometer (calculated from Equation (2.5) using $T_{\text{min}} = 0.01\,\mu\text{N m}$ and the appropriate sample strain, see Section 2.2.1) this limiting value is also indicated. In (a) and (b), the shaded grey regions correspond to $\omega \geq 20\,\text{rad s}^{-1}$ where significant experimental noise is visible, presumably due to fluid inertia (see the discussions in Section 2.2.1).

As can be seen, the rheological responses of CMC and MUC5AC solutions are very distinct. In a first instance, the CMC solutions are predominantly liquid like ($G'' > G'$) and exhibit a classical Maxwellian response for all concentrations across nearly all frequencies probed (Figures 4.3.2c and 4.3.2d), while the MUC5AC samples exhibit the weakly varying power law dependencies described previously (Figures 4.3.2a and 4.3.2b). Further, the

MUC5AC samples at pH2 are gels for all concentration values measured (i.e. $G' > G''$), while at pH7 they appear to be critical gels at 1 wt % ($G' \approx G''$), as described in Section 4.2.2, and subsequently exhibit predominantly solid-like responses for higher concentrations. For the softest samples, when a significant number of the data points lie near or below the low torque limit of the rheometer (calculated from Equation (2.5) using $T_{\min} = 0.01\,\mu\text{N m}$ and the appropriate sample strain, see Section 2.2.1), the minimum measurable modulus $G_{\min}$ is also indicated as a line. Finally, for the MUC5AC samples, fluid inertia effects appear to dominate the rheological response at high frequencies ($\omega \gtrsim 20\,\text{rad s}^{-1}$), as observed by the increased noise and the quadratic dependence of the moduli on ω (see the discussion in Section 2.2.1 as well as [21]). We consequently shade these regions of the graphs in order to highlight that the apparent rheological response may not truly be an intrinsic feature of the sample being tested.

In order to clearly contrast the nature of the macrorheological responses of solutions of CMC and MUC5AC, the results from Figure 4.3.2 are replotted in a simplified form in Figure 4.3.3.

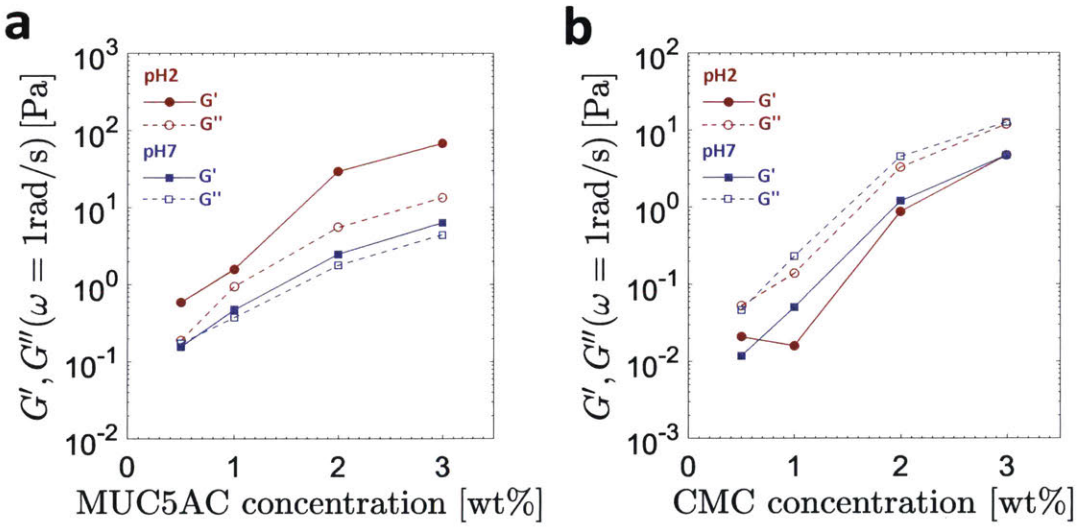

Figure 4.3.3: Storage (filled symbols and solid lines) and loss (unfilled symbols and dashed lines) moduli at a frequency of $\omega = 1\,\text{rad s}^{-1}$ as a function of polymer concentration at pH2 (red circles) and pH7 (blue squares) for MUC5AC (a) and CMC (b).

In Figure 4.3.3, the storage (filled symbols and solid lines) and loss (unfilled symbols and dashed lines) moduli at a frequency of $\omega = 1\,\text{rad s}^{-1}$ are plotted as a function of polymer concentration at both pH2 (red circles) and pH7 (blue squares) for MUC5AC (Figure 4.3.3a) and CMC (Figure 4.3.3b).

One immediately striking difference between the macrorheological responses of solutions of the two polymers is the insensitivity of CMC to the pH level. Despite CMC being a charged polymer, the storage and loss moduli curves at pH2 and pH7 for this material are nearly coincident, with data points for G' at low concentrations likely affected by experimental noise (see Figures 4.3.2a and 4.3.2b). This finding suggests that additional mechanisms

beyond charge-screening effects and subsequent changes to polymer flexibility are responsible for the increase in the viscoelastic moduli observed under acidic conditions in MUC5AC gels. In contrast, both the G' and G'' curves at pH2 for MUC5AC gels lie above their corresponding curves at pH7. Additionally, the fundamentally different functional dependencies of the viscoelastic moduli on ω are conveyed by the relative magnitude of G' and G''. For MUC5AC gels (Figure 4.3.3a), the sol-gel transition is observed at pH7 as a function of concentration, while at pH2 the samples are more solid-like at all concentrations considered. In contrast, for CMC (Figure 4.3.3b), $G'' > G'$ at $\omega = 1\,\mathrm{rad\,s^{-1}}$ for all concentrations measured.

4.3.3 Effect of particle size on the microrheology of CMC and MUC5AC solutions

In Section 4.3.2 we demonstrated that charge-screening effects alone cannot account for the pronounced pH-dependence of the rheology of MUC5AC gels. We now explore a first possible reason for the breakdown of the GSER in mucin gels by probing non-continuum effects and material heterogeneity. To do so, we study the microrheology of 1 wt % MUC5AC gels at pH2 and pH7 using carboxylated particles ranging in size from 200 nm to 5 µm. In order to have a reference for these measurements, we begin by considering the effect of particle size on the microrheological response of CMC solutions, for which non-continuum effects should be significantly less present.

CMC solutions

Before beginning our discussion of the effect of particle size on the microrheology of CMC solutions, one additional subtlety of particle tracking analysis should be noted. Conventionally during particle tracking, one of the parameters that must be specified is the minimum length requirement for a trajectory to be retained [46, 47], since particles are capable of moving in and out of frame during the recording of an image sequence. When a constant frame rate is used, this length requirement denotes an absolute time requirement for which the particle must be in view. However, when a non-constant frame rate is used, the absolute time associated with a specific frame length requirement increases for particles that first come into focus later in the video due to the progressive decrease of the camera frame rate.

In Figure 4.3.4, we consider the effect of the minimum trajectory length requirement on the microrheology of CMC solutions at 1 wt % and pH2 using 200 nm particles.

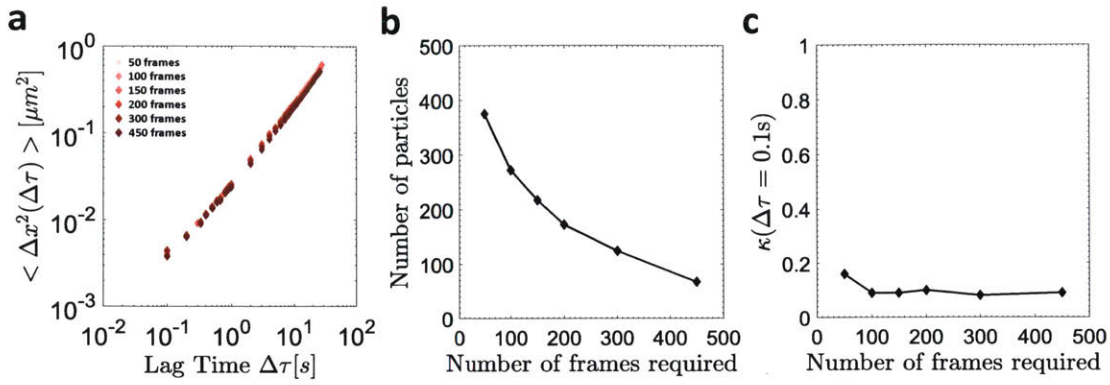

Figure 4.3.4: Effect of the minimum trajectory length requirement on the microrheology of CMC solutions at 1 wt % and pH2 using 200 nm particles. (a) MSD as a function of $\Delta\tau$ for different values of the minimum trajectory length. (b) Number of particles retained and (c) non-Gaussian parameter $\kappa(\Delta\tau = 0.1\text{s})$ as a function of the minimum frame length requirement.

As can be seen in Figure 4.3.4a, for relatively homogeneous solutions such as CMC, the effect of the minimum trajectory length requirement on the measured MSD is minimal. Since the motion of all of the particles is essentially the same, whether or not they are able to remain in view for a given number of frames is simply related to their initial spatial location within the capillary tube. As may be expected, as the minimum frame requirement is increased, the number of particles retained decreases (Figure 4.3.4b). Finally, the value of the non-Gaussian parameter remains constant at $\kappa(\Delta\tau = 0.1\text{s}) \approx 0.1$ regardless of the minimum frame length requirement (Figure 4.3.4c). Similar trends are observed for the same system at pH7, with the non-Gaussian parameter remaining constant at $\kappa(\Delta\tau = 0.1\text{s}) \approx 0.16$ as the minimum trajectory length requirement is increased.

Next, in Figure 4.3.5, we plot the MSD of the 200 nm, 500 nm, 1 µm, 2 µm, and 5 µm particles in 1 wt % in CMC solutions at pH2 (Figure 4.3.5a) and pH7 (Figure 4.3.5b) as a function of the lag time $\Delta\tau$. For consistency, the longest minimum frame requirement of 450 frames is used, although as can be seen from Figure 4.3.4b, for the smallest particles this frequently results in fewer than 100 particles being retained.

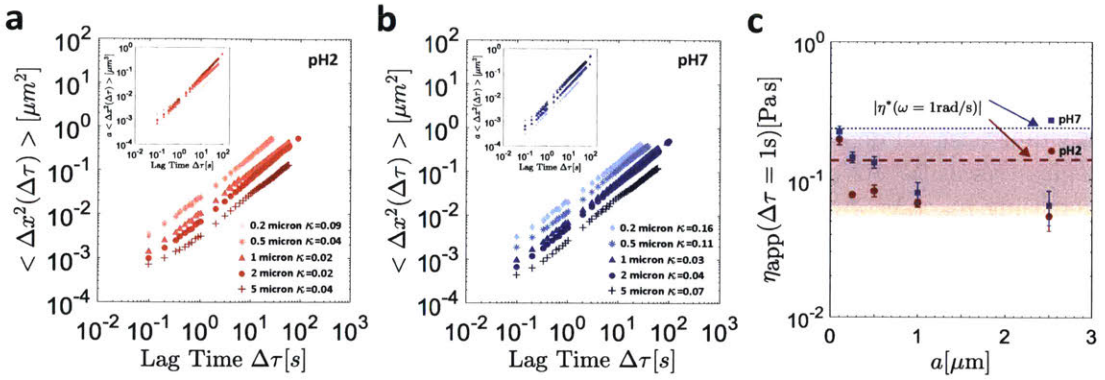

Figure 4.3.5: MSD as a function of the lag time $\Delta\tau$ for 200 nm, 500 nm, 1 µm, 2 µm, and 5 µm particles in 1 wt % CMC solutions at pH2 (a) and pH7 (b). The insets of both figures present the collapsed version of this data in which the MSD is scaled by the particle radius. In (c), the apparent viscosity η_{app} at a lag time of $\Delta\tau = 1\,\text{s}$ (see Equation (4.11)) is shown as a function of the particle radius a at pH2 (red circles) and pH7 (blue squares). The lines denote the complex viscosity $|\eta^*(\omega)|$ at a frequency of $\omega = 1\,\text{rad}\,\text{s}^{-1}$ obtained from separate SAOS experiments (pH2: dashed red lines, pH7: dotted blue lines). The shaded regions (pH2: red, pH7: blue) are guides for the eye that capture the particle size-dependent spread in the apparent microrheological viscosity.

As can be seen, the trends in the MSD are very similar at both pH levels, and when these results are scaled by the particle radii, a reasonable collapse onto a single master curve is observed (insets of Figures 4.3.5a and 4.3.5b). In order to quantify the effect of particle size, Equation (2.28) is fitted to each MSD curve in order to obtain an associated value of the generalized diffusion coefficient D_α and the anomalous diffusion coefficient α for each particle size. Since the functional form of the MSD generally varies with lag time, this is done by fitting Equation (2.28) to five distinct regions of the MSD curves ($0.1\,\text{s} \leq \Delta\tau \leq 0.3\,\text{s}$, $0.3\,\text{s} \leq \Delta\tau \leq 1\,\text{s}$, $1\,\text{s} \leq \Delta\tau \leq 3\,\text{s}$, $3\,\text{s} \leq \Delta\tau \leq 10\,\text{s}$, $10\,\text{s} \leq \Delta\tau \leq 30\,\text{s}$) and determining corresponding average and standard deviation values of α and D_α for every particle size. In certain cases for the smaller particles, MSD data at lag times of $\Delta\tau = 30\,\text{s}$ was not available, in which case we took the final MSD region for fitting to be $10\,\text{s} \leq \Delta\tau \leq \Delta\tau_{\text{end}}$, where $\Delta\tau_{\text{end}}$ was the longest lag time for which MSD data was available. We note that this is the approach taken throughout the remainder of the text to determine the average values and standard deviations of these parameters. Using these results, an apparent viscosity η_{app} at a lag time of $\Delta\tau = 1\,\text{s}$ can be obtained for each particle size by equating Equations (2.28) and (2.42), i.e.

$$\eta_{\text{app}}(\Delta\tau = 1\,\text{s}) = \frac{k_B T}{6\pi D_\alpha a}. \tag{4.11}$$

We note that the term 'apparent' is used since in general, the MSD does not depend linearly on the lag time for these viscoelastic systems, and hence the front factors of Equations (2.28) and (2.42) cannot truly be equated due to the different powers of $\Delta\tau$ arising in both equations. However, by considering the MSD at a lag time of 1 s, $\Delta\tau = \Delta\tau^\alpha = 1\,\text{s}$ and hence an approximate comparison can be drawn.

In Figure 4.3.5c, this apparent viscosity at $\Delta\tau = 1\,\text{s}$ is plotted as a function of particle

size at pH2 (red circles) and pH7 (blue squares). The lines denote the complex viscosity $|\eta^*(\omega)|$ at a frequency of $\omega = 1\,\mathrm{rad\,s^{-1}}$ obtained at pH2 (dashed red lines) and pH7 (dotted blue lines) from separate SAOS experiments, and the shaded regions (red for the pH2 data and blue for the pH7 data) are simply guides for the eye that bound the values of η_{app}, thus providing a visual depiction of the particle size-dependent spread in the apparent microrheological viscosity. As can be seen, at both pH levels, there appears to be a weak trend of decreasing $\eta_{\mathrm{app}}(\Delta\tau = 1\,\mathrm{s})$ as a function of increasing particle size. By taking the quotient of the apparent viscosity for each particle size with that measured for 1 µm particles at each pH level, the apparent viscosity is found to deviate by at most a factor of 2.4 in the case of the 200 nm particles at pH2. For reference, if a similar exercise is repeated for the data in water shown in Figure 2.3.4a, excluding the 200 nm particles which are addressed in detail in Figures 2.3.4b and 2.3.4c and using a single fit for D_α and α to the MSD data due to the shorter nature of these trajectories, the greatest deviation from the apparent viscosity of the 1 µm carboxylated particles at a delay time of $\Delta\tau = 1\,\mathrm{s}$ is a factor of 1.5 measured for the 5 µm particles. We note, however, that this trajectory appears to be affected by residual drift, and for the remaining particles the apparent viscosity deviates by no more than a factor of 1.08.

As a final consideration with CMC, in Figure 4.3.6a we compare the macrorheological response of 1 wt % CMC gels at pH2 with the predicted viscoelastic moduli from SPT using 1 µm particles. For completeness, since this data is available, we also plot the SAOS data obtained using the larger 40 mm 2° cone-and-plate setup.

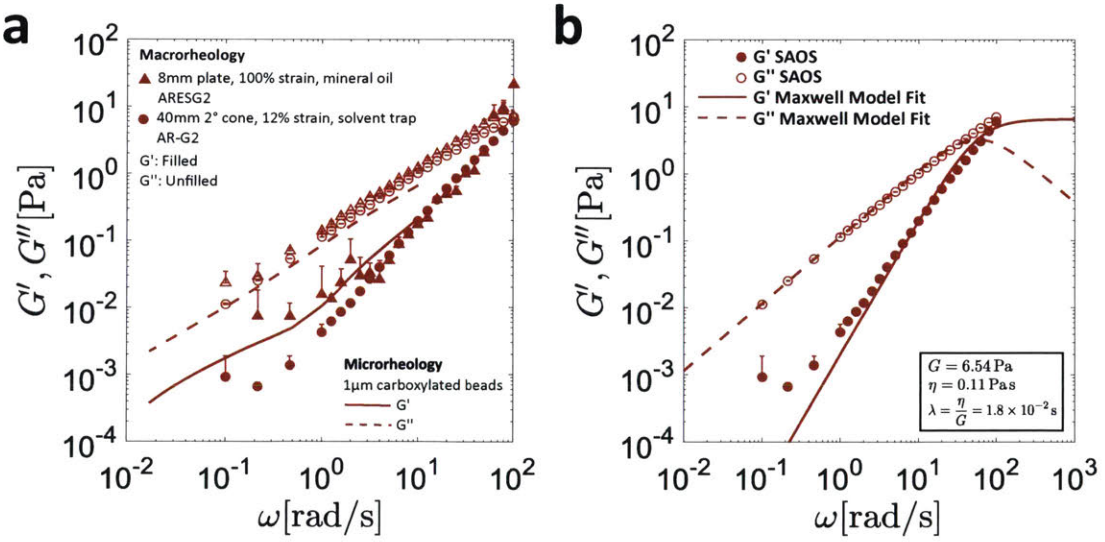

Figure 4.3.6: (a) Comparison of the viscoelastic moduli of 1 wt % CMC gels at pH2 measured in SAOS (symbols; G': filled, G'': unfilled) and the predictions from the microrheological response of 1 µm particles (lines; G': solid, G'': dashed). Data obtained using an 8 mm parallel plate setup on an ARESG2 is shown as triangular symbols, while data obtained using a 40 mm 2° cone-and-plate setup on an AR-G2 is shown as circular symbols. (b) Fit of the linear viscoelastic Maxwell model (lines; G': solid, G'': dashed) to the SAOS data obtained with the 40 mm 2° cone-and-plate setup. The values of the fitted parameters are indicated.

In stark contrast to the data in Figure 4.2.1a, good agreement is observed between the viscoelastic moduli determined both microscopically and macroscopically. Indeed, for a homogeneous, rheologically simple system such as CMC, for which the MSD data of the particles was minimally affected by the minimum trajectory length requirement (Figure 4.3.4) and for which the apparent viscosity was only somewhat sensitive to particle size, this result is not surprising. We can estimate the mesh size ξ of the 1 wt % CMC solution at pH2 through the relationship $\xi \sim \left(\frac{k_B T}{G}\right)^{\frac{1}{3}}$ [117], where G is the plateau modulus of the solution. In order to extract G, in Figure 4.3.6b we fit a linear viscoelastic Maxwell model (see Section 2.2.2) to the SAOS data obtained using the 40 mm 2° cone-and-plate setup. For this model it is straightforward to show that [27]

$$G'_{\text{Maxwell}}(\omega) = G\frac{(\lambda\omega)^2}{1+(\lambda\omega)^2} \tag{4.12}$$

and

$$G''_{\text{Maxwell}}(\omega) = G\frac{\lambda\omega}{1+(\lambda\omega)^2}, \tag{4.13}$$

where $\lambda = \frac{\eta}{G}$ is the relaxation time of the material. Performing this fit, we obtain that $G = 6.54\,\text{Pa}$, allowing us to estimate a value of $\xi = 86\,\text{nm}$ for the mesh size of the CMC solution at 1 wt %. Therefore, the fact that all of the probe particles are larger than this measured mesh size is consistent with particle size effects being small for the CMC solutions. However, this result for ξ is only approximately twice as small as the smallest 200 nm particles used, which may explain in part why particle size effects are small but non-negligible (compared to, say, those in water). Using diffusing wave spectroscopy (DWS), Lu and Solomon [118] also observed small but non-zero particle size effects for probes ranging in size from $0.3 - 2.2\,\mu\text{m}$ in solutions of hydrophobically modified ethoxylated urethane (HEUR) associating polymers (AP) at concentrations $\lesssim 3\,\text{wt}\,\%$, while with the same technique van Zanten et al. [119] observed nearly no probe size effects in 7 wt % PEO solutions for particle sizes ranging from $\approx 0.2 - 1.5\,\mu\text{m}$. We note that both of these particle size ranges are narrower than the one considered in this study.

Nevertheless, for the 1 µm particles, our estimate for ξ suggests that the probes should be much larger than the mesh size and consequently able to sample the entire gel environment, which is consistent with the good agreement observed between the micro- and macrorheology data in Figure 4.3.6.

MUC5AC solutions

Having considered the effect of particle size on the microrheology of CMC solutions, we now repeat these experiments in MUC5AC gels at pH2 and pH7. We begin by considering the effect of the minimum trajectory length requirement during tracking on the MSD of 200 nm particles in 1 wt % MUC5AC solutions at pH2 (Figure 4.3.7a) and pH7 (Figure 4.3.7b).

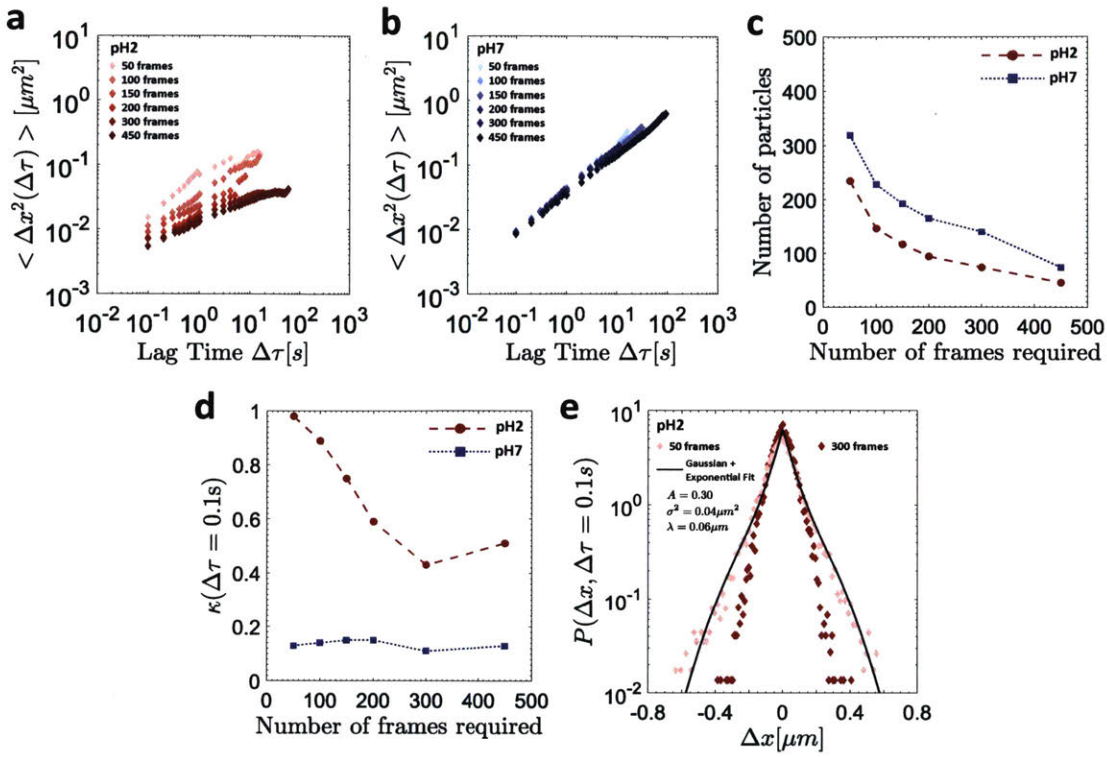

Figure 4.3.7: Effect of the minimum trajectory length requirement on the MSD of 200 nm particles in 1 wt % MUC5AC solutions at pH2 (a) and pH7 (b). In (c) and (d), the number of particles retained and the non-Gaussian parameter $\kappa(\Delta\tau = 0.1\,\mathrm{s})$, respectively, are plotted as a function of the frame requirement at pH2 (red circles and dashed lines) and pH7 (blue squares and dotted lines). In (e), the van Hove distributions at a lag time of $\Delta\tau = 0.1\,\mathrm{s}$ at pH2 are shown for trajectory length requirements of 50 and 300 frames. The distribution corresponding to trajectory lengths of 50 frames is also fit with a mixed probability distribution function constructed as the weighted sum of a Gaussian and an exponential distribution, as described in [7], and the fitting parameters used are indicated.

As can be seen in Figure 4.3.7b, similarly to the CMC solutions, the effect of the minimum trajectory length on the MSD of the 200 nm particles in the 1 wt % MUC5AC solutions at pH7 is minimal. In contrast, at pH2, a large decrease in the MSD is observed as the minimum trajectory length is increased (Figure 4.3.7a). For both pH levels, a similar trend of a decreasing number of retained particles with increasing frame length requirement is observed (Figure 4.3.7c).

In Section 4.2.2 it was observed that at pH2 the trajectories of 1 µm carboxylated particles in 1 wt % MUC5AC gels are heterogeneous, with a wide range of MSDs observed between individual particles (see Figure 4.2.4b). The result of this heterogeneity is that the requirement of a larger minimum trajectory length biases the retained particles towards the slower population, since fast-moving particles are less likely to be in view for this prolonged duration. For smaller minimum trajectory length requirements, the faster population of particles is still able to remain in frame for the specified frame duration, and consequently the ensemble average MSD of the retained particles appears larger. This effect is magnified

by the use of a non-constant frame rate, since a particle that comes into view later on during imaging must actually stay in frame for even longer from an absolute time perspective than one that was in frame at the very beginning due to the decreasing camera frame rate. Clearly then, in highly heterogeneous systems care should be taken in selecting the minimum trajectory length requirement, as a result of the bias that this introduces to the identity of the retained particle population.

This effect can be nicely visualized by examining the step size distribution of the retained particles for various minimum trajectory lengths. In Figure 4.3.7d, the non-Gaussian parameter $\kappa(\Delta\tau = 0.1\,\mathrm{s})$ is plotted as a function of the minimum trajectory length. Similarly to in CMC, At pH7, κ is relatively constant, and remains at the low values associated with more homogeneous particle trajectories. In contrast, at pH2 a decrease in κ is observed as a function of increasing trajectory length. By plotting the van Hove distributions for trajectory length requirements of 50 and 300 frames (Figure 4.3.7e), it is clear that the probability of larger steps decreases at 300 frames, as seen by the narrowing of the van Hove distribution, consistent with the notion that only slower-moving particles are retained for longer minimum trajectory length requirements. In contrast, at 50 frames, the presence of faster moving particles results in a broader range of individual MSD trajectories, and the van Hove distribution can be described by a mixed probability distribution function constructed as the weighted sum of a Gaussian and an exponential distribution, as described in Section 4.2.2 and shown as the solid black line. The fitting fitting parameters used to generate this curve are shown in Figure 4.3.7e.

With these considerations in mind, we next consider the effect of particle size on the microrheology of MUC5AC gels in Figure 4.3.8. We enforce the longest minimum trajectory requirement of 450 frames for all particle sizes both to maximize the range of lag times over which MSD information is obtained as well as to mitigate the biases discussed previously. However, it is important to note that for the smallest and most mobile particles ($\lesssim 500\,\mathrm{nm}$ in diameter), this frequently results in the retention of substantially fewer than 100 particles. For particles $1\,\mu\mathrm{m}$ in diameter or larger, the effect of the minimum trajectory length requirement on the MSD is already significantly less pronounced due to the reduced mobility of these larger probes.

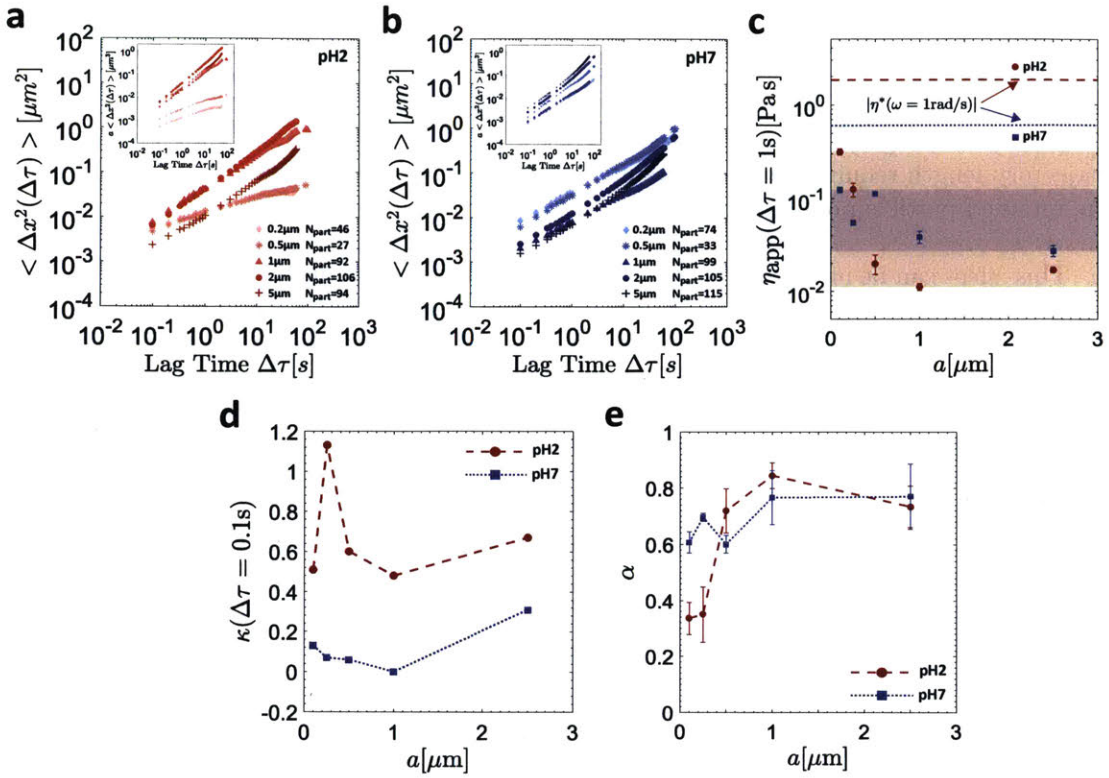

Figure 4.3.8: MSD as a function of lag time $\Delta\tau$ for 200 nm, 500 nm, 1 µm, 2 µm, and 5 µm particles in 1 wt % MUC5AC solutions at pH2 (a) and pH7 (b). The insets of both figures present the collapsed version of this data in which the MSD is scaled by the particle radius. The lines denote the complex viscosity $|\eta^*(\omega)|$ at a frequency of $\omega = 1\,\mathrm{rad\,s^{-1}}$ obtained from separate SAOS experiments (pH2: dashed red lines, pH7: dotted blue lines). In (c), the apparent viscosity η_{app} at a lag time of $\Delta\tau = 1\,\mathrm{s}$ (see Equation (4.11)) is shown as a function of the particle radius a at pH2 (red circles) and pH7 (blue squares). The shaded regions (pH2: red, pH7: blue) are guides for the eye that capture the particle size-dependent spread in the apparent microrheological viscosity. In (e) and (f), the non-Gaussian parameter $\kappa(\Delta\tau = 0.1\,\mathrm{s})$ and the anomalous diffusion exponent α are plotted as a function of the particle radius a at pH2 (red circles and dashed lines) and pH7 (blue squares and dashed lines).

One immediately apparent result in the inset of Figure 4.3.8a is the poor collapse of the MSD curves scaled by the particle radii at pH2. In order to quantify this, we once again plot the apparent viscosity η_{app} at a lag time of $\Delta\tau = 1\,\mathrm{s}$ as a function of particle size at pH2 and pH7 in Figure 4.3.8c. As previously explained, the lines denote the complex viscosity $|\eta^*(\omega)|$ at a frequency of $\omega = 1\,\mathrm{rad\,s^{-1}}$ (pH2: dashed red lines, pH7: dotted blue lines) obtained from separate SAOS experiments, and the shaded regions (pH2: red and pH7: blue) are visual bounds on the values of η_{app}. Similarly to CMC (see Figure 4.3.5), at pH7 an overall decrease in η_{app} with increasing particle size is observed, with the greatest deviation in apparent viscosity from the value corresponding to that measured for 1 µm particles being a factor of 4.1 for the 5 µm particles. In contrast (inset of Figure 4.3.8a), at pH2 relatively good collapse in the scaled MSD is observed for particles $\geq 1\,\mu\mathrm{m}$ in diameter, while the

smaller particles appear significantly less mobile. From Figure 4.3.8c, this is reflected in the large values of η_{app} for the 200 nm and 500 nm particles. Quantitatively, the apparent viscosity experienced by the 200 nm particles at $\Delta\tau = 1\,s$ is 16.0 times larger than that measured using 1 µm probes. In Figure 4.3.8(d), the non-Gaussian parameter $\kappa(\Delta\tau = 0.1\,s)$ is plotted as a function of the particle size. At both pH2 and pH7 this parameter is relatively independent of particle size, and the larger deviation in $\kappa(\Delta\tau = 0.1\,s)$ for the 500 nm particles at pH2 may arise from the relatively small number of particles imaged under these conditions (see Figure 4.3.8a). At pH7, small values of κ corresponding to homogeneous particle trajectories are measured, while at pH2 heterogeneous trajectories and larger κ are reported for all particle sizes. Finally, in Figure 4.3.8e, the anomalous diffusion coefficient α is plotted as a function of particle size at both pH levels. Although a small overall increase in α is observed with particle size at pH7, this increase is far more dramatic at pH2, with particle motion transitioning from strongly subdiffusive for the 200 nm and 500 nm particles ($\alpha \approx 0.3$) to $\alpha \approx 0.8$ for the largest particle sizes.

As a final consideration in this section, given the pronounced effect of particle size on the microrheology of mucin gels at pH2 observed in Figure 4.3.8a, we compare the macrorheological response of 1 wt % MUC5AC gels at pH2 with the predicted viscoelastic moduli from SPT.

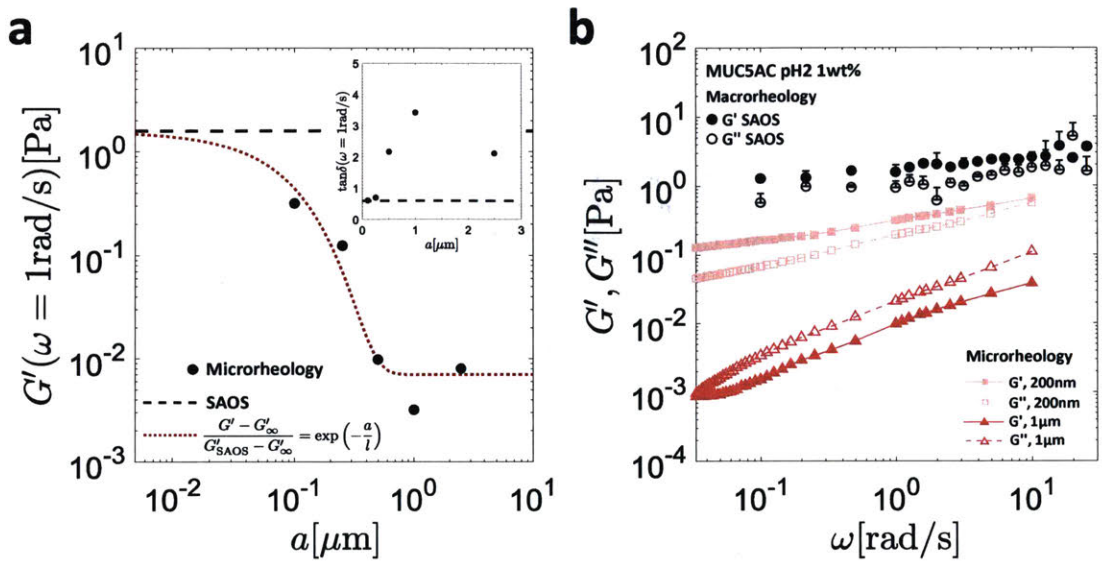

Figure 4.3.9: (a) Storage modulus G' predicted from microrheology at a frequency of $\omega = 1\,\text{rad}\,\text{s}^{-1}$ as a function of the particle radius a (black filled circles). The dashed black line indicates the value of G'_{SAOS} measured using SAOS at the same frequency. These data are fit to an exponential distribution of the form $G' = G'_\infty + (G'_{\text{SAOS}} - G'_\infty)\exp\left(-\frac{a}{l}\right)$, resulting in an exponential length scale of $l = 78.3\,\text{nm}$. This fit is shown as the dotted red line. In the inset, the microrheological measurements of $\tan\delta(\omega = 1\,\text{rad}\,\text{s}^{-1}) = \frac{G''(\omega=1\,\text{rad}\,\text{s}^{-1})}{G'(\omega=1\,\text{rad}\,\text{s}^{-1})}$ are shown as a function of the particle radius a (solid black circles), and the dashed black line once again denotes the value of this parameter measured using SAOS. (b) Comparison of the macrorheological response of 1 wt % MUC5AC gels at pH2 (black circles; G': filled, G'': unfilled) and the predicted viscoelastic moduli from SPT for minimum trajectory length requirements of 450 frames using 200 nm (G': solid lines and filled squares, G'': dashed lines and unfilled squares) and 1 μm (G': solid lines and filled upright triangles, G'': dashed lines and unfilled upright triangles) particles.

In Figure 4.3.9a, the elastic modulus G' at $\omega = 1\,\text{rad}\,\text{s}^{-1}$ obtained from SPT is plotted as a function of the particle radius a. These data are shown as solid black circles. Further, the dashed black line indicates the value of G'_{SAOS} measured using SAOS at the same frequency. As can be seen, the elastic modulus decreases with increasing particle size up to $a \approx 0.5\,\mu\text{m}$, and remains relatively constant for particle diameters $\geq 1\,\mu\text{m}$. Further, for all particles sizes, the elastic moduli measured with SPT are smaller than the bulk value obtained from macrorheology. In order to also demonstrate the effect of particle size on the loss modulus G'', $\tan\delta$ at $\omega = 1\,\text{rad}\,\text{s}^{-1}$ predicted from SPT is plotted as a function of particle radius a (black circles) in the inset of Figure 4.3.9a, with the dashed black line once again denoting the value of the bulk measurement at the same frequency. As can be seen, the microrheological environment probed by the particles transitions from being predominantly solid-like ($\tan\delta < 1$) and in good agreement with the bulk value for particles 500 nm in diameter and smaller to predominantly liquid-like ($\tan\delta > 1$) for larger particles. In order quantify the functional dependence of the gel properties on the particle size, the data in the main plot of Figure 4.3.9a are fitted to the empirical functional form

$$G' = G'_{\infty} + (G'_{\mathrm{SAOS}} - G'_{\infty}) \exp\left(-\frac{a}{l}\right), \tag{4.14}$$

where G'_{SAOS} is the bulk value measured in SAOS and G'_{∞} is taken to be the average value of $G'(\omega = 1\,\mathrm{rad\,s^{-1}})$ for the 3 largest particles. This fitted curve is shown as the dashed red line. The exponential length scale l obtained from this fit is $l = 78.3\,\mathrm{nm}$, which implies that particles 156.6 nm in diameter would sample an elastic modulus corresponding to approximately 37 % of the bulk value G'_{SAOS}. Further, from this fit, we can estimate that in order to measure a microscopic elastic modulus that is at least 90 % as large as G'_{SAOS}, particles approximately 16.6 nm in diameter would need to be used.

Finally, in Figure 4.3.9 we plot the full frequency spectra of the viscoelastic moduli predicted from SAOS and from SPT using 200 nm and 1 µm particles with minimum trajectory length requirements of 450 frames imposed. In agreement with Figure 4.3.9a, the viscoelastic moduli predicted by the 200 nm particles are greater than those measured using 1 µm probes. For the 1 µm particles, the linear viscoelastic response predicted from SPT is predominantly liquid-like ($G'' > G'$), and the moduli are nearly 3 orders of magnitude lower than those measured using SAOS. For the 200 nm probes, the linear viscoelastic response transitions to being predominantly solid-like and, similarly to the SAOS data, weak power law dependencies of G' and G'' on ω are observed. Further, the magnitude of the moduli are approximately two orders of magnitude larger than those measured using the larger 1 µm particles. From the results in Figure 4.3.7a, we can expect that if a smaller minimum trajectory length requirement were used, the viscoelastic moduli predicted from the MSD of the 200 nm particles would decrease, and may even transition to being predominantly liquid-like over certain frequencies.

4.3.4 Effect of particle surface chemistry on the microrheology of MUC5AC solutions

Having established in the previous section that non-continuum effects and material heterogeneity almost certainly play a role in the breakdown of the GSER in mucin gels, we now consider a second possible mechanism: particle-mucin interactions. In order to do so, we consider the response of 500 nm and 1 µm particles with two surface chemistries: the negatively charged, carboxylated particles used in Section 4.3.3 and particles functionalized with a polyethylene glycol (PEG) corona (refered to as 'PEG-ylated' particles), which have previously been shown to have near neutral zeta potentials at pH2 and pH7, as well as to be non-adherent to bovine submaxillary mucins.

In Figure 4.3.10, we plot the measured MSD as a function of $\Delta\tau$ for both particle sizes and surface chemistries at pH2 (Figure 4.3.10a) and pH7 (Figure 4.3.10b). The values of the non-Gaussian parameter κ at a lag time of $\Delta\tau = 0.1\,\mathrm{s}$ and the anomalous diffusion exponent α are also indicated. A minimum trajectory length requirement of 450 frames is enforced in all cases. We note again that for the smaller and more mobile 500 nm particles, this results in the retention of substantially fewer than 100 particles (see the discussion in Section 4.3.3 as well as Figures 4.3.8a and 4.3.8b).

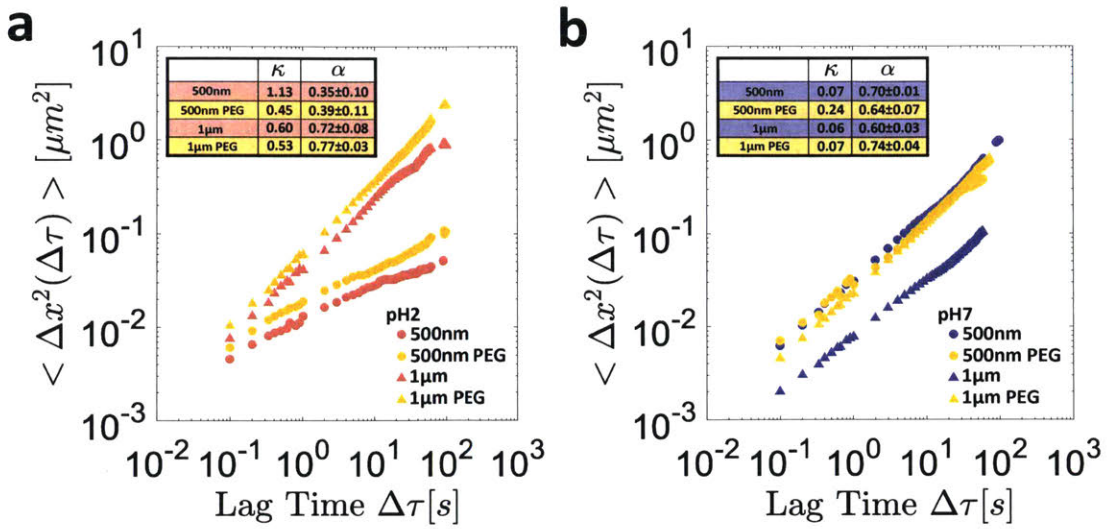

Figure 4.3.10: MSD as a function of the lag time $\Delta\tau$ for a minimum trajectory length of 450 frames for 500 nm (circles) and 1 μm (triangles) PEG-ylated (yellow symbols) and carboxylated particles at pH2 ((a), pink symbols for carboxylated particles) and pH7 ((b), blue symbols for carboxylated particles). The values of the non-Gaussian parameter κ measured at a lag time of $\Delta\tau = 0.1$ s and the anomalous diffusion exponent α are also indicated.

At pH2, a small increase in the MSD of the PEG-ylated particles relative to the carboxylated ones is observed for both particle sizes. The values of κ and α measured for both surface chemistries for a given particle size are similar, although the non-Gaussian parameter associated with the 500 nm particles is larger for the PEG-ylated particles ($\kappa(\Delta\tau = 0.1\,\text{s}) = 1.13$) than the carboxylated ones ($\kappa(\Delta\tau = 0.1\,\text{s}) = 0.45$). At pH7 the trends are less clear. For the 1 μm particles an increase is observed in the MSD (and α) of the PEG-ylated particles relative to the carboxylated ones, although κ is similarly small for both surface chemistries. In contrast, for the 500 nm particles, the MSDs are nearly coincident for both surface chemistries, although the non-Gaussian parameter is higher for the PEG-ylated particles ($\kappa(\Delta\tau = 0.1\,\text{s}) = 0.24$) than the carboxylated ones ($\kappa(\Delta\tau = 0.1\,\text{s}) = 0.24$).

Although it appears from these results that the effect of particle surface chemistry on the microrheological response in MUC5AC gels is not negligible, it is important to note that in general, sticking interactions between particles and their environment should result in an *overprediction* of the viscoelastic moduli from microrheology, as a result of the particles appearing 'slower' due to a reduced mobility associated with binding. Indeed, as seen in Figure 4.3.10, the effect of a non-interacting surface chemistry at both pH levels is either to increase slightly the mobility of the particles, or to have essentially no effect. Consequently, such interactions cannot explain the sizable *underprediction* of the macroscopic viscoelastic moduli using SPT in MUC5AC gels at pH2 (see Figure 4.2.1a). Further, from the magnitude of the changes associated with the MSD, particle-medium interactions appear to play a significantly smaller role than particle-size effects (see Section 4.3.3) in terms of reconciling the disagreement between the macroscopic and microscopic rheological responses.

4.3.5 Effect of sample age on the microrheology of MUC5AC solutions

As a final note mechanism leading to the breakdown of the GSER in mucin gels, we consider the effect of sample aging on the microrheology of MUC5AC gels. Philippe et al. [120] have shown through a combination of rheology and light scattering that pig gastric mucus gels spontaneously restructure with age. Specifically, they observe the formation of larger, more compact domains, over time, as well as a decrease in the elastic modulus, which they attribute to a loss of network connectivity arising from this coarsening or compaction [120]. They conclude from their results then that following an initial disruption of the original network due to sample preparation, or arrested phase separation, the mucus gel rapidly reforms in analogy to colloidal and polymeric systems undergoing phase separation [120].

Therefore, in order to determine whether similar aging was present in the reconstituted MUC5AC gels, we repeated the microrheological experiments in 1 wt % MUC5AC gels with the 1 µm carboxylated particles at both pH2 and pH7 after a delay of several hours; ≈ 7 h for the gel at pH2, and ≈ 8.5 h for the gel at pH7. Sample ages are indicated as being approximate because of the significant time required to acquire the necessary number of movies for these long experiments: total experiment time was frequently nearly 1 h in length for an individual sample. Samples were kept at 4 °C between experiments, but were allowed to equilibrate at room temperature for approximately 1 h prior to the experiment performed at the later time point. The results from these experiments are shown in Figure 4.3.11 below, and the values of the non-Gaussian parameter κ at a lag time of $\Delta\tau = 0.1$ s as well as the anomalous diffusion exponent α are indicated.

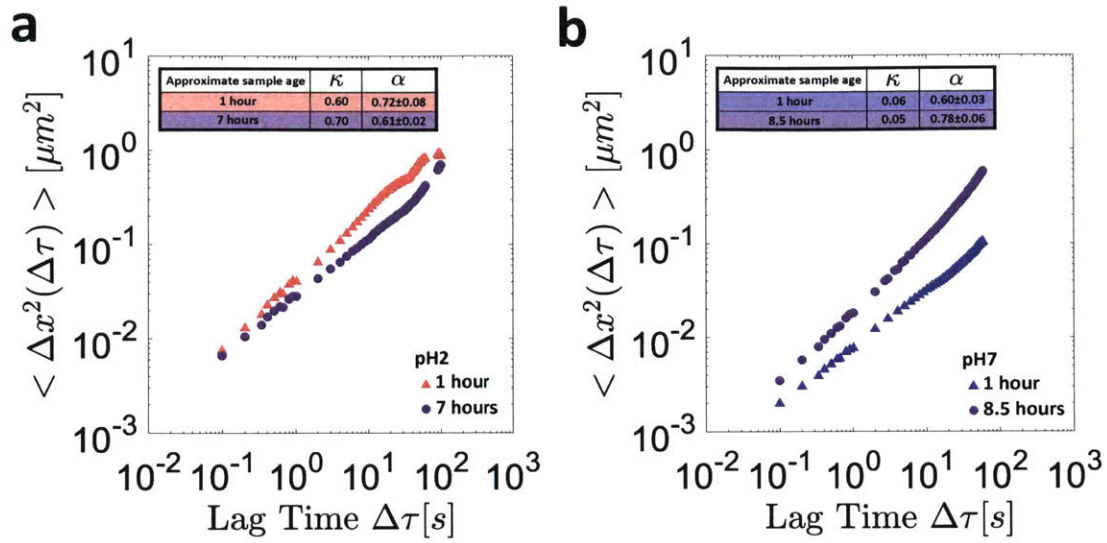

Figure 4.3.11: MSD as a function of the lag time $\Delta\tau$ for a minimum trajectory length of 450 frames for 1 µm carboxylated particles imaged after approximately 1 h as well as after a delay of several hours in 1 wt % MUC5AC gels at pH2 (a) and pH7 (b). In (a), the pink triangles correspond to a sample age of $\approx$ 1 h, and the purple circles correspond to a sample age of approximately 7 h, while in (b) the blue triangles correspond to a sample age of $\approx$ 1 h, and the purple circles correspond to a sample age of approximately 8.5 h. The values of the non-Gaussian parameter κ measured at a lag time of $\Delta\tau = 0.1$ s and the anomalous diffusion exponent α are also indicated.

At pH2, the microrheological response at both time points is similar, as seen by the comparable values of both κ and α. At pH7, the particles appear more mobile after the aging period, as observed by the comparably low levels of heterogeneity but the increase in α ($\alpha = 0.60 \pm 0.03$ after 1 h and $\alpha = 0.78 \pm 0.06$ after 8.5 h). This increase in particle mobility may be due to an increased susceptibility of the mucin network to protease activity at pH7 compared to under acidic conditions.

Therefore from these results it appears that, particularly at pH2, sample coarsening or aging does not strongly influence the microrheology of mucin gels over the time ranges considered, and therefore is not a primary mechanism resulting in the breakdown of the GSER.

4.3.6 Visualization of the mucin network

As a final exercise, we sought to visualize the microstructural differences in the mucin networks at pH2 and pH7 that were inferred from the rheological studies performed. In order to do so, we utilized a positively charged fluorescent reporting peptide of sequence $(AK)_{10}$-NH_2 which was synthesized, purified, and identified by the Swanson Biotechnology Center at the Koch Institute at MIT (Cambridge, MA, USA) following the protocol outlined in [10]. The isoelectric point of lysine (K) is pI = 9.74, and consequently the fluorescent reporting peptides are positively charged at both pH2 and pH7. Further, although it was explained in Section 4.2.2 that at pH2 the mucin molecules are closer to neutrally charged compared

to the net negative charge they possess at pH7, the pKa of the carboxylate groups of the sialic acid residues on the oligosaccharide chains is $pK_a = 2.6$, and consequently while the majority of them will be protonated at pH2, some negative residues will still be present. As such, it is expected that these peptides will bind electrostatically to the mucin molecules at both pH levels, although the strength of these interactions is likely reduced at pH2 owing to the more neutral charge of the mucin molecules.

Peptides were dissolved in H7 buffer (20 mM HEPES, 20 mM NaCl, pH7) to a final concentration of 300 µM prior to use, and added to 1 wt % MUC5AC gels at pH2 and pH7 at a volume ratio of 1 : 20 peptide solution: MUC5AC gel. The resulting mixture was subsequently vortex mixed and then loaded into a capillary tube and allowed to sit for approximately 2 – 2.5h prior to imaging. As before, imaging was performed using a Zeiss LD Plan-Neofluar 10x/0.4 Corr Ph2 objective lens and a Hamamatsu Flash 4.0 C11440-22CU camera.

In Figure 4.3.12, images taken from within the capillary tubes are shown for 1 wt % MUC5AC gels at pH2 (left) and at pH7 (right).

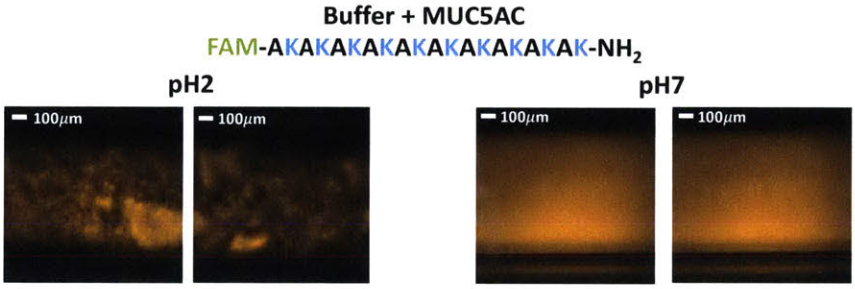

Figure 4.3.12: Images of the 1 wt % MUC5AC gels at pH2 (left) and pH7 (right) with a 300 µM solution of the positively charged, fluorescent reporting peptide $(AK)_{10}$-NH_2 added at a volume ratio of 1 : 20 peptide solution: MUC5AC gel.

As can be seen, significant differences are apparent in the gel structures at both pH levels. In the MUC5AC gels at pH7, uniform fluorescence is observed, suggesting a uniform distribution of mucin molecules. This is consistent with the results from microrheology that suggest that these gels are relatively homogeneous. In contrast, at pH2, large degrees of heterogeneity are observed, with patches of various sizes and fluorescence intensities interspersed with seemingly mucin-free regions.

In order to verify that these differences were truly due to the presence of mucins and not simply the different pH levels, these experiments were repeated without mucins by adding the peptide solutions at the same volume ratio to the 10 mM phosphate and sodium citrate buffers alone at both pH levels. As can be seen in Figure 4.3.13, homogeneous fluorescence was observed in the absence of MUC5AC and both pH2 and pH7, suggesting that the heterogeneous microstructure visualized in the left panel of Figure 4.3.12 is truly owed to the presence of the mucin molecules.

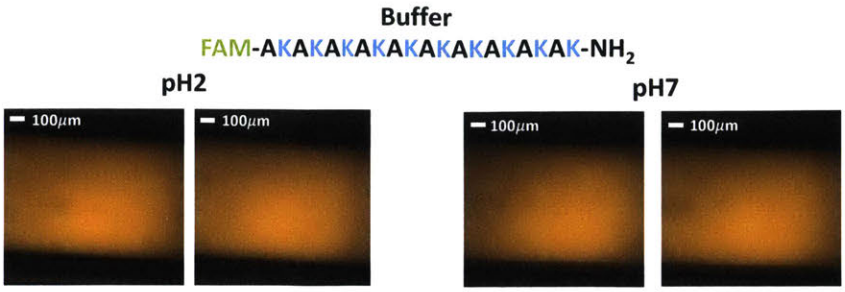

Figure 4.3.13: Control images of the pH2 (left) and pH7 (right) 10 mM phosphate and sodium citrate buffers only with a 300 μM solution of the positively charged, fluorescent reporting peptide $(AK)_{10}$-NH_2 added at a volume ratio of 1 : 20 peptide solution: buffer.

4.3.7 Section summary

In summary, motivated by the disagreements between the micro- and macrorheological responses of MUC5AC gels observed in Section 4.2, we have performed an in depth study of the structure of the mucin network of MUC5AC gels at pH2 and pH7 using a combination of rheological and imaging tools. These rheological experiments were further placed in context by comparing the results with those obtained in solutions of the charged, synthetic polymer CMC.

The macrorheology of MUC5AC gels was found to be pH-sensitive for mucin concentrations ranging from $0.5 - 3$wt %, with the gels at pH2 being stiffer than those measured at pH7. In all cases, the viscoelastic moduli responded as weak power laws of the oscillation frequency, as was noted in Section 4.2. In contrast, CMC solutions were minimally pH-responsive, and exhibited predominantly liquid-like responses well described by a linear viscoealstic Maxwell model over the same range of concentrations. These findings suggest that charge-screening and correspondingly polymer chain flexibility alone cannot account for the significant pH-responsiveness of MUC5AC gels, and suggests that other mechanisms, such as those discussed in Section 4.2.2 including the creation of hydrophobic cross-links, are at play.

Next, we explored three possible mechanisms for the breakdown of the GSER in order to explain the discrepancy between the micro- and macrorheological response of MUC5AC gels. First, we studied non-continuum effects and the effect of probe size on the microrheology of 1 wt % CMC and MUC5AC solutions at pH2 and pH7. For CMC solutions at both pH levels and MUC5AC at pH7, probe size effects were present but small, as characterized by an apparent viscosity determined for each particle size. In contrast, the MUC5AC gels at pH2 exhibited substantial probe size effects. Specifically, the mobility of smaller 200 nm and 500 nm particles was significantly reduced compared to $1 - 5$μm particles when particle size was controlled for. Another experimental subtlety regulating the apparent MSD of the smallest probes was the minimum trajectory length requirement imposed when tracking the particles. As the minimum trajectory length was increased, the apparent MSD of the particles decreased as a result of the exclusion of the fastest particles, presumably located within the mucin-poor regions of the phase-separated gel, from the retained population.

As a second mechanism leading to the breakdown of the GSER, we investigated the effect of particle-mucin interactions by performing microrheological experiments with 500 nm and 1 µm PEG-ylated particles in 1 wt % MUC5AC gels at pH2 and pH7. These particles had previously been reported to have a nearly neutral zeta potential at both pH2 and pH7, as well as to be non-adherent to bovine submaxillary mucins using a mucin adsorption assay. At pH2, a small increase in mobility of the PEG-ylated particles was observed for both particles in comparison to the carboxylated particles, while at pH7 an increase was seen for 1 µm particles but the MSD curves at 500 nm were nearly coincident. Therefore, we can conclude from these results that the effect of particle surface chemistry on the microrheological response in MUC5AC gels is not negligible. However, it is important to note that because, in general, sticking interactions between particles and their environment reduce particle mobility (as confirmed by these experiments and the increased mobility of the PEG-ylated particles), such interactions cannot explain the sizable *underprediction* of the macroscopic viscoelastic moduli using SPT in MUC5AC gels at pH2 (see Figure 4.2.1a).

As a last rheological experiment, we assessed the effect of sample aging as a possible mechanism for the breakdown of the GSER by repeating the microrheological measurements using 1 µm carboxylated probes in 1 wt % MUC5AC gels at pH2 and pH7 after a delay of several hours. At pH2, very little effect of aging was observed, while at pH7 particle mobility was increased, possibly due to higher levels of protease activity under neutral pH conditions. Ultimately, however, we can conclude that aging effects are unlikely to be able to explain the large disagreement between the micro- and macrorheology of MUC5AC gels, at least within the time frames considered.

Finally, in order to try to visualize the network changes leading to these microrheological observations, we added positively charged fluorescent peptide probes to 1 wt % MUC5AC gels at pH2 and pH7. These cationic probes have previously been shown to bind electrostatically to negatively charged mucin molecules at pH7 [99]. Indeed, striking differences were observed in the fluorescence patterns, which were interpreted to represent the spatial configuration of the mucin network, between the two pH levels. At pH7, the sample appeared uniformly fluorescent, while at pH2, large degrees of heterogeneity are observed, with patches of various sizes and fluorescence intensities interspersed with seemingly mucin-free regions.

Therefore, from all of these results and those in Section 4.2, we summarize our emerging picture of the MUC5AC gels at 1 wt % and pH2 in Figure 4.3.14 below. As a result of the biochemical processes including the destruction of salt bridges and the formation of additional hydrophobic cross-links [7], the MUC5AC gel microphase separates at pH2 into regions of varying apparent viscosity η_{app}. Based on the particle mobility measured, it appears that some of these regions are sufficiently soft to be accessible to all probe particles used, and hence we can estimate a characteristic mesh size for these regions as $\xi \gtrsim 5\,\mu m$. Because of the apparent reduced mobility of particles of size 500 nm and smaller, it appears that there exist stiffer regions of the MUC5AC gel at pH2 that are accessible to those particles but not to the larger ones, which sets and upper bound on the mesh size for these domains. The fact that the viscoelastic moduli determined from the smallest particles (200 nm) with the longest minimum trajectory length requirement imposed still underpredict the macroscopic moduli measured using SAOS (Figure 4.3.9) suggests that there exist even stiffer regions of the gel (with a characteristic mesh size smaller than 200 nm) that are inaccessible to all of

the probe particles but contribute significantly to the overall macrorheological response.

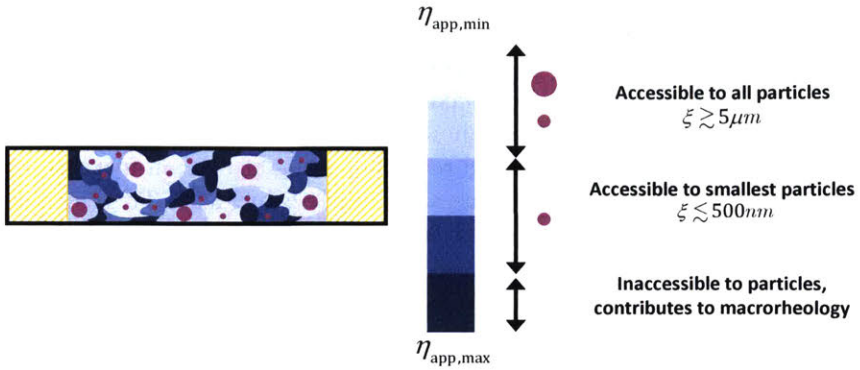

Figure 4.3.14: Schematic of the 1 wt % MUC5AC gel network at pH2 inspired by the image in [19], in turn adapted from [121]. The gel is microphase separated into regions of varying apparent viscosity η_{app}, which are either soft enough to be accessible to all particles (i.e. $\xi \gtrsim 5\,\mu m$), the smallest particles (i.e. $\xi \lesssim 500\,nm$), or stiff enough to be accessible to no particles at all. Importantly, however, these stiffest regions still provide an important contribution to the macrorheological response of the gel.

Ultimately, while our understanding of this system is far from complete, we expect that an improved insight into the structure of mucin networks and the principal interaction mechanisms at play will be particularly important in a number of biological contexts, including for understanding how the rheo-mechanical properties of mucus hydrogels are altered by a number of environmental factors in the context of both regular physiological function as well as by pathological and therapeutic agents.

5 | Development of a constitutive model for assessing the temporal stability of saliva

5.1 Introduction

The development of a nonlinear viscoelastic constitutive model that can qualitatively describe the rheology of a sticky or physically-associating reversible network of polymer chains has applications to a wide variety of biological problems. For instance, protein and polysaccharide interactions in animal cytoskeletons and plant cell walls, respectively, have been accurately described using Glassy Worm-Like Chain Models [122], while DNA/protein interactions and cell division are highly dependent on interactions with the surrounding tissue network [123, 124]. It is generally not possible to describe the rheology and mechanics of such complex biopolymeric systems by considering the dynamics of the constituent chains in isolation [123, 125]. However, the macroscopic rheological response of mucus and other bodily fluids has been successfully modeled by incorporating associative network considerations (see for instance the work by Ewoldt et al. on Hagfish slime [126] or by Broedersz et al. on actin networks [127]). The 'sticky' elements of the biological macromolecules in these systems originate from a number of different association types, including hydrogen bonding, ion complexation, disulphide linkages, and local crystallization domains [128]. Physical associations between chain segments can generally be accounted for by confining the segment ends to lie in an energy well of width r_c and depth ΔG [122, 123, 125, 129] that depends on the type of interactions in the system and the level of tension in the chain segments that form the network. As the elastically active network is strained by extensional deformation and individual segments are stretched, the energy well they must overcome becomes increasingly shallow, and the rate of chain dissociation increases. This is analogous to rejuvenation concepts in soft glasses, where thermally activated jumping between local traps occurs [122].

The particular physically associating network of interest to this study is the salivary network; a glycoprotein-based hydrogel formed by a complex set of interactions between the constituent mucin chains including charge-mediated carbohydrate-carbohydrate interactions, weak calcium-mediated physical cross-links, stronger disulphide bonds, and hydrophobic interactions [76, 77, 130]. This complex network results in saliva being highly viscoelastic, and indeed without the ability of saliva to form viscoelastic thin films, speech and swallowing would be severely impaired, and oral decay would be inevitable [76, 131, 132]. Characterization and quantification of saliva viscoelasticity is also becoming increasingly important as a diagnostic tool, largely as a result of the ease and safety of obtaining fluid samples,

as compared to more commonly used biofluid sources such as blood [133]. For instance, Basilevsky et al. have explored the degradation of sputum upon exposure to certain bacteria as measured through changes in its elastic properties [11], while Zussman et al. have noted that differences in saliva viscoelasticity between teenagers and the elderly may explain why the most common dental health issues plaguing these two age groups differ [134].

As early as 1922, however, in his ground-breaking studies of saliva's *potere filante* (or 'filament forming potential'), Aggazzotti observed that the rheological properties of saliva are not constant with time [135]. In a series of experiments, he found that both the shear viscosity (as measured with a viscometer) and the extensional properties of saliva (as measured by the maximum length of a fluid filament that was formed by stretching a sample from the end of a capillary tube) decreased as the age of the sample (or time since it was extracted from the mouth) increased. He further noted that the solubility of the salivary components upon addition of acetic acid increased with sample age [135]. At the time, Aggazzotti attributed these observations to "changes in the physical state, the molecular constitution, of the mucin" [135]. More recent studies on the size of salivary proteins by Esser et al. [133] measured using Surface Enhanced Laser Desorption/Ionization Time of Flight Mass Spectrometry (SELDI-TOF-MS) have shown quantitatively that with time, enzymatic and biological activity lead to degradation of the mucin molecules contained in the saliva. Despite this, the vast majority of the literature on the shear and extensional rheological properties of saliva makes no mention of the age of the sample used, which, in addition to the disparity in measurement techniques, may help to explain why reported values differ so greatly [76].

In this chapter, we present data on the shear properties (steady shear viscosity and SAOS measurements of the linear viscoelasticity) and extensional rheology (as measured with a Capillary Breakup Extensional Rheometer (CaBER)) of saliva at six different sample age times ($0\,\text{h} < t_{\text{age}} < 24\,\text{h}$). We show that the shear rheology remains largely unchanged, while the extensional properties of saliva deteriorate completely over the time period in question. We quantify these changes in the extensional rheology through the development of a Sticky Finitely Extensible Network (SFEN) model, extended from the work of Tripathi et al. for synthetic associative polymers [129], in which saliva is modeled as a physically associating network of finitely extensible elastic segments. We show that this model can accurately describe the capillary thinning and filament rupture behaviour of saliva using parameters that are consistent with the biological properties of the mucin chains. This model can systematically account for the observed temporal changes through a progressive decrease in the molecular weight of the primary polymer component (MUC5B) in the mucin network.

5.2 The Salivary Network

The viscoelastic properties of whole saliva can be largely attributed to its principal structural element: the high molecular weight mucin MUC5B [76], introduced in Section 3.1 and depicted schematically in Figure 5.2.1a. The intact MUC5B molecule found in secretions consists of $50 - 100$ macromonomer subunits [70], which we term 'muc-mers', each with a molecular weight of approximately $M_{W,MUC} \approx 2\,\text{MDa}$ [70], assembled via disulphide bonds (shown schematically as light blue filled circles in Figure 5.2.1a) in a linear fashion, leading

to an overall estimated molecular weight of $M_W \approx 150\,\text{MDa}$ [70]. The overall supramolecular mucin network, first presented in Figure 3.1.2c and reproduced in a simplified form in Figure 5.2.1b is formed by topological entanglements and hydrophobic cross-linking interactions between the non-glycosylated regions of these enormous biopolymers, as well as other weak associations such as ion complexation and electrostatic repulsion [4, 76].

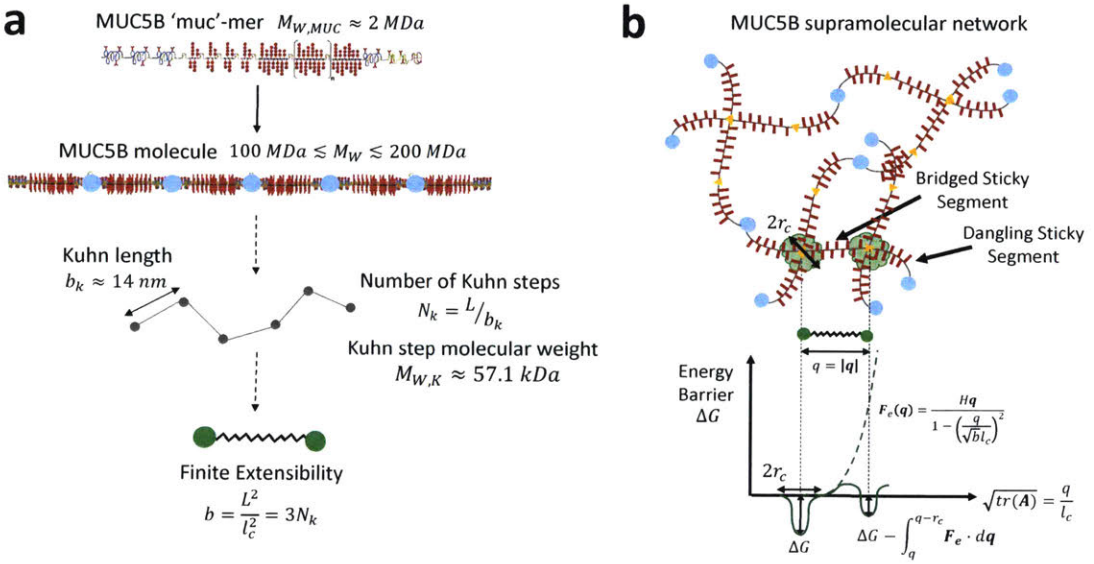

Figure 5.2.1: Schematic description of the MUC5B mucin network parameters used in this chapter. (a) Coarse-graining of an individual MUC5B molecule to a bead-spring chain. The schematic representations of the MUC5B muc-mer and macromonomer are reproduced from [4] with permission from Elsevier. (b) Organization of the MUC5B supramolecular network with both dangling and bridged sticky segments, as well as a schematic representation of the SFEN parameters relevant for considerations of network formation and inter-chain associations.

To simplify the problem, we coarse-grain the mucin macromonomer structure by approximating the chains to be random walks of N_k Kuhn steps of Kuhn length b_k [23]. The persistence length of MUC5AC, which is a genetic relative of MUC5B showing significant homology in its non-glycosylated domains [66], has been estimated by Cao et al. at pH7 using Dynamic Light Scattering to be approximately $l_p = 7\,\text{nm}$ [102]. From this result, we can obtain an estimate for the Kuhn length of MUC5B from the relationship $b_k = 2l_p = 14\,\text{nm}$. Additionally, from the fully extended MUC5B muc-mer length of $Q_{0,MUC} = N_{k,MUC} b_k = 500\,\text{nm}$ measured by Kesimer et al. [70], the number of Kuhn steps per muc-mer and their molecular weight $M_{W,k}$ can be approximated as $N_{k,MUC} \approx 35$ and $M_{W,k} = M_{W,MUC}/N_{k,MUC} \approx 57.1\,\text{kDa}$. Finally, the finite extensibility b of an intact MUC5B molecule with n_c muc-mers and a resulting molecular weight of $M_W = n_c M_{W,MUC}$, which is defined as the square of the ratio of the fully extended chain length to its equilibrium size, can be calculated from $b = 3M_W/M_{W,k} = 3N_k$ [23]. This results in a finite extensibility of $b \approx 8000$ based on the initial molecular weight of the entire MUC5B molecule, $M_W \approx 150\,\text{MDa}$.

Following Rubinstein and Colby [136], the plateau modulus of a polymer network with well defined entanglement and cross-link molecular weights ($M_{W,e}$ and $M_{W,x}$ respectively) is given by

$$G \approx \rho k_B N_A T \left(\frac{1}{M_{W,e}} + \frac{1}{M_{W,x}} \right),$$

where ρ is the density of the polymer, k_B is the Boltzmann constant, N_A is Avogadro's number, and T is the temperature. In the case of mucins, however, the structural and association details of the MUC5B network are not yet well understood, and consequently $M_{W,e}$ and $M_{W,x}$ are not well-defined [4, 137]. In this case, we employ the Rubinstein and Colby definition for the plateau modulus G_s of a general polymer network with apparent strand molecular weight $M_{W,s}$ [136], allowing us to obtain an estimate for the molecular weight of a sticky segment as

$$M_{W,s} = \frac{c k_B T N_A}{G_s}, \tag{5.1}$$

where c is the concentration of MUC5B which has been determined by Raynal et al. to be $c = 233\,\mu g\,ml^{-1}$ in saliva [81]. In general, the plateau modulus of a typical biopolymeric gel is not as clearly identifiable as that for a polymer melt, ${G_N}^0$ [138]. Nevertheless, we can estimate G_s from SAOS data, and with this in place, the number of physical interactions, or 'sticky' points, per mucin macromonomer follows immediately as $z = M_W/M_{W,s}$. Finally, we fix the interaction strength of these sticky sites that assemble the physically associated network at $\Delta G \approx 6k_BT$; an average value for weak physical interactions such as hydrophobic interactions and electrostatic repulsion [139].

With these biological parameters in place, in the section to follow, we develop a model that respects these molecular dimensions and allows us to investigate the nonlinear properties of mucin solutions, particularly at the large Hencky strain values relevant to CaBER experiments near filament breakup.

5.3 Model Description

We follow the approach of Tripathi et al. [129], who studied the nonlinear shear and extensional rheological properties of hydrophobically modified ethoxylate-urethane (HEUR) telechelic systems, to model the salivary network. This model, extended from the ideas of Tanaka and Edwards [140, 141] and Vaccaro and Marrucci [142], is particularly suitable as it focuses specifically on the nonlinear rheological properties that dominate filament thinning measurements, and can account for a wide range of interaction types and number of interaction sites [129]. Telechelic HEUR polymers contain both hydrophilic central regions and hydrophobic end groups which physically associate with one another in flower-like micelles to minimize their exposure to the surrounding aqueous environment [129], introducing the 'sticky' character to the network. We introduce an analogous term to capture the physical interactions in the salivary network, and allow for destruction and reformation of network junctions at these points [129].

The number density of elastically active segments (meaning those that form inter-chain bridges and participate in the network) is denoted by ν and depends on the depth of the

energy well ΔG through the expression [140]

$$\nu = n\left(\frac{\exp\left(\Delta G/k_BT\right)}{1+\exp\left(\Delta G/k_BT\right)}\right) \tag{5.2}$$

where $n = cN_A/M_{W,s}$ is the total number density of sticky segments. When ΔG is large compared to the thermal energy, $\nu \approx n$ and all chain segments are considered active and able to contribute to the accumulation of polymer stresses in the network [129].

Following Tanaka and Edwards [140], we define the exit rate of the network junctions, Ω_{exit}, as the product of the natural thermal vibration frequency Ω (where $10^8\,\text{Hz} < \Omega < 10^{10}\,\text{Hz}$) and the quasi equilibrium likelihood of reaching a transition state given the activation barrier ΔG, i.e.

$$\Omega_{exit} = \Omega \exp\left(-\Delta G/k_BT\right). \tag{5.3}$$

The depth of the relevant energy well ΔG under flow depends, however, on the extent to which the chain segments are stretched, which can be characterized by the end-to-end vector $\boldsymbol{q}$ of each sticky segment. These concepts related to network formation and inter-chain associations are depicted schematically in Figure 5.2.1b.

The fraction of bridged chains as a function of chain stretch and time can be specified by a distribution function $\Psi_a(\boldsymbol{q},t)$. Ψ_a can also be defined in terms of the probability density function ψ_a for a single active chain through $\Psi_a = \nu_a\psi_a$ where $\nu_a \leq \nu$ is the number of *bridged*, elastically active chain segments (and hence $(\nu - \nu_a)$ is the number of *dangling* elastically active chain segments), and ψ_a is normalized by $\int \psi_a dV = 1$. Unlike Tripathi et al. [129], we consider only the bridged chains (or species A in their work) to contribute to the stress tensor and we neglect contributions from temporarily dangling segments (or species B). Since our model allows for both network dissociation and rejoining, the number of bridged chains ν_a consequently varies with the state of stress in the network.

By considering the interactions of the junction points with the flow (see discussions by van den Brule and Hoogerbrugge [143] and Bird et al. [23]), the conservation equation for the probability distribution function can be written in the form of a Smoluchowski expression

$$\frac{\partial \Psi_a}{\partial t} = -\frac{\partial}{\partial \boldsymbol{q}} \cdot \left[(\nabla \boldsymbol{v})^T \cdot \boldsymbol{q}\Psi_a\right] - M(q,t)\Psi_a + \tilde{L}(q,t), \tag{5.4}$$

where $M(q,t)$ and $\tilde{L}(q,t)$ are the destruction and creation rate of junction points, respectively. Multiplying Equation (5.4) by the second moment tensor $\boldsymbol{qq}$ and integrating over configuration space [129] yields

$$\langle \boldsymbol{qq}\rangle_{(1)} = -M\langle \boldsymbol{qq}\rangle + \hat{L}\boldsymbol{I}, \tag{5.5}$$

where $\hat{L} = 4\pi/3\int_0^\infty \tilde{L}q^4 dq$ [23], $\boldsymbol{I}$ is the identity tensor, and the subscript (1) denotes the upper convected derivative defined as

$$\langle \boldsymbol{qq}\rangle_{(1)} = \frac{D\langle \boldsymbol{qq}\rangle}{Dt} - \{(\nabla \boldsymbol{v})^T \cdot \langle \boldsymbol{qq}\rangle + \langle \boldsymbol{qq}\rangle \cdot (\nabla \boldsymbol{v})\}. \tag{5.6}$$

Finally, by expressing the stretching of the network in terms of a microstructural defor-

mation tensor defined as

$$\boldsymbol{A} = \frac{\langle \boldsymbol{qq} \rangle}{l_c^2}, \tag{5.7}$$

where $l_c = \sqrt{N_k} b_k / \sqrt{3}$ is the characteristic equilibrium size of an entire network macromonomer [129], we arrive at a differential equation governing the evolution of $\boldsymbol{A}$

$$\boldsymbol{A}_{(1)} = -M\boldsymbol{A} + L\boldsymbol{I}, \tag{5.8}$$

where $L = \hat{L}/l_c^2$. Following the approach originally proposed by Tanaka and Edwards [140, 141] and later extended by Vaccaro and Marrucci [142] and Tripathi et al. [129], we can incorporate finite extensibility mediated network behaviour by defining the network destruction rate to be the (nonlinear) product of the natural thermal vibration frequency and a stretch-dependent exit frequency, i.e.

$$M(\boldsymbol{q}) = g(c, M_{W,s})\Omega \exp\left(-\frac{1}{k_B T}\left\{\Delta G - \int_q^{q-r_c} \boldsymbol{F_e} \cdot d\boldsymbol{q}\right\}\right), \tag{5.9a}$$

where $g(c, M_{W,s})$ is a scaling function determined from equilibrium measurements that depends on the chain segment concentration and molecular weight and $\boldsymbol{F_e}(\boldsymbol{q})$ is the stretch-dependent tensile elastic force acting on a segment in the network. Note that for the remainder of this chapter, to simplify notation since the concentration and strand molecular weight are not changed during our experiments, we combine $g(c, M_{W,s})$ and the network exit rate Ω_{exit} from Equation (5.3) into a single, scaled timescale associated with the lifetime of network junctions: $\lambda_{exit} = 1/(g\Omega_{exit})$. This allows us to rewrite Equation (5.9a) as

$$M(\boldsymbol{q}) = \frac{1}{\lambda_{exit}} \exp\left(\frac{1}{k_B T}\left\{\int_q^{q-r_c} \boldsymbol{F_e} \cdot d\boldsymbol{q}\right\}\right). \tag{5.9b}$$

The upper limit of integration in Equation (5.9b) represents the distance that a stretched network segment with length $q = |\boldsymbol{q}|$ must be displaced through to escape the energy barrier of width r_c associated with a sticky domain, as illustrated in Figure 5.2.1b. Representing the chain segments as finitely-extensible non-linear elastic (FENE) springs, we can express the deformation-dependent force using the Warner expression [129] as

$$\boldsymbol{F_e} = \frac{H\boldsymbol{q}}{1 - \left(q/(\sqrt{b}l_c)\right)^2}, \tag{5.10}$$

where $H = k_B T / l_c^2$ is the spring constant [144] and $Q_0 = \sqrt{b} l_c$ is the fully extended length of the macromonomer chain. Substitution of this result into Equation (5.9b) and applying the usual Peterlin closure approximation allows us to arrive at an expression for the ensemble average dissociation rate

$$M(tr(\boldsymbol{A})) = \frac{1}{\lambda_{exit}}\left[\frac{1 - \left(\sqrt{tr(\boldsymbol{A})} - X\right)^2/b}{1 - tr(\boldsymbol{A})/b}\right]^{b/2}, \tag{5.11}$$

where $X = r_c/l_c$ is the width of the energy barrier normalized by the equilibrium chain size and $tr(\boldsymbol{A})$ indicates the trace.

To balance the destruction rate of elastically active segments ($M(tr(\boldsymbol{A}))$), a creation term denoted by L in Equation (5.8) is required [37]. We follow Vaccaro and Marrucci [142], as well as Ng et al. [145] and Ewoldt et al. [126], and choose a constant stretch-independent creation term L such that under no flow conditions, the distribution is stationary with $\boldsymbol{A}_{(1)} = \boldsymbol{0}$. We thus obtain

$$L = \frac{1}{\lambda_{exit}} \left[\frac{1 - (\sqrt{3} - X)^2/b}{1 - 3/b} \right]^{b/2}. \tag{5.12}$$

which for large $b \gg 3$ simplifies to $L \approx \lambda_{exit}^{-1}$. The microstructural deformation tensor $\boldsymbol{A}$ is related to the polymer stress tensor $\boldsymbol{\tau}_p$ through the Kramers expression [23]

$$\boldsymbol{\tau}_p = -nkT[f(tr(\boldsymbol{A}))\boldsymbol{A} - \boldsymbol{I}], \tag{5.13}$$

where $f(tr(\boldsymbol{A}))$ is the FENE term that accounts for finite extensibility within the chain segments. Using the Peterlin closure approximation [23], we can write the following expression for the ensemble average stretch in the network

$$f(tr(\boldsymbol{A})) = \frac{1}{1 - tr(\boldsymbol{A})/b}. \tag{5.14}$$

At equilibrium ($\boldsymbol{\tau}_p = \boldsymbol{0}$), Equations (5.13) and (6.12) imply that $tr\boldsymbol{A}_{eq} = 3/(1 + 3/b) \approx 3$ for the large values of the finite extensibility parameter b used in this study.

Equations (5.8)-(6.12) represent a set of evolution equations for the polymeric contribution to the stress in a Sticky Finitely Extensible Network which we refer to as SFEN for compactness. The evolution equation for the number density of bridged active segments is found by integrating Equation (5.4) over configuration space [129], yielding

$$\frac{d\nu_a}{dt} = -M\nu_a + L(\nu - \nu_a). \tag{5.15}$$

Further, for the specific case of a time-varying shear-free or elongational flow, the SFEN equations for the number density of bridged elastically active segments and the non-zero individual components of the microstructural deformation tensor $\boldsymbol{A}$ become:

$$\frac{dA_{zz}}{dt} = 2\dot{\epsilon}A_{zz} - MA_{zz} + L \tag{5.16}$$

$$\frac{dA_{rr}}{dt} = -\dot{\epsilon}A_{rr} - MA_{rr} + L \tag{5.17}$$

where $\dot{\epsilon}(t)$ is the instantaneous strain rate imposed by the kinematics of the flow under consideration. For the various specific elongational flow types considered in the sections to follow, the time evolution of flow stresses are determined by solving the governing SFEN equations ((5.15)-(5.17)) in combination with the appropriate expressions for the flow kinematics, where the junction destruction, $M(tr(\boldsymbol{A}))$, and creation, L, rates are given by Equations (5.11) and (5.12), respectively. We note that in the limit of a steady state shear flow of vanishing strength, it is straightforward to show that the steady state shear viscosity predicted by the SFEN model is $\eta_0 = \eta_s + \nu k_B T \lambda_{exit}/2$, where η_s is the solvent viscosity and the steady state value of the number of bridged active chains is $\nu_{a,eq} = \nu/2$.

5.3.1 Response of the SFEN model under simple elongational flow conditions

To explore the nonlinear response of this model for a physically associated biopolymer network, we first consider a simple, homogeneous, elongational flow at constant strain-rate $\dot{\epsilon}_0$. In Figure 5.3.1a, we plot the predicted evolution in the transient extensional viscosity $\eta_e^+ = (\tau_{zz} - \tau_{rr})/\dot{\epsilon}_0$ normalized by the steady state elongational viscosity $\eta_{e,0} = 3\eta_0$ as a function of the accumulated strain $\epsilon = \dot{\epsilon}_0 t$ at various values of the Weissenberg number $Wi = \dot{\epsilon}_0 \lambda_{exit}$. In Figure 5.3.1b, this same information is presented as a three-dimensional surface as a function of dimensionless time and Weissenberg number. The trajectories in Figure 5.3.1a correspond to horizontal lines in Figure 5.3.1b at each of the values of Wi indicated.

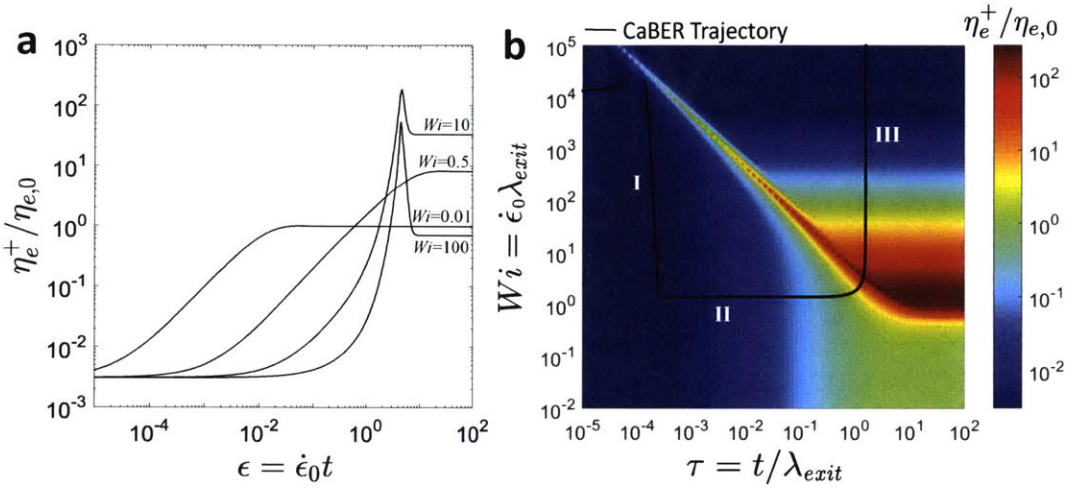

Figure 5.3.1: (a) SFEN model predictions for the normalized extensional viscosity $\eta_e^+/\eta_{e,0}$ under simple, homogeneous, elongational flow conditions at constant strain-rate $\dot{\epsilon} = \dot{\epsilon}_0$ as a function of the total accumulated strain $\epsilon = \dot{\epsilon}_0 t$ for $Wi = \dot{\epsilon}_0 \lambda_{exit} = 0.01, 0.5, 10$, and 100. (b) Surface plot of the SFEN model predictions for the normalized extensional viscosity $\eta_e^+/\eta_{e,0}$ as a function of both Wi and the non-dimensionalized time $\tau = t/\lambda_{exit}$ under simple, homogeneous elongational flow conditions (coloured surface) as well as the trajectory followed during a filament thinning (CaBER) experiment for which $\dot{\epsilon} = -(2/R)\, dR/dt$ (solid black line). The regions indicated with roman numerals in the CaBER trajectory correspond to viscocapillary thinning (I), elastocapillary thinning (II), and the terminal thinning regime (III) [146]. In both (a) and (b), the chosen parameters correspond to those determined for saliva at $t_{age} = 0\,\text{h}$ in Section 5.4: $b = 8000$, $X = 0.02$, $\Delta G = 6k_BT$, $\lambda_{exit} = 0.26\,\text{s}$, $\eta_s/\eta_0 = 0.003$, and $E_c = \nu k_B T/(\sigma/R_0) = 0.02$.

At time $t = 0^+$, there are no accumulated stresses in the polymer network and consequently $\eta_e^+(t = 0^+) = 3\eta_s$, with the solvent contributing exclusively to the extensional viscosity. As the accumulated strain increases the polymeric contributions to the stress grow. For $Wi = \dot{\epsilon}_0 \lambda_{exit} \leq 0.5$, the chains do not stretch sufficiently for dissociation to become significant, and the extensional viscosity plateaus at the expected equilibrium value of $\eta_e^+(t \to \infty) = \eta_{e,0} = 3\eta_0$. As the strain rate $\dot{\epsilon}_0$ is increased, it is clear that the coil-stretch

transition is approached and the extensional viscosity changes dramatically at an approximately constant value of the product $(Wi)_c(\tau) = (\dot{\epsilon}_c\lambda_{exit})(t/\lambda_{exit}) = \dot{\epsilon}_c t = \epsilon_c$ corresponding to the diagonal 'line' at approximately 45° formed by the surface contours in Figure 5.3.1b. At larger strains $\epsilon > \epsilon_c$ the extensible segments of the network begin to stretch closer to their full extent, and the nonlinear terms associated with finite extensibility and network dissociation come increasingly into play. This is seen in Figures 5.3.1a and 5.3.1b as an initial strain hardening and increase in the extensional viscosity η_e^+ followed by a dramatic rupture of the network and decrease of the extensional viscosity at a large Hencky strain $\epsilon_c \approx 4$. We note that similar extensional viscosity overshoots in highly branched but non-physically associated LDPE networks have been modeled by Hoyle et al. [147].

5.3.2 Response of the SFEN model during Capillary Breakup Extensional Rheometry (CaBER)

We now consider the response of the model during a filament thinning experiment in a CaBER device. Unlike the constant homogeneous strain rates considered above, the dynamics of the problem are specified by assuming a time-varying and axisymmetric uniaxial elongational flow $[v_r = -\frac{1}{2}\dot{\epsilon}(t)r, v_z = \dot{\epsilon}(t)z]$ in a cylindrical filament of radius $R(t)$, from which it follows that the time-varying strain rate is given by

$$\dot{\epsilon}(t) = -\frac{2}{R}\frac{dR}{dt}. \tag{5.18}$$

Following [146], we can combine force balances in the radial and axial directions to eliminate the unknown pressure inside the thinning filament and obtain the following force balance, in which the capillary stress is balanced by a combination of the extensional stress difference resulting from the viscous solvent and the deforming and physically associated polymer network:

$$\frac{\sigma}{R} = 3\eta_s\dot{\epsilon} + (\tau_{p,zz} - \tau_{p,rr}), \tag{5.19}$$

where σ is the surface tension of the fluid. Using the definition of the strain rate in Equation (5.18), the microstructural deformation terms A_{zz} and A_{rr} (Equations (5.16) and (5.17)) and the governing force balance (Equation (5.19)) can be written in the form

$$\frac{dA_{zz}}{dt} = -\frac{4}{R}\frac{dR}{dt}A_{zz} - MA_{zz} + L, \tag{5.20}$$

$$\frac{dA_{rr}}{dt} = \frac{2}{R}\frac{dR}{dt}A_{rr} - MA_{rr} + L, \tag{5.21}$$

$$\frac{\sigma}{R} = -\frac{6}{R}\frac{dR}{dt}\eta_s + \nu_a k_B T f(A_{zz} - A_{rr}), \tag{5.22}$$

where the junction destruction, $M(tr(\boldsymbol{A}))$, and creation, L, rates are given by Equations (5.11) and (5.12), respectively.

The resulting equation set comprises a stiff initial value problem that can be integrated in time (e.g. using Matlab from $R = R_0$ and $\nu_a = \nu_{a,eq}$ at $t = 0$) for different initial conditions to compare with experimental measurements (as has been done previously in [148, 149, 150, 151, 152] for other constitutive models). As the filament thins under capillary

pressure, the strain rate $\dot{\epsilon}(t)$ given in Equation (5.18) and total Hencky strain $\epsilon(t)$ correspondingly evolve in time. In Figure 5.3.1b, we superimpose a CaBER trajectory (solid black line) labeled with regions (I)-(III) onto the three-dimensional extensional viscosity surface, using the same physical parameters as for the simple elongational flow curves. We must also specify an elastocapillary number which compares the ratio of elastic to capillary forces, and an appropriate value for mucin filaments with $\sigma \approx 72\,\text{mN m}$ and $R_0 \approx 0.5\,\text{mm}$ is $E_c = \nu k_B T/(\sigma/R_0) = 0.02$. We can define three general dynamical regimes as shown in Figure 5.3.1b: (I) viscocapillary thinning during which the solvent extensional stresses predominantly balance the capillary pressure; (II) a constant strain-rate regime of elastocapillary thinning (termed the 'middle elastic time' by Entov and Hinch [146]) during which axial polymer stresses balance capillary pressure but the chains remain far from their finite extensibility limit ($b^{(\text{II})} \gg A_{zz}^{(\text{II})} \gg A_{rr}^{(\text{II})}$, $f^{(\text{II})} \approx 1$); and (III) a terminal regime during which the polymers approach their maximum extension and filament rupture occurs [146]. As can be seen, following a rapid initial strain hardening and decrease in the strain-rate $\dot{\epsilon}$ associated with rapid filament thinning during the viscocapillary regime (I), the strain-rate and extensional viscosity both plateau at nearly constant values during regime II, and finally, as the chains approach their maximum extension (regime III), the elastic forces become large and the destruction rate $M(tr(\boldsymbol{A}))$ (Equation (5.11)) diverges, leading to a rapid destruction of the network and filament rupture. In this final region (III) the extensional viscosity continues to decrease with increasing strain as the number of elastically active chains decrease until ultimately the extensional viscosity is reduced to the initial solvent contribution.

Constant strain-rate elastocapillary thinning (Regime II)

In order to use our SFEN model to interpret experimental CaBER data with salivary mucins, the significance of the filament thinning rate, typically extracted from the time constant associated with the exponential radius decay characteristic of regime II [146], must be understood in the context of the SFEN parameters.

For many moderate molecular weight systems with finite chain extensibility, there is already significant axial microstructural stretch incurred in the system by the time this regime occurs following the initial viscocapillary thinning regime (I). However the inequality $A_{zz} \ll b$ still holds (see for instance Wagner, et al. [150]). Under these conditions, a Taylor series expansion can be used to simplify Equation (5.11) for the destruction rate to the form

$$M^{(\text{II})}(tr(\boldsymbol{A})) \approx \frac{1}{\lambda_{exit}}\left[1+\delta\right], \tag{5.23}$$

where the superscript II indicates explicitly the elastocapillary regime (II) and

$$\delta = \frac{\sqrt{tr(\boldsymbol{A})}Xb}{b - tr(\boldsymbol{A})} \approx \frac{\sqrt{A_{zz}^{(\text{II})}}Xb}{b - A_{zz}^{(\text{II})}}. \tag{5.24}$$

In the limit of infinitely extensible springs ($b \to \infty$) or negligible sticky effects ($X \to 0$), $\delta \to 0$. For finitely extensible springs, Wagner et al. [150] provide an implicit analytical expression for the axial microstructural deformation $A_{zz}^{(\text{II})}$ at the transition point between regimes I and II, which can be used in this instance to obtain an estimate for δ during the middle elastic time (II). A more detailed explanation regarding the derivation of this approx-

imate result for $A_{zz}^{(\mathrm{II})}$ is provided in Appendix B.1. In reality, of course, $A_{zz}^{(\mathrm{II})}$ and hence the destruction rate M are not constant during regime II, but for moderately extensible chains this approximation is reasonable [150] and, as we will see, allows for the development of an approximate analytic expression governing the time-dependent evolution of the filament radius during this regime.

Using the approximation in Equation (5.23) for M and $L \approx 1/\lambda_{exit}$, Equation (5.15) can be solved explicitly (with the initial condition $\nu_a(t=0) = \nu_{a,eq} = \nu/2$) to yield

$$\nu_a^{(\mathrm{II})}(t) \approx \frac{\nu}{2+\delta}\left[\frac{\delta}{2}\exp\left(-\frac{(2+\delta)t}{\lambda_{exit}}\right)+1\right] \approx \frac{\nu}{2+\delta}, \tag{5.25}$$

and so indeed in this regime the number density of sticky segments is approximately constant in time. The remaining 'middle elastic time' approximations ($b \gg A_{zz}^{(\mathrm{II})} \gg A_{rr}^{(\mathrm{II})}$, $f^{(\mathrm{II})} \approx 1$) allow us to simplify Equation (5.20) to the form

$$\frac{dA_{zz}^{(\mathrm{II})}}{dt} \approx -\frac{4}{R^{(\mathrm{II})}}\frac{dR^{(\mathrm{II})}}{dt}A_{zz}^{(\mathrm{II})} - \frac{1+\delta}{\lambda_{exit}}A_{zz}^{(\mathrm{II})}, \tag{5.26}$$

which has the solution

$$A_{zz}^{(\mathrm{II})}(t) \approx \left(\frac{1}{\xi^{(\mathrm{II})}(t)}\right)^4 \exp\left(-\frac{t(1+\delta)}{\lambda_{exit}}\right) \tag{5.27}$$

given the initial conditions $A_{zz}(t=0) = 1$ and $R(t=0) = R_0$, where $\xi^{(\mathrm{II})}(t) = R^{(\mathrm{II})}(t)/R_0$ is the dimensionless radius of the filament which we seek to determine.

Finally, the governing SFEN force balance (Equation (5.22)) can similarly be simplified in regime II to

$$\frac{\sigma}{R^{(\mathrm{II})}} \approx \nu_a^{(\mathrm{II})} k_B T A_{zz}^{(\mathrm{II})}, \tag{5.28}$$

and by substituting Equations (5.25) and (5.27) into (5.28), we obtain an explicit expression for the evolution of the filament radius during the 'middle elastic time', or regime II:

$$\xi^{(\mathrm{II})}(t) \approx \left(\frac{E_c}{2+\delta}\right)^{\frac{1}{3}} \exp\left(-\frac{t(1+\delta)}{3\lambda_{exit}}\right). \tag{5.29}$$

The longest relaxation time of a polymer solution (λ_0) is typically extracted from the period of exponential radius decay during a CaBER experiment using the expression $\xi^{(\mathrm{II})} \sim \exp(-t/3\lambda_0)$ [146, 148]. Comparison of this expression and Equation (5.29) reveals that monitoring the rate of filament decay in regime (II) given by $\dot{\epsilon}^{(\mathrm{II})} = -(2/\xi)\dot{\xi} = (2/3)\lambda_0^{-1}$ therefore provides a direct measure of the network junction exit rate λ_{exit}^{-1}, and that these two quantities are related through the expression

$$\dot{\epsilon}^{(\mathrm{II})} \approx \frac{2}{3}(1+\delta)\lambda_{exit}^{-1}. \tag{5.30}$$

When sticky effects are larger and the assumption in Equation (5.25) of a nearly constant number density of bridged active segments ν_a does not hold, a more sophisticated analysis

(presented in Appendix B.2) can be used to find a more accurate expression for the local filament thinning rate in regime II.

Terminal asymptotic behaviour (Regime III)

Finally, we consider the asymptotic behaviour of the SFEN model as the thinning filament approaches rupture and breakup. In this regime (denoted III in Figure 5.3.1b), the chains are essentially fully stretched ($A_{zz}^{(\mathrm{III})} \approx b$) [146] and as such we can approximate that the time rate of change of the axial microstructural deformation vanishes ($\dot{A}_{zz}^{(\mathrm{III})} \to 0$). Consequently, the destruction rate of elastically active segments far outweighs the creation rate (i.e. $M^{(\mathrm{III})} \gg L^{(\mathrm{III})}$). Entov and Hinch show that for a dilute suspension of FENE-P springs in this terminal regime, the FENE term approaches $f^{(\mathrm{III})} \to 2\dot{\epsilon}^{(\mathrm{III})}\lambda_0$ and each segment essentially behaves as a fully stretched rigid rod, resulting in a constant polymeric contribution to the viscosity given by [146]

$$\eta_{FENE-P}^{(\mathrm{III})} = \frac{2}{3} n k_B T \lambda_0 b. \tag{5.31}$$

Furthermore, the filament radius in this region evolves linearly as $R^{(\mathrm{III})}(t) = \sigma(t_{break} - t)/(6\eta^{(\mathrm{III})})$.

Considering the analogous regime in the SFEN model, for $A_{zz} \approx b$, Eq (5.16) reduces to $\dot{\epsilon}^{(\mathrm{III})} \approx M/2$ which reveals, by direct comparison with Eq (5.15), that

$$\dot{\epsilon}^{(\mathrm{III})} = -\frac{1}{2\nu_a^{(\mathrm{III})}} \frac{d\nu_a^{(\mathrm{III})}}{dt}. \tag{5.32}$$

Combining this result with the kinematic definition of the strain rate (Equation (5.18)) and integrating, we obtain that

$$\nu_a^{(\mathrm{III})} = \frac{\nu_a^*}{R^{*4}} \left(R^{(\mathrm{III})}\right)^4 \tag{5.33}$$

where ν_a^* and R^* are the number density of bridged chains and the filament radius when this terminal regime begins. It is clear that as the filament thins and $R^{(\mathrm{III})}$ decreases the number of bridged elastically active chains decreases very rapidly.

Making use of the definition of the FENE term f (Eq (6.12)), we arrive at an analogous, strain-rate dependent expression to that of Entov and Hinch for the evolution in the nonlinear stretching of the chains in regime III:

$$f^{(\mathrm{III})} \approx \frac{\sqrt{b}}{2X}\left[(2\dot{\epsilon}\lambda_{exit})^{2/b} - 1\right]. \tag{5.34}$$

Neglecting the radial microstructural deformation A_{rr} and the small contribution of the solvent stress, the late-time force balance is given by

$$\frac{\sigma}{R^{(\mathrm{III})}(t)} \approx \nu_a^{(\mathrm{III})}(t) k_B T f^{(\mathrm{III})}(t) A_{zz}^{(\mathrm{III})}(t). \tag{5.35}$$

Substituting Equations (5.33) and (5.34) as well as the approximation $A_{zz}^{(\mathrm{III})} \approx b$ into this expression allows us to obtain an expression for the evolution of the filament radius

during regime III (non-dimensionalized by its value at the start of the terminal regime, $\xi^{(III)}(t) = R^{(III)}(t)/R^*$), in terms of time non-dimensionalized by the exit rate of network segments ($\tau = t/\lambda_{exit}$):

$$\int \frac{1}{\xi^{(III)}} \left[1 + \frac{1}{K\left(\xi^{(III)}\right)^5}\right]^{-\frac{b}{2}} d\xi^{(III)} = \int -\frac{d\tau}{4} \tag{5.36}$$

where the constant K is given by

$$K = \frac{1}{2}\left[\frac{\nu_a^* k_B T b}{\sigma/R^*}\right]\left(\frac{\sqrt{b}}{X}\right). \tag{5.37}$$

The first term in Equation (5.37), in square brackets, is proportional to the ratio of the steady state extensional stress of a dumbbell suspension [144] to the capillary pressure in the filament at the start of regime III. From the definitions of b and X, we see that the second term, in parentheses, is the ratio of the fully extended length of a network segment to the width of the energy activation barrier r_c. We term the inverse of this parameter the "stickiness number", i.e.

$$Sk = X/\sqrt{b}. \tag{5.38}$$

When Sk is small (or when K is large), which is achieved either by having network segments that are extremely extensible ($b \to \infty$), or by having negligibly wide junction energy wells ($r_c \to 0$), physical association effects are negligible. In this limit, Equation (5.36) reduces to

$$\int \frac{1}{\xi^{(III)}} d\xi^{(III)} = \int -\frac{d\tau}{4}, \tag{5.39}$$

and so the terminal filament thinning kinematics are exponential in nature with $\xi \sim \exp(-\tau/4)$.

Conversely, as Sk becomes larger, as achieved by either less extensible stiffer chains or a wide junction energy well, network effects are no longer negligible. In this regime, as $\xi^{(III)} \to 0$, Equation (5.36) simplifies to

$$\int K^{b/2}\left(\xi^{(III)}\right)^{5b/2-1} d\xi^{(III)} = \int -\frac{d\tau}{4}, \tag{5.40}$$

and an explicit analytical expression for the late-time decay of the filament radius can be found:

$$\xi^{(III)} \to (5b/8)^{\frac{2}{5b}} K^{-1/5}(\tau_{crit} - \tau)^{\frac{2}{5b}}, \tag{5.41}$$

where τ_{crit} is the non-dimensional breakup time of the filament. In practice, as a result of the difficulty of obtaining an explicit analytic expression for τ_{crit} in terms of the model parameters and initial conditions, we estimate the value of this singular point numerically as the time at which the non-dimensional filament radius $\xi = R/R_0$ reaches a vanishingly small value (taken to be $\xi \leq 5 \times 10^{-8}$ in the present study).

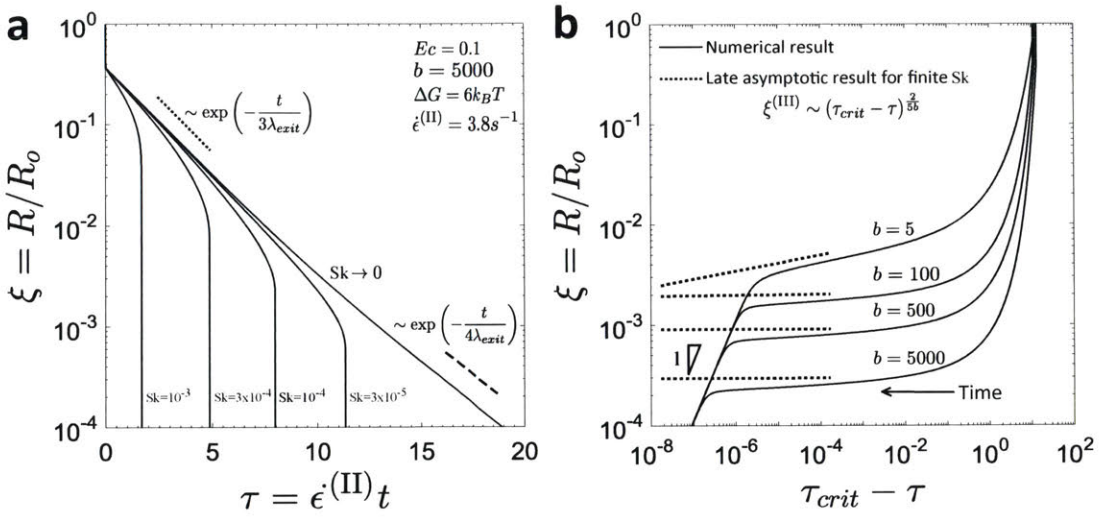

Figure 5.3.2: Filament thinning dynamics of the SFEN model, with $\Delta G = 6k_BT$, $E_c = 0.1$, and $\dot{\epsilon}^{(II)} = 3.8\,\mathrm{s}^{-1}$. In (a), the effect of the stickiness number Sk on the evolution of the filament radius is shown for a value of the finite extensibility parameter comparable to those estimated for the mucin macromonomers ($b = 5000$). The exponential elastocapillary (II) and terminal (III) thinning regimes described in Equations (5.29) and (5.39) for the case of vanishing stickiness effects $Sk \to 0$ are shown as the dotted and dashed lines, respectively. In (b), the asymptotic decay to breakup of the SFEN model during filament thinning experiments is shown as a function of time from the singularity ($\tau_{crit} - \tau$) for four values of the finite extensibility parameter b with the energy well width to the equilibrium macromonomer size ratio fixed at $X = 10^{-3}$. The b-dependent decay during regime III (Equation (5.41)) is shown as the dotted line. The final late-time linear decay of the filament radius as a result of the residual solvent contribution at very small length scales is made apparent by the indication of the region with slope 1.

In Figure 5.3.2a, the SFEN predictions for the radial evolution of a thinning filament are shown for various values of the stickiness number Sk. The exponential elastocapillary thinning regime (II) described in Equation (5.29) for the limit of $Sk \to 0$ and hence $\delta \to 0$ is shown by the dotted line. Clearly, as Sk increases and network effects become large, the slope during regime (II) becomes increasingly steep, as described in Equations (5.30) as well as the additional discussion in Appendix B.2, and the filament ruptures earlier. In the limit of $Sk \to 0$, the exponential terminal thinning dynamics described in Equation (5.39) are recovered, as indicated by the dashed line. In Figure 5.3.2b, the late time asymptotics of the SFEN model are shown as a function of time from the breakup singularity. Unlike the linear decay of a FENE-P filament close to rupture [146], the evolution of the filament radius for the SFEN model in regime (III) depends on the finite extensibility b of the network segments, although in practice this analytic result saturates quickly for large values of b (see Equation (5.41)).

When plotted in terms of Figure 5.3.2b which reflects distance from the finite time singularity corresponding to filament rupture, it is clear that there is in fact a fourth thinning regime at very small length and time scales. Once the associating mucin network has ruptured and polymer stresses have been removed, solvent stresses present the only opposition

to capillary pressure and (consistent with the appropriate force balance in Equation (5.22)) a final universal linear decay of the filament is expected as shown in Figure 5.3.2b with a slope of unity. This decay is faster than that for a FENE-P filament (Equation (5.31)) as it arises from the viscous solvent alone [146]. We note here that Renardy has also investigated the breakup behaviour of fluid filaments for a number of constitutive models [153, 154, 155, 156], and our results are consistent with his conclusion that Newtonian breakup asymptotics are ultimately observed for finitely extensible dumbbell models (although the functional forms of the FENE and SFEN stretch terms do, of course, differ).

To summarize this section, we have developed a Sticky Finitely Extensible Network (SFEN) model for an associating polymeric network whose parameters respect the known biological properties of mucin molecules and whose dynamics can be related to the filament thinning theory traditionally used to interpret CaBER experimental data. Interestingly, the terminal dynamics of this model depend on the finite extensibility b of the network segments and on a dimensionless stickiness number Sk that incorporates the width of the energy well and the length of the chains (c.f. Equations (5.11) and (5.38)). With this analysis in place, we proceed in the following section to compare the predictions of the SFEN model during CaBER filament thinning with experimental data of saliva at various sample ages t_{age}, and use these results to comment on the effect of enzymatic degradation on reported measures of saliva extensional rheology.

5.4 Results and Discussion

Saliva samples used in this work were obtained without stimulation following the procedure outlined in [87]. Donors were instructed to refrain from eating or drinking for one hour prior to collection. Vacuum was drawn in a closed collection vial using an Amersham VacuGene Pump, into which a tube terminating in the donor's mouth was inserted, and saliva was allowed to accumulate. Once collected, the saliva was not treated and was stored at room temperature. All shear rheology tests were performed using a stress controlled ARG2 rheometer (TA Instruments, New Castle, DE, USA) with a 60 mm, 2° cone-and-plate fixture on a Peltier plate at a constant temperature T = 25 °C. Extensional rheometry tests were performed using a Capillary Breakup Extensional Rheometer (CaBER, Cambridge Polymer Group) with plate diameter $D = 6$ mm, initial plate separation $L_i = 2$ mm and final plate separation $L_f = 9.1$ mm. The top plate reached its final height in a strike time of $t_{strike} = 50$ ms using a stepper motor, and the diameter of the resulting filament was tracked using a laser micrometer with a resolution of 10 µm.

In Figure 5.4.1a, the results of CaBER experiments are shown for measurements taken immediately after sample procurement, as well as after the sample had been sitting (untreated, at room temperature) for $t_{age} = 1, 3, 5$, and 10 h. Data for the sample at $t_{age} = 24$ h are not shown since samples at that age were unable to form filaments that persisted beyond the plate strike time of $t_{strike} = 50$ms. Consistent with previous data from Zussman et al. [134], the experimental results show a clear exponential thinning region (regime II) followed by rapid filament failure (regime III).

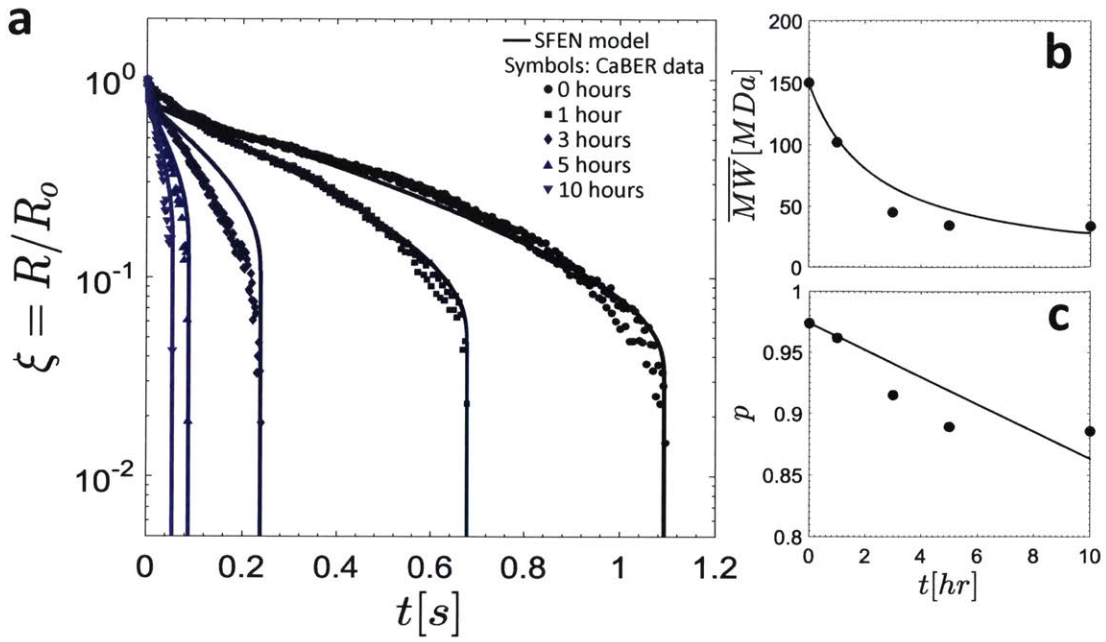

Figure 5.4.1: (a) Comparison of the SFEN model predictions with CaBER data for saliva at various sample ages. In (b) and (c), the fitted values for the weight averaged macromonomer molecular weight $\overline{M_W}$ and the reaction probability p, respectively, are shown as filled circles, and the theoretical predictions for the same parameters obtained using a randomly initiated depolymerization model are shown as the solid lines.

In Figure 5.4.2, the results of SAOS experiments (Figure 5.4.2a) and steady state flow (Figure 5.4.2b) for the same samples discussed in Figure 5.4.1a as well as the sample at $t_{age} = 24\,\text{h}$ are presented. Small variations (less than a factor of 2) are observed between the samples, and appear to be more likely attributable to sample inhomogeneity than clearly discernible trends with sample age. A more detailed discussion of the steady state flow data shown in Figure 5.4.2b and the predictions of the SFEN model in steady simple shearing flow is presented in Appendix B.3.

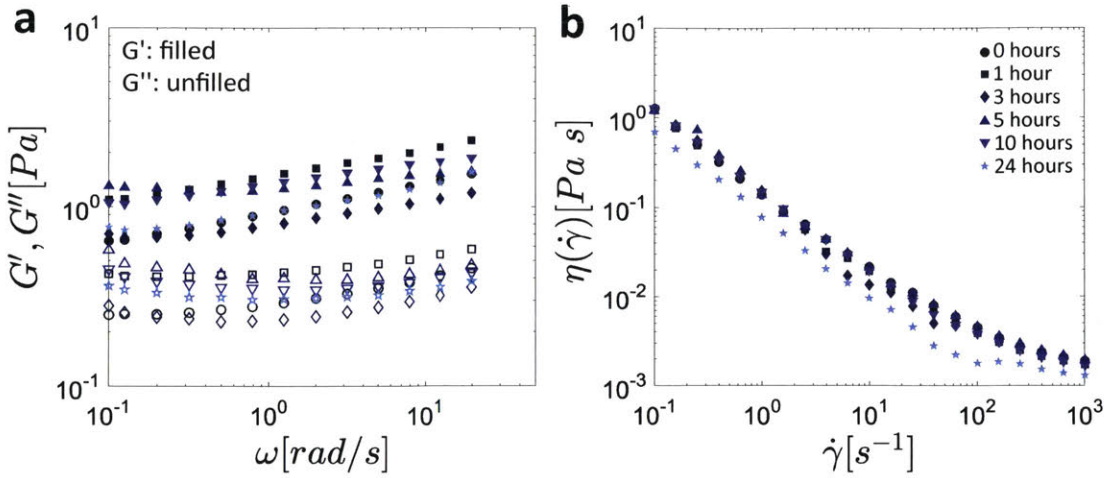

Figure 5.4.2: The shear rheology of whole saliva as measured by (a) small amplitude oscillatory shear (SAOS) and (b) steady simple shear flow. In Appendix B.3 we show that in the shear-thinning regime, the SFEN model predictions are only weakly dependent on the sample age (set using the appropriate parameters from Table 5.2), in agreement with our experimental observations.

The dependence of the moduli on the angular frequency, shown in Figure 5.4.2a, is nearly power law-like in nature; a signature of physically associated biopolymer networks with very large numbers of interaction modes [17]. As a result, no clear unique plateau value of the storage modulus can be defined (as expected [138]), and so we take as an approximate value $G_s \approx 2.5 \pm 0.5\,\text{Pa}$ for all sample ages. Using Equation (5.1), this fixes the molecular weight of each sticky segment at $M_{W,s} \approx 2.3 \times 10^5\,\text{Da}$, which results in approximately $z = 9$ sticky segments per muc-mer. In all cases, as seen in Figure 5.4.2b, saliva viscosity is quite strongly shear thinning (with a power law index $n \approx 0.11$) with no evidence of a plateau viscosity at low shear rates, and an asymptotic solvent viscosity of $\eta_s \approx 10^{-3}\,\text{Pa s}$. We note that this broad power law frequency dependence can be described quantitatively in compact form using the fractional Maxwell model, as has been recently shown in [157].

Further, recognizing that the real mucin system is polydisperse [133], we define the initial, mass-averaged, molecular weight of an entire MUC5B molecule as $\langle M_W(t_{age}=0)\rangle = \overline{M_W}(t_{age}=0) = 150\,\text{MDa}$ [70], where $\langle ... \rangle$ denotes an ensemble average. The width of the energy wells r_c is obtained by manually fitting the SFEN model to the experimental data in order to achieve a consistent filament breakup time using the fixed, remaining parameters at $t_{age} = 0\,\text{h}$. The obtained result of $r_c = 8.35\,\text{nm}$ is consistent with experimental data from Israelachvili and Pashley on the distance over which the strength of a hydrophobic interaction decays exponentially ($l \approx 10\,\text{nm}$) [158] as well as the Debye length for electrostatic interactions in biological systems ($l \approx 1-3\,\text{nm}$) [101]. Finally, the rate of filament decay in regime II ($\dot{\epsilon}^{(\text{II})}$) for each saliva sample is obtained by fitting the exponential thinning region of the appropriate CaBER data set in Figure 5.4.1a to the expression $\xi^{(\text{II})} \sim \exp\left(-\frac{\dot{\epsilon}^{(\text{II})}}{2}t\right)$.

Using the shear rheological data presented in Figure 5.4.2 along with the various parameter definitions from this and previous sections, we can define the full set of 10 parameters needed for the SFEN model, which we use to fit the CaBER data in Figure 5.4.1a. These

parameters are summarized in Table 5.1, and their numerical values are provided. In Appendix B.4, we investigate the effect of varying a subset of these physical parameters on the filament thinning dynamics.

Table 5.1: List of SFEN model parameters, along with their definitions and numerical values. The effect of varying a subset of these parameters on the filament thinning dynamics is considered in Appendix B.4.

Parameter	Definition	Numerical value
$\overline{M_W}$	Mass-averaged molecular weight of MUC5B molecule	150 MDa at $t_{age} = 0$ h
$M_{W,s}$	Molecular weight between association points	230 kDa
$M_{W,k}$	Kuhn segment molecular weight	57.1 kDa
b_k	Kuhn length	14 nm [102]
r_c	Energy well width	8.35 nm
ΔG	Energy well depth	$6k_BT$
c	MUC5B concentration in saliva	0.23 kg m^{-3} [70]
η_s	Solvent viscosity	1×10^{-3} Pa s
σ	Saliva surface tension	72×10^{-3} N m
R_0	Initial filament radius (CaBER experiment)	5×10^{-4} m

In Figure 5.4.1a, the filament thinning predictions of the SFEN model are compared with CaBER data at various sample ages. The CaBER data is collected from the time that the plate separation has occurred (and hence the time reported is actually $(t - t_{strike})$ to be consistent with the model), and the measured radius is normalized by the filament radius R_0 at the time the plates have separated. The initial condition for the filament radius of the SFEN model is taken to be $R(t = 0) = R_0$, but since the model does not account for the initial plate separation period, the initial axial microstructural stretch is taken to be slightly larger than the equilibrium value of $A_{zz} = 1$ but still much smaller than the maximum value of the finite extensibility parameter b, namely $A^0_{zz}/b \approx 0.05$. The initial radial microstructural deformation value is set to the equilibrium value of $A^0_{rr} = 1$ and all chains are assumed to be in their equilibrium configuration such that $\nu_a(t = 0) = \nu_{a,eq} = \nu/2$. Visual inspection confirms that Equation (5.30) provides a good estimate for the network junction rate λ^{-1}_{exit} for the first two age points ($t_{age} = 0$ h and $t_{age} = 1$ h), but at later sample ages when the extensibility is reduced a higher order estimate is needed (see the discussion in Appendix B.2). For both expressions, we use the implicit expression for $A^{(II)}_{zz}$ at the transition between regimes (I) and (II) provided in [150] to approximate δ and hence the destruction rate M, where we take the polymer viscosity to be $\eta_p = \nu k_B T/(3\dot{\epsilon}^{(II)})$.

Esser et al. have shown that the distribution of protein molecular weight in saliva is highly sensitive to sample age as a result of enzymatic activity and protein breakdown [133]. Consequently, we hypothesized that the dramatic decrease in elasticity observed in the filament thinning data shown in Figure 5.4.1a as the saliva samples age could be attributed to a time-dependent decrease in the mass-averaged molecular weight of the mucin molecules. For $t_{age} > 0$ h, the same procedure previously described was used to fit the mass-averaged molecular weight $\overline{M_W}(t)$ for all of the sample ages considered. In so doing, we assume that the width of the activation barrier r_c measured at $t_{age} = 0$ h as well as all other parameters

except for the finite extensibility ($b = 3\overline{M_W}/M_k$) and the network exit junction rate λ_{exit}^{-1} remained constant with age. The fitted results for $\overline{M_W}(t)$ are shown as the solid circles in Figure 5.4.1b, and a summary of the age-dependent SFEN model parameters at all sample ages is provided in Table 5.2.

Table 5.2: Age-dependent SFEN model parameters for saliva. For stickiness numbers $Sk \gtrsim 5.0 \times 10^{-4}$, the higher order approximation relating the network junction exit rate (λ_{exit}^{-1}) to the rate of filament decay in regime II ($\dot{\epsilon}^{(II)}$) presented in Appendix B.2 was used. These values are indicated by an asterisk.

t_{age}[h]	$\overline{M_W}$[MDa]	$\dot{\epsilon}^{(II)}$ [s^{-1}]	λ_{exit}^{-1} [s^{-1}]	b	Sk
0	150	3.8	3.8	8000	2.2×10^{-4}
1	102	5.2	4.9	5500	3.3×10^{-4}
3	45	19	7.5*	2400	7.4×10^{-4}
5	34	43	16*	1800	9.8×10^{-4}
10	33	68	24*	1800	1.0×10^{-3}

It is clear from Table 5.2 that the finite extensibility of the elastic network strands decreases dramatically with age ($b \sim \overline{M_W}$), and this increases the nonlinearity in the FENE springs which then increases the exit rate of chains from the associative network (c.f. Equation (5.11)). This is confirmed by the experimental observation of a strong dependence of the extensional properties of saliva on sample age, as measured by both the rate of filament thinning in the intermediate elastic time (see Table 5.2 and Equation (5.30)) and the time to breakup for the data CaBER presented in Figure 5.4.1a. By contrast, in the shear thinning reimge the shear rheology is relatively age-invariant as seen in Figure 5.4.2. This latter finding, discussed in additional detail in Appendix B.3, could be related to the fact that while the chains shorten due to enzymatic activity, the concentration of mucin remains constant, and hence shear measurements at moderate strain values remain largely unaffected as the product ($c\overline{M_W}$) is unchanged. Our SFEN model is able to capture the evolution in the extensional viscosity through allowing a single parameter ($\overline{M_W}(t)$) to decrease with sample age. The very rapid rupture of the filament just before breakup at young sample ages is quite distinct from that observed in high molecular weight polymer solutions, and is also well described by the model through the incorporation of the stretch-dependent dissociation term (see Equation (5.11)). Indeed, for young samples (small t_{age}), the mass-averaged molecular weight $\overline{M_W}$ and hence the finite extensibility parameter b are large, resulting in a small value of the stickiness number Sk (Equation (5.38)). Consistent with Figure 5.3.2a, the thinning filaments are able to persist for longer, but their eventual breakup is more dramatic and sudden. Conversely, following degradation, the relatively less extensible mucin chains lead to larger values of Sk, and the lifetime of the filaments correspondingly decreases.

We model the enzymatic 'cutting' of the concatenated mucin chains as a randomly initiated depolymerization [159] process of the concatenated muc-mers. Indeed, the assembly (or disassembly in our case) of supramolecular networks is often analyzed in the framework of classical polymerization theory (see the book chapter by Anthamatten [160] for additional details). In a step growth polymerization process, the weight fraction distribution of molecules n_c muc-mers in length is given by $W_c(n_c) = n_c(1-p)^2 p^{n_c-1}$ [161], where p is the degree of polymerization. From this definition, it follows that the mass-averaged, most

probable number of concatenated muc-mers in a molecule is given by

$$n_c^* = \sum_{n_c} n_c W_c = (1+p)/(1-p). \tag{5.42}$$

Using the fitted values of the mass averaged molecular weight $\overline{M_W} = n_c^* \times M_{W,MUC}$ from Table 5.2, the degree of polymerization p can be found at each sample age time point t_{age} using this formula. These results are shown as solid circles in Figure 5.4.1c.

For randomly initiated depolymerization in which complete degradation of all molecules is expected, MacCallum [159] has shown that the reaction probability p can be approximated to vary linearly in time as $p(t) = p_0 - \alpha t$, where α is the degradation rate and p_0 is the initial degree of polymerization. Although the exact magnitude of α depends on the initial distribution of polymer molecular weights, this simple linear relationship holds even without such information [159]. From this result and Equation (5.42), it is straightforward to obtain that the mass-averaged molecular weight of the mucin molecules should vary in time as

$$\overline{M_W}(t) = M_{W,MUC}\left[1 + \frac{2}{\frac{1}{p_0 - \alpha t} - 1}\right]. \tag{5.43}$$

These predicted expressions for $p(t)$ and $\overline{M_W}(t)$ are fit to the experimental data and shown as the solid lines in Figures 5.4.1b and 5.4.1c. From these fits, we obtain an estimate for the muc-mer degradation rate as $\alpha = 0.011\,\mathrm{h}^{-1}$, and $p_0 = 0.97$.

5.5 Summary

In conclusion, we have shown that the transient extensional rheology of whole saliva (as measured with CaBER) is extremely sensitive to sample age (Figure 5.4.1a), while the corresponding shear rheological properties (SAOS and steady state flow, as shown in Figures 5.4.2a and 5.4.2b respectively) are relatively invariant. In order to explain these observations, we have developed a Sticky Finitely Extensible Network (SFEN) model based on the approach of Tripathi et al. [129], which respects the known biological dimensions of mucins, and models saliva as an associating network of finitely extensible elastic segments. This model incorporates linear viscoelasticity as well as filament thinning and network rupture, and is likely to prove useful for modeling a number of biopolymeric networks under various flow conditions. Capillary thinning experiments prove particularly useful because we show (c.f. Equation (5.30)) that the rate of filament thinning during regime II is a direct measure of the exit rate of chain segments from the network. The stretch-dependence of this exit rate is taken into account by the SFEN model and results in progressively faster network rupture as the filament thins.

By assuming a decrease in the mass-averaged molecular weight of the MUC5B molecules with sample age (consistent with salivary measurements of enzymatic activity and protein degradation [133]), the finite extensibility b of the network chains decreases as well, resulting in an increase in the importance of supramolecular network effects, which are quantified by a newly-introduced stickiness parameter Sk. Increasing values of Sk lead to more rapid growth in elastic stresses and sudden rupture of the network as shown in Figures 5.3.2a and

5.4.1a. This final rupture is much faster than the rate of thinning predicted by the FENE-P model for extensible polymer solutions [146, 148].

Our measurements and corresponding model for the evolution in network extensibility and molecular weight demonstrate the importance of carefully monitoring and stating sample age in reports of saliva and mucin network rheology. This provides a plausible explanation for why previous rheological data on saliva reported in the literature varies so greatly, and emphasizes the care that should be taken in interpreting diagnostic information from rheological measurements of saliva if sample age and degradation are not accounted for.

6 | Characterization and quantification of food solution texture using fractional models

6.1 Introduction

For many food products, textural attributes are strong drivers of consumer preference [162]. In addition to the importance for the sensory experience associated with food, texture plays a critical role in determining what can and cannot be consumed for people suffering from mastication and swallowing disorders, which are collectively known as dysphagia [163, 164, 165]. As a result of the difficulty that many of these patients have with swallowing very tough foods such as meat, softer diets are commonly followed [165]. Moreover, higher viscosity, 'thicker', liquids are generally preferred over 'thinner' ones due to the increased risk of aspirating thin liquids [163].

Quantification of food consistency is complicated by at least two important factors, however: i) the inevitable variations in perceived texture across individuals, and ii) the absence of a concise mathematical framework and robust set of measurable parameters for doing so. As an illustrative example of individual variations, at a lecture delivered in 1970 at the Technical University in Budapest, the English rheologist G. W. Scott Blair noted that since the French 'seldom spread jam on their bread', texture and hole density play a diminished role compared to taste in their enjoyment of bread, resulting in consistency being a much larger concern for bread-makers selling their fare to jam-spreading Britons [166].

To assess concepts such as consistency, sensory panel testing requires a number of individuals to consume a product in a well-controlled manner and rate various 'sensory attributes' against a given standard. For example, one could attempt to quantify the crunchiness of an apple on a numerical scale for which a ripe peach is a 1 and a really fresh stick of celery is a 10. Each individual will likely show differences in sensory perception, rendering such attributes difficult (if not impossible) to measure objectively. An additional consideration relates to common reference points. Unlike for simple colours and sound, for example, such references are not obvious for oral mechanoreception, where the medium to be sensed needs to be moved and manipulated inside the oral cavity to reach the locations where it is sensed (tongue, palate, cheeks, etc...). This manipulation in the oral cavity is likely to vary from person to person, and is consequently difficult to standardize.

To address the second issue, the development of a mathematical framework for the quan-

tification of food consistency to reduce the need for subjective assessments is needed. Food materials are generally inhomogeneous and exhibit markedly different properties depending on the time- and length-scales of observation. This structural complexity adds some difficulties for material characterization; in general, simple physical laws such as Newton's law of viscosity for liquids and Hooke's law for elastic solids are insufficient [17, 39]. A classical approach to develop models for rheologically complex materials has been to conceptualize networks of springs and dashpots to incorporate elements capturing both an elastic and a viscous response in the sample stress as it responds to imposed deformations [23]. Classic examples include the Maxwell model (one spring and one dashpot in series), which has been successfully applied to polymer fluids for small displacement gradients, as well as the Kelvin-Voigt model (one spring and one dashpot in parallel), which can compactly describe the creep of solid-like materials [23].

These constitutive formulations have also been employed in the characterization of food rheology, for instance, Schofield and Scott Blair used an intricate network of springs to model the response of gluten and starch in bread dough [167]. Kokini [168] investigated the applicability of a range of constitutive equations in rheological studies of pectin solutions and gluten doughs. While he was able to adequately model the rheological response of the individual foods using specifically tailored models, he concluded that 'new models need to be designed which are capable of accounting for the diverse and complex structural properties of foods'. With their concise and elegant framework and minimal number of parameters, fractional rheological models, introduced in Section 2.2.2, appear to be excellent candidates for doing so.

Originally, Scott Blair and coworkers applied these models towards the classification of industrial materials such as rubber and bitumen [13, 169]. Since then, their utility in the field of food rheology has also been recognized. Simpson et al. have argued that classical Fickian models are insufficient to describe diffusion processes through food substances, particularly the diffusion of water during dehydration processes, as a result of the morphological changes that these complex fluids undergo on the microscopic level as the water content decreases [170]. They propose that fractional diffusional models, with their non-integer dependence of concentration on both space and time, are more broadly applicable [170]. Oroian et al. have modeled the linear viscoelastic response of honey using a fractional rheological model [171], while Song et al. applied a similar approach to the modeling of xanthan gum solutions [172]. These latter authors concluded that the weak dependence of the storage and loss moduli on frequency during small amplitude oscillatory shear flows, as measured by the fractional value of the time derivative of the material strain, was an indication of a weak gel-like structure in these xanthan gum solutions. In their studies of product aging, Quinchia et al. have also modeled the linear viscoelastic response of a commercial strawberry pudding using power laws, although the direct connection to fractional calculus was not made at the time by these authors [173]. As a final example, Faber et al. have recently applied fractional models towards the evaluation of the effect of fat and water content on technological measures such as the firmness, rubberiness, and springiness of cheese at different temperatures [174, 175].

In this chapter, we first use fractional constitutive models to predict the linear and nonlinear viscoelastic response of a well defined, benchmark system designed to produce fluids with specific food textures at appropriate concentrations: the xanthan gum based food-thickening dysphagia product Resource ® Thicken Up Clear (referred to henceforth

as TUC) produced by Nestlé. Based on early sensory panel reports of the perceived texture of various starch-based food solutions [176], the National Dysphagia Diet Task Force (NDDTF) classifies food solutions with shear viscosities of $1 \leq \eta \leq 50\,\mathrm{mPa\,s}$ as having a 'thin' consistency, viscosities in the range $51 \leq \eta \leq 350\,\mathrm{mPa\,s}$ are described as having a 'nectar-like' consistency, higher viscosities $351 \leq \eta \leq 1750\,\mathrm{mPa\,s}$ correspond to a 'honey-like' consistency, and $\eta > 1750\,\mathrm{mPa\,s}$ is termed a 'spoon-thick' consistency (also referred to as 'pudding-like'), with all measurements performed at a shear rate of $\dot{\gamma} = 50\,\mathrm{s}^{-1}$ and at 25 °C [163]. We note that in other countries such as the United Kingdom and Australia, the viscosities along which these textural divisions are drawn are similar, but the specific descriptive term associated with each consistency varies [177].

In this chapter, we first use fractional constitutive models to predict the linear and nonlinear viscoelastic response of a well defined, benchmark system designed to produce fluids with specific food textures at appropriate concentrations: the xanthan gum based food-thickening dysphagia product Resource ® Thicken Up Clear (referred to henceforth as TUC) produced by Nestlé. Based on early sensory panel reports of the perceived texture of various starch-based food solutions [176], the National Dysphagia Diet Task Force (NDDTF) classifies food solutions with shear viscosities of $1 \leq \eta \leq 50\,\mathrm{mPa\,s}$ as having a 'thin' consistency, viscosities in the range $51 \leq \eta \leq 350\,\mathrm{mPa\,s}$ are described as having a 'nectar-like' consistency, higher viscosities $351 \leq \eta \leq 1750\,\mathrm{mPa\,s}$ correspond to a 'honey-like' consistency, and $\eta > 1750\,\mathrm{mPa\,s}$ is termed a 'spoon-thick' consistency (also referred to as 'pudding-like'), with all measurements performed at a shear rate of $\dot{\gamma} = 50\,\mathrm{s}^{-1}$ and at 25 °C [163]. We note that in other countries such as the United Kingdom and Australia, the viscosities along which these textural divisions are drawn are similar, but the specific descriptive term associated with each consistency varies [177].

In this chapter, we show that the values of the quasiproperties and power law indices of the fractional models describing different concentrations of TUC can be used to quantify the different levels of viscoelasticity associated with each of these descriptors. We then apply this framework towards the characterization of selected plant extracts whose constituent biopolymers are known to impart significant viscoelasticity and show that the rheological response of these materials can also be well described by fractional models. Examples include extracts from okra plants, chia seeds, and flax seeds, as well as gums typically used in food manufacturing and stabilization, including guar and tara gums [178, 179]. Since we have observed similar trends in the rheological behaviour of whole human saliva (which plays a significant role in mouth-feel and food textural perception [131]), we include a similar analysis of saliva as well. We conclude that in general, the specification of a single shear viscosity at $\dot{\gamma} = 50\,\mathrm{s}^{-1}$ might be insufficient to uniquely capture the rheological response associated with conventional food textural terms such as 'nectar' and 'pudding'. Instead, we show that by quantifying the rheological response of these liquid foodstuffs in terms of two constitutive parameters obtained from the fractional models, a 'consistency phase space' can be developed which allows for an improved mapping of these descriptive textural terms to quantitative values of the material viscoelasticity.

6.2 Background

6.2.1 Experimental details

Commercial formulations of Thicken Up Clear (TUC) were purchased from the storefront Treasure Zone on Amazon. Solutions were prepared by combining the appropriate amount of TUC powder with deionized water and then vigorously stirring using a magnetic stir bar at 300 rpm for 3 minutes at room temperature. The solutions were then mixed gently on a roller mixer for 2 hours to insure complete hydration. The procedural details for each of the other biopolymer solutions and saliva are provided in Section 6.4.

Shear measurements were performed using a TA Instruments (New Castle, DE, USA) stress controlled AR-G2 rheometer with a 60 mm, 2° cone-and-plate fixture. All experiments were performed on a Peltier plate at a constant temperature T = 25 °C. We follow the recent recommendation of Wagner et al. [180] by requiring the accumulation of material strains in excess of $\gamma \geq 5$ in all of the biopolymer solutions before reporting viscosity data during steady state flow measurements. This recommendation was made in response to various reports in the literature of a curious region of shear thickening at low shear rates ($\dot{\gamma} \lesssim 0.1\,\mathrm{s}^{-1}$) in high molecular weight synthetic and biopolymer solutions, leading to an apparent local maximum in the shear viscosity [180]. Wagner et al. demonstrate that when total strains of $\gamma \geq 5$ are allowed to accumulate during each steady state flow measurement at each share rate, proper sample equilibration eliminates this non-monotonic response in the apparent steady shear viscosity [180].

6.2.2 Theoretical and modeling details

Balancing the desire for parsimonious and physically meaningful models with accurate descriptions of measured material properties persists as a major challenge in food process engineering, particularly for multi-component and multi-scale materials where an *a priori* understanding or description of the material microstructure is absent. Freund and Ewoldt have recently proposed a fitting regimen using Bayesian statistics to select an optimal rheological model from a pool of pre-defined candidate models [181]. The selection of a single candidate model is driven by the product of two fitness terms: one that reflects the ability of the model to faithfully reproduce the data, and a data independent term reflecting *a priori* knowledge of the model based on physical intuition [181]. These authors argue that fractional models are generally able to reproduce data very well (thus resulting in a high score for the reproducibility term), but claim that physical intuition for fractional models is generally lacking (resulting in a low score for the intuition component) [181]. Despite the subjectiveness of the latter criterion, their Bayesian analysis concludes that for some complex fluids such as gluten gels, models such as the CGRM (Critical Gelation Rouse Model) which can be represented in a compact fractional framework are in fact the most appropriate choice [181]. Further, Bagley has shown in several papers that a broad range of generalized Rouse-Zimm like models can also be represented in the form of fractional viscoelastic constitutive equations [182, 183, 184].

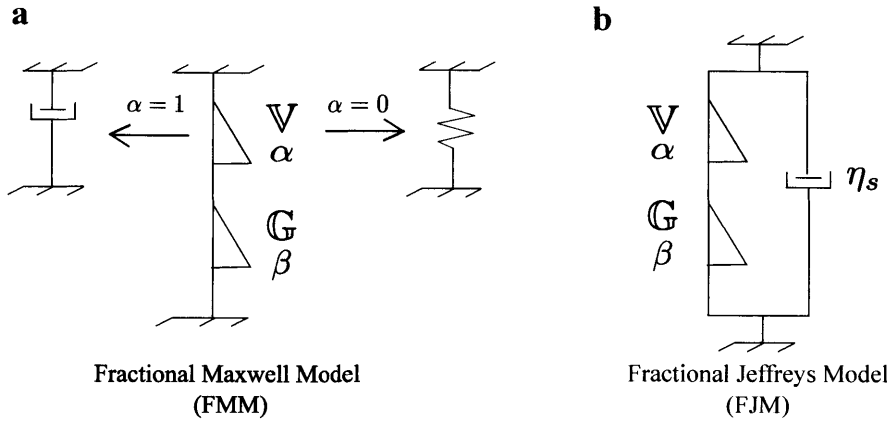

Fractional Maxwell Model (FMM)

Fractional Jeffreys Model (FJM)

Figure 6.2.1: Schematic representation of the fractional Maxwell model (FMM) as two 'spring-pots' in series and the definition of a spring-pot as a mechanical element that interpolates between a spring ($\alpha = 0$) and a dashpot ($\alpha = 1$). (b) Fractional Jeffreys model (FJM) with two spring-pots in series arranged in parallel with a purely viscous (dashpot) element to account for solvent viscosity.

Jaishankar and McKinley [17] have recently demonstrated that the fractional Maxwell model (FMM, depicted schematically in Figure 6.2.1a) is very well suited to capture the linear response of aqueous biopolymer solutions such as xanthan gum and the food biopolymer solutions considered in this manuscript. The mathematical details of the FMM are discussed at length elsewhere [17, 185]. Briefly, this model consists of two spring-pots (or 'Scott Blair elements') in series. The first we denote with a quasiproperty $\mathbb{V}$ with units of [Pa s$^\alpha$] and fractional derivative order α, and the second with quasiproperty $\mathbb{G}$ [Pa s$^\beta$] and fractional derivative order β, where we take $0 \leq \beta < \alpha \leq 1$ without loss of generality [17]. Clearly, when $\alpha \to 1$ and $\beta \to 0$, the classical Maxwell model is recovered (see Figure 6.2.1a). In general, the FMM model gives rise to power law responses in the linear viscoelastic relaxation modulus $G(t)$, with the exponent α capturing the slope $\mathrm{d}G(t)/\mathrm{d}t$ at long times (or low frequencies), and the exponent β capturing the slope at short times (or high frequencies) [17]. The FMM expression for the complex modulus $G^*(\omega)$ as a function of frequency is given in compact form [17] as

$$G^*_{FMM}(\omega) = \frac{\mathbb{V}(i\omega)^\alpha \mathbb{G}(i\omega)^\beta}{\mathbb{G}(i\omega)^\alpha + \mathbb{V}(i\omega)^\beta}. \tag{6.1}$$

The individual components of storage and loss moduli can consequently be obtained by separating the complex modulus into its real and imaginary parts, $G^*(\omega) = G'(\omega) + iG''(\omega)$, yielding

$$G'_{FMM}(\omega) = G'_{FJM}(\omega) = \mathbb{V}\tau^{-\alpha}\frac{(\omega\tau)^\alpha \cos(\pi\alpha/2) + (\omega\tau)^{2\alpha-\beta}\cos(\pi\beta/2)}{(\omega\tau)^{2(\alpha-\beta)} + 2(\omega\tau)^{\alpha-\beta}\cos(\pi(\alpha-\beta)/2) + 1} \tag{6.2}$$

and

$$G''_{FMM}(\omega) = \mathbb{V}\tau^{-\alpha}\frac{(\omega\tau)^\alpha \sin(\pi\alpha/2) + (\omega\tau)^{2\alpha-\beta}\sin(\pi\beta/2)}{(\omega\tau)^{2(\alpha-\beta)} + 2(\omega\tau)^{\alpha-\beta}\cos(\pi(\alpha-\beta)/2) + 1}, \tag{6.3}$$

where $\tau = (\mathbb{V}/\mathbb{G})^{1/(\alpha-\beta)}$ is a characteristic time scale of the FMM [27]. Provided $1 \geq \alpha > 1/2 > \beta \geq 0$, so that the model response is not purely viscous or purely elastic at any point over the entire frequency range, it can be shown that the viscoelastic moduli show a crossover from a dominantly viscous to a dominantly elastic response as the frequency increases [27]. The crossover frequency ω_c at which $G'(\omega_c) = G''(\omega_c)$ can be found by equating Equations (6.2) and (6.3), giving an alternate way of determining a single characteristic time of the FMM. The crossover time scale $\tau_c \equiv 1/\omega_c$ is given by the expression [27]:

$$\tau_c = \frac{1}{\omega_c} = \tau \left[\frac{\cos(\pi\beta/2) - \sin(\pi\beta/2)}{\sin(\pi\alpha/2) - \cos(\pi\alpha/2)}\right]^{1/(\alpha-\beta)}. \tag{6.4}$$

Either τ or τ_c can be used to compactly provide a single scalar metric combining all four constitutive parameters in the FMM. Because τ_c can be related to a visually distinct measure (the crossover frequency at which $G'(\omega_c) = G''(\omega_c)$), we choose to report values in Table 6.1 using this parameter.

To demonstrate qualitatively and quantitatively the descriptive ability of the FMM over a generalized Maxwell model corresponding to an ensemble of M discrete Maxwell modes (or N = 2M parameters), we compare the cost function of the FMM versus an M-mode Maxwell model describing the linear viscoelastic properties of the $c = 1.2\,\text{wt}\,\%$ preparation of TUC. We undertake this exercise to determine what number, if any, of linear Maxwell modes will model the linear viscoelastic data as well as the 4 parameter FMM. Since the optimal parameter values for each mode of the M-mode Maxwell model are unknown, and the parameter space is increasingly difficult to explore as the number of parameters is increased, we perform repeated minimizations of the cost function

$$\epsilon = \sum_{i=1}^{n_{\text{data}}} \left(\frac{(G'_i - G'_{i,\text{fit}})}{G'_i}\right)^2 + \left(\frac{(G''_i - G''_{i,\text{fit}})}{G''_i}\right)^2 \tag{6.5}$$

using the genetic algorithm command *ga* in Matlab. For each minimization, we initialize the genetic algorithm with the larger of 300 or 100×M children (where M is the number of Maxwell modes), which then evolve to determine the best fit to the candidate data. We constrain all initial and evolved model parameters to be positive numbers, following physicality arguments, and do not place constraints upon the magnitude of these parameters. The genetic algorithm is halted once the 1000^{th} generation is reached or the average relative change in the best fit determined across successive generations differs by less than 1×10^{-6}. We show the results of this fitting procedure in Figure 6.2.2a.

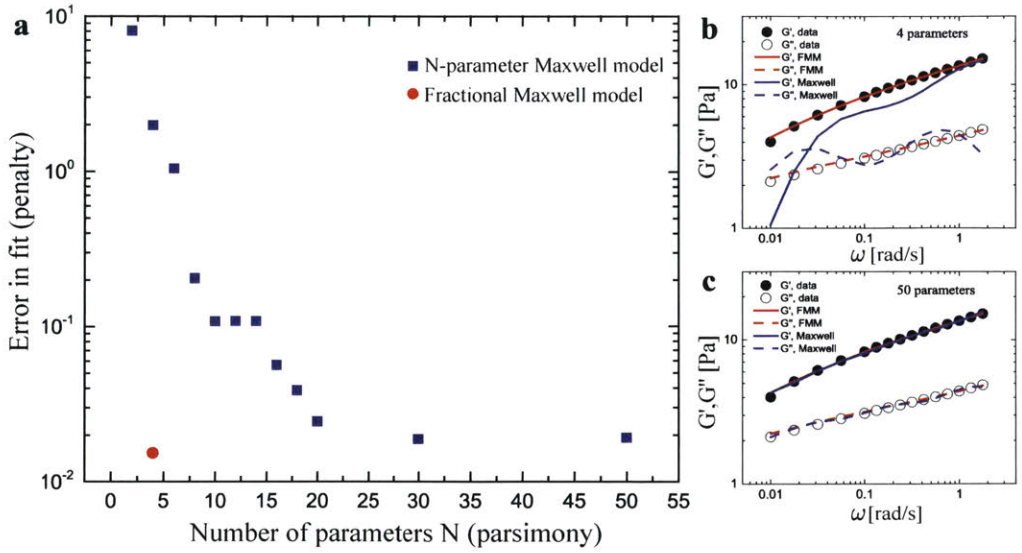

Figure 6.2.2: Comparison of the goodness of fit for M-mode Maxwell models against the FMM, as fitted to experimental SAOS data for $c = 1.2\,\text{wt}\,\%$ TUC. In (a), the error (penalty function) is plotted as a function of the number of model parameters N (parsimony) for both models. In (b) and (c), the predictions of the 4 parameter FMM (red lines) and the experimental data (circles) are plotted, along with the model predictions for an M = 2 mode (N = 4 parameter) Maxwell model (b) and an M = 25 mode (N = 50 parameter) Maxwell model (c) (blue lines).

The results in Figure 6.2.2 demonstrate the superiority of the FMM over all M-mode Maxwell models tested. Further, for the same number of parameters, the FMM performs almost two orders of magnitude better (as measured by the error in fit) than the M = 2-mode (N = 4-parameter) generalized Maxwell model. These data also indicate that the cost function of the M-mode Maxwell model converges nearly quadratically to a limiting plateau error value (at around 20 parameters or 10 modes). Note that even with 50 parameters the Maxwell model exhibits a greater error than the FMM. We communicate the effect of these errors in Figures 6.2.2b and 6.2.2c, showing the performance of the FMM and 2-mode Maxwell model (both having four parameters) in Figure 6.2.2b, and the FMM with a 25-mode Maxwell model (both having similar values of the penalty function) in Figure 6.2.2c, along with the data to which each model is fitted.

For some of the food solutions we consider in this study, large degrees of shear thinning result in the solvent viscosity playing an important role in the non-linear steady state flow response, particularly at high shear rates. In order to account for this, we introduce a purely viscous element (a dashpot) in parallel with the FMM mechanical elements, resulting in the fractional Jeffreys model (FJM), shown schematically in Figure 6.2.1b. The effect of this modification is to guarantee a plateau in the viscosity at high shear rates, η_s, and also results in a linear increase in the loss modulus ($G''(\omega)$) measured in Small Amplitude Oscillatory Shear (SAOS) flow at high frequencies. Analysis of the frequency response using Fourier transforms results in the addition of a purely imaginary term in the complex modulus that

is linearly proportional to the oscillation frequency:

$$G^*_{FJM}(\omega) = \frac{\mathbb{V}(i\omega)^\alpha \mathbb{G}(i\omega)^\beta}{\mathbb{G}(i\omega)^\alpha + \mathbb{V}(i\omega)^\beta} + i\eta_s\omega. \tag{6.6}$$

In order to select the best model (FMM or FJM) for each food solution, both models were fit to the SAOS data using the Matlab function *fminsearch* with the criterion of minimizing the error defined in Equation (6.5). Subsequently, the model with the lower fitting error ϵ_N was selected as the optimal choice for the given food solution, where

$$\epsilon_N = \frac{1}{2n_{\text{data}}} \sum_{i=1}^{n_{\text{data}}} \left(\frac{|G'_i - G'_{i,\text{fit}}|}{G'_i} \right) + \left(\frac{|G''_i - G''_{i,\text{fit}}|}{G''_i} \right) \times 100\% \tag{6.7}$$

is a modified version of Equation (6.5) which estimates the average percent error of the model at each data point. The two exceptions were the okra and chia solutions, for which the low values of the viscoelastic moduli limited the range of frequencies over which $G'(\omega), G''(\omega)$ could be measured. In these cases, the FJM was used (despite it showing a slightly higher ϵ_N) in order to more faithfully reproduce the shear viscosity data. Further discussion of this is provided in Section 6.4.2.

In the next section, we use these fractional constitutive models to fit both the linear and non-linear experimental rheological data for the TUC solutions at various concentrations, and demonstrate how the values of the quasiproperties resulting from the model fits can serve as indicators of food texture.

6.3 Fractional rheological modeling of aqueous solutions of Resource ® Thicken Up Clear

6.3.1 Linear rheology of TUC

We begin by measuring the rheological response of solutions of various concentrations of TUC under the linear deformation of Small Amplitude Oscillatory Shear (SAOS). This particular fluid was selected as a 'benchmark' as a result of its shelf-stability, well controlled and constant composition, and reproducible rheological properties. Strain sweep experiments (not shown) indicate that the linear viscoelastic regime for TUC solutions extends to $\gamma \lesssim 5\,\%$, with some small amount of variation between the various concentrations. As such, each SAOS measurement was performed at a strain amplitude within this calculated range, varying between $1\,\% \lesssim \gamma \lesssim 3\,\%$ for all TUC solutions tested. The results of these measurements are shown in Figures 6.3.1a and 6.3.1b.

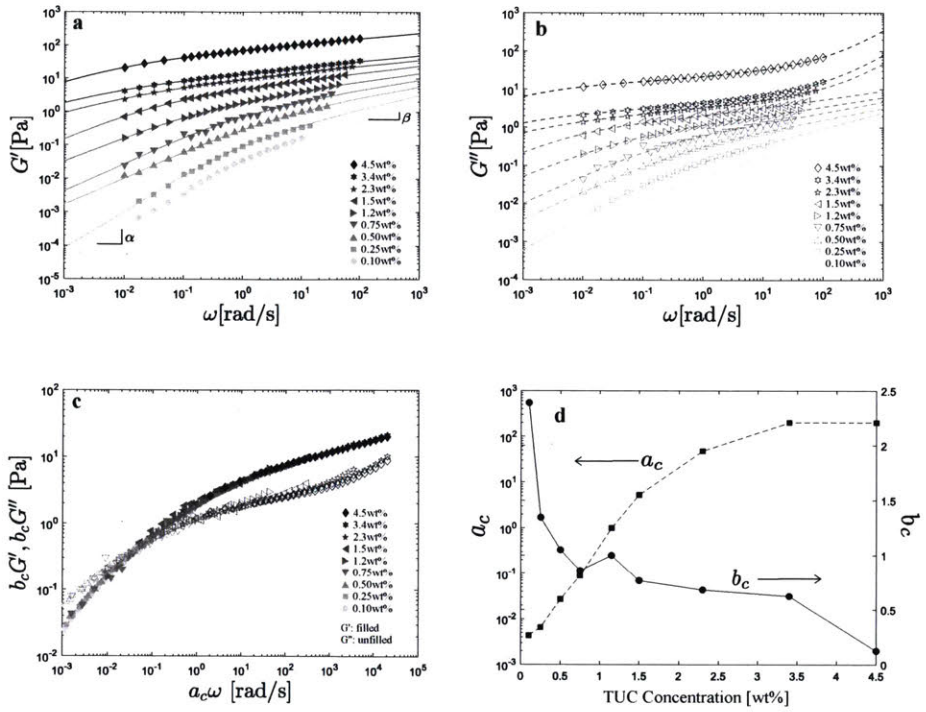

Figure 6.3.1: (a) Storage modulus $G'(\omega)$ and (b) loss modulus $G''(\omega)$ for the TUC solutions. The symbols denote the experimentally obtained data and the solid and dashed lines denote the model fits, with individual parameter values specified for each concentration in Table 6.1. The data from Figures (a) and (b) are shifted to form a master curve using the $c = 1.2\,\text{wt}\,\%$ preparation of TUC as a reference. The frequency is reduced using a shift factor a_c and the moduli $G'(\omega)$ and $G''(\omega)$ are reduced using a common shift factor b_c. The master curves are shown in (c), and the shift factors are plotted as a function of TUC concentration in (d).

Using the principle of Time-Concentration-Superposition [186, 187, 188], the data from Figures 6.3.1a and 6.3.1b are collapsed against the $c = 1.2\,\text{wt}\,\%$ preparation of TUC. For each of the other TUC concentrations, an appropriate shift factor a_c is determined which reduces the frequency of the SAOS data $\omega_r = a_c\omega$, as well as a vertical shift factor b_c which is taken to be the same for both G' and G'' [188]. The rheological master curves resulting from this superposition are shown in Figure 6.3.1c, where it is clear that the linear viscoelastic response of all concentrations of TUC can be neatly collapsed to single curves for $G'(\omega_r)$ and $G''(\omega_r)$ respectively. In Figure 6.3.1d, we plot these shift factors as a function of TUC concentration. As expected, the vertical shift factor b_c is a nearly monotonically decreasing function of concentration. The frequency shift factor a_c initially exhibits a strong dependence on the solution concentration, but appears to saturate (or, possibly, to shift outside of the experimental range) at high concentrations ($c \gtrsim 2\,\text{wt}\,\%$) as the complex modulus data becomes increasingly power law-like. This change in the shape of the G'' curves between the terminal and high frequency regions has been reported previously in the literature for polystyrene solutions above the entanglement concentration [189], suggesting that $c_e \approx 2\,\text{wt}\,\%$ for the TUC solutions. This value is in reasonable agreement with the reported

value of $c_e \approx 0.5\,\text{wt}\,\%$ for pure xanthan gum solutions measured by Choppe et al. [187], given that xanthan gum constitutes only approximately 1/3 of the contents by weight of TUC [190].

In Table 6.1, the best fitting fractional constitutive model (fractional Maxwell, FMM, or fractional Jeffreys, FJM), the values of all model parameters, and the value of the fitting error ϵ_N are presented for each TUC concentration tested.

Concentration [wt %]	$\mathbb{V}$ [Pa s$^\alpha$]	α	$\mathbb{G}$ [Pa s$^\beta$]	β	η_s [Pa s]	τ_c [s]	f_{50}	ϵ_N [%]	Model
0.10	0.12	0.92	0.12	0.39	-	9.1×10^{-2}	1.0	2.6	FMM
0.25	0.38	0.93	0.23	0.42	-	1.4×10^{-1}	0.95	3.0	FMM
0.50	0.82	0.76	0.78	0.31	-	5.7×10^{-1}	0.88	2.0	FMM
0.75	2.4	0.77	1.3	0.30	-	1.9×10^{0}	0.78	7.5	FMM
1.2	8.2	0.69	2.8	0.25	-	2.1×10^{1}	0.77	0.83	FMM
1.5	48	0.73	5.4	0.23	-	1.1×10^{2}	0.48	3.4	FMM
2.3	95	0.57	10	0.19	3.6×10^{-2}	$1.5\times10^{4*}$	0.41	1.0	FJM
3.4	260	0.60	15	0.18	6.4×10^{-2}	$1.2\times10^{4*}$	0.42	1.1	FJM
4.5	1100	0.62	75	0.17	2.8×10^{-1}	$3.3\times10^{3*}$	0.41	0.43	FJM

Table 6.1: FMM and FJM model parameters for the TUC solutions of various concentration. For each solution, the best fitting model (FMM or FJM) is indicated, along with the quasiproperties $\mathbb{V}$ and $\mathbb{G}$, fractional exponents α and β, and solvent viscosity η_s (when appropriate) obtained from the model fits to the experimental data (Equations (6.1) and (6.6)). In addition, the characteristic relaxation times τ_c (Equation (6.4)) and fitting errors (ϵ_N) for the selected models are shown. Finally, the difference between the Cox-Merz prediction and the measured shear viscosity at $\dot{\gamma} = 50\,\text{s}^{-1}$ is denoted by the parameter f_{50} (see [17] and Section 6.3.2).

It is worth noting, however, that at high TUC concentrations ($c \gtrsim 2\,\text{wt}\,\%$), the crossover frequency $\omega_c = 1/\tau_c$ is below the minimum frequency tested ($\omega_{\text{min}} = 10^{-2}\,\text{rad/s}$). As a result, for these concentrations, τ_c is obtained by extrapolation and is thus less accurately determined. These points are indicated by an asterisk in Table 6.1.

From Table 6.1, we observe that for concentrations $c \lesssim 2\text{wt}\%$, the TUC solutions are better modeled by the FMM than the FJM model. As the moduli of the solutions increase, higher test frequencies can be attained experimentally before the raw phase angle in the linear viscoelastic measurement exceeds 175°. At these high frequencies, the role of the solvent viscosity begins to play an increasingly important role in the SAOS response, and the FJM model (see Figure 6.2.2b), with its additional term accounting for the solvent viscosity, is better able to describe the material response. We anticipate that if the SAOS response for the more dilute solutions at similarly high frequencies were able to be obtained, this same contribution from the solvent viscosity would be observed. From the small values of the fitting error ($\epsilon_N \lesssim 10\,\%$) in Table 6.1 and the fits shown in Figure 6.3.1 (solid (G') and dashed (G'') lines, respectively), it is evident that both models can provide excellent descriptions of the linear viscoelasticity of these xanthan gum-based solutions over a wide range of frequencies ($10^{-2} \leq \omega \leq 10^{2}\,\text{rad/s}$) with a small number of model parameters.

6.3.2 Non-linear rheology of TUC

Following the assessment of the linear rheological response of the TUC solutions using SAOS, steady shear flow measurements were performed to determine the nonlinear viscometric response. In Figure 6.3.2, the results of these measurements are shown using filled symbols.

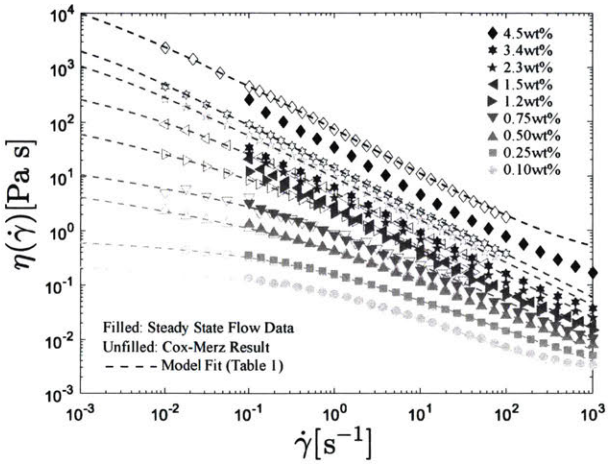

Figure 6.3.2: Steady state flow data for the TUC solutions. The filled symbols denote the data obtained experimentally during a steady state flow experiment, the unfilled symbols denote the calculated Cox-Merz result using the SAOS data presented in Figure 6.3.1, while the lines denote the fractional model predictions, specified for each concentration in Table 6.1.

To describe this nonlinear shear rheology data using our fractional models, we use the empiral Cox-Merz rule which relates the complex viscosity to the shear viscosity through the expression [23, 191]

$$\eta(\dot{\gamma})|_{\dot{\gamma}=\omega} \approx |\eta^*(\omega)|. \tag{6.8}$$

The hollow symbols plotted in Figure 6.3.2 show the magnitude of the complex viscosity [23], calculated from the SAOS data for each fluid using the definition

$$|\eta^*(\omega)| = \frac{\sqrt{G'(\omega)^2 + G''(\omega)^2}}{\omega}. \tag{6.9}$$

Finally, the dashed lines denote the predicted shear viscosity obtained by applying the Cox Merz rule to the complex viscosity calculated from the FMM and FJM expressions for G' and G'' given in Equations (6.2), (6.3), and (6.6). This results in the following expressions:

$$\eta_{\text{FMM}}(\dot{\gamma}) = \frac{\mathbb{V}\mathbb{G}\dot{\gamma}^{\alpha+\beta-1}}{\sqrt{(\mathbb{V}\dot{\gamma}^{\alpha})^2 + (\mathbb{G}\dot{\gamma}^{\beta})^2 + 2\mathbb{V}\dot{\gamma}^{\alpha+\beta}\mathbb{G}\cos(\pi(\alpha-\beta)/2)}} \tag{6.10}$$

and

$$\eta_{\text{FJM}}(\dot{\gamma}) = \frac{\mathbb{V}\mathbb{G}\dot{\gamma}^{\alpha+\beta-1}}{\sqrt{(\mathbb{V}\dot{\gamma}^{\alpha})^2 + (\mathbb{G}\dot{\gamma}^{\beta})^2 + 2\mathbb{V}\dot{\gamma}^{\alpha+\beta}\mathbb{G}\cos(\pi(\alpha-\beta)/2)}} + \eta_s. \tag{6.11}$$

From Figure 6.3.2, it is clear that for the same range of less concentrated TUC solutions for which the FMM model was better suited than the FJM model ($c \lesssim 2\,\text{wt}\,\%$), the magnitude of the complex viscosity is an excellent approximation of the steady state flow viscosity. Furthermore, for $\alpha \neq 1$, there is no predicted low shear rate plateau viscosity: asymptotic analysis of Equations (6.10) and (6.11) shows that the viscosity instead diverges as $\eta(\dot{\gamma}) \sim \dot{\gamma}^{\alpha-1}$ for $\dot{\gamma}\tau_c \ll 1$ although the shear stress still vanishes (as expected at low shear rates) as $\tau_{yx} = \eta(\dot{\gamma})\dot{\gamma} \sim \dot{\gamma}^{\alpha}$. This divergence in shear viscosity with bounded shear stress predicted by the fractional constitutive models is in agreement with what is observed experimentally in many complex biopolymer fluids including saliva and food solutions [17, 192, 193]. Consistent with previous findings for biopolymer solutions, however, as the TUC fluids enter the fully entangled regime ($c > c_e$), the steady shear viscosity predicted using the Cox-Merz rule (Equations (6.10) and (6.11)) begins to systematically overestimate the corresponding experimental measurement [17, 191, 193]. Jaishankar and McKinley show that this is because of chain alignment and disentanglement in strong shearing flows which gives rise to a strain-dependent damping function [17]. To quantify this discrepancy, we follow [17] and calculate an offset factor $f_{\dot{\gamma}} = \eta(\dot{\gamma})/|\eta^*(\omega)|$ which indicates the magnitude of the discrepancy. We evaluate this factor at the shear rate widely deemed relevant for oral evaluation of liquid texture, $\dot{\gamma} = 50\,\text{s}^{-1}$ [176],

$$f_{50} \equiv \left.\frac{\eta(\dot{\gamma})}{|\eta^*(\omega)|}\right|_{\omega=\dot{\gamma}=50\text{s}^{-1}} \tag{6.12}$$

which we also include in Table 6.1. For the lowest TUC concentration ($c = 0.1\,\text{wt}\,\%$), $f_{50} = 1.01$, which is reflected in the excellent agreement between the complex and steady state shear viscosities observed in Figure 6.3.2. As the TUC concentration is increased, f_{50} begins to decrease, and reaches a plateau value of $f_{50} \approx 0.41$ for the most concentrated solutions, comparable to the value computed analytically by Jaishankar and McKinley [17] using a fractional KBKZ model which incorporates a strain dependent damping function. Nevertheless, we see that from a single rheological test protocol (a frequency sweep in SAOS), the FMM and FJM models provide very good estimates of the steady shear viscosity of TUC solutions over a wide range of shear rates from application of the Cox-Merz rule, with a single correction factor arising from strain-dependent damping in the relaxation modulus at high sample concentrations.

As a final result in this section, we collapse the steady shear viscosity data presented in Figure 6.3.2 onto a single master curve, using the concentration-dependent shift factors shown in Figure 6.3.1d that were determined from the linear viscoelastic measurements. From Equation (6.9), it follows that the shifted or reduced value of the steady shear viscosity η_r predicted by the Cox-Merz rule is given by

$$\eta_r(a_c\dot{\gamma}) = \frac{\sqrt{(b_cG'(a_c\dot{\gamma}))^2 + (b_cG''(a_c\dot{\gamma}))^2}}{a_c\omega} = \frac{b_c}{a_c}|\eta^*(a_c\dot{\gamma})|. \tag{6.13}$$

In Figure (6.3.3), we plot the shifted experimental steady state flow data (solid symbols), the shifted values of the dynamic viscosity predicted from the Cox-Merz rule (Equation (6.9), unfilled symbols), and the shifted predictions of the FMM/FJM models (dashed lines) evaluated using Equation (6.13) and the model parameters in Table 6.1. For the sake of clarity and preserving readability, we only show alternate values of the nine TUC concentrations for which steady shear viscosity was collected.

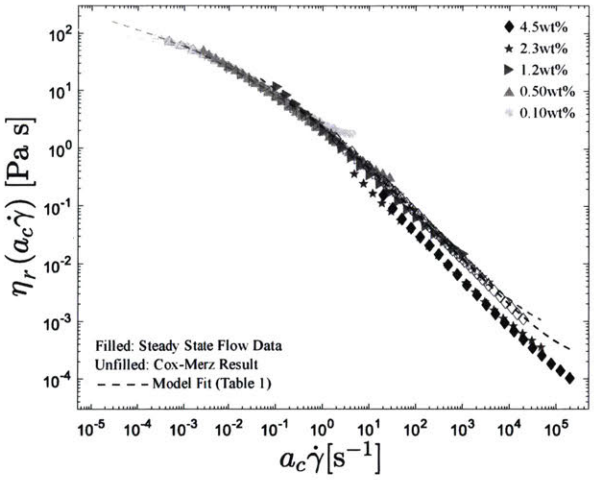

Figure 6.3.3: Master curve for steady state flow data of TUC solutions. Only alternate concentrations are shown for clarity. The shift factors a_c and b_c are those determined previously for the G', G'' master curve. The filled symbols denote the data obtained experimentally during a steady state flow experiment, the unfilled symbols denote the calculated Cox-Merz result using the linear viscoelastic data presented in Figure 6.3.1, and the lines denote the fractional model predictions using Equation (6.13) and the model parameters specified for each concentration in Table 6.1.

As with the linear viscoelastic measurements, the steady shear viscosity data for the TUC solutions collapses quite nicely onto a single master curve. It can be seen, however, that above $a_c\dot{\gamma} \approx 1\,s^{-1}$ the curves appear to separate onto two distinct branches depending on whether their TUC concentration is greater than or less than the estimated entanglement concentration of $c_e \approx 2\,wt\,\%$. In this case, for the entangled TUC solutions, the steady shear viscosities calculated using the Cox-Merz rule once again slightly over-predict the steady shear flow measurements [17, 193], and in fact collapse well onto the master curve defined by the lower viscosity (unentangled) solutions.

Having demonstrated how fractional constitutive models can accurately and parsimoniously describe both linear viscoelastic and steady shear rheology data, in the next section, we apply this same framework towards modeling the rheological response of other selected plant extracts whose constituent carbohydrate biopolymers have been previously reported to impart significant viscoelasticity, and to human whole saliva, which is of keen interest in the study of mouth-feel and food textural perception [131].

6.4 Rheology of food biopolymer solutions and saliva

In this section we use the fractional constitutive models discussed previously to model the rheological response of food biopolymer solutions including two galactomannan heteropolysaccharide solutions: 0.4 wt % tara gum procured from TIC Gums (White Marsh, MD) (3 : 1 ratio of mannose : galactose along its backbone [194]) and 0.5 wt % guar gum procured from Sigma Aldrich (St Louis, MO) (2 : 1 ratio of mannose : galactose along its

backbone), as well as extracts from chia seeds, flax seeds, okra, and human whole saliva.

The principal polysaccharide of flax seed (75 % by mass), has a molecular weight of MW $\approx$ 1.2 MDa, and is a neutral arabinoxylan (0.24 : 1 ratio of arabinose : xylose), with sidechains consisting of varying galactose and fucose residues [195]. The principal polysaccharide of chia seed has a molecular weight of MW $\approx 0.8 - 2$ MDa and consists of a mixture of xylose and mannose (17 %), glucose (2 %), galacturonic acid (5 %), and arabinose (2 %) [192]. Flax and chia seed extracts were prepared by combining seeds procured from a local grocery store with deionized water at a mass ratio of 1 : 25 for the flax seeds, following Ziolkovska [195], and 1 : 40 for the chia seeds, following Capitani et al. [192]. Both mixtures were then stirred at 300 rpm on a hot plate at 80 °C for 30 minutes. There was little difficulty in separating the flax seeds from the supernatant, which was generally clear of particulates. In contrast, the chia seed solution required straining through a conventional metal kitchen strainer, with scraping used in order to encourage passage of liquids through the mesh, and then filtering using 100 µm filter paper in order to remove large particulate matter. Thermogravimetric analysis using a Perkin Elmer Pyris 1 Thermogravimetric Analyzer (TGA) revealed that the weight percent of solid particulates in the flax seed solutions was approximately 0.4 wt %, but it was not possible to obtain a similar estimate for the chia seed solutions due to the absence of an obvious plateau in the sample weight following evaporation of the water.

The principal polysaccharide found in okra plants has a molecular weight of MW $\approx$ 1.4 MDa, and consists primarily of galactose, rhamnose, and galacturonic acid [196]. Solutions were prepared using fresh okra plants obtained from a local grocery store. Pods were sliced in half lengthwise following removal of the ends, and the seeds and pith were removed as well. The halves were then cut into approximately 2 cm pieces along their cross-section, and combined with deionized water at a mass ratio of 1 : 10 (plant : water). As with the chia and flax seeds, the cut okra mixtures were stirred at 300 rpm on an 80 °C hot plate for 30 minutes. The supernatant was then separated from the plants and centrifuged at 2000 rpm for 4 minutes to remove large particulate matter. A similar TGA analysis approximated the solid mass content of the okra extract at 0.1 wt %.

Saliva samples used in this chapter were obtained without stimulation using the procedure outlined in Frenkel and Ribbeck [87]. Donors were instructed to refrain from eating or drinking for one hour prior to collection. Vacuum was drawn in a closed collection vial using an Amersham VacuGene Pump, into which a tube terminating in the donor's mouth was inserted, and saliva was allowed to accumulate. The collected saliva received no further treatment and was stored at room temperature. Rheological experiments were performed within one hour of collection to ameliorate effects associated with enzymatic degradation of the salivary mucins [133].

6.4.1 Linear rheology of food biopolymer solutions and saliva

We begin by measuring the linear viscoelastic response of the food biopolymer solutions and saliva and show these results in Figure 6.4.1.

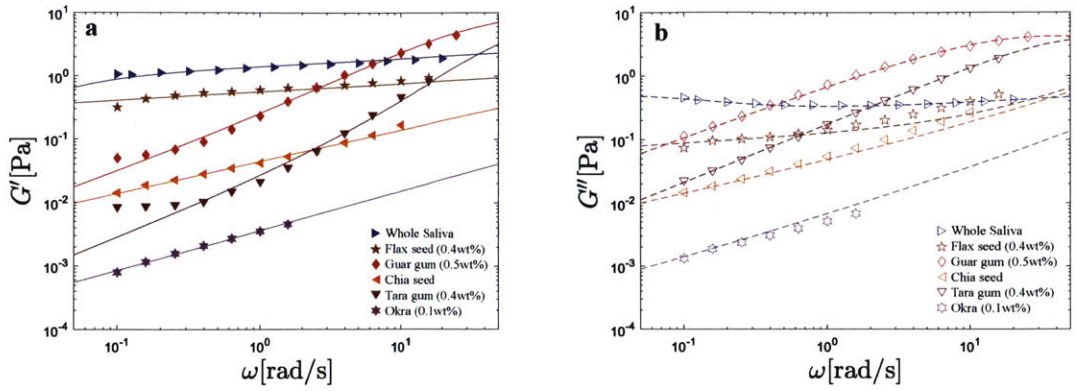

Figure 6.4.1: (a) Storage modulus $G'(\omega)$ and (b) loss modulus $G''(\omega)$ for the food biopolymer solutions and saliva. The symbols denote the experimentally obtained data, while the lines denote the model fits, specified for each sample in Table 6.2. As for the TUC solutions, all SAOS measurements were performed at a strain amplitude within the linear viscoelastic regime of each biopolymer solution as determined by separate strain sweep experiments (results not shown).

Using the same approach as for the TUC solutions, the FMM or FJM was selected for each biopolymer solution, and we indicate the best fitting model and corresponding values of the model parameters plus the corresponding fitting errors in Table 6.2.

Solution	$\mathbb{V}$ [Pa s$^\alpha$]	α	$\mathbb{G}$ [Pa s$^\beta$]	β	η_s [Pa s]	τ_c [s]	ϵ_N [%]	Model
Chia seed	0.00	-	6.1×10^{-2}	0.50	5.0×10^{-3}	-	8.9	FJM
Flax seed (0.4 wt %)	0.00	-	0.56	0.14	9.0×10^{-3}	-	13	FJM
Okra (0.1 wt %)	0.00	-	6.4×10^{-3}	0.62	1.5×10^{-3}	-	11	FJM
Guar gum (0.5 wt %)	0.74	0.83	7.9	8.2×10^{-2}	-	5.6×10^{-2}	7.4	FMM
Tara gum (0.4 wt %)	0.18	0.92	8.7	0.00	-	1.7×10^{-2}	12	FMM
Whole Saliva	37	1.0	1.4	0.13	-	3.2×10^{1}	4.1	FMM

Table 6.2: FMM and FJM model parameters for the food solutions and saliva. The material parameters are defined in Equations (6.2), (6.3), and (6.6).

The chia, flax, and okra solutions are relatively weak gels with low viscosities, and are better fit by the FJM with a single dashpot ($\mathbb{V} \to 0$). In contrast, the 0.5 wt % guar gum and 0.4 wt % tara gum as well as whole human saliva are more broadly viscoelastic over a wide range of frequencies and are thus better fit by the FMM. Additional discussion of the model selection for these materials is provided in Section 6.5.2. As with the TUC solutions, both models are able to reproduce the experimental data for the biopolymer solutions and saliva well, despite the wide range of differing behaviours and magnitudes of the linear viscoelastic properties observed in the two classes of fluids. However, as a result of inertial limitations to the range over which linear viscoelastic measurements could be performed for the low viscosity food solutions, the high shear rate plateau viscosities measured during steady simple shearing flow for the food solutions that are better fit by the FJM were often not observable in the SAOS response. As such, improving the model fit to the shear viscosity data comes

at the cost of poorer agreement with the SAOS data, which explains in part the somewhat higher fitting error ($\epsilon_N \lesssim 15\,\%$) for these solutions. In contrast, for the more viscoelastic TUC solutions, the effects of the background viscosity could be accurately measured for the most concentrated solutions, and the viscoelastic moduli could be accurately measured up to high frequencies in the absence of inertial effects. Consequently, this tradeoff did not exist and the fitting error remained small.

6.4.2 Non-linear rheology of food biopolymer solutions and saliva

In Figure 6.4.2, the steady shear viscosity as a function of shear rate is plotted for the food biopolymer solutions and saliva, with the data divided into two separate plots for clarity. The Cox-Merz rule does a good job of predicting the shear viscosity for the food biopolymer solutions, but it is interesting to note that a significant discrepancy is encountered for whole saliva, as was observed in much more highly concentrated polymer solutions, such as the TUC for $c = 3.4\,\text{wt}\,\%$ or $c = 4.5\,\text{wt}\,\%$ (c.f. Figure 6.3.2). This suggests that despite its low values of steady shear viscosity, during the linear deformations of small amplitude oscillatory shear flow, the physical cross-linking present in saliva from electrostatic and hydrophobic interactions [76] plays an important role in the weak gel-like response measured in oscillatory shear, but these effects are largely eliminated during the large strain deformations associated with steady shear flows [17].

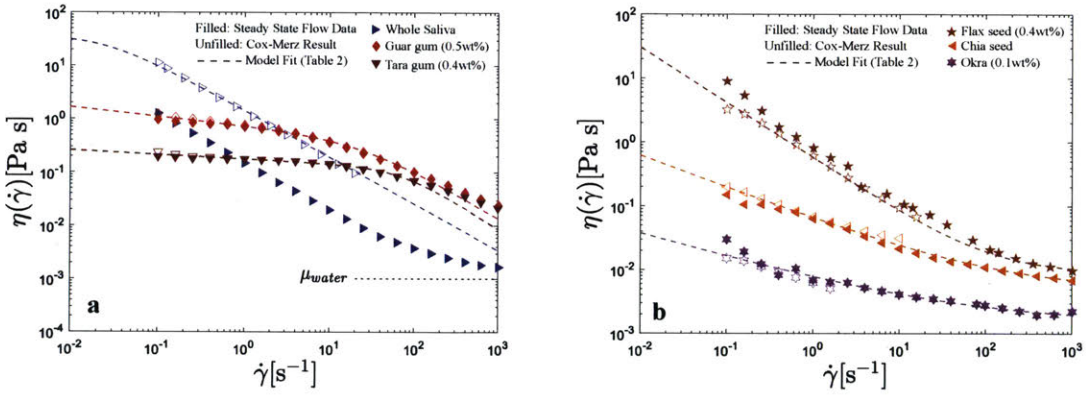

Figure 6.4.2: Steady state flow data for the food biopolymer solutions and saliva, divided into two separate plots (a) and (b) for clarity. The filled symbols denote experimental data obtained from steady state flow, and the hollow symbols denote the calculated values using the SAOS data from Figure 6.4.1 in conjunction with the Cox-Merz rule. The lines denote the model fits evaluated using Equations (6.10) and (6.11), specified for each concentration in Table 6.2.

6.5 Rheological interpretation of food consistency and texture using fractional models

6.5.1 The Nutting Square

In Sections 6.3 and 6.4, the ability of fractional constitutive models to quantitatively describe the rheological response of complex materials using a minimal number of parameters was demonstrated. As first proposed by Scott Blair [197], the magnitude of these parameters can also provide a useful framework for classifying and characterizing complex materials. In order to do so, we begin by considering the general deformation law modified by Scott Blair from the original version proposed by Nutting [40],

$$\psi_\beta = S^\beta \sigma^{-1} t^k, \tag{6.14}$$

where σ is the shear strain, S is the shearing stress, t is time, β is a pressure coefficient that approximates to unity for many materials, k is the coefficient of dissipation, and ψ_β is a measure of the firmness of the material whose units depend on the magnitudes of k and β. This equation has been shown to accurately describe the rheological response of a range of complex materials [13] including rubbers [198], asphalts [199], and thermoplastics [200].

Rewriting Equation (6.14) in terms of the notation introduced earlier in Section 2.2.2 (i.e. $S \to \sigma$ and $\sigma \to \gamma$) and taking $\beta = 1$, we arrive at a modified version of this general deformation law:

$$\sigma = \psi_\beta \gamma t^{-k}. \tag{6.15}$$

Note that we use σ to denote stress here instead of τ (as was used in Section 2.2.2) in order to avoid confusion with the notation used in this chapter for the characteristic relaxation time of the material. In this form, the relationship between Equation (6.15) and the fractional constitutive equations introduced in Section 2.2.2 is more apparent. For instance, for a constant strain $\gamma = \gamma_0$, Equation (6.15) reduces to

$$G(t) = \frac{\sigma(t)}{\gamma_0} = \psi_\beta t^{-k}, \tag{6.16}$$

which is analogous to the relaxation modulus $G(t)$ predicted using a single spring-pot model in response to a step strain experiment [27]

$$G(t) = \frac{\mathbb{V} t^{-\alpha}}{\Gamma(1-\alpha)}, \tag{6.17}$$

where $\Gamma(z)$ is the Gamma function. Similarly for a constant stress σ_0, the expression for the compliance $J(t)$ obtained from Equation (6.15) is

$$J(t) = \frac{\gamma(t)}{\sigma_0} = \frac{t^k}{\psi_\beta}, \tag{6.18}$$

while that predicted by the single spring-pot model is [27]

$$J(t) = \frac{\mathbb{V} t^{\alpha}}{\Gamma(1+\alpha)}. \tag{6.19}$$

Clearly then, the dissipation exponent k is simply the fractional derivative order α, and the parameter ψ_β is a generalization of the quasiproperty V. Scott Blair sought to interpret the relative magnitudes of k, ψ_β, and β in order to substantiate the classification of complex materials according to eight rheological parameters he termed essential: viscosity, elasticity, elastic fore- and after-effects and hysteresis, fall in viscosity with rising stress, tendency of the material to show a true yield value, fall in viscosity or consistency produced by shearing (both non-recoverable and recoverable in a finite time), hardening produced by shearing, and rupture properties [13]. In order to do so, he represented k, ψ_β, and β in a three-dimensional diagram he termed the 'Nutting Square' which is reproduced in Figure 6.5.1 below [13]. The magnitudes of k and β determine the rectangular coordinates in the plane of the page, while the magnitude of ψ_β gives the height above the unit plane.

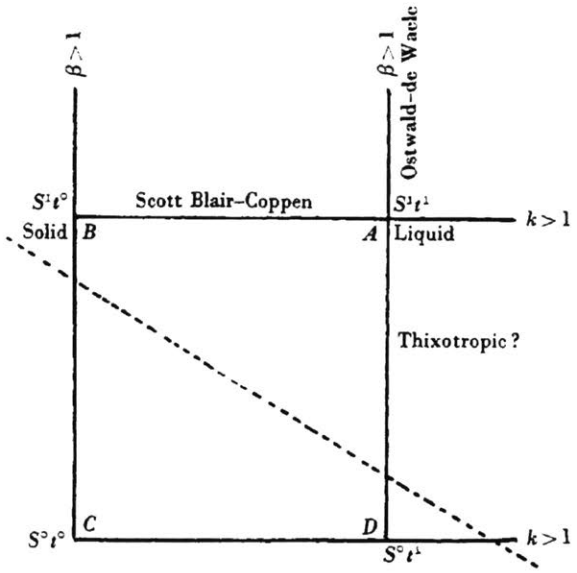

Fig. 1. The Nutting square

Figure 6.5.1: 'Nutting Square' proposed by Scott Blair and Caffyn [13] for representing the properties of complex materials. Reproduced with permission from IOP Publishing.

Focusing on the line defined by $\beta = 1$, we see that the point $A\{k = 1, \beta = 1\}$ corresponds to purely liquid behaviour, while the point $B\{k = 0, \beta = 1\}$ corresponds to purely elastic behaviour. Viscoelastic materials therefore lie on the line defined by $\{0 < k < 1, \beta = 1\}$.

In the section to follow, we use these concepts to develop a material parameter space for quantifying food texture, which is, in effect, a two-dimensional plane of the Nutting Square corresponding to $\beta = 1$. We show that by representing the parameters of the fractional constitutive models that describe the food solutions at a shear rate of $\dot{\gamma} = 50\,\mathrm{s}^{-1}$ in this way, both the elastic and viscous characters of the food solutions can be succinctly captured, which allow for a more precise quantification of food texture.

6.5.2 Development of a material parameter space for quantifying food texture

The selection of $\dot{\gamma} = 50\,\mathrm{s}^{-1}$ as the shear rate at which viscosity measurements are performed for food texture characterization (including for the 'nectar', 'honey', and 'pudding' standards set by the NDDTF for starch-based solutions discussed earlier [163]) is generally attributed to the approach devised by F.W. Wood for analyzing his early food sensory panel data [176]. Although Wood acknowledges that 'simple viscosity measurements cannot be used directly to assess the consistency of liquid foods' [176], partially as a result of the different ways that food is handled in the mouth, he nevertheless felt that the range of shearing stresses accessible in the mouth during food consumption must be universal enough for simple characterizations to be meaningful [176]. Consequently, he asked panelists to taste various soups and sauces, and to indicate the Newtonian fluid to which each was closest in consistency [176]. By measuring the steady state flow properties of each of these non-Newtonian soups and sauces, he determined that $\dot{\gamma} = 50\,\mathrm{s}^{-1}$ was the shear rate at which the viscosity of the liquid foods most often matched that of the Newtonian standard to which they were compared, and thus concluded that this must be a relevant characteristic shear rate for food processing in the mouth [176].

In addition to selecting a Newtonian fluid of comparable consistency, many of the panelists in Wood's study reported that they forced the cream or soup to flow by squeezing it between the tongue and the roof of the mouth by raising the tongue suddenly [176]. Interestingly, this selection of a high frequency deformation to comparably assess the various liquid foods is consistent with what is known about the flow behaviour of polymer solutions at different concentrations. As evidenced in Figure 6.3.2, as the concentration of a polymer solution is increased, the onset of shear thinning begins at successively lower shear rates [201]. This can be understood by considering the Weissenberg number $\mathrm{Wi} = \dot{\gamma}\tau_c$ for each of these steady state flow curves; a dimensionless parameter quantifying flow nonlinearity that combines the rate of an imposed deformation ($\dot{\gamma}$) and the characteristic relaxation time of the fluid (τ_c). For $\mathrm{Wi} \ll 1$, or relatively weak flows, molecular deformations are able to relax sufficiently quickly to avoid being deformed by the flow, and as a result the fluid behaves essentially in a Newtonian fashion corresponding to the zero-shear-rate plateau. Conversely, once the timescale of rearrangement or relaxation of the constituent polymers exceeds that associated with flow deformation, i.e. $\mathrm{Wi} \gtrsim 1$, the chains are not able to relax sufficiently quickly and thus are forced to align and deform in the flow direction, resulting in the progressive decrease in the fluid viscosity, or shear thinning.

Adam and Delsanti have shown that as the concentration of a polymer solution increases and the chains begin to interact and entangle, the longest viscoelastic relaxation timescale of the fluid scales as $\tau_c \sim (c/c^*)^{3(1-\nu)/(3\nu-1)}$, where c^* is the critical overlap concentration and ν is the excluded volume exponent [202]. Therefore, for more concentrated polymer solutions with higher crossover times τ_c, shear thinning occurs at smaller values of $\dot{\gamma}$, and from Table 6.1, it is clear that satisfying $\dot{\gamma} \gtrsim 11\,\mathrm{s}^{-1}$ results in $\mathrm{Wi} \gtrsim 1$ for all of the TUC solutions. Consequently, at the shear rate of $\dot{\gamma} = 50\,\mathrm{s}^{-1}$ proposed by Wood, it is reasonable to expect that all of the TUC solutions are undergoing nonlinear deformation leading to shear thinning in the fluid viscosity, and thus it seems reasonable to compare fluid properties under these flow conditions. If a much smaller shear rate, say $\dot{\gamma} = 1\,\mathrm{s}^{-1}$, were selected, then the measured physical properties of the less concentrated solutions which have not yet begun to

shear thin may not be directly comparable with those of the more concentrated ones since they are not experiencing comparable perturbations of the underlying fluid microstructure.

We now proceed to show how fractional constitutive models are able to compactly capture a number of these important ideas. First, we note that from Figures 6.3.1a, 6.3.1b, and 6.4.1, it is clear that while multi-mode models such as the FMM or FJM are required to describe the flow behaviour of these food biopolymer solutions over the entire deformation range probed, at frequencies in the vicinity of $\omega \simeq 50\,\mathrm{rad/s}$ (or $\dot{\gamma} \simeq 50\,\mathrm{s}^{-1}$ from application of the Cox-Merz rule), the storage and loss moduli of all of these solutions can also be well approximated locally by even simpler power law viscoelastic relationships. This observation was formalized by Jaishankar and McKinley [17], who demonstrated using Taylor series expansions that in the absence of non-linear damping, the rate-dependent shear viscosity predicted by the FMM and the Cox-Merz rule takes on the limiting expressions of

$$\lim_{\dot{\gamma} \ll 1/\tau_c} \eta(\dot{\gamma}) \approx \mathbb{V}\dot{\gamma}^{\alpha-1} \tag{6.20}$$

and

$$\lim_{\dot{\gamma} \gg 1/\tau_c} \eta(\dot{\gamma}) \approx \mathbb{G}\dot{\gamma}^{\beta-1}. \tag{6.21}$$

Such relationships arise naturally from the response of a single spring-pot or Scott Blair element, for which the complex moduli can be expressed compactly (following [42]) as

$$G^* = i\omega\eta^* = \mathbb{K}\omega^n(\cos(\pi n/2) + i\sin(\pi n/2)). \tag{6.22}$$

This result and others for the single Scott Blair element can be obtained from the expressions given above for the FMM model by setting $\mathbb{V} \to 0$ (plus $\eta_s = 0$ for the FJM). Additionally, for notational uniformity, we have replaced $\mathbb{G}$ with $\mathbb{K}$ and β with n to be consistent with the conventional nomenclature used to describe inelastic power law fluids [23]. The quasiproperty $\mathbb{K}$ is then typically referred to as the 'consistency' of the fluid (with units of $\mathrm{Pa\,s^n}$).

From Equation (6.22), the steady shear viscosity of a viscoelastic material described by a single spring-pot can be calculated using the Cox-Merz rule and the magnitude of the complex viscosity as

$$\eta(\dot{\gamma})|_{\dot{\gamma}=\omega} \simeq |\eta^*(\omega)| = \mathbb{K}\omega^{n-1}. \tag{6.23}$$

Equation (6.23) implies that iso-viscosity curves for a specified viscosity value (denoted generically by the value $\hat{\eta}$) can be plotted for fixed values of $\dot{\gamma}$ as a function of $\mathbb{K}$ and β. Selecting the shear rate of interest $\dot{\gamma} = 50s^{-1}$ and a viscosity value $\hat{\eta}$, Equation (6.23) reduces to the constraint

$$\hat{\eta} = \eta(\dot{\gamma} = 50s^{-1}) = \mathbb{K}(50)^{n-1}. \tag{6.24}$$

Solving for n as a function of $\mathbb{K}$ yields

$$n = [1 + \log\hat{\eta}/\log 50] - \log\mathbb{K}/\log 50. \tag{6.25}$$

From this equation, it is clear that the slope of these iso-viscosity contours in $\{n, \mathbb{K}\}$

space is set by the desired shear rate of interest, i.e.

$$\left.\frac{dn}{d\log\mathbb{K}}\right|_{\dot{\gamma}=50\mathrm{s}^{-1}} = -\frac{1}{\log 50}$$

and its locus in this space is set by the relative magnitude of $\hat{\eta}$.

Using the limiting expressions for $\eta(\dot{\gamma})$ in Equations (6.20) and (6.21) and the relative magnitude of $\dot{\gamma} = 50\,\mathrm{s}^{-1}$ and the crossover frequency $\omega_c = 1/\tau_c$, we select from Tables 6.1 and 6.2 the quasiproperty and fractional exponent which characterize this high frequency, predominantly elastic response for the TUC solutions, food extracts, and saliva, and plot these values in Figure 6.5.2. We note that for materials described by a single spring-pot (okra, flax, and chia) for which a crossover frequency does not exist, the same quasiproperty and fractional exponent describe the material response for all frequencies of interest and hence first comparing $\dot{\gamma} = 50\,\mathrm{s}^{-1}$ and ω_c is not necessary. For all other materials except tara gum, $\omega_c < \dot{\gamma} = 50\,\mathrm{s}^{-1}$ and hence we take $\mathbb{K} = \mathbb{G}$ and $n = \beta$, while for tara gum we select $\mathbb{K} = \mathbb{V}$ and $n = \alpha$. In this viscoelastic power law space which is parametrized by the values of $\{n, \mathbb{K}\}$, the lower ordinate axis ($n = 0$) corresponds to the limit of a Hookean solid, and then the abscissa corresponds to the magnitude of the elastic shear modulus $\mathbb{K} = G$. Similarly, the upper ordinate axis $n = 1$ corresponds to the limit of a Newtonian liquid, and then the abscissa corresponds to the viscosity $\mathbb{K} = \eta$. The interior of this parameter space describes in a compact fashion the viscoelastic response of power law fluids. We also plot iso-viscosity contours in Figure 6.5.2 (the border lines of the shaded regions) corresponding to the textures named 'nectar', 'honey', and 'pudding' for weakly shear thinning starch solutions specified by the NDDTF.

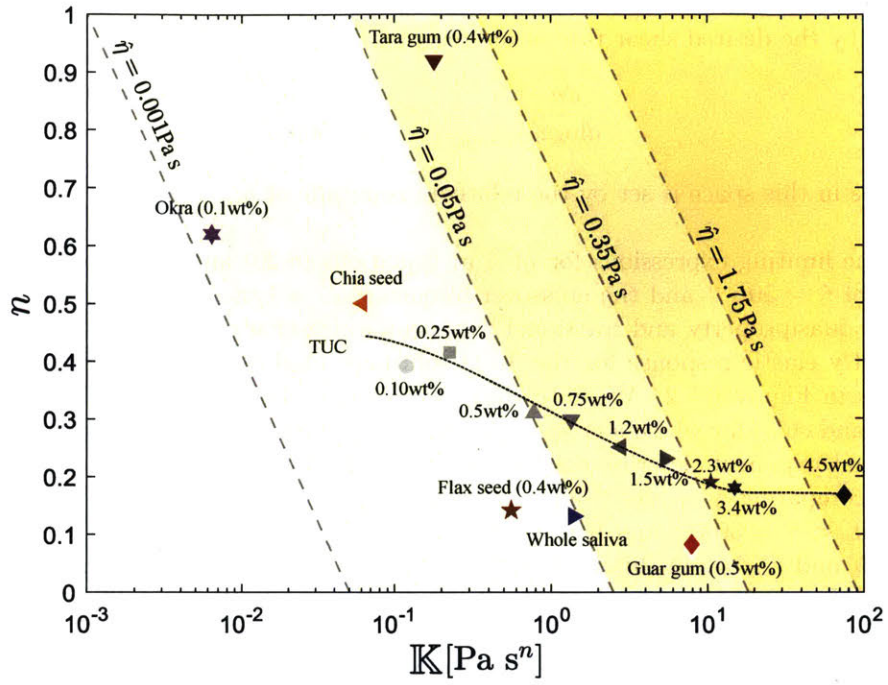

Figure 6.5.2: Fractional parameter phase space for food consistency. The markers correspond to the values of the quasiproperty $\mathbb{K}$ and fractional exponent n best describing the shear-thinning in the steady shear viscosity of the TUC solutions, food extracts, and whole saliva at $\dot{\gamma} = 50\,\mathrm{s}^{-1}$. The dashed diagonal lines bordering the shaded regions denote iso-viscosity curves at $\dot{\gamma} = 50\,\mathrm{s}^{-1}$ corresponding to the 'nectar', 'honey', and 'pudding' preparations of starch solutions by the NDDTF. The line connecting the TUC solution markers is a guide for the eye.

As shown in Figure 6.5.2, as the concentration of TUC is increased, the quasiproperty $\mathbb{K}$ increases monotonically, affirming its interpretation as an indicator of the viscoelastic modulus of the solution $|G^*| \simeq \mathbb{K}(50)^n$. In conjunction, the fractional exponent n begins at a value of $n \approx 0.40$ for low concentrations, somewhat below the Rouse limit (corresponding to $n = 1/2$ [184]), and then decreases as the TUC concentration is increased before leveling off at a high-concentration plateau of $n \approx 0.18$. A dashed line indicating these trends has been added to the TUC data in Figure 6.5.2 as a guide for the eye. It is instructive then to consider the location of the different food extracts and saliva in comparison to this family of TUC solutions. The dependence of the viscoelastic moduli of human whole saliva, flax seed extract, and guar gum on frequency (for frequencies $\omega \approx 50\,\mathrm{rad/s}$) is weaker than those of the most concentrated TUC solutions ($n \approx 0.13$), consistent (from Equation (6.24)) with higher levels of shear thinning, while the magnitude of their quasiproperty $\mathbb{K}$ is consistent with the TUC solutions of moderate concentrations. The okra and chia seed extracts both exhibit very small values of $\mathbb{K}$, and moderate values of n, near or slightly above the Rouse limit, consistent with classical polymer solutions. Finally, the quasiproperty or consistency $\mathbb{K}$ of the tara gum solution is comparable to those of saliva and the flax seed extract, but its fractional exponent is much higher ($n = 0.92$), corresponding to much lower levels of shear thinning.

Plotting the rheological response of these complex viscoelastic fluids during steady state flow and oscillatory shear in this novel material parameter space allows us to capture both the viscous and elastic characteristics of the fluids, whereas traditional comparison of conventional steady state flow curves or regression to inelastic models such as the Cross or Carreau models fails to discriminate these relevant features. In addition, this representation in $\{n, \mathbb{K}\}$ space makes it strikingly clear that considering the shear viscosity of a solution alone is insufficient to fully characterize its texture. To illustrate this, consider the following exercise. The NDDTF has determined that the lowest shear viscosity at $\dot{\gamma} = 50\,\mathrm{s}^{-1}$ for a food solution to have the texture of a pudding is $\eta(50\,\mathrm{s}^{-1}) = 1.75\,\mathrm{Pa\,s}$. If one were asked to procure a pudding using this criterion, it would be natural to begin with the simplest fluid choice, a Newtonian liquid, and perhaps select maple syrup, which is known to have a viscosity in that range [203]. Since Newtonian fluids are purely viscous, they are characterized using fractional nomenclature as having $n = 1$ and $\mathbb{K} = \mu$. Maple syrup would therefore lie on the line of $\hat{\eta} = 1.75\,\mathrm{Pa\,s}$, at the top of the graph where $n = 1$. Our own experience with eating, however, is likely sufficient to cast doubt on whether maple syrup is the most appropriate choice to mimic a pudding. In more quantitative terms, it appears that a $c \approx 4\,\mathrm{wt}\,\%$ solution of TUC would also satisfy this viscosity criterion, yet its location on the phase space in Figure 6.5.2 is at nearly the opposite end of the ordinate axis, approaching the limit of of $n \to 0$, where a truly 'elasto-plastic' or yield-stress-like response is recovered. More accurate phase boundaries demarcating textures such as 'pudding' must therefore correspond to more complex loci than the straight lines given by Equation (6.25). It appears as well that since the fractional exponents of all of the TUC solutions and human whole saliva lie below $n = 0.5$, an element of elasticity is essential in the development of dysphagia products, which is consistent with the idea that foods that remain in a cohesive 'bolus' are safer and easier to swallow [31].

6.6 Summary

In this chapter we have modeled the linear and nonlinear rheological response of a benchmark viscoelastic liquid food, the dysphagia product Resource ® Thicken Up Clear (TUC), as well as various plant extracts and human whole saliva, using fractional rheological models. Using the Matlab genetic algorithm function, we have shown that the FMM does a *better* and more parsimonious job of capturing the rheological response of the TUC solutions (using a representative concentration of $c = 1.2\,\mathrm{wt}\,\%$) than an N-element Maxwell model consisting of up to 50 true physical elements, justifying the use of this more compact representation even at the expense of possible lost physical meaning [181]. We note, however, that for these biopolymer solutions, the breadth of the viscoelastic spectrum is extremely large. The physical meaning of a model containing 10 modes, or 20 parameters (which is the number required for the multi-mode Maxwell model to begin to be comparable to the FMM in terms of goodness of fit to experimental data), becomes increasingly difficult to interpret and unwieldy to use in simulations of viscoelastic flows.

In addition, we have shown that by expressing the viscosity of these liquid foods at the shear rate of $\dot{\gamma} = 50\,\mathrm{s}^{-1}$ (widely deemed relevant for oral evaluation of liquid texture [176]) in terms of the quasiproperty $\mathbb{K}$ and the fractional exponent n arising from these fractional models, far more information about the nonlinear fluid rheology can be gleaned

than is usually possible from a traditional steady state flow curve. This extension requires no additional material parameters, but just an application of the Cox-Merz rule. For instance, after ascertaining a characteristic deformation rate for the material of interest, the magnitude of the quasiproperty $\mathbb{K}$ can clearly be interpreted as an indicator of the complex modulus of the solution, while n provides a direct measure of the solution elasticity and the degree of shear thinning. Additionally, by considering the location of the different plant extracts and whole human saliva in relation to the dysphagia solutions in the phase space formed by $\mathbb{K}$ and n, we can begin to relate these fractional parameters to textural and oral sensory perception terms such as the concepts of a 'pudding' and a 'nectar' in a useful and quantifiable way. Ultimately, we believe that this fractional constitutive framework could be a useful tool for the interpretation of future sensory studies and in the design of liquid food solutions with specifically tailored consistencies or properties.

7 | Conclusions and future directions

The mechanical properties of biological hydrogels are derived from their polymeric microstructures, and consequently by manipulating the polymer network through mechanisms such as structural changes to the polymer itself or to the environmental conditions (such as pH level or ion concentration), biological gels with a range of different rheological properties can be generated. This is a common strategy in regular physiological function. For instance, local adjustment of the pH and mucin concentration throughout the organ systems of the body results in stiff, elastic mucus gels in the stomach and thin, watery films on the ocular surface. However, numerous pathological conditions also exploit this adaptability, and diseases related to mucus barrier dysfunction range from cystic fibrosis to preterm birth. Because of this interrelationship between mechanical properties and polymeric microstructure, quantification and modeling of the rheological response of these materials can provide insight into the structural changes that may be contributing to altered or impaired function. Consequently, in this thesis we have built on existing experimental and theoretical tools, and developed novel ones, for relating the mechanical properties of biological gels to their microstructure and biological function.

In Chapter 2, we laid the groundwork for the development of these tools by reviewing experimental and theoretical aspects of performing both micro- and macrorheological measurements on biological gels. In Chapter 3, we reviewed the physicochemical properties of mucus and its primary solid component, the glycoprotein mucin, because of its relevance to much of the work presented in this thesis. Further, we explored the use of reconstituted mucin gels as model systems for native mucus. We found qualitative similarities in both the micro- and macrorheology of these two materials under some conditions, but concluded that for certain mucus samples including whole saliva, reconstituted mucin gels do not reproduce the mechanical response of the native tissue. These findings may assist in providing a framework for extending the analysis of experimental observations made in mucin gels, ranging from drug delivery to bulk rheological measurements, to expected outcomes *in vivo*.

We then applied these theoretical and experimental concepts to the study of three biologically relevant complex fluid systems. In Chapter 4, we studied the association dynamics and network structure of reconstituted mucin gels using micro- and macrorheology in order to gain insight into the structure of native mucus. We found that analyses of thermal fluctuations on the length scale of micron-sized particles were not predictive of the linear viscoelastic response of mucin gels. However, when taken together, the results from both techniques provided complementary insight into the structure of the network. Specifically, we demonstrated that macroscopic stiffening of mucin gels could be brought about in different ways by targeting specific associations within the network using environmental triggers

such as modifications to the pH, surfactant, and salt concentration. In order to better understand the disagreement between the micro- and macrorheological response of mucin gels, we next explored three possible mechanisms for the breakdown of the GSER in this system: non-continuum effects, particle-mucin interactions, and sample aging. By varying the size of the microrheological probe particles, we found that non-continuum effects play a sizable role in this disagreement due to microphase separation within the mucin gels under acidic conditions and the presence of localized gel regions of varying stiffnesses. This finding was further supported through imaging techniques and direct visualization of the mucin network using fluorescently labeled peptide probes. We expect that the improved insight into the structure of mucin networks developed in this work will be important for understanding how the rheo-mechanical properties of mucus hydrogels are altered by environmental factors in the context of both regular physiological function as well as pathological and therapeutic agents.

The ability of the mechanical properties of mucus to indicate disease-induced microstructural changes has prompted the use of these samples as diagnostics. For instance, the mechanical properties of cervical mucus change over the course of the menstrual cycle, and ovulation can be tracked quite simply by a qualitative assessment of the extensional rheology of this material [204]. Further, the mechanical properties of cervical mucus have been found to be indicative of preterm birth risk at the macroscopic level [205], and using microrheology significant differences have been found between samples from pregnant and ovulating women, as well as present but non statistically significant differences between samples from women at high and low risk for preterm birth [10]. Consequently, while micro- and macrorheological measurements of mucus appear to be promising diagnostic tools, it is important to consider their experimental limitations. In order to achieve a good signal-to-noise ratio during macrorheological experiments, either a large sample volume or a stiff sample is required. In contrast, native mucus samples are frequently scarce, and depending on their origin can be quite soft. Consequently, although it was shown in this thesis that the macrorheology of mucus and mucin gels can be measured using an 8 mm parallel plate setup requiring only $\approx 15\,\mu l$ of sample, care will need to be taken if statistically significant differences are desired to be inferred between measurements performed under these conditions. In fact, one future direction may be to develop simplified quantitative macrorheological devices with improved signal-to-noise ratios for small test volumes. Such devices may be especially useful if they are designed to be portable in order to perform bedside measurements which would mitigate effects of sample aging and degradation.

Performing particle tracking experiments in mucus samples poses an entirely different set of challenges. The static error of the measurement system imposes a lower bound on particle displacements that can be measured, which translates to an upper bound on the modulus of samples that can be characterized using this technique [19]. For 1 µm particles, this limit has been reported in [19] to be approximately $G_{\max} \approx 1\,\text{Pa}$, which is in reasonable agreement with the static error determined experimentally in Section 2.3.1. Consequently, although the mucin gels considered throughout this thesis have generally been softer than this limit, particularly from a microrheological perspective, native mucus samples and high concentration mucin gels can be expected to exceed it, as demonstrated by some of the samples in Section 3.2.4. Although the static error can be reduced by increasing the exposure time of the camera as was done in [10], this has the negative consequence of increasing the dynamic error of the measurements (see the discussion in Section 2.3.1). Therefore, a useful future extension of this work may be to use alternate, light scattering-based microrheological techniques such

as diffusing wave spectroscopy (DWS) [206] to characterize native mucus samples. For 1 µm particles, the operating range of DWS is reported to be $0.1\,\text{Pa} \lesssim G_{\max} \lesssim 10,000\,\text{Pa}$ [19], although this technique may require larger sample volumes [19]. Another approach may be to employ active techniques such as magnetic-microrheology which can generally enable measurements at larger shear moduli due to the probes being driven by external forces as opposed to thermal forces alone [19]. Such techniques also present the advantage of being able to measure nonlinear material responses which are inaccessible to passive techniques.

Beyond these complications related to the choice of measurement technique, technical challenges were also encountered with the capillary tube setup used for the microrheological experiments presented in this thesis. In a first instance, the need to vortex mix tracer particles into the mucus gels frequently introduced air bubbles into the more viscoelastic samples, which resulted in expansive or contractile motion within the field of view due to buoyancy-driven motion of the bubbles that could not be easily removed during image processing and analysis. Further, in more viscoelastic samples, drift was also a commonly encountered issue, although the mechanism leading to it remains unclear. Although uniform drift can ostensibly be removed using de-drifting algorithms, its presence is nevertheless undesirable, and particularly problematic for longer duration videos. Both of these technical challenges point to potential benefits of modifying the design of the capillary tube setup used here. As possible starting points, the use of devices such as sonicators to remove air bubbles may be a promising approach, although it would be necessary to determine the effect of such a treatment on the integrity of the samples. Further, redesigning the method by which the tubes are sealed may be a solution for reducing drift.

In Chapter 5, we studied the temporal stability of saliva using both shear and extensional macrorheological measurements, and found that while the shear rheology was quite insensitive to sample age over a 24 hour period following sample collection, the filament thinning dynamics varied dramatically, with the characteristic relaxation time of the saliva and the breakup time of a fluid thread decreasing significantly with sample age. We interpreted our results within the framework of a Sticky Finitely Extensible Network (SFEN) model which respects the known physical dimensions and properties of the mucin molecules in saliva, and models them as a network of physically associating and finitely extensible polymer chains. Our model predicts an initially strain-hardening response in the transient extensional rheology, followed by a sudden extensional thinning and filament rupture as the chains approach their maximum extensibility and the tension between junction points increases rapidly. We showed that the model can accurately capture the changes observed in the filament thinning dynamics with sample age by incorporating a steady decrease in the molecular weight of the supramolecular aggregates of mucin. Our findings in this chapter highlight the sensitivity of saliva to degradation, and demonstrate the importance of considering sample age and enzymatic degradation when reporting extensional rheological measurements of saliva.

Interestingly, one of the short-comings of the SFEN model is that, while it can accurately capture the filament thinning dynamics of saliva under uniaxial extensional flows, it does not predict the power law responses in the linear viscoelastic moduli observed experimentally during SAOS. Physically, associative biopolymer networks such as mucin generally possess hierarchical microstructures with complex topologies formed from numerous different moieties which permit intermolecular associations of different strengths. During the large, non-linear deformations associated with filament thinning experiments, significant

network stretching and segmental flow alignment reduces the relative importance of these physically-associated supramolecular relaxation modes, and a single characteristic time-scale is sufficient to adequately model the fluid response, as demonstrated by success of the SFEN model in extension. Groot et al. [207] have shown by solving the Smoluchowski equation for small deformations that physical association dramatically broadens the linear viscoelastic spectrum, and consequently we expect that incorporating a broad range of network association strengths into the SFEN model may improve its predictive ability for linear viscoelastic measurements. In order to be able to do so, a better understanding of the number of interaction sites on mucin molecules as well as the range of interaction strengths between cross-links will be beneficial. We acknowledge, however, that such measurements are difficult to make on these structurally complex molecules.

As a final system, in Chapter 6 we developed a fractional calculus-based framework for improving the quantification of the mechanical properties of polysaccharide-based food solutions in order to facilitate the development of specific textures for liquid food consumption and for the design of dysphagia products. We demonstrated that fractional rheological models, including the fractional Maxwell model (FMM) and the fractional Jeffreys model (FJM), are able to succinctly and accurately predict the linear and nonlinear viscoelastic response of a range of liquid food solutions. These included a benchmark fluid, the dysphagia product Resource ® Thicken Up Clear, various plant extracts whose constituent polysaccharides have been reported to impart significant viscoelasticity, and human whole saliva. These fractional constitutive models quantitatively describe both the linear viscoelasticity of all of the liquid foods as well as the shear thinning of their steady shear viscosity (through application of the Cox-Merz rule), and outperform conventional multi-mode Maxwell models with up to 50 physical elements in terms of the goodness of fit to experimental data. Further, by accurately capturing the shear viscosity of the various liquid food solutions at the shear rate of $\dot{\gamma} = 50\,\mathrm{s}^{-1}$ (widely deemed relevant for oral evaluation of liquid texture), we showed that two of the constitutive parameters of the fractional Maxwell model can be used to construct a state diagram that succinctly characterizes both the viscous and elastic properties of the different fluids. Our work has laid the foundation of an improved framework for assigning quantitative values to largely heuristic food textural terms, which may improve the design of future liquid foods of specific desired consistencies or properties.

The three case studies in this thesis have demonstrated the usefulness of measuring the mechanical properties of biological gels in the context of interpreting their microstructures and function. The analytical tools that have been developed here are broad in their scope, ranging from the adaptation and development of polymeric constitutive models to microrheological analysis. Consequently, we expect that the findings of this thesis will provide a starting point for interpreting the mechanical properties of a variety of complex fluids in a broad range of contexts.

A | Supplementary information to Chapter 4

A.1 Matlab code for calculation of the MSD with non-constant camera frame rate

The following is a reproduction of the publicly available Matlab code 'Kehl.m' uploaded by the user Maxime Deforet. It is available at https://www.mathworks.com/matlabcentral/fileexchange/41858-kehl-a-fast-no-loop-method-to-compute-msd.

```
function [MSD,tau] = Kehl(Trajectory)

% Kehl.m measures the mean squared displacement (MSD) from a trajectory.
% Kehl is written by Maxime Deforet, May 21 2013. MSKCC.
% Contact : maxime.deforet@gmail.com

% This code contains no loop. Each step is "vectorized", therefore pretty
% fast.
% The idea is to compute all the possible pairings in only one time.

% Trajectory = list of T positions (x,y,t). Or (x,t) or (x,y,z,t) or even
% higher dimension (x1,x2,x3,...t)
% tau is the list of all the possible time intervals within the trajectory.
% MSD is a list of mean squared displacements, for each value of tau.

% MSD(tau) = sqrt( x(i)^2 - x(i+tau)^2 ), averaged over i.

T =  size(Trajectory,1); % T is the number of point in the trajectory;

[ I j ] = find(triu(ones(T), 1)); % list of indices of possible pairings
D = zeros(T, T);
D( I + T*(j-1) ) = (sum(abs( Trajectory(I,1:end-1) - Trajectory(j,1:end-1) ).^

% Time intervals between the two points of each pairing :
dt = zeros(T, T);
dt( I + T*(j-1) ) = -( Trajectory(I,end) - Trajectory(j,end) );
```

```
% Then D is a list of squared distances. dt is a list of corresponding
% time intervals. Now we have to average all D values over different dt
% values

% We first remove all 0 values from dt matrix, and from D as well.
idx_0=find(dt==0);
dt(idx_0)=[];
D(idx_0)=[];

% Then we sort dt in ascending order, and sort D in the same way.
[DT,idx]=sort(dt(:));
DD=D(idx);
% We now have DD and DT, respectively a list of squared distances, and
% the corresponding time intervals.

% Now we have to compute the mean DD for each possible value of DT.
% Let's get the first and last indices of each set of DT
First_idx=find(DT-circshift(DT,1)~=0);
Last_idx=find(DT-circshift(DT,-1)~=0);
% For instance, DT=1 start at First_idx(1) and end at Last_idx(1)
%               DT=2 start at First_idx(2) and end at Last_idx(2)...

% To get the average, we first compute the cumulative (starting from 0), then we
% get "the derivative of the cumulative".
C=cumsum([0,DD]);
% For each possible value of DT, the mean of DD is the difference between
% the initial index and the last index of the cumulative, divided by the
% number of elements between those two indices :
MSD=(C(Last_idx+1)-C(First_idx))'./(Last_idx-First_idx+1);
tau=DT(First_idx); % list of intervals


% plot(tau,MSD)
```

B | Supplementary information to Chapter 5

B.1 Determination of the microstructural deformation at the transition point between regimes I and II

In a previous study of the filament thinning dynamics of FENE-P fluids, Wagner et al. [150] have provided an implicit analytic expression for the axial microstructural deformation A_{zz}^* at the transition between the viscocapillary filament thinning regime (I) and the elastocapillary regime (II). This result is constructed by equating the expressions for the filament thinning rate $\dot{\epsilon}$ and the axial microstructural deformation A_{zz} during regimes I and II at the transition time t^* between the two regimes, as illustrated in Figure B.1.1a.

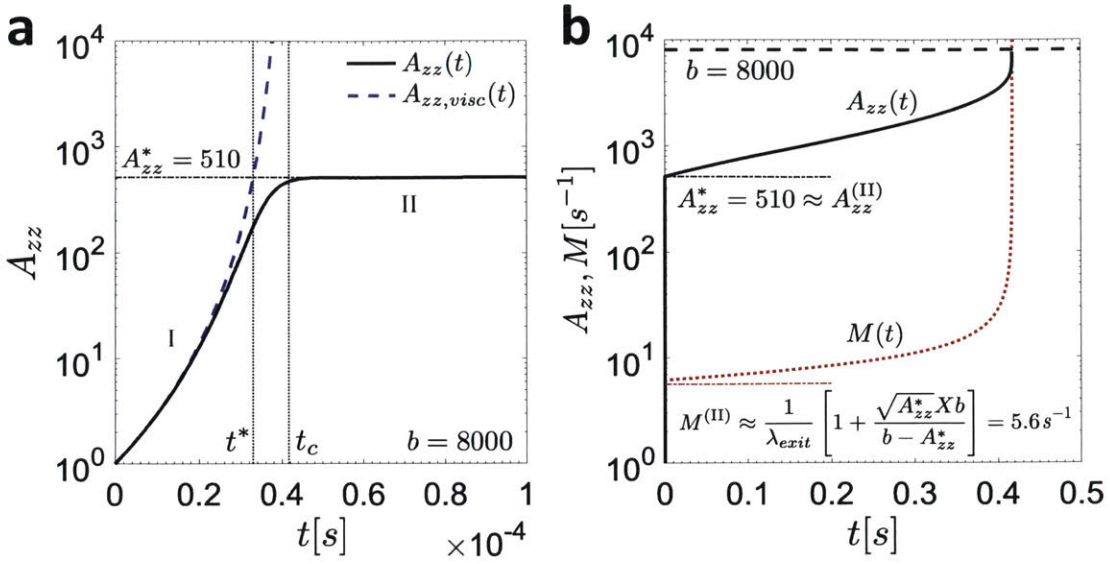

Figure B.1.1: (a) Evolution of the axial microstructural deformation A_{zz} (solid black curve) near the transition time t^* between regimes I and II. The curve corresponding to the analytic expression for A_{zz} during the viscocapillary regime (Equation (B.3)) is shown as the dashed blue line, and the approximate value of A^*_{zz} calculated using the method outlined in Wagner et al. [150] is shown as the black dashed-dotted line. (b) Full temporal evolution of A_{zz} (solid black line) and the network junction destruction rate M (dotted red line) for the model parameters in Table 5.2 corresponding to $t_{age} = 0\,\text{h}$ ($b = 8000$, $\lambda^{-1}_{exit} = 3.8\,\text{s}^{-1}$). The value of the finite extensibility $b = 8000$ is shown as the black dashed line, and the approximate values of $A^{(II)}_{zz}$ and $M^{(II)}$ at the crossover from regime I to regime II are shown as the dashed-dotted black and red lines, respectively.

During regime I (before the polymer chains experience significant microstructural deformation), the viscous stress of the solvent presents the primary opposition to capillary pressure, and hence Equation (5.22) can be approximated as

$$\frac{\sigma}{R} = 3\eta_s \dot{\epsilon}_{visc}. \tag{B.1}$$

For a low viscosity solvent such as water, this results in a high initial rate of thinning. At the critical time t^* when regime II begins and viscous and polymer stresses are of the same order, Equation (B.1) must hold simultaneously with the complete force balance (suitably modified to account for the previously outlined assumptions valid in the case of negligible sticky effects: $b \gg A_{zz} \gg A_{rr}$, $f \approx 1$ [146]):

$$\frac{\sigma}{R} = 3\eta_s \dot{\epsilon}^* + \nu_a k_B T A^*_{zz}, \tag{B.2}$$

which implies that the strain rate must drop in regime II to some lower value $\dot{\epsilon}^* < \dot{\epsilon}^*_{visc}$. Furthermore, the axial microstructural deformation at the transition time t^* must be continuous between both regimes. It is straightforward to show using Equation (5.20) from the main text (with $M = L = \lambda^{-1}_{exit}$) that during the viscocapillary regime (I), the evolution equation for A_{zz} is given by

$$A_{zz,visc} = \left(\frac{t_c}{t_c - t}\right)^4 \exp\left(-\frac{t}{\lambda_{exit}}\right), \tag{B.3}$$

where t_c is the breakup time of a purely Newtonian fluid $t_c = 6\eta_s R_0/\sigma$ [150] and λ_{exit} is the lifetime of network junctions as defined in Equation (5.30). This result is shown as the dashed blue line in Figure B.1.1a, while the full numerical solution of A_{zz} is shown as the solid black curve. Additionally, as seen in Figure B.1.1a, at the onset of regime II when sticky effects are still negligible, the rate of change of A_{zz} is very small. Hence, using the assumption $dA_{zz}/dt \approx 0$ and the FENE-P evolution equation for A_{zz}, Wagner et al. [150] show that the axial microstructural deformation at the transition between regimes I and II can be written as

$$A_{zz} = b\left(1 - \frac{1}{2\lambda_{exit}\dot{\epsilon}^*}\right). \tag{B.4}$$

Although the FENE-P and SFEN evolution equations for A_{zz} differ (as a result of the incorporation of the network junction destruction (M) and reformation (L) terms in the case of the latter model), numerical simulations reveal that in regime I and early in regime II, before chain stretching and network dissociation effects become important, the approximation in Equation (B.4) is also reasonable for the SFEN model. Therefore, combining and rearranging Equations (B.1)-(B.4), an implicit result for the transition time t^* can be found as:

$$\frac{1}{2}\left(1 - \frac{\exp\left(-\frac{t^*}{\lambda_{exit}}\right)}{b}\left(\frac{t_c}{t_c - t^*}\right)^4\right)^{-1} = \frac{\frac{2\lambda_{exit}}{(t_c - t^*)} + \frac{\nu_a k_B T b \lambda_{exit}}{3\eta_s}}{1 + \frac{2\nu_a k_B T b \lambda_{exit}}{3\eta_s}}. \tag{B.5}$$

Solving this expression numerically for t^* and inserting the result into Equation (B.3) yields the desired value of A^*_{zz}. For the conditions at $t_{age} = 0\,\text{h}$ given in Table 5.2, we find that $A^*_{zz} \approx 510$ and $t^* \approx 0.33 \times 10^{-4}$ s. The elastocapillary thinning regime (II) is thus entered very quickly.

In Figure B.1.1b, the full temporal evolution of A_{zz} is shown for the parameters corresponding to $t_{age} = 0\,\text{h}$ in Table 5.2 as the solid black curve. We note that in order to clearly illustrate the expected evolution of A_{zz} during all filament thinning regimes in Figure B.1.1b, A_{zz} was initialized at its true equilibrium value of $A_{zz}(t = 0) = 1$ as opposed to the slightly higher value chosen in Figure 5.4.1a that accounts for the axial microstructural deformation incurred during the initial period of plate separation during CaBER experiments (which is not accounted for in this asymptotic analysis). As can be seen, the value of A^*_{zz} calculated implicitly provides an excellent approximation for the value of the axial microstructural deformation at the transition point between regimes I and II. Further, the maximum value of A_{zz} at filament breakup is the finite extensibility b (shown by the dashed black line), as expected.

In order to demonstrate how this result is useful for determining the chain segment destruction rate during regime II (denoted $M^{(\text{II})}$ in Section 5.3.2 of the main text), we also plot the evolution of M in Figure B.1.1b as the dotted red line. As can be seen, the assumption of a nearly constant destruction rate $M^{(\text{II})}$ during this regime (calculated using the result for A^*_{zz} as well as Equations (5.23) and (5.24)) is a reasonable one, and the

quantitative agreement between the the full numerical solution for M during regime II and the approximate value of $M^{(\mathrm{II})}$ is quite good. Without the use of Equations 5.23 and 5.24, the equilibrium expression $M_{eq} \approx 1/\lambda_{exit} = 3.8\,\mathrm{s}^{-1}$ significantly underpredicts the exit rate from the network.

B.2 Filament thinning rate in the limit of large sticky effects

We begin by noting that Equation (5.24) can be rewritten in terms of our new stickiness parameter defined in Equation (5.38):

$$\delta = \frac{\sqrt{A_{zz}^{(\mathrm{II})} b}}{1 - A_{zz}^{(\mathrm{II})}/b} Sk = \frac{\sqrt{A_{zz}^{(\mathrm{II})}/b}}{1 - A_{zz}^{(\mathrm{II})}/b} (bSk)\,. \tag{B.6}$$

As sticky effects become increasingly important, the Taylor series expansion for the destruction rate M and the predicted near time-invariance of the number density of bridged sticky segments ν_a (Equations (5.23) and (5.25), respectively) become less and less accurate. Although the first effect is difficult to mitigate due to the large values of b relevant to the biological system in this study, it is possible to address the second and in doing so improve our analytic result during regime II by recognizing that in the limit of large sticky effects, the product of the stress-dependent network dissociation term M and the number density of bridged segments ν_a dominates over the product of the rejoining term L and the number density of dangling segments $(\nu - \nu_a)$. As such, Equation (5.15) is better approximated as

$$\frac{d\nu_a^{(\mathrm{II})}}{dt} \approx -\frac{(1+\delta)}{\lambda_{exit}} \nu_a^{(\mathrm{II})}, \tag{B.7}$$

which can readily be solved to yield

$$\nu_a^{(\mathrm{II})}(t) \approx \frac{\nu}{2} \exp\left(-\frac{t(1+\delta)}{\lambda_{exit}}\right) \tag{B.8}$$

using the same initial condition as before of $\nu_a(t = 0) = \nu_{a,eq} = \nu/2$. In this case, substitution of Equations (B.8) and (5.27) into (5.28) yields a similar expression for the evolution of the filament radius during regime II

$$\xi^{(\mathrm{II})}(t) \approx \left(\frac{E_c}{2}\right)^{\frac{1}{3}} \exp\left(-\frac{2(1+\delta)t}{3\lambda_{exit}}\right), \tag{B.9}$$

although it is clear that now the rate of filament thinning is increased due to sticky finitely extensible segments being pulled out of the network. The network junction exit rate and the filament thinning rate are hence related through:

$$\dot{\epsilon}^{(\mathrm{II})} = -\frac{2}{\xi}\frac{d\xi}{dt} \approx \frac{4}{3}(1+\delta)\lambda_{exit}^{-1}. \tag{B.10}$$

B.3 Comparison of experimental data and SFEN model predictions for shear rheological experiments

In the main text, we discussed the response of the SFEN model to both steady simple elongational flow as well as during the axisymmetric uniaxial elongational flow relevant to CaBER experiments. Here, we consider steady simple shearing flow $[v_x = \dot{\gamma}y, v_y = 0]$ (where $\dot{\gamma}$ is a spatially uniform, constant shear rate) in order to compare the SFEN model predictions with the shear rheological data presented in Figure 5.4.2.

The evolution equations for the microstructural deformation tensor during a transient simple shearing flow are readily found to be

$$\frac{dA_{xx}}{dt} = 2\dot{\gamma}A_{xy} - MA_{xx} + L, \tag{B.11}$$

$$\frac{dA_{xy}}{dt} = \dot{\gamma}A_{yy} - MA_{xy}, \tag{B.12}$$

and

$$\frac{dA_{yy}}{dt} = -MA_{yy} + L, \tag{B.13}$$

where the expressions for M and L are given in Equations (5.11) and (5.12), respectively, and the evolution equation for the number of bridged, active chain segments is given in Equation (5.15). The expression for A_{zz} is identical to the one for A_{yy}. Following the procedure described in the main text, these coupled differential equations can be integrated simultaneously using a numerical solver with the initial conditions $\nu_a = \nu_{a,eq}, A_{xx} = 1, A_{xy} = 0$, and $A_{yy} = 1$ to calculate the response in a simple shearing flow. From the steady state value of A_{xy}, the shear viscosity at a given shear rate can then readily be found from $\eta(\dot{\gamma}) = \eta_s + \tau_{xy}/\dot{\gamma}$, where $\tau_{xy} = \nu_a k_B T f(tr(\boldsymbol{A}))A_{xy}$.

In addition to computing the evolution in the shear viscosity by integrating the above system of equations numerically, a semi-analytic expression can also be developed. We begin by solving Equations (B.11)-(B.13) simultaneously at steady state to obtain expressions for the components of the microstructural deformation tensor:

$$A_{xx} = \frac{L}{M}\left(1 + \frac{2\dot{\gamma}^2}{M^2}\right), \tag{B.14}$$

$$A_{xy} = \frac{\dot{\gamma}}{M^2}L, \tag{B.15}$$

and

$$A_{yy} = \frac{L}{M}. \tag{B.16}$$

To simplify notation, we let $T = tr(\boldsymbol{A}) = A_{xx} + 2A_{yy}$, and note here that the destruction rate $M = M(T)$ only (c.f. Equation (5.11)). From Equations (B.14) and (B.16) we consequently obtain that

$$T = \frac{2\dot{\gamma}^2 L}{M^3} + \frac{3L}{M} = \frac{L}{M}\left(3 + 2\frac{\dot{\gamma}^2}{M^2}\right). \tag{B.17}$$

Rearranging Equation (B.17), an explicit expression for the dependence of the shear rate $\dot{\gamma}$ on the trace of the microstructural deformation tensor can be found as

$$\dot{\gamma} = \frac{M}{\sqrt{2}}\left[\frac{MT}{L} - 3\right]^{1/2}. \tag{B.18}$$

Substituting this expression into Equation (B.15), A_{xy} can similarly be expressed in terms of T only:

$$A_{xy} = \frac{L}{\sqrt{2}M}\left[\frac{MT}{L} - 3\right]^{1/2}. \tag{B.19}$$

By solving for the values of $\dot{\gamma}(T)$ and $A_{xy}(T)$ at various values of T within in its physical range of $3 \leq T \leq b$, the dependence of A_{xy} on $\dot{\gamma}$ can readily be constructed.

In Figure B.3.1, the SFEN model predictions for the shear viscosity $\eta(\dot{\gamma})$ as a function of the shear rate $\dot{\gamma}$ are plotted as dashed lines for each sample age t_{age} at which CaBER experiments were performed using the appropriate model parameters listed in Table 5.2. In addition, we also plot the result of the semi-analytic solution (filled red diamonds) given in Equations (B.18) and (B.19) for the set of parameters from Table 5.2 corresponding to $t_{age} = 0\,\text{h}$, and excellent agreement with the full numerical solution is observed.

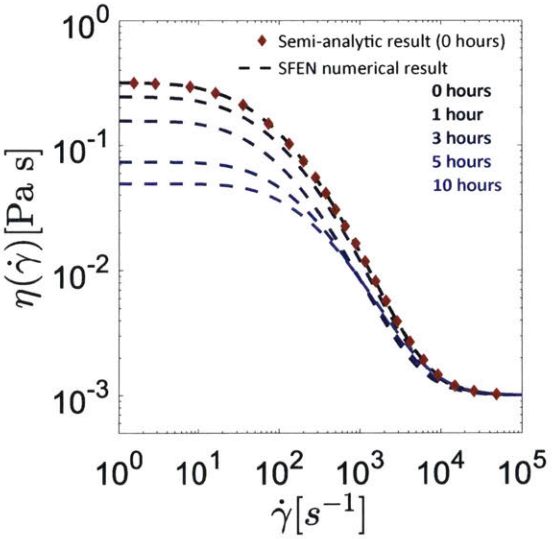

Figure B.3.1: The numerical predictions of the SFEN model under steady simple shearing flow conditions for the parameter sets in Table 5.2 corresponding to all five sample ages at which CaBER experiments were performed (dashed lines). In addition, the the semi-analytic SFEN result for $t_{age} = 0\,\text{h}$ is shown as filled red diamonds.

As can be seen in Figure B.3.1, the largest effect of sample aging predicted by the SFEN

model under steady simple shearing flow conditions is a steady decrease in the zero shear-rate viscosity η_0. This can easily be understood from the limiting expression presented in Section 5.3 for this parameter, $\eta_0 = \eta_s + \nu k_B T \lambda_{exit}/2$, as well as the significant increase in the junction exit rate λ_{exit}^{-1} as a function of sample age reported in Table 5.2. During the regime of strong shear thinning, however, only a minimal variation between the steady state shear flow curves $\eta(\dot{\gamma})$ corresponding to the various sample ages is predicted by the model. This is in keeping with our experimental observation of the shear rheology of saliva being relatively insensitive to sample aging and the associated enzymatic degradation of the mucin macromolecules (Figure 5.4.2), in contrast to the strong decrease observed in its extensional rheology (Figure 5.4.1a).

Although certain features of the experimental steady state flow data (Figure 5.4.2b) are well described by the SFEN model, complete qualitative and quantitative agreement cannot be expected. In particular, the model prediction of a well-defined zero shear-rate viscosity stands in sharp contrast to the experimental data, which suggests that $\eta(\dot{\gamma})$ diverges with a weak power law dependence on the shear rate as $\dot{\gamma} \to 0$. If a zero shear-rate viscosity does exist for the saliva sample at $t_{age} = 0\,\mathrm{h}$, it must occur for values of $\dot{\gamma}$ below the minimum shear rate measured and reported in Figure 5.4.2b, $\dot{\gamma} = 0.1\,\mathrm{s}^{-1}$. Hence, the onset of experimental shear thinning at $\dot{\gamma}^* \lambda_{exit} \approx 1$ would occur at a critical shear rate $\dot{\gamma}^*$ substantially smaller than that predicted by the SFEN model ($\dot{\gamma}^* \approx 10\,\mathrm{s}^{-1}$ for $t_{age} = 0\,\mathrm{h}$). This suggests that the longest relaxation timescale for undegraded saliva under steady state shearing flow conditions is in fact much longer than that derived from the rate of filament thinning during CaBER experiments, $\dot{\epsilon}^{(\mathrm{II})}$, from which the characteristic time scale λ_{exit} of the SFEN model is calculated (Equation (5.30)). This is consistent with the experimental results from several other studies of the shear and extensional rheological properties of associating polymer networks. For instance, Kheirandish et al. found that the longest relaxation time measured in small amplitude oscillatory shear flow was up to two orders of magnitude larger than that measured using CaBER for solutions of hydrophobically modified alkali-swellable emulsion (HASE) polymers [208], and up to four orders of magnitude larger in solutions of their non-hydrophobically modified (ASE) counterparts [209]. We note that the longest relaxation time from shear for the ASE polymer solutions was measured using both small amplitude oscillatory shear flow as well as by fitting a Giesekus model to steady state shear flow data [209]. Similar findings have also been reported in highly viscous alginate solutions by Storz et al. [210] and Rodríguez-Rivero et al. [211].

Physically, biopolymers such as mucin generally possess complex, hierarchical microstructures with numerous types of interaction moieties which enable a range of intermolecular associations of different strengths [76]. Consequently, the rheological response of solutions of such supramolecular assemblies cannot typically be characterized well by a single relaxation mode or timescale [17, 157]. Indeed, using a molecular model for associative polymer networks, Groot et al. have shown that inter-chain physical association dramatically broadens the linear viscoelastic spectrum of these solutions and results in a substantially lower crossover frequency during SAOS [207]. Similarly, using a time marching algorithm that accounts for hindered fluctuations, Ahmadi et al. have shown that the relaxation time of solutions of entangled polymers with sticky side groups increases as the number of stickers is increased [212]. We can expect then that during experiments in which only small, linear deformations are imposed, the incorporation of this broad spectrum of relaxation modes into the constitutive model will be essential for quantitative predictions of experimental data.

By contrast, during the large, non-linear deformations associated with filament thinning experiments and also in high shear rate steady state flow measurements, significant network stretching and flow alignment disrupts these slow supramolecular relaxation modes, and a single characteristic time-scale (such as λ_{exit} in the case of the SFEN model) is sufficient to characterize the fluid rheological response. Finally, the SFEN model assumes that only bridged segments contribute to the polymer stress response, when in reality a variety of configurations and multichain structures which all relax and contribute differently to the overall polymer stress are possible for chain segments with functionalized end groups. These configurations, such as loops and higher order bridged structures, have been illustrated in schematic form by Annable et al. [213]. These different supramolecular configurations play an increasingly important role when chain stretch is more modest and junctions are readily both created and destroyed, whereas during large chain stretching and high rates of network destruction, the rheological contributions of these higher order assemblies is expected to be less prominent.

In summary, we note that although the predictions of the SFEN model under uniaxial flow conditions agree quantitatively with our CaBER measurements for saliva and are also in qualitative agreement with our observations in steady state shear flow, the development of a constitutive model capable of quantitatively capturing both the non-linear rheological response of associating polymer networks as well as their very broad relaxation spectra during linear viscoelastic deformations remains an open challenge.

B.4 Effect of varying the SFEN model parameters on the predicted filament thinning dynamics

In Figure B.4.1, we assess the effect of varying the magnitude of the finite extensibility b (B.4.1a), energy well depth ΔG (B.4.1b), energy well width r_c (B.4.1c), and initial filament radius R_0 (B.4.1d) on the filament thinning dynamics predicted by the SFEN model. We do so by plotting the predicted temporal evolution of the non-dimensional filament radius $\xi(t) = R(t)/R_0$ for the original set of parameters given in Tables 5.1 and 5.2 at $t_{age} = 0\,\mathrm{h}$ (solid black curves) as well as when a single parameter among this subset of four variables is varied (dotted red and dashed blue curves).

These particular parameters were selected as a result of the important role they play in setting the key physical groups relevant to the SFEN model: the finite extensibility b and the energy well width r_c strongly influence the magnitude of the dimensionless stickiness parameter Sk defined in Equation (5.38), which dominates the late time asymptotic filament dynamics as evidenced in Equations (5.36) and (5.37). In addition, b fixes the flexibility of the associated mucin molecules, which determines when the onset of non-linear chain stretching and rapid network junction destruction occurs (Equation (5.11)). The capillary pressure σ/R_0 is the driver for filament thinning throughout the CaBER experiment, and thus plays an important role during all four regimes. Finally, the most complex interaction to understand systematically is the role of of the energy well depth ΔG. Naturally, this parameter affects the number of elastically active chain segments ν, as seen in Equation (5.2), although in practice this effect saturates quickly as ΔG grows and $\nu \to n$. We note that although the energy well depth undoubtedly affects the exit rate of network junctions

Ω_{exit} (Equation (5.3)), in experiments with natural or reconstituted biopolymer gel networks such as saliva it is impossible to determine the scale parameter $g(c, M_{W,s})$ (defined in Equation (5.9a)) independently. This is because one cannot easily vary the molecular weight or the mass concentration of a single purified component of these gels (which was possible for solutions of the synthetic linear telechelic block copolymer HEUR chains used in the groundbreaking experiments of Annable et al. [213]). The composite parameter $g(c, M_{W,s})\Omega \exp(-\Delta G/k_B T)$ (see Equation (5.11)) is thus fitted to filament thinning data of the as-constituted mucin network in order to satisfy the relationship between the filament thinning rate in regime II ($\dot{\epsilon}^{(II)}$) and the lifetime of network junctions (λ_{exit}) outlined in Equation (5.30). Therefore, to explore theoretically how changes in the energy well depth of the associative stickers would change the filament thinning rate observed experimentally, we use a *gedankenexperiment* in which we hold $g(c, M_{W,s})\Omega$ constant and vary the well depth by $\pm 1 k_B T$ per molecule.

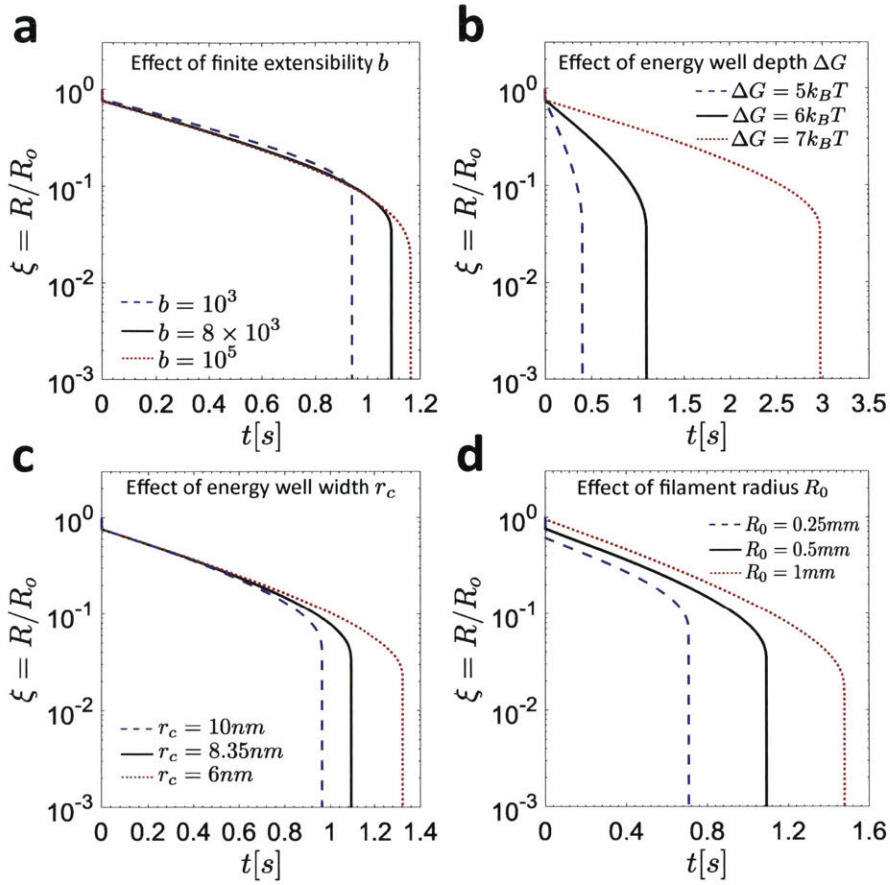

Figure B.4.1: Effect of varying the finite extensibility b (a), the energy well depth ΔG (b), the energy well width r_c (c), and the initial filament radius R_0 (d) on the temporal evolution of the non-dimensional filament radius ξ predicted by the SFEN model. The solid black curves in each model correspond to the original set of parameters defined in Tables 5.1 and 5.2 for the sample at $t_{age} = 0$ h. The dashed blue and dotted red lines correspond to the predictions of the SFEN model with a single parameter changed compared to this original set, with the new value indicated in the figure. In (a), the stickiness parameters associated with each curve are $Sk = 6.3 \times 10^{-4}$ for $b = 10^3$, $Sk = 2.2 \times 10^{-4}$ for $b = 8 \times 10^3$, and $Sk = 6.3 \times 10^{-5}$ for $b = 10^5$, while in (b) $Sk = 2.7 \times 10^{-4}$ for $r_c = 10$ nm, $Sk = 2.2 \times 10^{-4}$ for $r_c = 8.35$ nm, and $Sk = 1.6 \times 10^{-4}$ for $r_c = 6$ nm.

As can be seen from Figure B.4.1, the sensitivity of the SFEN model predictions to the values of the model parameters varies. For instance, as b is changed from $b = 8 \times 10^3$ to $b = 1 \times 10^3$ and from $b = 8 \times 10^3$ to $b = 1 \times 10^5$ (Figure B.4.1a), the slope during the exponential thinning regime remains essentially unchanged, and the time to breakup changes by approximately 15% and 5%, respectively. The SFEN model predictions are more sensitive to the choice of the energy well depth (ΔG) and width (r_c), as well as the initial filament radius R_0 (or, equivalently, the surface tension σ). Increasing or decreasing the energy well depth by $1k_BT$ (Figure B.4.1b) modifies the slope during regime II substantially, and results in an approximately 168% increase or 63% decrease in the time to breakup, respectively. In the case of r_c, as seen in Figure B.4.1c, the time to breakup decreases by approximately

13% as the energy well width is increased from $r_c = 8.35\,\text{nm}$ to $r_c = 10\,\text{nm}$, and increases by approximately 20% as r_c is decreased to $r_c = 6\,\text{nm}$. As for the initial filament radius R_0, the time to breakup varies by approximately 35% as R_0 is either doubled or halved from its original value of $R_0 = 0.5\,\text{mm}$, as seen in Figure B.4.1d. Clearly then, although the numerical values of the SFEN model parameters do all lie within the expected range based on what they represent physically, small modifications to these parameters undoubtedly affect the filament thinning dynamics predicted by the model. As such, independent measurement of the model variables using other experimental techniques (such as estimation of the persistence length l_p [102] and energy well depth [214] from dynamic light scattering data and measurement of the linear viscoelastic spectra and fluid microstructure using atomic force microscopy [215] or microrheology [122]) is essential for quantitatively describing the rheological response of other biopolymer networks using the SFEN model.

Bibliography

[1] R. M. Donlan. Biofilms: Microbial life on surfaces. *Emerging Infectious Diseases*, 8(9):881–890, 2002.

[2] A. Birjiniuk, N. Billings, E. Nance, J. Hanes, K. Ribbeck, and P. S. Doyle. Single particle tracking reveals spatial and dynamic organization of the Escherichia coli biofilm matrix. *New Journal of Physics*, 16(8):085014, 2014.

[3] S. R. Eisenberg and A. J. Grodzinsky. Swelling of articular cartilage and other connective tissues: Electromechanochemical forces. *Journal of Orthopaedic Research*, 3(2):148–159, 1985.

[4] R. Bansil and B. S. Turner. Mucin structure, aggregation, physiological functions and biomedical applications. *Current Opinion in Colloid and Interface Science*, 11:164–170, 2006.

[5] H.-Y. Lee, L. Han, P. Roughley, A. J. Grodzinsky, and C. Ortiz. Age-related nanostructural and nanomechanical changes of individual human cartilage aggrecan monomers and their glycosaminoglycan side chains. *Journal of Structural Biology*, 181(3):264–273, 2013.

[6] H. C. G. de Cagny, B. E. Vos, M. Vahabi, N. A. Kurniawan, M. Doi, G. H. Koenderink, F. C. MacKintosh, and D. Bonn. Porosity governs normal stresses in polymer gels. *Physical Review Letters*, 117(21):217802, 2016.

[7] C. E. Wagner, B. S. Turner, M. Rubinstein, G. H. McKinley, and K. Ribbeck. A rheological study of the association and dynamics of MUC5AC gels. *Biomacromolecules*, 18(11):3654–3664, 2017.

[8] A. L Garland, W. G. Walton, R. D. Coakley, C. D. Tan, R. C. Gilmore, C. A. Hobbs, A. Tripathy, L. A. Clunes, S. Bencharit, M. J. Stutts, L. Betts, M. R. Redinbo, and R. Tarran. Molecular basis for pH-dependent mucosal dehydration in cystic fibrosis airways. *Proceedings of the National Academy of Sciences*, 110(40):15973–15978, 2013.

[9] J. Perez-Vilar and R. C. Boucher. Reevaluating gel-forming mucins' roles in cystic fibrosis lung disease. *Free Radical Biology and Medicine*, 37(10):1564–1577, 2004.

[10] K. B. Smith-Dupont, C. E. Wagner, J. Witten, K. Conroy, H. Rudoltz, K. Pagidas, V. Snegovskikh, M. House, and K. Ribbeck. Probing the potential of mucus permeability to signify preterm birth risk. *Scientific Reports*, 7(1):10302, 2017.

[11] A. V. Bazilevsky, V. M. Entov, and A. N. Rozhkov. Breakup of a liquid bridge as a method of rheological testing of biological fluids. 46(4):613–622, 2011.

[12] C. E. Wagner and G. H. McKinley. Age-dependent capillary thinning dynamics of physically-associated salivary mucin networks. *Journal of Rheology*, 61(6):1309–1326, 2017.

[13] G. W. Scott Blair and J Caffyn. The classification of the rheological properties of industrial materials in the light of power-law relations between stress, strain and time. *Journal of Scientific Instruments*, 19(6):88–93, 1942.

[14] W. M. Gelbart and A. Ben-Shaul. The "new" science of "complex fluids". *Journal of Physical Chemistry*, 100(31):13169–13189, 1996.

[15] H. Singh, M. Boland, and A. Thompson. 2.5.2.4 Milk lipids as an emulsion. In *Milk Proteins - From Expression to Food.* Elsevier, 2nd edition, 2014.

[16] C. W. Bamforth. The foaming properties of beer. *Journal of the Institute of Brewing*, 91(6):370–383, 1985.

[17] A. Jaishankar and G. H. McKinley. A fractional K-BKZ constitutive formulation for describing the nonlinear rheology of multiscale complex fluids. *Journal of Rheology*, 58(6):1751–1788, 2014.

[18] T. M. Squires and T. G. Mason. Fluid mechanics of microrheology. *Annual Review of Fluid Mechanics*, 42:413–438, 2010.

[19] E. M. Furst and T. M. Squires. *Microrheology.* Oxford University Press, New York, 1 edition, 2017.

[20] B. E. Scharfman, A. H. Techet, J. W. M. Bush, and L. Bourouiba. Visualization of sneeze ejecta: steps of fluid fragmentation leading to respiratory droplets. *Experiments in Fluids*, 57(2):24, 2016.

[21] R. H. Ewoldt, M. T. Johnston, and L. M. Caretta. Experimental challenges of shear rheology: How to avoid bad data. In *Complex Fluids in Biological Systems*, pages 207–241. Springer, 2015.

[22] W. G. Chen, J. Witten, S. C. Grindy, N. Holten-Andersen, and K. Ribbeck. Charge influences substrate recognition and self-assembly of hydrophobic FG sequences. *Biophysical Journal*, 113(9):2088–2099, 2017.

[23] R. B. Bird, R. C. Armstrong, and O. Hassager. *Dynamics of Polymeric Liquids, Fluid Mechanics (Volume 1).* Wiley and Sons, 1987.

[24] J. M. Dealy and K. F. Wissburn. *Melt rheology and its role in plastics processing: theory and applications.* Van Nostrand Reinhold, 1990.

[25] R. H. Ewoldt, A. E. Hosoi, and G. H. McKinley. New measures for characterizing nonlinear viscoelasticity in large amplitude oscillatory shear. *Journal of Rheology*, 52(6):1427–1458, 2008.

[26] D. Giles and C. Macosko. Shear Rheometry.

[27] A. Jaishankar. *The linear and nonlinear rheology of multiscale complex fluids.* PhD thesis, MIT, 2014.

[28] R. G. Larson. *The structure and rheology of complex fluids.* Oxford University Press, New York, 1999.

[29] A. Jaishankar, M. Wee, L. Matia-Merino, K. K. T. Goh, and G. H. McKinley. Probing hydrogen bond interactions in a shear thickening polysaccharide using nonlinear shear and extensional rheology. *Carbohydrate Polymers*, 123:136–145, jun 2015.

[30] S. Tabatabaei, H. T. Jahromi, M. F. Webster, P. R. Williams, A. J. Holder, K. E. Lewis, G. A. Davies, L. Griffin, P. Ebden, and C. Askill. A CABER computational-experimental rheological study on human sputum. *Journal of Non-Newtonian Fluid Mechanics*, 222:272–287, 2015.

[31] A. S. Burbidge and B. J. D. Le Révérend. Biophysics of food perception. *Journal of Physics D: Applied Physics*, 49(11):114001, 2016.

[32] G. H. McKinley and T. Sridhar. Filament-stretching rheometry of complex fluids. *Annual Review of Fluid Mechanics*, 34(1):375–415, 2002.

[33] J. M. Zahm, E. Puchelle, C. Duvivier, and J. Didelon. Spinability of respiratory mucous. Validation of a new apparatus: the filancemeter. *Bulletin Européen de Physiopathologie Respiratoire*, 22(6):609–613, 1986.

[34] S. L. Anna and G. H. McKinley. Elasto-capillary thinning and breakup of model elastic liquids. *Journal of Rheology*, 45(1):115–138, 2001.

[35] J. Eggers. Nonlinear dynamics and breakup of free-surface flows. *Reviews of Modern Physics*, 69(3):865–930, 1997.

[36] R. B. Bird, C. F. Curtiss, R. C. Armstrong, and O. Hassager. *Dynamics of polymeric liquids, Kinetic theory (Volume 2).* Wiley and Sons, 1987.

[37] M. S. Green and A. V. Tobolsky. A new approach to the theory of relaxing polymeric media. *The Journal of Chemical Physics*, 14(80), 1946.

[38] N. W. Tschoegl. *The phenomenological theory of linear viscoelastic behavior: an introduction.* Springer-Verlag, Berlin, 1989.

[39] G. W. Scott Blair. The role of psychophysics in rheology. *Journal of Colloid Science*, 2(1):21–32, 1947.

[40] P. G. Nutting. A new general law of deformation. *Journal of the Franklin Institute*, 191(5):679–685, 1921.

[41] G. W. Scott Blair. Analytical and integrative aspects of the stress-strain-time problem. *Journal of Scientific Instruments*, 21(5):80–84, 1944.

[42] A. Jaishankar and G. H. McKinley. Power-law rheology in the bulk and at the interface: quasi-properties and fractional constitutive equations. *Proceedings of the Royal Society A: Mathematical, Physical and Engineering Sciences*, 2012.

[43] T. H. Larsen and E. M. Furst. Microrheology of the liquid-solid transition during gelation. *Physical Review Letters*, 100(14):146001, 2008.

[44] T. G. Mason and D. A. Weitz. Optical measurements of frequency-dependent linear viscoelastic moduli of complex fluids. *Physical Review Leters*, 74(7):1250–1253, 1995.

[45] T. Savin and P. S. Doyle. Static and dynamic errors in particle tracking microrheology. *Biophysical Journal*, 88(1):623–638, 2005.

[46] V. Pelletier and M. Kilfoil. Software Research Tools, Kilfoil Lab, 2007.

[47] J. C. Crocker and E. R. Weeks. Particle tracking using IDL, 2011.

[48] O. Lieleg, I. Vladescu, and K. Ribbeck. Characterization of particle translocation through mucin hydrogels. *Biophysical Journal*, 98(9):1782–1789, 2010.

[49] R. Metzler, J.-H. Jeon, A. G. Cherstvy, and E. Barkai. Anomalous diffusion models and their properties: non-stationarity, non-ergodicity, and ageing at the centenary of single particle tracking. *Physical Chemistry Chemical Physics*, 16(44):24128–24164, 2014.

[50] R. Metzler and J. Klafter. The random walk's guide to anomalous diffusion: a fractional dynamics approach. *Physics Reports*, 339(1):1–77, 2000.

[51] G. D. J. Phillies. In complex fluids the Gaussian Diffusion Approximation is generally invalid. *Soft Matter*, 11(3):580–586, 2015.

[52] P. Georgiades, P. D. A. Pudney, D. J. Thornton, and T. A. Waigh. Particle tracking microrheology of purified gastrointestinal mucins. *Biopolymers*, 101(4):366–377, 2014.

[53] H. Scher and E. W. Montroll. Anomalous transit-time dispersion in amorphous solids. *Physical Review B*, 12(6):2455, 1975.

[54] B. Dybiec. Anomalous diffusion on finite intervals. *Journal of Statistical Mechanics: Theory and Experiment*, 2010(01):P01011, 2010.

[55] I. Y. Wong, M. L. Gardel, D. R. Reichman, E. R. Weeks, M. T. Valentine, A. R. Bausch, and D. A. Weitz. Anomalous diffusion probes microstructure dynamics of entangled F-actin networks. *Physical Review Letters*, 92(17):178101, 2004.

[56] A. V. Weigel, B. Simon, M. M. Tamkun, and D. Krapf. Ergodic and nonergodic processes coexist in the plasma membrane as observed by single-molecule tracking. *Proceedings of the National Academy of Sciences*, 108(16):6438–6443, 2011.

[57] B. Wang, S. M. Anthony, S. C. Bae, and S. Granick. Anomalous yet Brownian. *Proceedings of the National Academy of Sciences*, 106(36):15160–15164, 2009.

[58] F. Evers, C. Zunke, R. D. L. Hanes, J. Bewerunge, I. Ladadwa, A. Heuer, and S. U. Egelhaaf. Particle dynamics in two-dimensional random-energy landscapes: Experiments and simulations. *Physical Review E*, 88(2):022125, 2013.

[59] J. P. Rich, G. H. McKinley, and P. S. Doyle. Size dependence of microprobe dynamics during gelation of a discotic colloidal clay. *Journal of Rheology*, 55(2):273–299, 2011.

[60] Y. Gao and M. L. Kilfoil. Direct imaging of dynamical heterogeneities near the colloid-gel transition. *Physical Review Letters*, 99(7):078301, 2007.

[61] E. S. Frenkel and K. Ribbeck. Salivary mucins in host defense and disease prevention. *Journal of Oral Microbiology*, 7(1):29759, 2015.

[62] L. A. Sellers, A. Allen, E. R. Morris, and S. B. Ross-Murphy. Mucus glycoprotein gels. Role of glycoprotein polymeric structure and carbohydrate side-chains in gel-formation. *Carbohydrate Research*, 178(1):93–110, 1988.

[63] C. T. Nordgård and K. I. Draget. Dynamic responses in small intestinal mucus: Relevance for the maintenance of an intact barrier. *European Journal of Pharmaceutics and Biopharmaceutics*, 95:144–150, 2015.

[64] P. Argüeso and I. K. Gipson. Epithelial mucins of the ocular surface: structure, biosynthesis and function. *Experimental Eye Research*, 73(3):281–289, 2001.

[65] S. K. Linden, P. Sutton, N. G. Karlsson, V. Korolik, and M. A. McGuckin. Mucins in the mucosal barrier to infection. *Mucosal Immunology*, 1(3):183–197, 2008.

[66] J. Dekker, J. W. A. Rossen, H. A. Büller, and A. W. C. Einerhand. The MUC family: An obituary. *Trends in Biochemical Sciences*, 27(3):126–131, 2002.

[67] D. J. Thornton, K. Rousseau, and M. A. McGuckin. Structure and function of the polymeric mucins in airways mucus. *Annual Review of Physiology*, 70:459–486, 2008.

[68] C. L. Hattrup and S. J. Gendler. Structure and function of the cell surface (tethered) mucins. *Annual Review of Physiology*, 70:431–457, 2008.

[69] C. Taylor, K. I. Draget, J. P. Pearson, and O. Smidsrød. Mucous systems show a novel mechanical response to applied deformation. *Biomacromolecules*, 6(3):1524–1530, 2005.

[70] M. Kesimer, A. M. Makhov, J. D. Griffith, P. Verdugo, and J. K. Sheehan. Unpacking a gel-forming mucin: a view of MUC5B organization after granular release. *American Journal of Physiology Lung Cellular and Mollecular Physiology*, 298(1):L15–L22, 2010.

[71] K. Godl, M. E. V. Johansson, M. E. Lidell, M. Mörgelin, H. Karlsson, F. J. Olson, J. R. Gum, Jr., Y. S. Kim, and G. C. Hansson. The N terminus of the MUC2 mucin forms trimers that are held together within a trypsin-resistant core fragment. *Journal of Biological Chemistry*, 277(49):47248–47256, 2002.

[72] D. Ambort, M. E. V. Johansson, J. K. Gustafsson, H. E. Nilsson, a. Ermund, B. R. Johansson, P. J. B. Koeck, H. Hebert, and G. C. Hansson. Calcium and pH-dependent packing and release of the gel-forming MUC2 mucin. *Proceedings of the National Academy of Sciences*, 109(15):5645–5650, 2012.

[73] H. E. Nilsson, D. Ambort, M. Bäckström, E. Thomsson, P. J. B. Koeck, G. C. Hansson, and H. Hebert. Intestinal MUC2 mucin supramolecular topology by packing and release resting on D3 domain assembly. *Journal of Molecular Biology*, 426(14):2567–2579, 2014.

[74] R. Bansil, J. P. Celli, J. M. Hardcastle, and B. S. Turner. The influence of mucus microstructure and rheology in Helicobacter pylori infection. *Frontiers in Immunology*, 4:310, 2013.

[75] M. A. McGuckin, S. K. Lindén, P. Sutton, and T. H. Florin. Mucin dynamics and enteric pathogens. *Nature Reviews Microbiology*, 9(4):265–278, 2011.

[76] R. G. Schipper, E. Silletti, and M. H. Vingerhoeds. Saliva as research material: Biochemical, physicochemical and practical aspects. *Archives of Oral Biology*, 52(12):1114–1135, 2007.

[77] J. P. Celli, B. S. Turner, N. H. Afdhal, R. H. Ewoldt, G. H. McKinley, R. Bansil, and S. Erramilli. Rheology of gastric mucin exhibits a pH-dependent sol-gel transition. *Biomacromolecules*, 8(5):1580–1586, 2007.

[78] S. K. Lai, Y.-Y. Wang, D. Wirtz, and J. Hanes. Micro- and macrorheology of mucus. *Advanced Drug Delivery Reviews*, 61(2):86–100, 2009.

[79] J. P. Celli, B. S. Turner, N. H. Afdhal, S. Keates, I. Ghiran, C. P. Kelly, R. H. Ewoldt, G. H. McKinley, P. So, S. Erramilli, and R. Bansil. Helicobacter pylori moves through mucus by reducing mucin viscoelasticity. *Proceedings of the National Academy of Sciences*, 106(34):14321–14326, 2009.

[80] O. W. Meldrum, G. E. Yakubov, M. R. Bonilla, O. Deshmukh, M. A. Mcguckin, and M. J. Gidley. Mucin gel assembly is controlled by a collective action of non-mucin proteins , disulfide bridges , Ca 2 + -mediated links , and hydrogen bonding. *Scientific Reports*, 8(1):5802, 2018.

[81] B. D. E. Raynal, T. E. Hardingham, D. J. Thornton, and J. K. Sheehan. Concentrated solutions of salivary MUC5B mucin do not replicate the gel-forming properties of saliva. *Biochemical Journal*, 362(Pt 2):289–296, 2002.

[82] B. D. E. Raynal, T. E. Hardingham, J. K. Sheehan, and D. J. Thornton. Calcium-dependent protein interactions in MUC5B provide reversible cross-links in salivary mucus. *Journal of Biological Chemistry*, 278(31):28703–28710, 2003.

[83] A. W. Larhed, P. Artursson, J. Gråsjö, and E. Björk. Diffusion of drugs in native and purified gastrointestinal mucus. *Journal of Pharmaceutical Sciences*, 86(6):660–665, 1997.

[84] J. S. Crater and R. L. Carrier. Barrier properties of gastrointestinal mucus to nanoparticle transport. *Macromolecular Bioscience*, 10(12):1473–1483, 2010.

[85] B. F. Smith and J. T. LaMont. Hydrophobic binding properties of bovine gallbladder mucin. *Journal of Biological Chemistry*, 259(19):12170–12177, 1984.

[86] N. L. Kavanaugh, A. Q. Zhang, C. J. Nobile, A. D. Johnson, and K. Ribbeck. Mucins suppress virulence traits of Candida albicans. *MBio*, 5(6):e01911—-14, 2014.

[87] E. S. Frenkel and K. Ribbeck. Salivary mucins protect surfaces from colonization by cariogenic bacteria. *Applied and Environmental Microbiology*, 81(1):332–338, 2015.

[88] M. Rubinstein and A. N. Semenov. Dynamics of entangled solutions of associating polymers. *Macromolecules*, 34(4):1058–1068, 2001.

[89] D. Snary, A. Allen, and R. H. Pain. Conformational changes in gastric mucoproteins induced by caesium chloride and guanidinium chloride. *Biochemical Journal*, 141(3):641–646, 1974.

[90] M. Boegh and H. M. Nielsen. Mucus as a barrier to drug delivery - Understanding and mimicking the barrier properties. *Basic and Clinical Pharmacology and Toxicology*, 116(3):179–186, 2015.

[91] D. F. Evans, G. Pye, R. Bramley, A. G. Clark, T. J. Dyson, and J. D. Hardcastle. Measurement of gastrointestinal pH profiles in normal ambulant human subjects. *Gut*, 29(8):1035–1041, 1988.

[92] I. Carlstedt, H. Lindgren, J. K. Sheehan, U. Ulmsten, and L. Wingerup. Isolation and characterization of human cervical-mucus glycoproteins. *The Biochemical journal*, 211(1):13–22, 1983.

[93] W. M. Saltzman, M. L. Radomsky, K. J. Whaley, and R. A. Cone. Antibody diffusion in human cervical mucus. *Biophysical Journal*, 66(2):508–515, 1994.

[94] Y.-Y. Wang, S. K. Lai, L. Ensign, W. Zhong, R. Cone, and J. Hanes. The microstructure and bulk rheology of human cervicovaginal mucus are remarkably resistant to changes in pH. *Biomacromolecules*, 14(12):4429–4435, 2013.

[95] D. B. Hill, P. A. Vasquez, J. Mellnik, S. A. McKinley, A. Vose, F. Mu, A. G. Henderson, S. H. Donaldson, N. E. Alexis, R. C. Boucher, and M. G. Forest. A biophysical basis for mucus solids concentration as a candidate biomarker for airways disease. *PloS one*, 9(2):e87681, 2014.

[96] S. Spurr-Michaud, P. Argüeso, and I. Gipson. Assay of mucins in human tear fluid. *Experimental Eye Research*, 84(5):939–950, 2007.

[97] B. Button, L.-H. Cai, C. Ehre, M. Kesimer, D. B. Hill, J. K. Sheehan, R. C. Boucher, and M. Rubinstein. A periciliary brush promotes the lung health by separating the mucus layer from airway epithelia. *Science*, 337(6097):937–941, 2012.

[98] R. Chatelin and P. Poncet. A parametric study of mucociliary transport by numerical simulations of 3D non-homogeneous mucus. *Journal of Biomechanics*, 49(9):1772–1780, 2016.

[99] L. D. Li, T. Crouzier, A. Sarkar, L. Dunphy, J. Han, and K. Ribbeck. Spatial configuration and composition of charge modulates transport into a mucin hydrogel barrier. *Biophysical Journal*, 105(6):1357–1365, 2013.

[100] K. Ribbeck and D. Görlich. The permeability barrier of nuclear pore complexes appears to operate via hydrophobic exclusion. *The EMBO Journal*, 21(11):2664–2671, 2002.

[101] A. J. Grodzinsky. *Fields Forces and Flows in Biological Systems*. Garland Science, New York, 2008.

[102] X. Cao, R. Bansil, K. R. Bhaskar, B. S. Turner, J. T. LaMont, N. Niu, and N. H. Afdhal. pH-dependent conformational change of gastric mucin leads to sol-gel transition. *Biophysical Journal*, 76(3):1250–8, 1999.

[103] H. Yamakawa and M. Fujii. Translational friction coefficient of wormlike chains. *Macromolecules*, 6(3):407–415, 1973.

[104] H. R. Bosshard, D. N. Marti, and I. Jelesarov. Protein stabilization by salt bridges: concepts, experimental approaches and clari cation of some misunderstandings. *Journal of Molecular Recognition*, 17(1):1–16, 2004.

[105] K. R. Bhaskar, D. H. Gong, R. Bansil, S. Pajevic, J. A. Hamilton, B. S. Turner, and J. T. LaMont. Profound increase in viscosity and aggregation of pig gastric mucin at low pH. *American Journal of Physiology-Gastrointestinal and Liver Physiology*, 261(5):G827–G832, 1991.

[106] A. V. Dobrynin, R. H. Colby, and M. Rubinstein. Polyampholytes. *Journal of Polymer Science Part B: Polymer Physics*, 42(19):3513–3538, 2004.

[107] G.-Z. Zheng, G. Meshitsuka, and A. Ishizu. Properties of an amphoteric cellulose derivative containing anionic carboxymethyl and cationic 2-hydroxy-3-(trimethylammonio) propyl substituents. *Journal of Polymer Science Part B: Polymer Physics*, 33(6):867–877, 1995.

[108] S. Assemi, J. Nalaskowski, and W. P. Johnson. Direct force measurements between carboxylate-modified latex microspheres and glass using atomic force microscopy. *Colloids and Surfaces A: Physicochem. Eng. Aspects*, 286(1-3):70–77, 2006.

[109] S. Barany, M. Nagy, and J. Skvarla. Electrokinetic potential of polystyrene particles in polyelectrolyte and polyelectrolyte mixtures solutions. *Colloids and Surfaces A: Physicochemical and Engineering Aspects*, 413:200–207, 2012.

[110] B. S. Schuster, J. S. Suk, G. F. Woodworth, and J. Hanes. Nanoparticle diffusion in respiratory mucus from humans without lung disease. *Biomaterials*, 34(13):3439–3446, 2013.

[111] X. Murgia, P. Pawelzyk, U. F. Schaefer, C. Wagner, N. Willenbacher, and C.-M. Lehr. Size-limited penetration of nanoparticles into porcine respiratory mucus after aerosol deposition. *Biomacromolecules*, 17(4):1536–1542, 2016.

[112] M. T. Valentine, P. D. Kaplan, D. Thota, J. C. Crocker, T. Gisler, R. K. Prud'homme, M. Beck, and D. A. Weitz. Investigating the microenvironments of inhomogeneous soft materials with multiple particle tracking. *Physical Review E*, 64(6):061506, 2001.

[113] A. V. Chechkin, F. Seno, R. Metzler, and I. M. Sokolov. Brownian yet non-Gaussian diffusion: From superstatistics to subordination of diffusing diffusivities. *Physical Review X*, 7(2):021002, 2017.

[114] L. Piculell, K. Thuresson, and O. Ericsson. Surfactant binding and micellisation in polymer solutions and gels: binding isotherms and their consequences. *Faraday Discussions*, 101:307–318, 1995.

[115] A.-L. Kjøniksen, B. Nyström, T. Nakken, O. Palmgren, and T. Tande. Effect of surfactant concentration, pH, and shear rate on the rheological properties of aqueous systems of a hydrophobically modifed chitosan and its unmodified analogue. *Polymer Bulletin*, 38(1):71–79, 1997.

[116] S. M. Hajji, M. B. Errahmani, R. Coudert, R. R. Durand, A. Cao, and E. Taillandier. A comparative study of 1, 2-hexanediol and 1, 2, 3-octanetriol in aqueous solutions by

different physical techniques. *The Journal of Physical Chemistry*, 93(12):4819–4824, 1989.

[117] C. P. Broedersz and F. C. MacKintosh. Modeling semiflexible polymer networks. *Reviews of Modern Physics*, 86(3):995–1036, 2014.

[118] Q. Lu and M. J. Solomon. Probe size effects on the microrheology of associating polymer solutions. *Physical Review E*, 66(6):061504, 2002.

[119] J. H. van Zanten, S. Amin, and A. A. Abdala. Brownian motion of colloidal spheres in aqueous PEO solutions. *Macromolecules*, 37(10):3874–3880, 2004.

[120] A.-M. Philippe, L. Cipelletti, and D. Larobina. Mucus as an arrested phase separation gel. *Macromolecules*, 50(20):8221–8230, 2017.

[121] T. Savin and P. S. Doyle. Statistical and sampling issues when using multiple particle tracking. *Physical Review E*, 76(2):021501, 2007.

[122] R. R. R. Vincent, B. W. Mansel, A. Kramer, K. Kroy, and M. A. K. Williams. Microrheological behaviour and nonlinear rheology of networks assembled from polysaccharides from the plant cell wall. *New Journal of Physics*, 15(035002), 2013.

[123] K. Kroy. Dynamics of wormlike and glassy wormlike chains. *Soft Matter*, 4(12):2323–2330, 2008.

[124] P. Kollmannsberger and B. Fabry. Linear and nonlinear rheology of living cells. *Annual Review of Materials Research*, 41:75–97, 2011.

[125] E. Evans and K. Ritchie. Dynamic strength of molecular adhesion bonds. *Biophysical Journal*, 72(4):1541–1555, 1997.

[126] R. H. Ewoldt, T. M. Winegard, and D. S. Fudge. Non-linear viscoelasticity of hagfish slime. *International Journal of Non-Linear Mechanics*, 46(4):627–636, 2011.

[127] C. P. Broedersz, M. Depken, N. Y. Yao, M. R. Pollak, D. A. Weitz, and F. C. MacKintosh. Cross-link-governed dynamics of biopolymer networks. *Physical Review Letters*, 105(23):1–4, 2010.

[128] L. Leibler, M. Rubinstein, and R. H. Colby. Dynamics of reversible networks. *Macromolecules*, 24(16):4701–4707, 1991.

[129] A. Tripathi, K. C. Tam, and G. H. McKinley. Rheology and dynamics of associative polymers in shear and extension: Theory and experiments. *Macromolecules*, 39(5):1981–1999, 2006.

[130] J. A. Voynow and B. K. Rubin. Mucins, mucus, and sputum. *Chest*, 135(2):505–512, 2009.

[131] J. H. H. Bongaerts, D. Rossetti, and J. R. Stokes. The lubricating properties of human whole saliva. *Tribology Letters*, 27(3):277–287, 2007.

[132] J. R. Stokes and G. A. Davies. Viscoelasticity of human whole saliva collected after acid and mechanical stimulation. *Biorheology*, 44(3):141–160, 2007.

[133] D. Esser, G. Alvarez-Llamas, M. de Vries, D. Weening, R. J. Vonk, and H. Roelofsen. Sample stability and protein composition of saliva: Implications for its use as a diagnostic fluid. *Biomarker Insights*, 3:25–37, 2008.

[134] E. Zussman, A. L. Yarin, and R. M. Nagler. Age- and flow-dependency of salivary viscoelasticity. *Journal of Dental Research*, 86(3):281–285, 2007.

[135] A. Aggazzotti. Modificazioni della viscosità della saliva mista dopo che è stata secreta in rapporto col potere filante e colla tensione superficiale. *Archivio di Fisiologia*, 20:3–15, 1922.

[136] M. Rubinstein and R. H. Colby. *Polymer Physics*. Oxford University Press, 2003.

[137] C. Taylor, A. Allen, P. W. Dettmar, and J. P. Pearson. The gel matrix of gastric mucus is maintained by a complex interplay of transient and nontransient associations. *Biomacromolecules*, 4(4):922–927, 2003.

[138] X. Ye, R. G. Larson, C. Pattamaprom, and T. Sridhar. Extensional properties of monodisperse and bidisperse polystyrene solutions. *Journal of Rheology*, 47(2):443–468, 2003.

[139] H. Lodish, A. Berk, S. L. Zipursky, P. Matsudaira, D. Baltimore, and J. Darnell. *Molecular Cell Biology*. W. H. Freeman and Company, New York, 4 edition, 2000.

[140] F. Tanaka and S. F. Edwards. Viscoelastic properties of physically crosslinked networks Part 1 . Non-linear stationary viscoelasticity. *Journal of Non-Newtonian Fluid Mechanics*, 43(2-3):247–271, 1992.

[141] F. Tanaka and S. F. Edwards. Viscoelastic properties of physically crosslinked networks Part 2. Dynamic mechanical moduli. *Journal of Non-Newtonian Fluid Mechanics*, 43(2-3):273–288, 1992.

[142] A. Vaccaro and G. Marrucci. A model for the nonlinear rheology of associating polymers. *Journal of Non-Newtonian Fluid Mechanics*, 92(2-3):261–273, 2000.

[143] B. H. A. A. van den Brule and P. J. Hoogerbrugge. Brownian dynamics simulation of reversible polymeric networks. *Journal of Non-Newtonian Fluid Mechanics*, 60(2-3):303–334, 1995.

[144] R. B. Bird, P. J. Dotson, and N. L. Johnson. Polymer solution rheology based on a finitely extensible beadspring chain model. *Journal of Non-Newtonian Fluid Mechanics*, 7(2-3):213–235, 1980.

[145] T. S. K. Ng, G. H. McKinley, and R. H. Ewoldt. Large amplitude oscillatory shear flow of gluten dough: A model power-law gel. *Journal of Rheology*, 55(3):627–654, 2011.

[146] V. M. Entov and E. J. Hinch. Effect of a spectrum of relaxation times on the capillary thinning of a filament of elastic liquid. *Journal of Non-Newtonian Fluid Mechanics*, 72(1):31–53, 1997.

[147] D. M. Hoyle, Q. Huang, D. Auhl, D. Hassell, H. K. Rasmussen, A. L. Skov, O. G. Harlen, O. Hassager, and T. C. B. McLeish. Transient overshoot extensional rheology of long-chain branched polyethylenes: Experimental and numerical comparisons between filament stretching and cross-slot flow. *Journal of Rheology*, 57(1):293–313, 2013.

[148] C. Clasen, J. P. Plog, W.-M. Kulicke, M. Owens, C. Macosko, L. E. Scriven, M. Verani, and G. H. McKinley. How dilute are dilute solutions in extensional flows? *Journal of Rheology*, 50:849–881, 2006.

[149] M. Cromer, L. P. Cook, and G. H. McKinley. Extensional flow of wormlike micellar solutions. *Chemical Engineering Science*, 64(22):4588–4596, 2009.

[150] C. Wagner, L. Bourouiba, and G. H. McKinley. An analytic solution for capillary thinning and breakup of FENE-P fluids. *Journal of Non-Newtonian Fluid Mechanics*, 218:53–61, 2015.

[151] B. Hallmark, D. I. Wilson, and N. Pistre. Characterization of extensional rheological filament stretching with a dual-mode Giesekus model. *AIChE Journal*, 62(6):2188–2199, 2016.

[152] R. Prabhakar, S. Gadkari, T. Gopesh, and M. J. Shaw. Influence of stretching induced self-concentration and self-dilution on coil-stretch hysteresis and capillary thinning of unentangled polymer solutions. *Journal of Rheology*, 60(3):345–366, 2016.

[153] M. Renardy. Self-similar breakup of a Giesekus jet. *Journal of Non-Newtonian Fluid Mechanics*, 97(2-3):283–293, 2001.

[154] M. Renardy. Similarity solutions for jet breakup for various models of viscoelastic fluids. *Journal of Non-Newtonian Fluid Mechanics*, 104(1):65–74, 2002.

[155] M. Renardy. Self-similar jet breakup for a generalized PTT model. *Journal of Non-Newtonian Fluid Mechanics*, 103(2-3):261–269, 2002.

[156] M. Renardy. Self-similar breakup of non-Newtonian liquid jets. *Rheology Reviews*, pages 171–196, 2004.

[157] C. E. Wagner, A. C. Barbati, J. Engmann, A. S. Burbidge, and G. H. McKinley. Quantifying the consistency and rheology of liquid foods using fractional calculus. *Food Hydrocolloids*, 69:242–254, 2017.

[158] J. Israelachvili and R. Pashley. The hydrophobic interaction is long range, decaying exponentially with distance. *Nature*, 300:341–342, 1982.

[159] J. R. MacCallum. The kinetics of depolymerization of addition polymers. *European Polymer Journal*, 2(4):413–422, 1966.

[160] M. Anthamatten. Hydrogen bonding in supramolecular polymer networks: glasses, melts, and elastomers. In S. Seiffert, editor, *Supramolecular Polymer Networks and Gels from the series Advances in Polymer Science*, volume 268, chapter 2, pages 47–99. Springer International Publishing, 2015.

[161] J. K. Stille. Step-growth polymerization. *Journal of Chemical Education*, 58(11):862–866, 1981.

[162] M. Jeltema, J. Beckley, and J. Vahalik. Food texture assessment and preference based on mouth behavior. *Food Quality and Preference*, 52:160–171, 2016.

[163] M. M. Ould Eleya and S. Gunasekaran. Rheology of barium sulfate suspensions and pre-thickened beverages used in diagnosis and treatment of dysphagia. *Applied Rheology*, 17(3):33137—-33137, 2007.

[164] M. Nystrom, W. M. Qazi, M. Bulow, O. Ekberg, and M. Stading. Effects of rheological factors on perceived ease of swallowing. *Applied Rheology*, 25(6):40–48, 2015.

[165] K. Wendin, S. Ekman, M. Bülow, O. Ekberg, D. Johansson, E. Rothenberg, and M. Stading. Objective and quantitative definitions of modified food textures based on sensory and rheological methodology. *Food and Nutrition Research*, 54(1):5134, 2010.

[166] G. W. Scott Blair. Rheology of foodstuffs. *Periodica Polytechnica Chemical Engineering*, 16(1):81–84, 1972.

[167] R. K. Schofield and G. W. Scott Blair. The relationship between viscosity, elasticity and plastic strength of a soft material as illustrated by some mechanical properties of flour dough IV - The separate contributions of gluten and starch. *Proceedings of the Royal Society of London A: Mathematical, Physical and Engineering Sciences*, 160(900):87–94, 1937.

[168] J. L. Kokini. Predicting the rheology of food biopolymers using constitutive models. *Carbohydrate Polymers*, 25(4):319–329, 1994.

[169] G. W. Scott Blair and F. M. V. Coppen. The subjective conception of the firmness of soft materials. *The American Journal of Psychology*, pages 215–229, 1942.

[170] R. Simpson, A. Jaques, H. Nuñez, C. Ramirez, and A. Almonacid. Fractional calculus as a mathematical tool to improve the modeling of mass transfer phenomena in food processing. *Food Engineering Reviews*, 5(1):45–55, 2013.

[171] M. Oroian, S. Amariei, I. Escriche, and G. Gutt. A viscoelastic model for honeys using the time-temperature superposition principle (TTSP). *Food and Bioprocess Technology*, 6(9):2251–2260, 2013.

[172] K.-W. Song, H.-Y. Kuk, and G.-S. Chang. Rheology of concentrated xanthan gum solutions: Oscillatory shear flow behaviour. *Korea-Australia Rheology Journal*, 18(2):67–81, 2006.

[173] L. A. Quinchia, C. Valencia, P. Partal, J. M. Franco, E. Brito-de la Fuente, and C. Gallegos. Linear and non-linear viscoelasticity of puddings for nutritional management of dysphagia. *Food Hydrocolloids*, 25(4):586–593, 2011.

[174] T. J. Faber, A. Jaishankar, and G. H. McKinley. Describing the firmness, springiness and rubberiness of food gels using fractional calculus. Part I: Theoretical framework. *Food Hydrocolloids*, 62:311–324, 2017.

[175] T. J. Faber, A. Jaishankar, and G. H. McKinley. Describing the firmness, springiness and rubberiness of food gels using fractional calculus. Part II: Experiments on semi-hard cheese. *Food Hydrocolloids*, 62:325–339, 2017.

[176] F. W. Wood. Psychophysical studies on the consistency of liquid foods. *Rheology and Texture of Food Stuffs, SCI Monograph*, (27):40–49, 1968.

[177] M. Atherton, N. Bellis-Smith, J. A. Y. Cichero, and M. Suter. Texture-modified foods and thickened fluids as used for individuals with dysphagia: Australian standardised labels and definitions. *Nutrition and Dietetics*, 64(SUPPL. 2):S53–S76, 2007.

[178] N. K. Mathur. Miscellaneous, less common galactomannans and glucomannans. In *Industrial Galactomannan Polysaccharides*, pages 145–156. CRC Press, 2011.

[179] N. K. Mathur. Guar Gum. In *Industrial Galactomannan Polysaccharides*, pages 61–92. CRC Press, 2011.

[180] C. E. Wagner, A. C. Barbati, J. Engmann, A. S. Burbidge, and G. H. McKinley. Apparent shear thickening at low shear rates in polymer solutions can be an artifact of non-equilibration. *Applied Rheology*, 26:54091, 2016.

[181] J. B. Freund and R. H. Ewoldt. Quantitative rheological model selection: Good fits versus credible models using Bayesian inference. *Journal of Rheology*, 59(3):667–701, 2015.

[182] R. L. Bagley and P. J. Torvik. A theoretical basis for the application of fractional calculus to viscoelasticity. *Journal of Rheology*, 27(3):201–210, 1983.

[183] R. L. Bagley and P. J. Torvik. On the fractional calculus model of viscoelastic behavior. *Journal of Rheology*, 30(1):133–155, 1986.

[184] A. W. Wharmby and R. L. Bagley. Generalization of a theoretical basis for the application of fractional calculus to viscoelasticity. *Journal of Rheology*, 57(5):1429–1440, 2013.

[185] H. Schiessel, R. Metzler, A. Blumen, and T. F. Nonnenmacher. Generalized viscoelastic models: their fractional equations with solutions. *Journal of Physics A: Mathematical and General*, 28(23):6567–6584, 1995.

[186] V. Adibnia and R. J. Hill. Universal aspects of hydrogel gelation kinetics, percolation and viscoelasticity from PA-hydrogel rheology. *Journal of Rheology*, 60(4):541–548, 2016.

[187] E. Choppe, F. Puaud, T. Nicolai, and L. Benyahia. Rheology of xanthan solutions as a function of temperature, concentration and ionic strength. *Carbohydrate Polymers*, 82(4):1228–1235, 2010.

[188] V. R. Raju, E. V. Menezes, G. Marin, W. W. Graessley, and L. J. Fetters. Concentration and molecular weight dependence of viscoelastic properties in linear and star polymers. *Macromolecules*, 14(6):1668–1676, 1981.

[189] Y. Heo and R. G. Larson. Universal scaling of linear and nonlinear rheological properties of semidilute and concentrated polymer solutions. *Macromolecules*, 41(22):8903–8915, 2008.

[190] Nestle Health Science. Resource Thicken Up Clear, 2012.

[191] V. Sharma and G. H. McKinley. An intriguing empirical rule for computing the first normal stress difference from steady shear viscosity data for concentrated polymer solutions and melts. *Rheologica Acta*, 51(6):487–495, 2012.

[192] M. I. Capitani, L. J. Corzo-Rios, L. A. Chel-Guerrero, D. A. Betancur-Ancona, S. M. Nolasco, and M. C. Tomás. Rheological properties of aqueous dispersions of chia (Salvia hispanica L.) mucilage. *Journal of Food Engineering*, 149:70–77, 2015.

[193] S. B. Ross-Murphy. Structure–property relationships in food biopolymer gels and solutions. *Journal of Rheology*, 39(6):1451–1463, 1995.

[194] Y. Wu, W. Ding, L. Jia, and Q. He. The rheological properties of tara gum (Caesalpinia spinosa). *Food Chemistry*, 168:366–371, 2015.

[195] A. Ziolkovska. Laws of flaxseed mucilage extraction. *Food Hydrocolloids*, 26(1):197–204, 2012.

[196] V. Kontogiorgos, I. Margelou, N. Georgiadis, and C. Ritzoulis. Rheological characterization of okra pectins. *Food Hydrocolloids*, 29(2):356–362, 2012.

[197] G. W. Scott Blair. The measurement of the rheological properties of some industrial materials. *Journal of Scientific Instruments*, 17(7):169, 1940.

[198] G. W. Scott Blair and F. M. V. Coppen. Psycho-physical significance of the dissipation coefficient of soft materials. *Nature*, 149(3766):22–23, 1942.

[199] D. C. Broome and L. Bilmes. Rheology of plastic materials. *Nature*, 147(3719):176, 1941.

[200] W. G. Wearmouth and I. I. Berenblut. Flow properties of some thermoplastics. *Nature*, 148(3740):26–27, 1941.

[201] R. K. Gupta. *Polymer and composite rheology.* CRC Press, New York, 2nd edition, 2000.

[202] M. Adam and M. Delsanti. Viscosity and longest relaxation time of semi-dilute polymer solutions: I. Good solvent. *Journal de Physique*, 44(10):1185–1193, 1983.

[203] Hydramotion. Hydramotion units of viscosity.

[204] F. C. Chretien, P. Engelmann, and R. Dubois. The variation of the mean spinability of human cervical mucus throughout the various stages of reproductive life. Automatic measurement and statistical study. *European Journal of Obstetrics and Gynecology and Reproductive Biology*, 9(5):289–297, 1979.

[205] A. S. Critchfield, G. Yao, A. Jaishankar, R. S. Friedlander, O. Lieleg, P. S. Doyle, G. McKinley, M. House, and K. Ribbeck. Cervical mucus properties stratify risk for preterm birth. *PloS one*, 8(8):e69528, 2013.

[206] D. J. Pine, D. A. Weitz, P. M. Chaikin, and E. Herbolzheimer. Diffusing-wave spectroscopy. *Physical Review Letters*, 60(12):1134–1137, 1988.

[207] R. D. Groot, A. Bot, and W. G. M. Agterof. Molecular theory of the yield behavior of a polymer gel: Application to gelatin. *The Journal of Chemical Physics*, 104(22):9220–9233, 1996.

[208] S. Kheirandish, I. Gubaydullin, W. Wohlleben, and N. Willenbacher. Shear and elongational flow behavior of acrylic thickener solutions. Part I: Effect of intermolecular aggregation. *Rheologica Acta*, 47(999), 2008.

[209] S. Kheirandish, I. Gubaydullin, and N. Willenbacher. Shear and elongational flow behavior of acrylic thickener solutions. Part II: effect of gel content. *Rheologica Acta*, 48(4):397–407, 2009.

[210] H. Storz, U. Zimmermann, H. Zimmermann, and W.-M. Kulicke. Viscoelastic properties of ultra-high viscosity alginates. *Rheologica Acta*, 49(2):155–167, 2010.

[211] C. Rodríguez-Rivero, L. Hilliou, E. M. Martín del Valle, and M. A. Galán. Rheological characterization of commercial highly viscous alginate solutions in shear and extensional flows. *Rheologica Acta*, 53(7):559–570, 2014.

[212] M. Ahmadi, L. G. D. Hawke, H. Goldansaz, and E. Van Ruymbeke. Dynamics of entangled linear supramolecular chains with sticky side groups: Influence of hindered fluctuations. *Macromolecules*, 48(19):7300–7310, 2015.

[213] T. Annable, R. Buscall, R. Ettelaie, and D. Whittlestone. The rheology of solutions of associating polymers: Comparison of experimental behavior with transient network theory. *Journal of Rheology*, 37(4):695–726, 1993.

[214] C. Semmrich, T. Storz, J. Glaser, R. Merkel, A. R. Bausch, and K. Kroy. Glass transition and rheological redundancy in F-actin solutions. *Proceedings of the National Academy of Sciences*, 104(51):20199–20203, 2007.

[215] J. Alcaraz, L. Buscemi, M. Grabulosa, X. Trepat, B. Fabry, R. Farré, and D. Navajas. Microrheology of human lung epithelial cells measured by atomic force microscopy. *Biophysical Journal*, 84(3):2071–2079, 2003.